The passage from microstrip to pixel silicon detectors for tracking particles in space

Author
Ester RICCI

Supervisor
Dr. Roberto IUPPA

UNIVERSITÀ DI TRENTO

Abstract

Tracking particle in space is a crucial instance on a large number of space experiments. Measurements of charged cosmic rays based on spectrometers, observation of γ-rays, study of space weather and many other applications require systems equipped with tracking detectors. The sensitive area of detectors required for tracking spans from cm^2 to m^2.

Silicon microstrip detectors have been the elective technology for tracking particles in space for several decades. Their stability, reliability and low power consumption are supported by years of expertise and provided a vast number of significant results on fundamental physics, reached with different experiments.

An example of magnetic spectrometers are AMS-02, operated on International Space Station, and the satellite-borne PAMELA, that measure the charged component of cosmic rays and use tracking planes immersed in a magnetic field produced by permanent magnets to discriminate matter from antimatter. AMS-02 mounts several squared meters of microstrip tracker.

The strip technology also has some limits. The spatial resolution depends on the pitch of the strips implanted on silicon buffer, that depends on the capabilities of the facility in charge of device construction. The fabrication sites have to use dedicated infrastructures, making costs relatively higher than the past. Moreover, it is difficult to reduce the detector thickness below about 150 μm. This thickness impacts on measurements because of multiple scattering and reduces the lower threshold of low energy nuclear experiments.

Another problem arises when the detector operates in radiation-dense environment. When the same frame shows multiple hits, the correct reconstruction of each interaction point is subject to degeneracy, due to the ambiguity in associating $x-$ and $y-$hits in the microstrip sensor. The problem worsens if we consider that microstrips show equivalent charge noise generally up to hundreds of electrons if we take into account all the contributions from readout electronics. The resulting signal-to-noise ratio is generally good, but rarely exceeding 10 for Minimum Ionising Particles (MIP).

The migration towards a new technology based on pixel devices is interesting because it solves some of these limitations. In particular the hit position is uniquely defined by the position of the pixels involved in the event and pixel detectors can be thinned down to about 50 μm, with a potential gain in resolution.

This thesis focuses on Monolithic Active Pixel Sensors (MAPS). They have

the advantage, with respect to both the microstrip detectors and the other pixel families, of having the first stages of readout (front-end amplification, discrimination, digitisation and zero suppression) included on the sensor substrate.

The detectors are realised with standard CMOS technology, the same used by foundries for most of commercial applications. Once the design is defined, the mass production of the devices is possible, and it reduces the cost of the single detector. Other pixel detectors do not provide this advantage since the design of sensors is based on different custom technologies, and after the production, the detector must be bump bonded to a readout chip, an expensive and low-yield technique.

MAPS also have some limits. The most critical for the use in space is power consumption. A second relevant problem to face is that most of the devices realised with this technique have a digital readout, that does not allow measurement of dE/dx, important for particle identification. The requirement of space experiments to cover large surfaces with a tracking detector implies that using pixels the number of channels to handle increases. MAPS approach solves this issue by including on the detector a smart readout that passes to the DAQ system only data from pixels interested by the event.

The MAPS detectors have been proposed for the first time at the end of the nineties. The technology reached maturity in the last years. The ALICE experiment, first of the four main LHC experiments, have installed MAPS detectors for its Inner Tracker Upgrade. For the upgrade the collaboration designed a new MAPS detector, ALPIDE. It is realised by TowerJazz foundry in 180 nm technology. The pixel pitch is 28 μm. The matrix is composed of 512×1024 pixels, for a total surface of 1.5×3 cm^2. Although smaller if compared to microstrip ladders, that can reach several tenths of squared cm, the ALPIDE is one of the largest detector realised with this technology.

Among the properties of ALPIDE, one particularly interesting for the space application is low power consumption. In ALICE, the low power consumption is required because of the difficulties of power distribution and cooling of the Inner Tracker. The power density is still one order of magnitude higher than for microstrip, but it starts to be interesting for space applications.

In this thesis, we explore the possibility to use ALPIDE to realise the tracker for the second High Energy Particle Detector (HEPD-02), a payload of the second China Seismo-Electromagnetic Satellite (CSES-02). The CSES constellation is devoted to the observation of Earth from space and in particular to the study of ionosphere perturbation that might be related to seismic activity on Earth.

We organised the study into two parts. The first is dedicated to the optimisation of the detector for space, dealing with the power consumption reduction, thermal control and space compliance tests, another section is devoted to the study of the ALPIDE response to low energy nuclei.

The section devoted to space compliance starts with a description of the strategies for power consumption reduction. Some strategies are applied to the detector (use of low-speed lines, smart clock distribution) and require an optimised design of the full tracker and trigger. The design of the different

sub-detectors allows distribution of the clock only to a limited section that has a higher probability of being involved in the event. With this approach, we can keep the power consumption of the full tracker below 10 W, as required by the design limits. High power consumption has a large impact on the temperature control of the device. The ALPIDE has an ideal operative temperature of about $30°$, which must be kept constant on the whole detector. ALICE cools down the detector with a water-based system, a solution not applicable in space, where convection is discouraged. A carbon fibre cold plate, designed to optimise the thermal conduction, is applied to control the temperature. The carbon fibre placement is studied to minimise the thickness of the plate and the impact of inert material on tracking performance.

The thesis reports the results of various tests of space compliance made on a modified ALICE tracker module, an engineering model of the HEPD-02 module. It was made of 14 ALPIDE detectors disposed into two columns and glued and wire bonded to a Flexible Printed Circuit (FPC). On the other side, the detectors are glued to a carbon fibre plate. The device has been tested according to the requirements of the Chinese Space Agency for vibrations and in thermal-vacuum.

A study of the response of the detector to low energy nuclei has been also carried out. The HEPD-02 detector is devoted to the detection of electrons between 3 and 150 MeV and protons between 30 and 300 MeV. We base the study on measurements, taken with protons and low energy nuclei at different test facilities in Italy, as well as simulations. Measurements have been analysed with different tools and used to build a model of the detector response. The only observable of the detector is the cluster, and in particular on the cluster size, i.e. the number of pixels over the set threshold for each interaction. The analysis characterises the dependence of the cluster dimension on the energy deposited in silicon by the particle. The energy release inside ALPIDE has been evaluated using GEANT4 simulations of the beam tests. The values obtained have been used as an input for the analysis and to initialise the charge diffusion process in the device in a second simulation tool, Synopsis TCAD. The TCAD simulation includes the electrical properties of silicon and reproduces the detector structure and the electrical property of the materials. The simulation results have been used to verify our knowledge of the detector details, evaluated as the capability of the simulation to reproduce the experimental data. The simulation is the base of a tool that I developed to predict the cluster size as a function of a given number of parameters. This tool works after the GEANT4 simulation and provides essential information for the event reconstruction software of the experiment.

In conclusion, this work reports on space compliance tests performed on the ALPIDE sensor, demonstrating technology readiness level 7 on the scale of space agencies. The dependence of the observed cluster size on the energy deposit has been fully characterised for highly ionising particles. This parametrisation will be a crucial element of the event reconstruction and particle identification algorithms of the HEPD-02 experiment. Given the energy of the nuclei under consideration, this study contains information useful for applications in proton

and hadrotherapy.

Contents

List of Figures

9

12

List of Tables

14

Acronyms

ADC Analog to Digital Converter.

ALICE A Large Ion Collider Experiment.

ALPIDE ALice PIxel DEtector.

AMS Alpha Magnetic Spectrometer.

APP AstroParticle Physics.

APSS Azienda Provinciale per i Servizi Sanitari.

ARCADIA Advanced Readout CMOS Architecture with Depleted Integrated sensor Arrays.

ASIC Application Specific Integrated Circuit.

BIRD Battery Operated Independent Radiation Detector.

BTF Beam Test facility.

CEPC Circular Electron Positron Collider.

CMB Compressed Baryonic Matter.

CMOS Complementary Metal-Oxide Semiconductor.

CS Cluster Size.

CSES China Seismo-Electromagnetic Satellite.

CTRL Control Line.

DAC Digital to Analog Converter.

DAMPE DArk Matter PArticle Explorer.

DAQ Data Aquisition.

DBSCAN Density-Based Spatial Clustering of Applications with Noise.

DTU Data Transmission Unit.

DUT Device Under Test.

ECAL Electromagnetic Calorimeter.

EL Event Length.

ENC Equivalent Noise Charge.

FBK Fondazione Bruno Kessler.

FIFO Fan-In Fan-Out.

FPC Flexible Printed Circuit.

FPGA Field Programmable Gate Array.

FWHM Full Width at Half Maximum.

GEANT GEometry ANd Tracking.

GRB γ-Ray Burst.

HEPD High Energy Particle Detector.

HERD High-Energy cosmic Radiation Detector.

HFT Heavy Flavour Tracker.

HIC Hybrid Integrated Circuit.

IB Inner Barrel.

IC Intrinsic Cluster Size.

INFN Istituto Nazionale di Fisica Nucleare.

ISS International Space Station.

ITS Inner Tracking System.

LAT Large Area Telescope.

LET Linear Energy Transfer.

LHC Large Hadron Collider.

LYSO Lutetium-yttrium oxyorthosilicate.

MAPS Monolithic Active Pixel Sensors.

MATISSE Monolithic AcTIve pixel SenSor Electronics.

MIMOSA Minimum Ionising particle MOS Active Pixel Sensor.

MIP Minimum Ionising Particle.

MOS Metal-Oxide Semiconductor.

MOSAIC MOdular System for Acquisition, Interface and Control.

MVD Micro Vertex Detector.

NIM Nuclear Instrument Module.

nMOS n-type Metal-Oxide Semiconductor.

NUD Neutron Detector.

OB Outer Barrel.

PAMELA Payload for Antimatter Matter Exploration and Light-nuclei Astrophysics.

PLL Phase Locked Loop.

pMOS p-type Metal-Oxide Semiconductor.

PMT Photo Multiplier Tube.

PSD Plastic Scintillator Detector.

PSI Paul Scherrer Institute.

PTC Proton Therapy Centre.

QGP Quark Gluon Plasma.

REM Radiation Environment Monitor.

RICH Ring-Imaging Cherenkov detector.

RMS Root Mean Square.

SDE Sentaurus Device Editor.

SDEVICE Sentaurus Device.

SERMS Studio degli Effetti delle Radiazioni sui Materiali per lo Spazio.

SN Signal-to-Noise.

SPS Super Proton Synchrotron.

spTAB Single Point Tape Automated Bonding.

STK Silicon Tungsten Tracker.

TCAD Technology Computer-Aided Design.

TF Transfer Function.

TIFPA Trento Institue for Fundamental Physics and Applications.

TOF Time Of Flight.

TRD Transition Radiation Detector.

VA Voltage Amplifier.

VME Versa Module Europa.

Chapter 1

The measurement of charged particle trajectories in space

Particle detection in space started with the very beginning of space exploration. Several studies from different experiments on balloons, run since 1910, had shown that the radioactivity increases with the altitude [90].

The interest in tracking the particle direction came later when the technologies for tracking particles started to be available, and space experiments started to design experiments based on this kind of devices.

Before reaching Earth, differently from photons and neutrinos, charged particles interact with the interstellar medium, that scatters and absorbs particles from astrophysical sources. These deviations are the intrinsic limit of the position resolution of the source of a particle or a burst of particles. Nevertheless, tracking can provide interesting information to improve the knowledge of a number of physical open problems.

The anisotropy of the cosmic ray distribution is another problem that can be investigate with a detector sensitive to the primary particle arrival direction [56] [17] [25] [3]. The anisotropy is in principle connected only to the propagation processes since the information on the particle source is almost completely lost. The main factors that modify particle trajectories are the interaction with galactic magnetic fields and also, to a lesser extent, with the interstellar medium. The study of this anisotropy provides information on the propagation models, and it is an object of investigation. Most of the results in this field have been carried out with detectors on Earth, mainly because these indirect measurements explore an energy range higher than the experiments in space [16].

At lower energy s tracking detector is useful to study the particles trapped in the Van Allen belts. Explorer I was the first mission that reported the observation of this particle excess in regions around Earth. Explorer III confirmed the

result. The analysis of the collected data allowed Van Allen to propose models for both the structure and composition of the trapped particles belts, that are named after him [87].

The study of trapped radiation gives some interesting insights on the structure of the Earth magnetic field and provides information on the interaction mechanisms between lithosphere, atmosphere and ionosphere.

The energy of this kind of radiation ranges up to several hundreds of MeV for protons and tens of MeV for electrons [89]. In this range the tracking of particles is significantly affected by multiple scattering inside the detector itself. The effect is particularly relevant for low-energy electrons.

A precise measurement of the incidence angle of the particle with respect of the detector is the key to reconstruct the particle trajectory inside the magnetic field. By knowing the local geomagnetic field direction [89] and intensity, for which several models are available, it is possible to reconstruct the pitch angle and provide information on the particle history.

Tracking detectors are also useful to measure e^+/e^- pairs produced by γ-rays conversion, or combined with a magnetic field, to evaluate the energies of particles not contained in calorimeters.

The study of the electron and positron production from γ annihilation is one possible measurement that can be realised with tracking detectors. It is possible to design a system based on alternated layers of dense material and detector that facilitates the conversion into e^+/e^- couple, then measuring the total energy of the induced shower and inferring the arrival direction of the photon from the e^+/e^- tracks.

The shower can be studied in more detail if the single particle is identifiable, i.e. if sensitive layers are finely segmented. Most of the latest missions devoted to γ-ray astrophysics apply this sampling approach. The best example of this structure of tracking detector was GLAST [21], then realised with some upgrades on the project as FERMI LAT [19], that will be discussed later in this chapter.

Tracking detector can also be used for the study of charged components of cosmic rays. In particular, they are used in spectrometers to extrapolate the momentum of the high energy components of cosmic rays. In this approach, several tracking planes are located inside a region where a magnet produces an intense magnetic field. The magnetic field deflects the charged particles that cross the tracking planes. From the hit positions in the different layers, it is possible to calculate the curvature of the track. This method allows identifying both the sign of the particle charge and the energy in a defined range. Magnetic field strength and tracking spatial resolution define the limits on the energy range of experiments. The most energetic particles undergo a smaller deflection, and a good spatial resolution is required to detect them.

Measurements collected with spectrometers provide information for a wide number of scientific purposes. It is crucial for the investigation of matter-antimatter asymmetry and the baryogenesis problem. Being able to measure the charge of the incoming particles, matched with other particle identification techniques, that allow to measure the mass of the particles, it is possible to separate protons and electrons from antiprotons and positrons. The study of

the relative fractions of the species has given remarkable results, as the positron fraction anomaly [6] [9], that are still under investigation.

1.1 Detection techniques

Position-sensitive detectors can be realised with different technologies. In principle, if a detector readout can be finely segmented, it can be used for particle tracking.

Ground-based experiments trackers can rely on two different technologies, depending on the spatial resolution required for the measurement and the surface to be covered. For high-resolution and relatively small surface detectors, silicon detectors are the most indicated solution [27].

When the surface to be covered becomes extremely large, for example for the most external layers of high energy physics experiments at LHC (ATLAS and CMS) the use of gaseous detectors offers a good compromise between spatial resolution and costs of realisation and operation of the devices.

The second solution is cost-effective and easy to assemble and operate on the ground, but it is difficult to be adapted for space. The gas that fills the gap of the detector deteriorates with particle interactions and needs to be processed to preserve the detection performance. The complexity of this process is not always acceptable in space missions. Another problem is that the gas needs the periodically refill if the experiment's lifetime is too long. Although refilling is quite simple on the ground, it is impossible in space, but for experiments hosted on International Space Station (ISS). Moreover, the weight of gas supplies has an impact on design and mass budget during the mission preparation. For all these reasons, gas detectors are not so common in space, in particular for missions with long life span.

An example of gas detector operating in space is the Transition Radiation Detector (TRD) of the Alpha Magnetic Spectrometer (AMS-02), operating on ISS since May 2011. The straw tubes that compose the detector are filled with a Xe/CO_2 (80%/20%) mixture at 1 bar. To compensate the gas losses, pressure is monitored and kept stable by refilling the system with gas from a vessel of Xe and a vessel of CO_2 installed on ISS. The vessels can be refilled with the supplies regularly shipped to the ISS [52].

It is difficult but possible to operate gaseous detectors in space, at least if volumes are small as for TRD detectors. Coverage of large surfaces, as required for particle tracking, is even more challenging and in most cases there exists alternatives that are easier to handle and provide better tracking performance.

1.1.1 Silicon strip detectors

Silicon detectors are the elective technology for tracking particle in space. There are two main families of silicon trackers: strip detectors and pixels. Pixel technologies will be described in detail in chapter 2. This chapter focuses on strip detectors, used to realise all the trackers already in use in space.
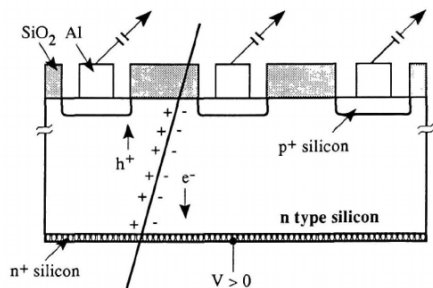
Figure 1.1: Schematic of a silicon particle detector [67].

A charged particle interacting with a material deposits a fraction of its energy, mainly by ionisation. Silicon detector are realised to collect the charge produced by the interaction. The design of silicon detector is based on p-n junction behaviour. Between the p and n layers, the charge distribution forms a strong electric field region. Application of a reverse bias expands the region interested by electric field (depletion region.

Since the thickness of this depletion region is inversely proportional to the doping, the best configuration for a detector is to realise a lightly doped silicon buffer of one type, for example n, and to implant on the surface a thin layer of heavily doped p layer, as shown in figure 1.1.

To realise a position-sensitive detector, the p-layer on the detector surface is implanted in strips. To optimise the device and reduce the bias required to extend the depletion region to the whole buffer, a heavily doped layer of silicon, activated with the same doping of the substrate, is applied on the other side of the wafer. It is also possible to implant the back layer in strips, oriented perpendicularly to the strips on top layer, to provide a point measurement using a single layer of silicon [67].

Strips are covered with a thin aluminium layer to apply bias and collect the current signal. The contact is usually wire bonded to the readout electronics, composed at least by a charge amplifier and an Analog to Digital Converter (ADC) that digitises the signal. The following stages of the readout depend on the aims of the tracker inside of the experiment.

The most important feature of silicon detectors is spatial resolution. Silicon strip space resolution depends on several elements that it is possible to group into two categories: those due to intrinsic fluctuations of interaction and charge collection and those due to noise of detector and readout electronics.

The first set of effects include the statistical fluctuation of energy loss, that

changes the number of carriers produced by the particle, and the effects of drift and diffusion in particle collection. The statistical fluctuation depends on the interaction of the particle with the matter. The drift and diffusion play an essential role, and knowledge and characterisation of these phenomena can help in detector design and operations. The drift speed depends on the electric field inside the silicon wafer, that can be tuned, within certain limits, by adjusting the bias applied to the detector. To maximise the efficiency of charge collection, the depletion region must involve the whole detector. By increasing the voltage, the electric field strength enhances, and the drift speed of charges towards collection electrodes increases. If a single strip collects all the signal, the limit on the spatial resolution will be the strip pitch. If more strips share the signal and the detector signal readout is analog[1], it is possible to apply simple algorithms to obtain a better estimation of the particle's impact point. Collection on multiple strips happens if there is enough ionisation in silicon and if collection time is long enough to allow electrons to arrive to electrodes in time. For a depleted detector, 300 μm thick, a diffusion radius of about 10 μm is expected, that decreases for high values of the electric field [82].

The second group of parameters includes the strip and readout pitch and the noise introduced by the electronics. Their optimisation is the main objective of the detector design stage. The most intuitive way to improve spatial resolution is to realise thinner strips. The strip dimensions are limited by the technology, the cost and readout complexity. Another limit is that the signal will be lower than when collected by a single strip, demanding for more sensitive readout electronic.

It is possible to improve the spatial resolution for a fixed pitch of the detector microstrip by inserting floating strips between readout strips, as shown in figure 1.2 [54]. This approach reduces the effective pitch of the detector. The charge collected by the intermediate diodes is then transferred to the readout by capacitive coupling. The total amount of charge is affected by losses due to inefficiencies but the spatial resolution is sensibly improved.

Characterisation of the noise introduced by the electronic readout is essential because the signal produced by the impinging particle can be small, in particular when more strips share the charge from the interaction.

The main contributions to the noise of the readout is the sum of a constant part, depending on the single experiment, and a part that depends on the capacitance of the strip to its neighbours and the back plane. The equivalent noise charge (ENC) can be calculated as [67]:

$$ENC = \alpha + \beta C$$

Another contribution to the electron noise comes from the detector leakage current of the detector and bias resistors [67]. For a leakage current I, the ENC

---

[1]Charge sharing impacts on resolution also in case of digital readout detectors. The problem will be discussed in chapter 2.2.1 for pixel detector.
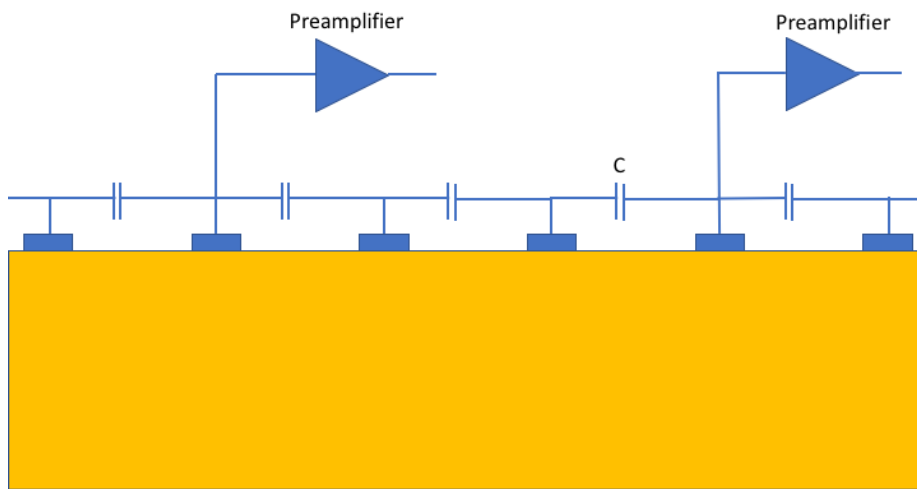
Figure 1.2: Schematic view of floating microstrip.

is given by:

$$ENC = \frac{e}{q} \times \sqrt{\frac{qIT_p}{4}}$$

where e is natural logarithm base, q is the electron charge , T_p is the peaking time.

Contribution due to bias resistor is given by the expression:

$$ENC = \frac{e}{q} \times \sqrt{\frac{T_p kT}{2R}}$$

where k is the Boltzman constant, T is the temperature and R the biasing resistor.

To minimise the noise, the detector must minimise capacitance and leakage current and maximise the biasing resistor [67].

1.2 Particle trackers in space experiments

There are many experiments equipped with a particle tracker, always based on silicon strip technology, in space. In general, it is possible to distinguish to families, depending on whether a magnet is part of the experiment or not. Magnetic spectrometers like PAMELA and AMS have been powerful tools to investigate scientific problems about cosmic rays and antimatter. When the tracker is coupled to a calorimeter, important results can be obtained also in γ-ray astronomy and indirect Dark Matter searches, as experiments like Fermi and DAMPE (DArk Matter PArticle Explorer) demonstrate.

1.2.1 FERMI LAT

The Large Area Telescope (LAT) is a payload of the Fermi Gamma-ray Space Telescope, launched by NASA on 2008 June 11. The project is a follow up of the successful EGRET mission, that provided the first catalogue of γ-ray sources of the galaxy [44].

It follows the success of the small scale prototype AGILE, launched on April 23, 2007 [80]. The detector realised for AGILE is a prototype of a segment of FERMI LAT described in this chapter.

The experiment has different objectives: determining the nature of unidentified sources of γ-rays, study the particle acceleration mechanisms produced by different celestial bodies, the study of γ-ray burst (GRBs) transients, the indirect search of dark matter. The detector is also included in the network devoted to the follow-up for electromagnetic signals after gravitational waves detection [76]. It is designed to detect photons with energies above 100 MeV up to the TeV.

The LAT, shown in figure 1.3, is composed of three subsystems: the Precision Converter-Tracker, the calorimeter and the anticoincidence detector. The detector is divided into 16 towers, each one operated independently from the
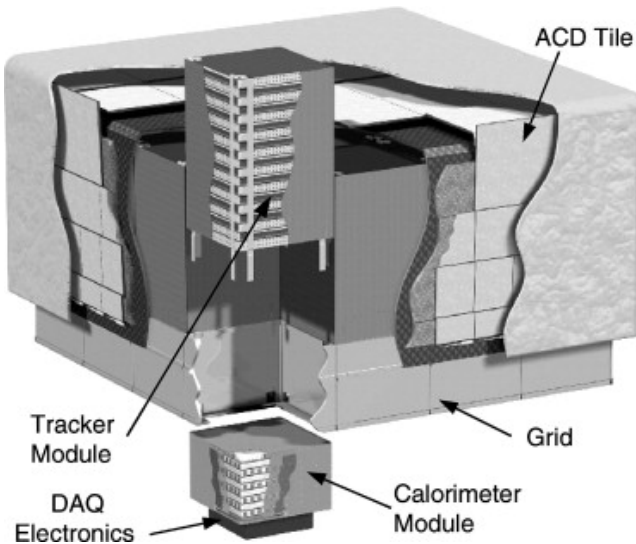
Figure 1.3: FERMI LAT structure [19].

others. This structure has several advantages. The first advantage is that it is easier to realise and operate a smaller detector, mostly because it does not require stitching of different silicon sensor, whose dimension are limited by construction requirements.Secondy, the segmentation increases the reliability of the system. In these conditions, if a single tower fails, 94% remains fully operational.

As already said, γ-ray detection is possible only if the primary photon converts into a e^+ e^- pair. The cross section of this process is proportional to Z and density of the target material. For this reason, the Precision converter-tracker alternates layers of tungsten and silicon microstrips planes.

Each tower has 16 planes of converter material and 18 tracking planes, consisting of two single-sided microstrip silicon detectors. Each silicon plane measures only along one direction, so two are required to fix a crossing point for the particle.

The silicon microstrip detector has a strip pitch of 228 μm and is 400 μm thick.

In order to maximise the direction reconstruction capabilities of the detector, the inert material should be kept as thin as possible to allow the detection of the first pair produced with the lowest multiple scattering contribution. This requirement conflicts with the need of material to convert the photon. The applied compromise solution is the following: the converter-tracker is divided into two sections, "front" and "back". On the front region, composed by the first 12 layers, there are thin (0.03 radiation length X_0) converter layers. On the back region, composed by the other four planes, the converter is about six times thicker.

The total power consumption of the precision converter-tracker is about 160
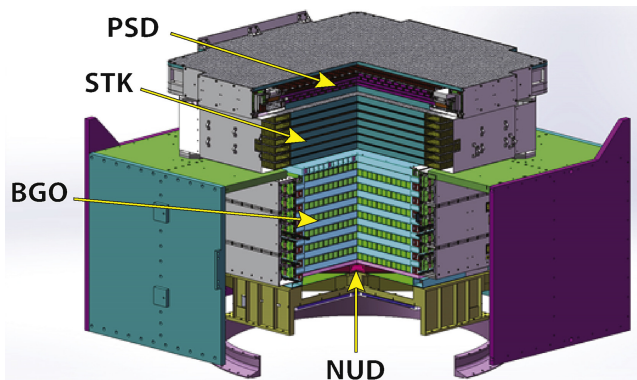
Figure 1.4: Dampe experiment [23].

W. It results that the power consumption of each channel is 180 μW. The total surface of silicon is about 74 m^2. The power consumption per unit area is 0.2 mW/cm^2 [20].

The following calorimeter has two main functions: to measure the energy of the e^+/e^- pair and to study the development of the shower. Each module is composed by 96 CsI(Tl) scintillator crystals, 2.7×2.0×32.6 cm^3. The crystals are arranged in eight layers of crossed bars. The bars dimensions are a compromise between the desired granularity for imaging and the maximum affordable number of electronic channels. The calorimeter depth is 8.6 X_0.

Each crystal is read out by photodiodes, two on each side. The photodiodes have a different size, to cover the broad dynamic range of the detector. The ratio of the signal amplitude on the two sides can be used to coarsely locate the hit position of the particles. The segmentation allows reconstructing the energy of not-contained events up to the TeV [19].

The last subsystem is the anticoincidence detector. It is used to suppress the background from charged cosmic ray components. γ-rays do not leave signals before they convert in e$^+$ e$^-$ pairs on the converter layers. If the anticoincidence detector records a signal, the primary particle is charged.

The anticoincidence system is made of scintillating plastic tiles, chosen for their good efficiency, reliability and low cost. Tiles are readout by wavelength shifting fibres embedded in the scintillators, each coupled with two photomultiplier tubes for redundancy.

The detector has been fully operational for the last ten years and it still provides important results and high-quality observations.

1.2.2 DAMPE

DAMPE (DArk Matter Particle Explorer) is designed to measure the spectrum of electron, positrons from 5 GeV to 10 TeV and the cosmic ray flux and composition from 10 GeV up to above 100 TeV [23]. DAMPE is sensitive also

to photons of energy as large as 5 GeV to 10 TeV, from point-like and extended sources. Four sub-detectors compose the experiment.

The Plastic scintillator Strip Detector (PSD) consists of a double-layer of scintillating fibres used as anticoincidence for photon discrimination and charge discrimination.

Then the silicon-tungsten tracker (STK), described later, and a calorimeter (BGO), made of 14 layers of BGO in hodoscopic arrangement. The calorimeter covers 31 X_0.

The last subsystem is the neutron detector (NUD) made of 16 planes of boron-loaded plastic scintillators tiles, each 1 cm thick. It is used to detect delayed neutrons and improve the detector capability to discriminate hadronic and electromagnetic showers.

The tracker of DAMPE bases its design on the experiences of previous space experiments like AGILE and FERMI. It follows the same structure of alternated layers of silicon microstrips detector and tungsten layers. Tungsten is 1 mm thick and is inserted in front of layers 2, 3 and 4 of the six composing the tracker.

The detectors are 90×95×0.32 mm^3, single side microstrip. The readout pitch is 121 μm, with a floating strip in between the read out channels, and provides a spatial resolution of about 70 μm [85]. Four detectors form a ladder. Each plane contains two layers of 16 ladders each. The strip direction on the two ladders is perpendicular to provide a position measurement.

The tracker covers a surface of about 7 m^2 and consumes about 90 W [23]. The power consumption for surface unit is 1.3 mW/cm^2.

The mission was successfully launched on 17 December 2015 and is still in data taking.

1.2.3   PAMELA

PAMELA (Payload for Antimatter Matter Exploration and Light-nuclei Astrophysics) is a part of the second Russian Italian Mission [47]. It is primarily devoted to the measure of antimatter fluxes, but also to the study of isotopic composition of the cosmic rays [29]. It was launched on June 2006 form Baikonur Cosmodrome [33].

The detector is organised into several sub-detectors: a magnetic spectrometer, used to reconstruct the sign and absolute value of the particle charge, an electromagnetic calorimeter, to reconstruct the incident particle energy and the spatial evolution of electromagnetic shower, a transition radiation detector for particle identification[2] and a plastic scintillator system providing both an anti-coincidence signal for particles coming from outside the acceptance of the detector and a time of flight measurement, again for particle identification purposes.

The magnetic spectrometer consists of a permanent magnet shaped in a tower structure 44.5 cm high, made up of five modules. The dimensions of the

---

[2]Because of the problems found during qualification tests, the TRD was not installed on the flight model of the experiment.
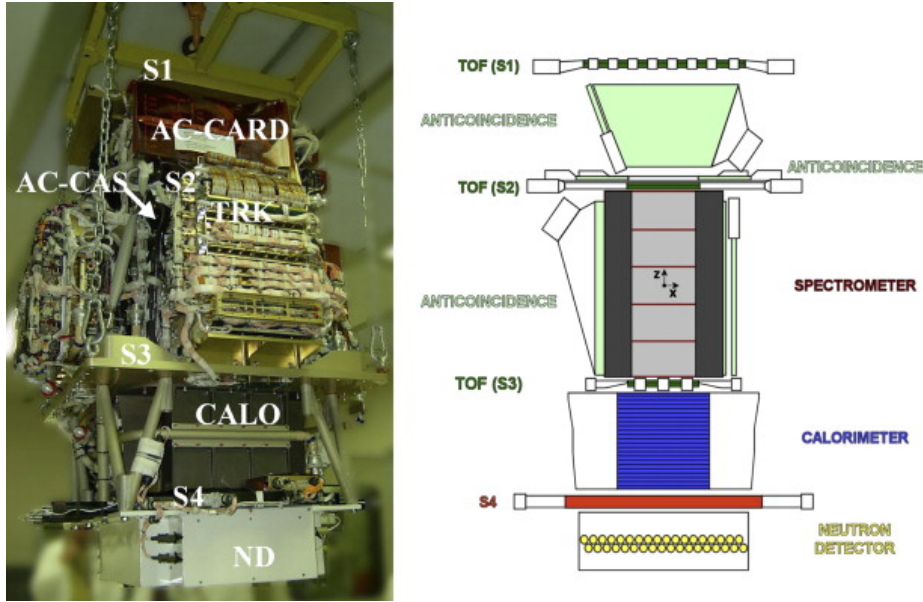
Figure 1.5: Pamela experiment: a picture and the layout schematics [33].

towers define the geometrical factor of the detector acceptance [5]. It is made of Nd-Fe-B alloy and features an average field as high as 0.43 T.

The silicon strip based tracker is located inside the magnetic cavity. There are six planes, each of them composed by six sensors, each one 23.33×70.00 mm^2, for a total dimension of 14×16 cm^2. The planes are 300 μm thick double-sided microstrip detectors produced by Hamamatsu. The implant strip pitch is 25 μm (readout pitch 50 μm) on the front side and 67 μm on back side. Strips are implanted orthogonally on the two sides to provide a point measure with a single plane. To simplify the read out system, the signals of back side strips are routed to the same side where the strips on front side are read out. The spatial resolution of the detector is about 3 μm [66].

The power budget assigned to the spectrometer is 63 W for a surface of 0.13 m^2. The power density of the system is then about 48 mW/cm^2, much higher than FERMI [69].

The electromagnetic calorimeter also uses microstrip detectors. In this case the silicon planes are alternated with tungsten layers, similarly to what reported for FERMI. In this case, the calorimeter is aimed to identify antiproton signals from electron background and positron signals from proton background. The 22 tungsten layers are 0.26 cm thick, for 16.3 X_0. Each plane lays between by two single-sided microstrip planes made of nine detectors 8×8 cm^2 each. Since each detector has only 32 strips, each plane counts 192 channels, for a total of 4224 readout channels.

The time of flight is made of plastic scintillator planes located at different
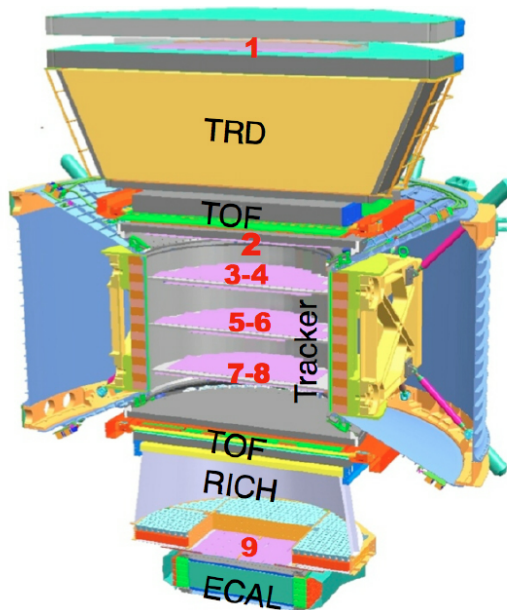
Figure 1.6: AMS-02 detector [79].

levels of the detector, as shown in figure 1.5. It measures the time intervals between the crossing of the different planes. The measure can be coupled with other information and used to provide particle identification.

The Transition Radiation Detector (TRD) measures the transition radiation produced by ultrarelativistic charged particles. It uses straw tubes filled with a mixture of Xe and CO_2 at a tension of 1400 V to maximise the photon detection efficiency. The measure provides additional information for particle identification.

PAMELA operations ended in 2017 after more than ten years of successful operations. The experiment greatly refined the measurement of the positron fraction excess in cosmic rays [6] and gave other contributions to cosmic ray physics.

1.2.4   AMS-02

The Alpha Magnetic Spectrometer (AMS) experiment was flown on Discovery space shuttle in June 1998 [8]. This first short measure was preliminary to the realisation of AMS-02, designed to be installed on the ISS.

AMS-02, in figure 1.6, is the second generation of the detector and it operates on the International Space Station (ISS) since 2011 May. As for PAMELA, the main aims of the mission are the search for dark matter and the study of antimatter via the precision measurements of cosmic rays charged components in an energy range between 0.5 GeV and the TeV, for Z lower than 26.

Figure 1.6 shows the detector structure. The sub-systems that compose the detector are: a 0.8 T magnet, a silicon tracker, a transition radiation detector (TRD), the Time-of-Flight (TOF), the ring-imaging Cherenkov detector (RICH) and an electromagnetic calorimeter. Anticoincidence planes surround the central section of the detector [13].

TOF consists of two segmented double planes of scintillators located before and after the tracker planes. Each of the 34 paddles is read out by PMTs via light guides optimised to align the PMTs with the magnetic fringe. TOF provides trigger to the whole experiment by coincidence signals and a measurement of the velocity as precise as 4%. It can also provide a measurement of the Z of the particle up to 20 using the scintillation light yield [32].

TRD consists of 20 layers of straw tube modules and polypropylene fibre radiators in an octagonal box. The first and last four layers are oriented perpendicularly to the other layers. The TRD is on the top of the experiment[3]. It is tuned to detect the transition radiation of ultrarelativistic particles. It separates protons and electrons populations [32].

The three main components of RICH are the radiator, made of silica aerogel tiles with a low refractive index that covers 90% of the active area, a central square of sodium fluoride tiles and a detector plane. The RICH provides a precise particle velocity measurement and charge sign discrimination up to $Z < 26$ [32].

The last subsystem of the detector is the electromagnetic calorimeter (ECAL). Scintillating fibres glued to lead foils are the sensitive part of the detector. Eleven layers of fibres form a super-layer with the fibre oriented in the same direction. Alternated super-layers have fibres oriented in perpendicular directions. The depth of the ECAL is 16 X_0. The detector aims to provide a measure of the energy of electromagnetic particles and it plays an essential role in electron-proton separation. It can also be used to provide shower shape reconstruction because of the fine segmentation [32].

The core of the experiment is the spectrometer, composed by the magnet and the tracker planes.

In its original design, AMS-02 mounted a superconducting magnet. Technical issues forced the collaboration to replace it with the permanent magnet from AMS-01 mission because of the extension of the ISS operations. The maximum capacity of the superfluid helium reservoir necessary to maintain 1.8 K was the ultimate limitation for the experiment lifetime. The drawback has been the reduction of the magnetic field is 0.14 T instead of 0.8 T on average [58].

The design of the tracker was modified after the change of magnet to reach the resolution goals of the experiment. The number of planes passed from 8 to 9 and they where disposed differently, as shown in figure 1.7.

Each plane of the silicon tracker is composed of several units called ladders, containing 7 to 15 modules of microstrip detectors. The sensors are $41.360 \times 72.045 \times 0.300$ mm^3 double face microstrip planes. The readout (implantation) pitch is 110 (27.5) μm on p side and (104) 208 μm on n side, the

---

[3]The first detector is actually the first plane of the tracker.
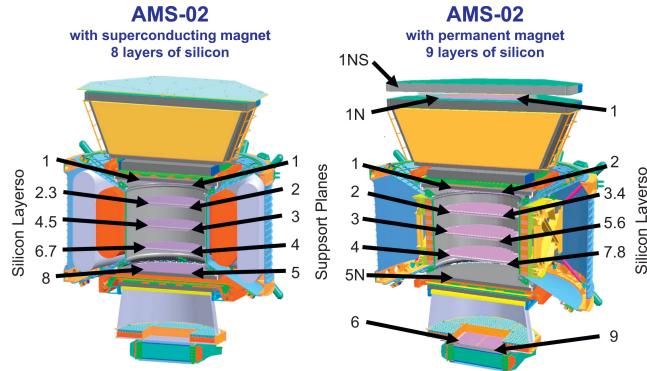
Figure 1.7: Differences in tracker planes disposition in AMS-02 with superconducting and permanent magnets [58].
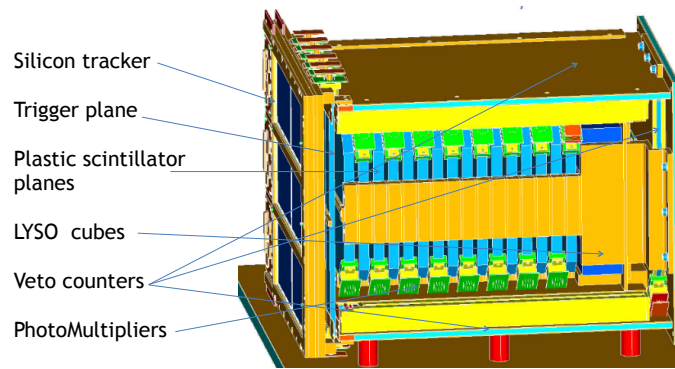
Figure 1.8: HEPD-01 detector.

detector is operated in total depletion mode. The spatial resolution of the detector is about 10 μm for p side and 30 μm for n side. The tracker covers a surface of about 6.4 m^2 and has a power consumption of 734 W, for a power consumption for surface unit of 12 mW/cm^2 [92].

In these ten years of data taking AMS-02 provided an insight on the physics of cosmic rays and precision measurements of a wide set of phenomena [9] [10] [11] [12].

1.2.5 HEPD-01

The High Energy Particle Detector (HEPD) is a payload of China Seismo-Electromagnetic Satellite (CSES), launched from Jiuquan Satellite launch centre in Mongolia on February 2, 2018. The satellite hosts several payloads devoted to the study of the Lithosphere-Atmosphere-Ionosphere coupling mechanisms [75].
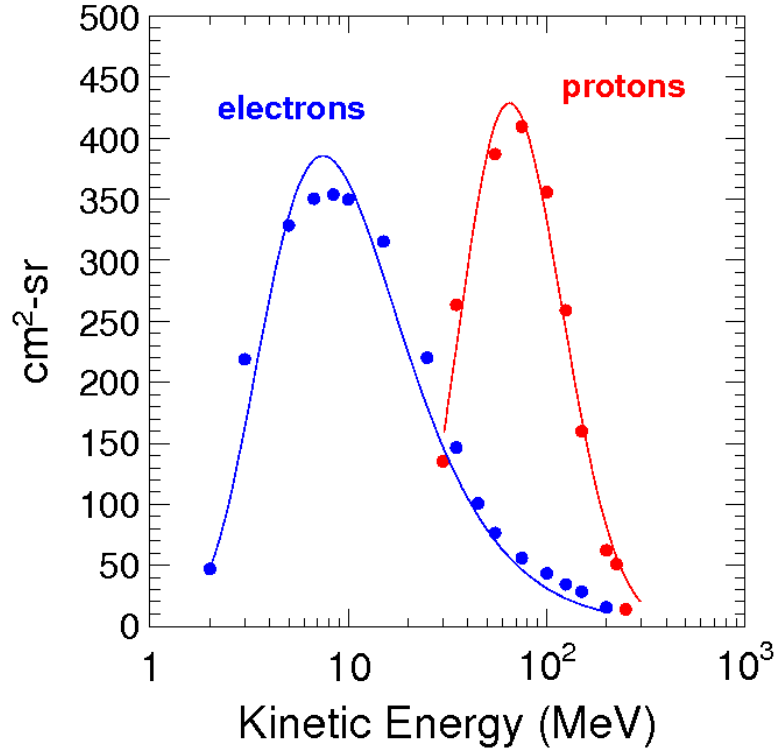
Figure 1.9: Acceptance of HEPD-01 detector [15].

Since this work is aimed to describe the study carried on to design a tracker for HEPD-02, more detailed description of HEPD-01 is given. Most subsystems of the experiment will remain unchanged in the new experiment.

The HEPD-01 is designed to detect protons between 30 MeV and 300 MeV and for electrons from 3 MeV to 100 MeV. It has an energy resolution better than 10% and an angular resolution better than 8° at 10 MeV.

Its main goal is the measurement of particle flux fluctuations, possibly related to seismic activity on Earth. It also investigates the stability of Van Allen belts and low-energy cosmic ray physics, in particular galactic and secondary particle spectra. Its data can also be used to study solar energetic particles (SEP) events. The acceptance of the experiment for electrons and protons is reported in figure 1.9.

As reported in figure 1.8, HEPD-01 sub-detectors are:

- Tracker

Figure 1.10: Calorimeter of HEPD-01 detector [15].

- Trigger

- Upper calorimeter

- Lower calorimeter

- Veto system

The trigger plane is divided into five bars $15 \times 30 \times 5\ mm^3$, disposed side by side below the tracker planes. Each bar is made of EJ-200 plastic scintillator and is read out by two Hamamatsu R9880-210 PMTs. The same PMTs reads out all the scintillators of the detector.

The sixteen planes of the upper calorimeter, shown in figure 1.10, are made of the same material of the trigger, and they have dimensions $150 \times 150 \times 10\ mm^3$. The planes are piled to form a tower. Each plane is read out by two PMTs located at the opposite corners of the square. Consecutive planes have the PMTs along opposite diagonals.
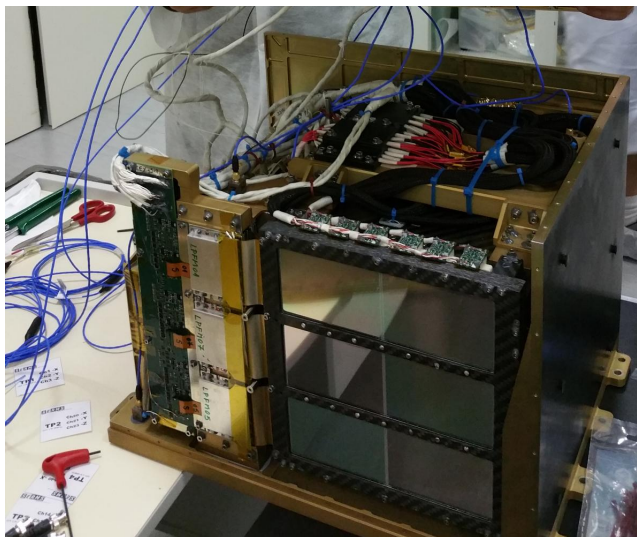
Figure 1.11: HEPD-01 detector. The tracker is visible in front of the setup [15].

The lower calorimeter is an array of nine LYSO cubes, 30x30x30 mm^3. Each cube is read out by a single PMT on the bottom of the detector.

The veto is made up of five planes of EJ-200 plastic scintillators and surrounds the detector on five sides. Each veto plane is read out by two PMTs, located at the opposite corners of the plane.

The detector separates nuclei and electrons as efficiently as 99.5%. It uses the comparison of dE/dx technique and the full energy releases on the calorimeters versus the energy deposited on the silicon tracker or the trigger plane [15].

The detector performance have been characterised before flight with cosmic muons and with electrons (30 MeV - 120 MeV energy range at Beam Test Facility or BTF in Frascati, Rome) and with protons (30 MeV - 230 MeV energy range at Proton Therapy Center, Trento) [15].

The HEPD-01 tracker, in figure 1.11, is made of two double-sided microstrip planes, divided into three ladders $70 \times 200 \times 0.3$ mm^3. The total size of each plane is then $210 \times 200 \times 0.3$ mm^3, and they are 10 mm away from each other. The strip implantation pitch is 91 μm, and there is one floating strip between the readout strips. The readout pitch is then 182 μm. The strips on the p side are oriented along the long dimension and orthogonally on the n side. The spatial resolution of the detector is about 50 μm [15]. The power consumption of the system is 10 W for a detector surface of 0.126 m^2. The power consumption for surface unit is 8 mW/cm^2.

To reduce the complexity of the system and the number of readout channels, the strips on the n side are grouped, as shown in figure 1.12. Strips as distant as ~ 70 mm share the same readout channel, arranging 3×384 readout strips on 384 channels. The number of readout channel is, therefore, the same on p

and n side for each ladder, 384 on the n side and 384 for the p side, for a total number of channels of 4608 for all the six ladders that compose the tracker. The uncertainty on the strips on n side involved in the event can be resolved using the signal from the trigger bars, which are parallel to the n strips and provide the information on the area of the tracker hit by the incoming particle.
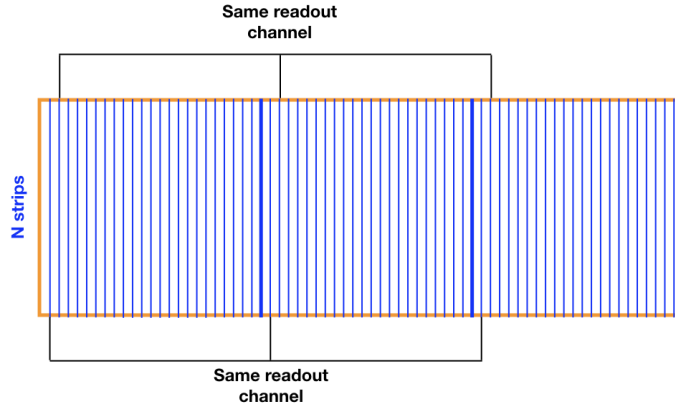
Figure 1.12: Scheme of a tracker ladder readout channel on n side.

Figure 1.13 shows the readout scheme of a side of HEPD-01 tracker. The signal readout and amplification is performed inside the Voltage Amplifier (VA) modules, each of them collecting signals from 64 channels. Three VAs send the signals to an ADC module. Each side of a ladder is then read out by six VA, connected to two ADCs.

Figure 1.14 shows the tracker response as a function of the energy of the protons measured during beam test in Trento. Data are compared with results of the Monte Carlo simulation of the experiment. The good agreement of the data sets confirms the good performance of the detector. The data are fit with a Bethe-Block function to find the conversion from ADC units to MeV .

Comparison of the signal deposited in silicon layers and on calorimeter is used for particle identification. Results from simulations are reported in figure 1.15.

The commissioning phase of HEPD-01, ended in August 2018, showed a behaviour of all sub-detectors coherent with the pre-flight characterisation. After almost two years of observation, the experiment is releasing its first results, mainly focused on flux measurements. For what concerns the galactic and sub-cutoff particles, data are limited by the fact that the satellite does not acquire data at geographical latitudes larger than $65°$. Nevertheless, the tilt of Earth magnetic field allows to collect data up to $75°$ degrees of magnetic latitude. The
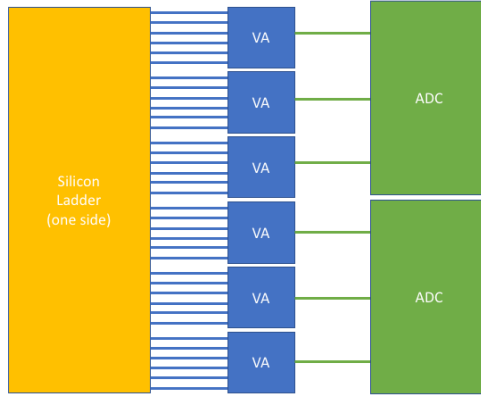
Figure 1.13: Readout scheme of HEPD-01 tracker ladder.
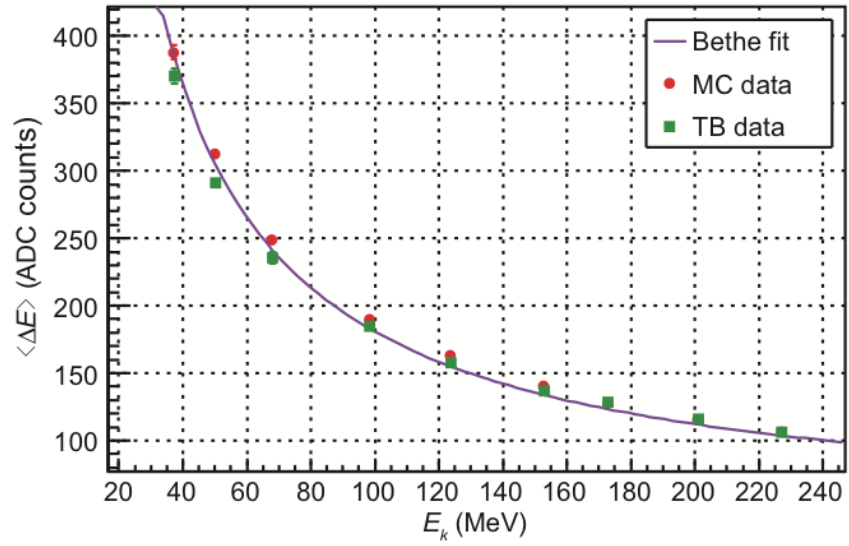
Figure 1.14: Measured proton dE/dx for a silicon ladder at different energies of the test beam in Trento, compared with Monte Carlo simulation [15]
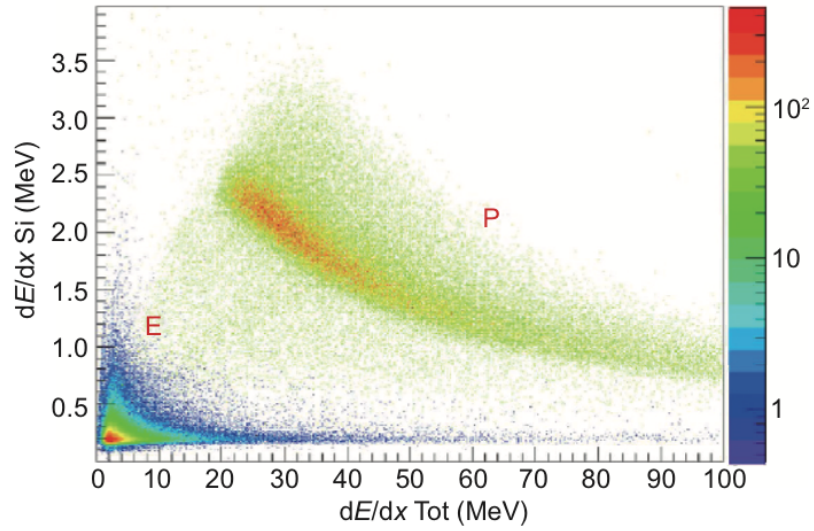
(a) HEPD-01 simulated electron vs proton separation.
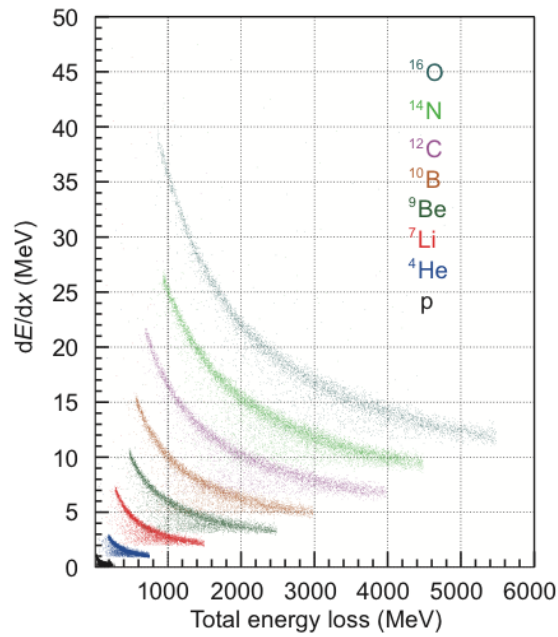
(b) HEPD-01 simulated nuclei separation.

Figure 1.15: Simulation results of particle discrimination capabilities of HEPD-01 [15].

38
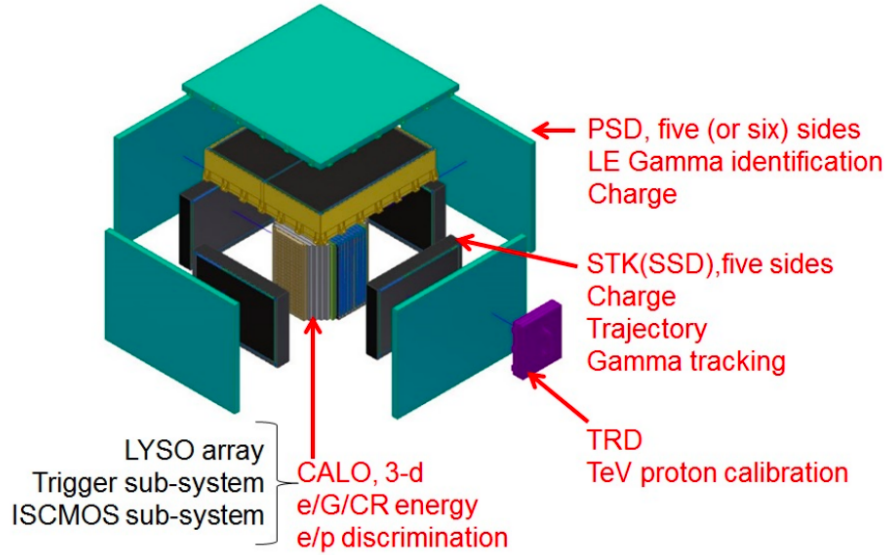
Figure 1.16: layout of HERD detector (exploded view) [41].

small observation time is compensated by the large acceptance of the detector and provides good exposure for low-energy cosmic ray physics.

1.2.6   Planned experiments: HERD

The experiments described in previous sections are still in operation, with the only exception of PAMELA, but their lifetime is limited. Moreover, their energy range does not exceed some TeV in the best cases (AMS-02). The realisation of new experiments, that will replace the existing missions and enlarge the accessible energy range, is important to understand more and more the universe.

An interesting project is the High-Energy cosmic Radiation Detector (HERD), that has been proposed as a payload of the Chinese Space Station, whose operations are planned to start in 2025 [34].

The design of the detector does not follow the schemes introduced for the other experiments and it is shown in figure 1.16. Starting from the centre and moving outwards, it is composed by a cubic calorimeter finely segmented, surrounded by silicon microstrip tracker planes on five sides. These central detectors are covered by plastic scintillator planes. A TRD is installed on the lateral side [34].

This innovative design increases the acceptance of the detector of about one order of magnitude with respect to the previous experiments. The requirements for the calorimeter is 1% energy resolution for 100 GeV electrons and 20% energy resolution for 100 GeV to 1 PeV protons. Tracker must have a angular resolution better than 0.1 deg at 20 GeV, and the plastic scintillator signal

discriminates between charged particles and γ-rays [34].

The experiment aims to investigate the electron and positron spectrum up to about 10 TeV and nuclei up to 100 TeV at most. This would be the first direct measurement of the most energetic components of cosmic rays.

The detector is also sensitive to high-energy γ-rays up to 1 GeV. A possible improvement of performance with respect to FERMI LAT will depend on the final design of the experiment, that is still under discussion.

Experiment	Year	Technology	Pitch [μm]	Resolution [μm]	Surface [m^2]	Power [W]	Power density [mW/cm^2]	Life Span [yr]
FERMI LAT	2008	Single side	228	−	74	160	0.2	Ongoing
DAMPE	2015	Single side	121	70	7	90	1.3	Ongoing
PAMELA	2006	Double side	50 (p) 67 (n)	3	0.13	63	48	11
AMS-02	2011	Double side	110 (p) 208 (n)	10 (p) 30 (n)	6.4	734	12	Ongoing
HEPD-01	2018	Double side	182	50	0.088	10	11	Ongoing

Table 1.1: Summary of the main properties of trackers installed on experiment described on this chapter.

1.3   Pixel detector in space

Some small applications, mainly located inside the ISS, use silicon pixel detectors in space. The main application is dosimetry and monitoring of the radioactive environment.

With the large number of projects of manned space missions foreseen for the next decades, the real-time measurement of the radioactive environment around the crew is crucial for safety reasons. Previous devices used tissue-equivalent gas, scintillators and semiconductors [53]. These detectors can be arranged to provide the equivalent dose directly on tissue, but the data are limited to the total dose. The measurements collected with silicon devices needs more careful calibration to translate the dose in silicon to the dose deposited in biological tissues, but the amount of information that they provide largely compensates this limit.

Pixel silicon devices measures the charge, the energy spectrum and the direction of each single particle impinging on them. Devices used for space applications are realised with a hybrid approach. Detectors and readout electronics are realised on different silicon substrates and bump-bonded one to the other. The front-end chip collects the information on charge collected in the sensitive layer and provides the bias to the detector. A sketch of this system is shown in figure 1.17.

NASA started to test some small prototypes on the ISS, using Timepix, realised by the Medipix2 collaboration as readout. The Timepix has 256×256 pixels with a pitch of 55 μm, proving an active area of 198.2 cm^2. The sensor dimensions are 16.120×14.111 mm^2, including inactive boundaries for connections [57]. The Timepix has been used and is planned to be used to realise
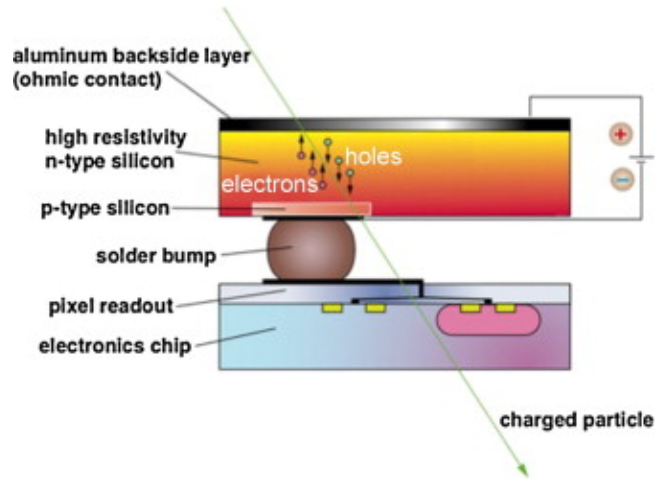
Figure 1.17: Bump bonding of front-end electronics on pixel detector [55].

small demonstrators in REM (Radiation Environment Monitor) project. The Timepix have been bump-bonded to 300 μm and 500 μm thick pixel detectors and installed in a small setup that can be connected to ISS laptops using a USB port. The data are then collected and downloaded every day for analysis. Data collected have been used to characterise the radiation environment in low Earth orbit and on the South Atlantic Anomaly region. Out of seven devices installed, only one experienced failure for reasons not directly connected to the detector. The other are fully operational since October 2012 [55].

A second setup, Battery-operated Independent Radiation Detector (BIRD), has been realised for the Orion Multi-Purpose Crew Vehicle, a NASA vehicle for crewed missions [24]. During the first test flight, EFT-1, the system provided an independent measurement of the radiation environment around various systems of the spacecraft. The BIRD was powered by batteries and the data stored inside an SD card. Accelerometers were used to start the data acquisition after the launch to save power and memory and to maintain the independence of the system. The mission lasted 4.5 hours, and the data analysis performed offline [24].

NASA plans further uses of these detectors. Meanwhile, the Medipix collaborations are working to new readout devices for future missions. In particular, it will be possible to pass from frame acquisition, in which all pixels are read out, to a data-driven readout where only small portions of the sensor are read-out, limited around the particle impact point. Medipix3 collaboration [70] has tested this feature, but the power requirements still exceed the supply provided by USB ports.

Silicon pixels detector R&D for space applications mainly focuses on dosimetry application, but they have never been used for particle tracking in physics experiments. All the detector operated in the test described in this section

covers small surfaces (below 1 cm^2) and operates autonomously. Moreover, all the devices tested are realised with a hybrid approach. Monolithic Active Pixel Sensors, silicon pixel detectors with readout circuitry integrated on the same substrate of the detector, have never been tested in space.

Chapter 2

Monolithic Active Pixel Sensors

2.1 New technology for tracking particle in space

In chapter 1 of this work, some space missions equipped with particle trackers have been described. The elective technology for all the applications is microstrip silicon detectors.

The main advantages of silicon microstrip detectors are the small power consumption of the sensors (see table 1.1), and the small number of the channels. For a given pitch, the number of channels increases linearly with the side size and as the square root of the detector surface.

This technology has, though, some limits to face, that are going to affect the design and the performance of future experiments.

The first problem is the procurement of the detectors. Only a small number of foundries has the expertise to realise microstrip, (FBK in Italy [30], Hamamatsu in Japan [73], BEL in India [81] and a small number of others) and since the detector must be designed and realised for each single application, the costs are high, about 100 $/$cm^2$

Moreover, the readout of the detector requires VA ASICs (Application Specific Integrated Circuit), that are specifically optimised for the mictostrip readout. These ASICs have a large cost and a high power consumption. The use of an external amplifier limits the control of the noise of the system, that depends on the noise of the connection between the detector and the amplifier. The noise effects must be corrected before the downlink of the data. The general procedure requires to calculate the average value of the signal on all the channels connected to the same VA, that is subtracted from the signal value. Then a cluster finding algorithm runs on all the channels of the experiment and identifies those which value is above a given S/N ratio value. Only the data from these channels are downlinked to Earth. The CPU is in charge of the procedure, that requires a high computational power and increases the dead time of the

experiment.

In table 1.1, the spatial resolution of several experiments is reported. The best performing case is PAMELA, that has a 3 μm spatial resolution. Other experiments quote a resolution that is about 10-30 μm, at least a factor 3 worse. To reach such a remarkable result, PAMELA detectors have a small pitch microstrips (50 μm on p-side, 67 μm on n-side), implanted on small silicon ladders. The use of large sized detectors increases the capacitive coupling of the microstrips, that must be longer. A high capacitive coupling increases the noise level and reduces the S/N ratio, spreading the charges on more microstrips.

The use of pixel detector, and in particular of Monolithic Active Pixel Sensors (MAPS) [84], solves most of the problems connected to the production and use of microstrip.

For what concerns the production, the MAPS are realised in standard CMOS (Complementary Metal-Oxide Semiconductor) technology, and can be mass-produced by foundries. The mass production reduces the costs of at least a factor 5 (expected cost is about $20\$/cm^2$).

Having the readout implanted on the detector, the costs for production and assembly are widely reduced. The problem of power consumption moves from the VA and CPU to the detector itself, and has to be properly studied. It will be widely discussed in this work (in particular in section 3.3). The implant of the amplification stage inside the detector (in some cases inside each pixel) reduces significantly the noise. A description of noise contributions is in section 2.2. It is also possible to equip the detector with zero-suppression algorithms, that process the data and sends to the external readout only the interesting information.

The spatial resolution of a pixel detector is about 3 μm [72]. It is at the same level of the best performing silicon microstrip detectors. The goal of sub-μm resolution has not been reached yet, but the improvements of technology are going to allow to realise pixel with smaller pitch, that will reduce upper limits of spatial resolution [64] [35].

Whereas silicon pixel detectors, and in particular MAPS, solve most of the limits of the silicon microstrip detectors, they don't have the same advantages. Since all the readout is inside the detector, its power consumption is widely higher than for microstrip. The best performing detector has a power consumption for surface unit of about 35 mW/cm^2 [72], higher than almost all the trackers of experiments in table 1.1.

The number of channels increases linearly with the surface, faster than for microstrip. The impact of the channel number increase is mitigated by the implementation of on-detector zero-suppression logic, but leads to a higher power consumption.

Other types of pixel detectors

This work focuses on MAPS detectors, but there are three main types of silicon pixel detectors: the planar pixels [51], the 3D pixels [65] and the MAPS [84].
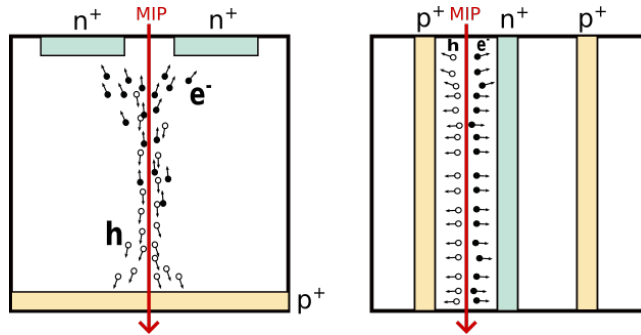
Figure 2.1: Schematic view of planar (on the left side) and 3D (on the right side) pixel design and charge collection [43].

As shown in figure 2.1, the planar and 3D pixels differ for the collection electrode structure. The planar pixel electrodes are implanted following the same procedure described for microstrip, described in section 1.1.1. In this case, a regularly spaced small region of about some μm squared is implanted. A reverse bias tension can be applied to the backside of the silicon buffer to polarise the diodes and enhance the efficiency of charge collection.

The 3D pixels are designed to be faster and more radiation hard than planar pixels. The collection electrodes extend inside the silicon buffer, as shown in right side of figure 2.1. This structure reduces the drift time of the charges towards the electrodes, and improves the radiation hardness by reducing the charges trapping probability.

Both these detectors need an external readout system. The readout front-end are usually bump-bonded to the detector, as shown in figure 1.17. They collect the signal from the electrodes and encode it in a format that can be interpreted by the Data Acquisition (DAQ).

The third kind of silicon detectors, MAPS, have the same electrode structure of planar pixels, and the readout integrated in the detector silicon buffer. This solution offers several advantages with respect to the other two families of pixels.

2.2 Monolithic Active Pixel Sensors

MAPS devices offer several advantages. The first is that they are realised with standard CMOS manufacturing processes. This approach reduces the costs of mass production to a fraction of costs for the production of custom processed detectors (other pixels and microstrip detectors). Another advantage is that the expensive assembly procedures required for hybrid pixels (bump-bonding) are no more required.

CMOS-fabricated sensors are the standard devices for visible light detection [45]. Visible light is made by many photons depositing all their energy on the first few microns of the detector, and the charge generated must be collected
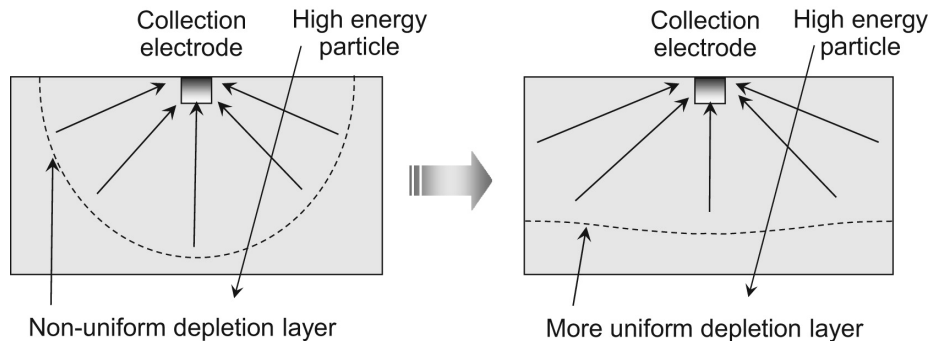
Figure 2.2: Differences in charge collection for depleted and undepleted detectors [77].

from a small volume. The charged particles instead have to be detected alone and traverse all the detector thickness, depositing their energy along the track. An efficient collection of charge in a volume at least some tens of μm thick has introduced a new challenge in detector design. The second challenge is the design of a readout circuitry that fits the small available surface and fulfils the experiment requirements.

Because of the differences in interaction of particles with silicon compared to visible light, the thickness and electrical properties of the silicon wafer have a significant impact on the detector design and performance. While standard CMOS devices are realised on low resistivity silicon, for particle detectors high resistivity of the substrate is recommended [42]. The high resistivity produces three advantages: (i) the lower doping enlarges the depletion region, (ii) it reduces the probability of trapping ionisation charges, (iii) it works around problems related to the low breakdown voltage of low resistivity bulks, originating when a reverse bias is applied.

Although it improves the charge collection efficiency and radiation hardness, back bias can not be applied to all the detectors. A scheme of the effects of bias on charge collection is shown in figure 2.2. In some detectors [72] [35] the charge collection can be entirely diffusion driven. In this case, there is only a small depletion region created by the p-n junction between the collection electrode and the epitaxial layer. The charges produced by the interacting particle diffuse inside the wafer until they reach the depletion region and are collected. The time required for charge collection is higher than for depleted detectors, and some of the charges can be lost. Moreover, the charge spreads among more pixels reducing the signal-to-noise (SN) ratio.

It is also possible to design fully depleted detectors [64] [49] [22], as shown in right side of figure 2.2. In this case, the charge collection is faster and the spread of charge cloud smaller, resulting in an improvement in both readout time and S/N ratio. The efficient charge collection also contributes to mitigating the radiation damages on the device. In both depleted and non-depleted detectors, the time of integration is small (up to about a μs for non depleted detectors)

not to include the contribution of the dark current to the measurements [77].

The radiation tolerance is one of the main challenges in MAPS design [83], in particular for high energy physics applications. As already said, a the performance of a depleted detector is more stable after irradiation. It is expected to tolerate at least 10^{15} n_{eq}/cm^2. Diffusion-based detectors have been tested up to 10^{13} n_{eq}/cm^2 without significant performance degradation [77] [60].

The main problem of these devices is not the degradation of the active region, but the damages produced on the CMOS circuitry implanted on the detector surface. The improvements of technology, that provides smaller linewidth implantation, enhance the radiation hardness of the circuitry.

The second critical point is power consumption. There are four main contributions to the consumption: the analog circuitry, the digital processing circuitry, the data transmission and the power consumption of sensing diodes. The power consumption impacts on the design of the detector because it is directly proportional to the material budget. A system with high power consumption requires power supply distribution system and cooling systems for heat dissipation. The cooling can be passive or active. In the case of active cooling, a gas or a liquid flush removes the heat. Passive cooling, instead, is realised introducing material layers with a good thermal conductivity that collect and remove the heat. In both cases, inhert materials are inserted and the X_0 of the tracker increases.

The power consumption of digital processing circuitry depends on the design of the readout architecture of the detector. It can be limited for example by avoiding to distribute the clock to all the pixels, but the solutions are case-dependent and are connected to the required performance. Data transmission power consumption can be limited by selecting low-voltage standards and providing an encoding of data that minimises the number of bits of the signal.

The power consumption of the sensor is negligible for a non-irradiated detector.

Some details are provided now for the analog power consumption. This contribution is usually comparable to the digital one, and together they constitute most of the power budget of the sensor. The analog power consumption directly follows the sensor design, i.e. the features it has in terms of S/N ratio, radiation hardness, intrinsic velocity and granularity. To some extent, the digital design follows these features.

The signal collected can be expressed as a voltage $V = Q/C_{eq}$, where Q is the charge collected, and C_{eq} is the equivalent pixel capacitance. V must be compared with the noise of the MOS transistors, which has two main contributions: (i) a contribution that decreases with the frequency, (ii) a contribution directly proportional to the absolute temperature and inversely proportional to the transconductance g_m of the transistor [77]. From the transistor parameters, it is possible to build a model that connects the noise to the power consumption. The fast development of signal produced by impinging particle allows to ignore slower contributions, such as leakage currents, that can be filtered.

The S/N ratio is calculated as the ratio between the signal in volts, expressed

as Q/C_{eq}, and the noise in volts. For the previous discussion, it results to be

$$\frac{S}{N} \sim \frac{Q}{C_{eq}}\sqrt{g_m}$$

The g_m is proportional to the transistor bias current in weak inversion and the square root of the bias current in strong inversion regime [77]. Assuming that bias current is the main component of front-end power consumption, the S/N ratio depends on the power consumption P as [77]:

$$\frac{S}{N} \sim \frac{Q}{C_{eq}} \sqrt[m]{P}$$

with $2 \leq m \leq 4$.

From this expression, the power consumption can be expressed as

$$P \sim \left(\frac{Q}{C_{eq}}\right)^{-m}$$

The minimisation of Q/C_{eq} ratio reduces the analog power consumption. The charge generated inside the detector depends on the incident particle properties and on the detector thickness. It is possible to produce thicker detectors, but it is difficult to obtain uniform epitaxial crystals with a thickness of more than some tens of microns. Moreover, to obtain good tracking performance the thickness of the detectors must be small, to minimise X_0. The input capacitance can be optimised during the sensor design, and it is an important point of detector development.

The detector design has to face another major critical point: the implant of transistors with a well of the same doping type of the collection electrode creates competition in charge collection. However, the implantation of both pMOS and nMOS transistors is mandatory to realise a full in-pixel readout circuitry. Different solutions have been explored to allow the installation of the full readout without affecting the charge collection. Some of these strategies are shown in figure 2.3.

A possible solution is to place the readout inside the collection well, as shown in figure 2.3a. In this case, there is no competition in charge collection, but the electrode must be large enough to host all the required elements. A large electrode implies a higher capacitance, that reduces the S/N ratio and increases the power consumption. If this solution is applied, it is important to minimise the readout logic. Rolling shutter readout can be installed [50], but usually there is no room to implement a data-driven readout system. LePIX [48] and SDA [68] collaborations realised and tested detector prototypes with this technique.

Another possible solution is to implant an insulating oxide layer between the high resistivity epitaxial layer and the readout circuitry on the surface. The performance is good [18], but the oxide layer reduces the radiation tolerance of the device, creating a region where defects accumulate faster.
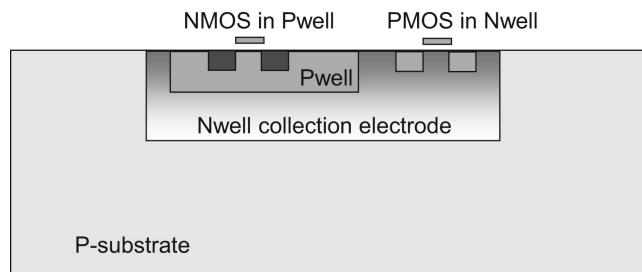
(a) Readout inside collecting n-type electrode.
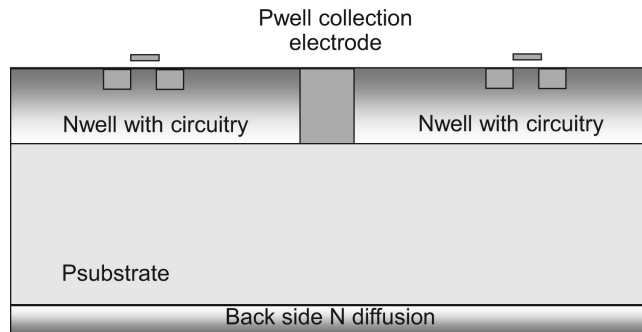
(b) Readout on the back plane.
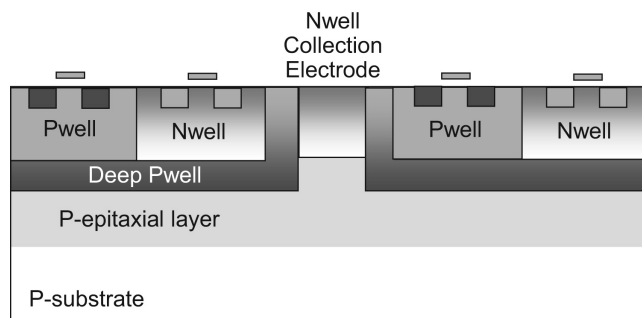
(c) Readout inside a deep p-well.

Figure 2.3: Different possible layouts for MAPS readout circuitry implantation [77].

Another design moves the collection diode to the backside of the detector, as shown in figure 2.3b. The readout is located inside a well of the opposite doping type of the substrate. The polarisation from the backside allows to collect the signal from an implant of the same type of the substrate. The prototypes realised with this technique have a good SN ratio [78], but the manufacturing is challenging for foundries.

The most effective technique consists in the realisation of a deep well of the same type of the substrate on the surface, as shown in figure 2.3c. The realisation of both pMOS and nMOS is possible because the shielding provided by the deep well preserves the efficiency in charge collection. The most mature example of this structure is ALPIDE, that will be discussed later in more details. Most of the detectors currently under development are based on this layout [49] [35] [40].

2.2.1 Space resolution of digital readout

Charge sharing among adjacent microstrip improves the spatial resolution. The statement is true also for pixel detectors that provide charge measurement, but a large fraction of MAPS has a binary output. In this case, it is commonly stated that the spatial resolution is given by

$$Resolution = \frac{P}{\sqrt{12}}$$

where P is the pitch of the pixel or of the strip. But this value is only an upper limit and it applies to the cases in which a single channel collects all the signal. When the charges produced by the interaction are shared among more channels the resolution limits will depend on the pixel pitch, on the thickness, and on the properties of interacting particle.

The problem is studied in [91] by using simulations. The analysis explores different pixel geometries and a wide range of incidence angles. Since the study focuses on detectors with binary readout, the observable is the cluster shape, defined as the pattern formed by pixels above the threshold.

The study is carried out for MIPs, for which the cluster size is expected to be small, between 1 and 4 pixels in most of the cases. The low number of pixels interested by the event simplifies the first step of the analysis: cluster shape classification.

For each shape, the distribution of the different incidence angles and hit positions of primary particles is recorded. In most cases, the same shape is produced by different combinations of angle and position of incidence. If a shape is produced only by a particular combination of incidence angle and position, the spatial resolution is maximised. In the other cases, the optimal space resolution is

$$\sigma_x^2 = \sum_{shapes} Pr(shapes)\min(dx_{shapes})^2$$

where $Pr(shapes)$ is the probability of a particular shape and dx_{shapes} the average quadratic distance from the true hit, in the x direction, conditioned on
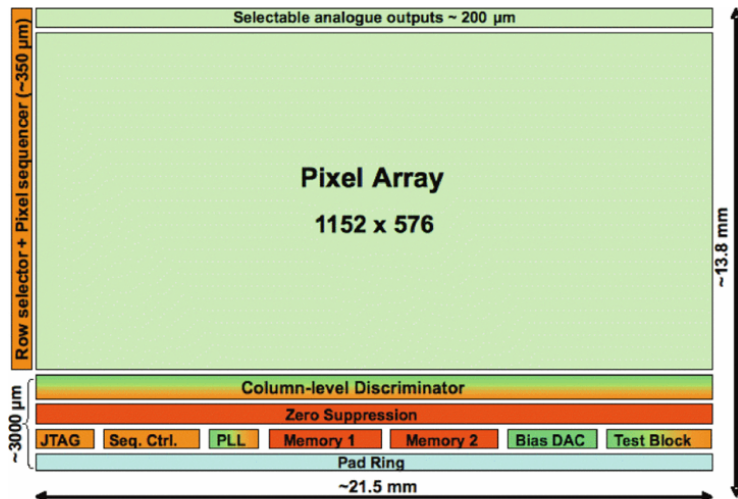
Figure 2.4: Schematic view of the MIMOSA-26 with the different functional blocks [26].

the shape s [91]. The same will hold for the y direction. The spatial resolution improves when $Pr(shapes)$ is small. For MIPs, it depends mainly on the incidence angle and it is in almost all the cases better than the limit value of pixel pitch/$\sqrt{12}$. For example, the ALPIDE (ALice PIxel DEtector) detector, that will be described in detail in section 2.4, has a pixel pitch of 28 μm. The resolution obtained for MIPs is about 3 μm [60], significantly lower than $28\mu m/\sqrt{12} \sim 8 \ \mu m$.

2.3 Case studies of MAPS detectors

2.3.1 MIMOSA-26

MIMOSA-26, realised in 2008 by MIMOSA (Minimum Ionising particle MOS Active pixel sensor) collaboration, is the detector chosen by EUDET consortium [74] to build a beam monitor telescope. The telescope is designed to provide a spatial reference during the tests of other devices. Its first campaign was carried on in 2009.

MIMOSA-26 is realised in AMS 0.35 μm OPTO technology. It consists of a 1152×576 pixel array with 18.4 μm pixel pitch. The full size of the sensor is $21.5 \times 13.8 \ mm^2$ [26]. A block diagram of the sensor is shown in figure 2.4.

In-pixel circuitry includes amplification and double sampling. The first sample is expected to collect the signal, the second gives a reference of the baseline level. The readout is in rolling shutter mode. The digitisation logic consists of a discriminator, located at the bottom of each column, that digitises the signal
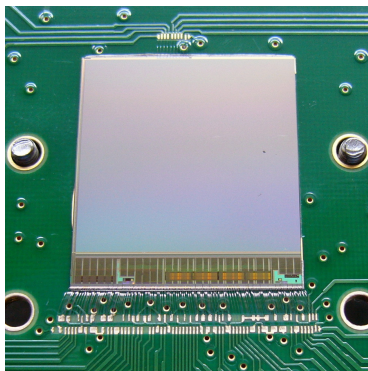
Figure 2.5: A picture of MIMOSA-28 [86].

after each double sampling of the column. With a clock frequency of 80 MHz, the readout time is 112 μs. The digital output of the discriminator is encoded by a zero-suppression logic producing a data set that stores the address of the first pixel and length of consecutive firing pixels. The buffer can save up to nine patterns for each row. An 80 $Mbits/s$ output transmits the data to the output. Depending on the occupancy, the compression factor spans from 10 to 10000.

From tests with ^{55}Fe, the equivalent noise charge is about 14 e$^-$ at 80 MHz of clock frequency. The detectors have been tested with 120 GeV π^- at CERN-SPS. The track is reconstructed with the signals collected by five detectors. The sixth, located in the middle of the array, is the device under test. As a function of the threshold, it is possible to measure the fake hit rate and the efficiency [26]. The efficiency is higher than the 99% with a fake hit rate of about 10^{-4}. The space resolution measured by extrapolating the track from the five reference detectors is about 4 μm. The static power consumption is about 300 mW. At 1% occupancy produces a dynamic power dissipation of 200 mW.

The requirements for EUDET application were fully satisfied. For high energy experiments, further developments were required in fake hit rates, working frequency and radiation tolerances.

2.3.2 MIMOSA-28

The first MAPS used in a high energy physics experiment is MIMOSA-28, realised in 2011, shown in figure 2.5. It has been installed on the heavy flavour tracker (HFT) of STAR experiment [71].

The detector is realised in CMOS 0.35 μm OPTO process in a wafer with a high resistivity epitaxial layer ($\geq 400\Omega\cdot cm$) with a thickness between 15 and 20 μm. The detector is thickness 50 μm or 120 μm, depending on the thinning applied. It has a 2×2 cm^2 sensitive area, and it is divided into 928 rows and 960 columns. Columns are divided in 15 regions. The pixel pitch is 20.7 μm.

Each pixel contains a sensing diode and an amplification circuitry based on nMOS transistors to avoid competition in charge collection with the electrodes.

The readout of the pixel consists of two sampling phases, to subtract the signal baseline.

The data are collected in rolling shutter mode and sent to a discriminator at the bottom of the columns. The discriminator compares the signal with a voltage reference. There are four sub-groups of discriminators, each of them equipped with its reference provided by different Digital-to-Analog Converter (DAC), to maximise the stability of the reference. The readout runs at 5 MHz along the column, for a readout time of 200 ns/row. The integration time is 185.6 μs [86].

After the analog to digital conversion of the signal, a sparse data scan algorithm selects up to 6 strings from each region of columns. A string is composed of one to four contiguous pixels in a row with a signal over threshold. Then a multiplexer reads out the banks and collects up to 9 strings by row, containing the row address, the number of strings in the same row, and an overflow bit if the string number in a row exceeds 9 and the column addresses of the pixel over the threshold. The collected data are stored in a memory buffer and read out using two LVDS outputs providing the 320 $Mbits/s$ speed required to empty the entire buffer within the integration time of the detector. This detector provides only the addresses of pixels interested by the event.

The noise level and charge to voltage conversion of pixels have been measured with a ^{55}Fe source. The noise results to be uniform on the active area, with an average value of less than 15 e$^-$ at 20°C and 40 MHz of readout clock frequency. The charge-to-voltage conversion factor results around 65 $\mu V/e^-$ [86]. The power consumption is about 730 mW at 3.3 V. The power consumption for surface unit is about 158 mW/cm^2 [86].

The detector has been tested at CERN SPS with 120 GeV π^-. The setup for the test consists in a telescope of six MIMOSA-28 detectors. The characterisation of the detector focused on efficiency, spatial resolution and fake hit rate, studied as a function of the threshold, before and after irradiation with a dose of 150 $kRads$.

The spatial resolution is about 4 μm for both irradiated and unirradiated detectors. The fake hit rate depends on the threshold voltage, and it is about 10^{-5} in the worst case, without significant changes before and after the irradiation. The efficiency is well above 98% for non-irradiated detectors and decreases after irradiation for high threshold values [86].

2.4   ALPIDE detector

The ALPIDE detector, designed for ALICE (A Large Ion Collider Experiment) Inner Tracker System (ITS) Upgrade (for the description see section 2.4.2), has been realised by TowerJazz in 180 nm CMOS Imaging Process technology [72] and produced in different sites around the world on high resistivity (> 1 $k\Omega cm$) p-doped silicon wafers.
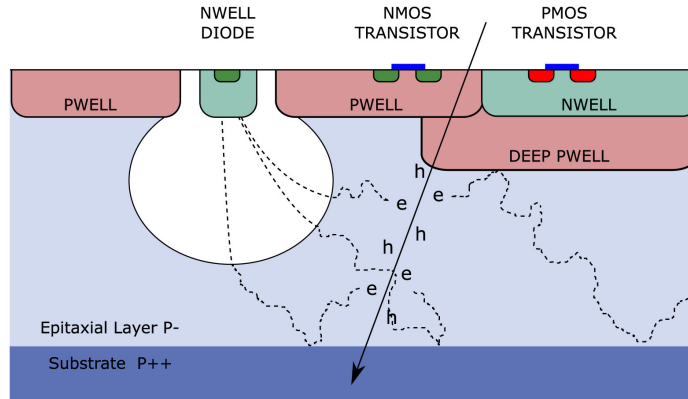
Figure 2.6: Schematic view of ALPIDE section [4].

2.4.1 Detector structure

The structure of the detector is shown in figure 2.6. The detector circuitry is implanted on a deep p-well (see figure 2.3c) to prevent competition in charge collection between the n-type collection electrodes and the pMOS substrate.

The detector full dimensions are 30×15 mm^2 and the thickness can be 50 or 100 μm [72]. The pixels[1] are 26.88×29.24 μm^2, and they are organised in double columns, as shown in figure 2.7a. The collection electrodes have a 2 μm diameter and a surface $\sim$100 times smaller than the pixel to reduce the capacitance and increase the S/N ratio. It is possible to apply a back bias to increase the depletion region around the electrode. The detector is fully efficient already with 0 V back bias.

Each pixel contains a continuously active analog front-end and a digital block, shown in figure 2.7b. The first block (input stage) includes the p-n junction, the reset block and the pulse injector, used to test and calibrate the pixel [72]. The second block (pixel analog front-end) includes the preamplifier and the discriminator. The signal collected by the junction is shaped by the preamplifier, that has a signal gain of 4 mV/e and reduces the time of the pulse from more than 100 μs to $\sim$ 2 μs [72]. Then the discriminator compares the pulse level with a reference current. The treshold is set for all the pixels of the detector with a dedicated group of parameters.

If the signal is above the threshold, the output of the discriminator is set to true. The hit is recorded if the signal from the discriminator is in coincidence with a STROBE signal. The STROBE signal is a global shutter, stated after a trigger command. Its duration in time can be set and spans from 50 ns to about 1.6 ms. When the STROBE signal is stated, an event frame is saved.

The frame is zero-suppressed by the priority encoders installed on the columns. The priority encoder collects the addresses of the pixels containing a hit and

---

[1]Although the pixels are not perfectly squared, the difference on the dimensions is small. In most of the analyses of this work, the pixels are considered squared with a pitch of 28 μm.
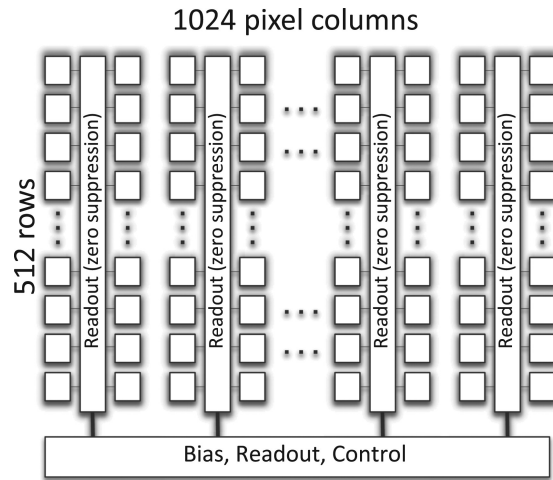
(a) Double column structure.
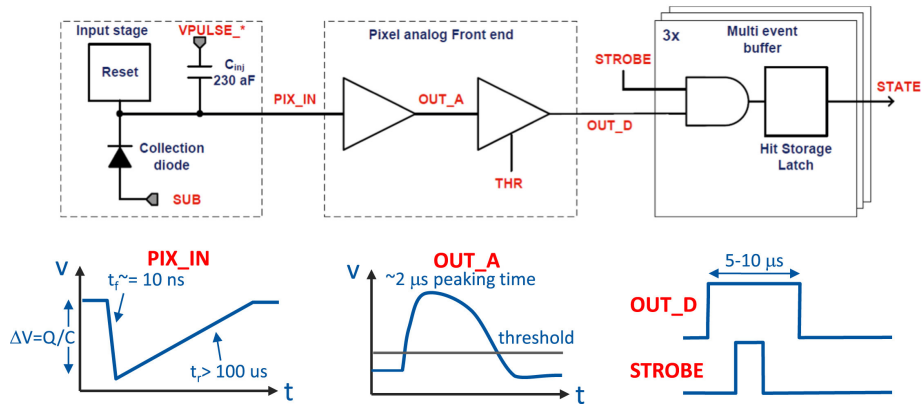
(b) Pixel front end.

Figure 2.7: Details of structure of ALPIDE [72].
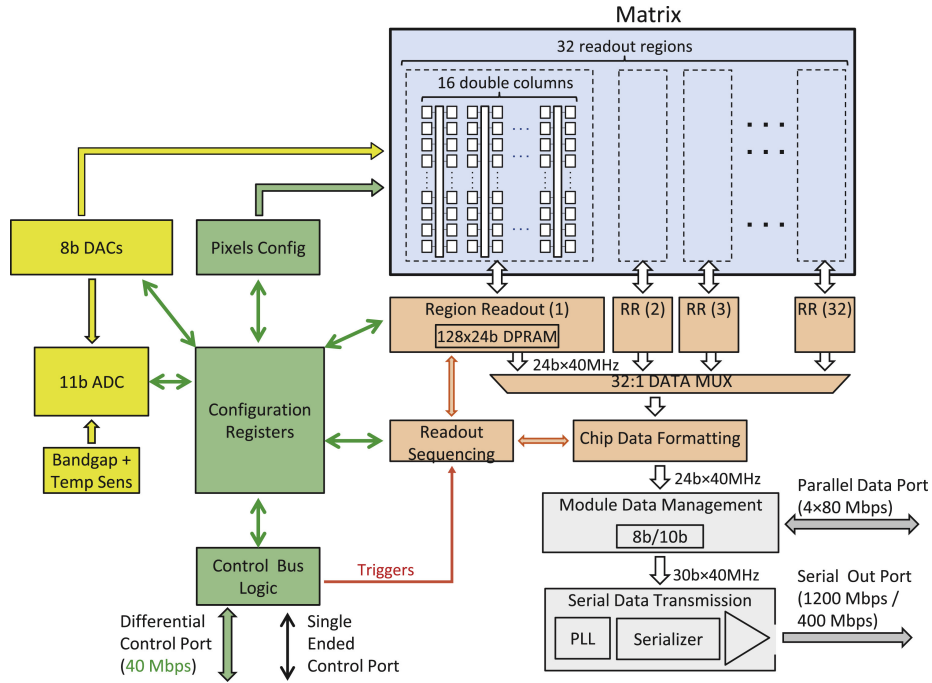
Figure 2.8: Block diagram of the ALPIDE detector [72].

sends the compressed information to the detector periphery. There is not a free running clock over the matrix, to minimise the activity if the pixels are not hit and reduce the power consumption. The priority encoders are also used to send commands from the periphery to the pixels [72].

In figure 2.8 a block diagram of the ALPIDE is shown. The blue rectangle represents the pixel matrix. The double columns are divided into 32 regions. Each region transmits the data collected from priority encoders to a readout DP RAM, in orange in the figure. Data stored on these registers are summarised and formatted in words by the periphery logic. Words pass to the Data Transmission Unit (DTU), in grey in the figure, that sends them to the high-speed Serial Output Port. The port has a 1.2 *Gbps* maximal line rate and it is unidirectional. It is used to transmit the words from the sensor to the readout system.

The sensor is equipped with a second differential line, the Differential Control Port (CTRL), in green in figure 2.8. The line is bidirectional and it is used to read and write register values and to send commands. The CTRL line has also access to the Data Formatting registers, and can therefore be used for the readout.

A third line is a single ended control port, that connects the detector to each others and it is used when the detectors are configured in master-slave mode (see section 2.4.2).

The complexity of DTU is shown in figure 2.9. The three main components
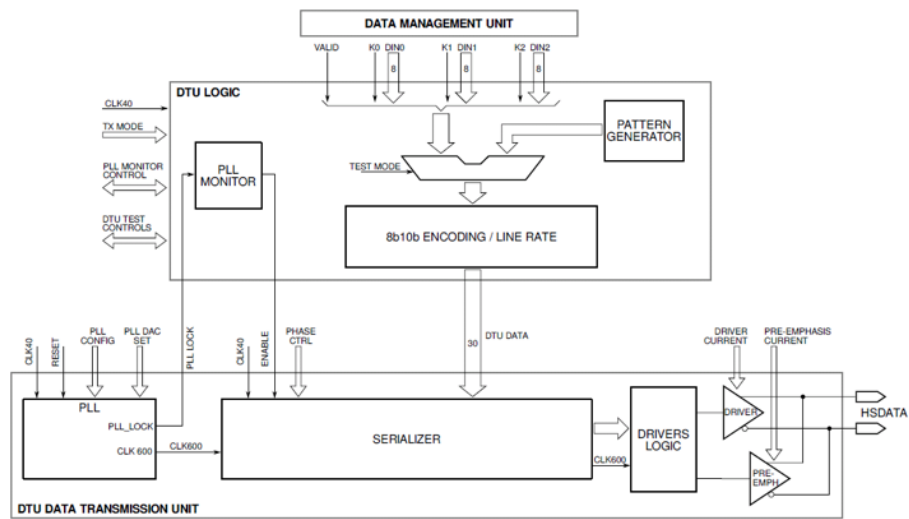
Figure 2.9: Scheme of DTU of ALPIDE [7].
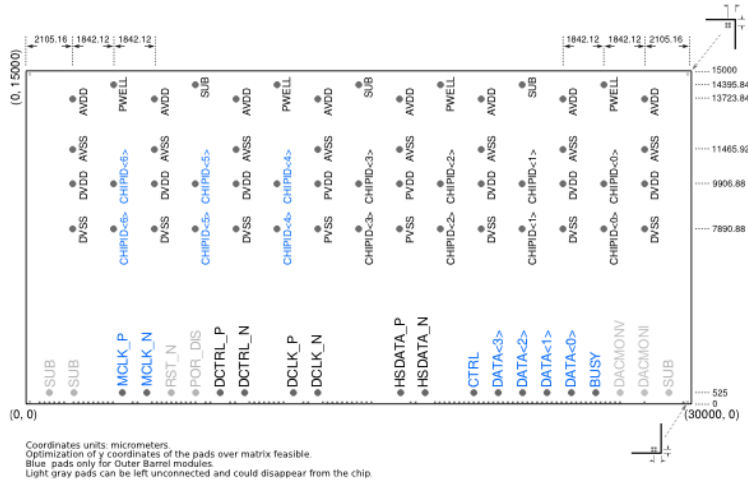
Figure 2.10: Pinot of the ALPIDE detector [14].

are the Double Data Rate serialiser, the output driver and the clock multiplication PLL. The serialiser complete the data encoding and sends them to a multiplexer controlled with the 600 MHz clock provided by the PLL. The multiplexer is connected to the output driver [61]. This block is responsible of most of the power consumption of the detector.

In figure 2.10, the positions of the pins of the ALPIDE are reported. Most of the pins are dedicated to the analog and digital power supply distributions. The pins highlighted in blue in the middle of the detector are dedicated to set the detector address. Their configuration is important to allow to communicate to multiple detectorss connected to the same control line. Pins on the bottom row are dedicated to communication between the detector and the external readout system. They handle the clock signal, the connections for data downlink and the control lines for detector configuration.

Readout modes

The detector can be programmed to operate in different modes:

- Triggered mode;

- Continuous mode.

The triggered mode is designed to sample the status of the pixels over a short interval of time. The strobe is typically set to some hundreds of ns and the trigger is controlled by an external source. The continuous mode is designed to sample the detector status with periodically repeated STROBE signals. In this case, the STROBE usually has the same duration of the interval between two consecutive trigger signals.

The two configurations are intended for different operation conditions, but the only difference introduced by setting the mode is the handling of the on-pixel memory buffer, when some pixels have already filled all the buffer. In triggered mode, if a new trigger is stated before the end of the matrix readout, the strobe signal is not generated. The frame for the second trigger is empty, and the previous event frame includes a flag. In continuous mode, the trigger statement during the readout of a event deletes data of the previous event to free space for the new frame. The interrupted frame contains all the pixels already stored and a flag to specify that some information is missing [14].

Data format

Word	Length [bits]	Binary coding
IDLE	8	1111_1111
CHIP HEADER	16	1010_<chip_id[3:0]>_<time_stamp[7:0]>
CHIP TRAILER	8	1011_<readout_flags[3:0]>
CHIP EMPTY FRAME	16	1110_<chip_id[3:0]>_<time_stamp[7:0]>
REGION HEADER	8	110_<region_id[4:0]>
DATA SHORT	16	01_<hit_position[13:0]>
DATA LONG	24	00_<hit_position[13:0]>_0_<hit_map[6:0]>
BUSY OFF	8	1111_0000
BUSY ON	8	1111_0001

Table 2.1: ALPIDE data format [14].

Table 2.1 reports the encoding of ALPIDE data. The words can encode all the possible detector statuses. After a trigger signal, if no pixels are over threshold the response is the CHIP EMPTY FRAME. If there are some hits, the response is more complex and is shown in figure 2.11. In this case, the first word is the CHIP HEADER, then the REGION HEADER of the first region interested by the event. Hits can be encoded in DATA SHORT or DATA LONG. In DATA SHORT, all the hits are transmitted individually. If the clustering is enabled and there is a group of pixels over threshold on the same double column, and the distance between the hits is less than 8 pixels, data can be encoded in DATA LONG. This format includes the address of the first pixel of the set and a pattern of 7 bits, shown in figure 2.12, that specifies the status of the following pixels. With this encoding, it is possible to reduce the number of words to read out.

If hits are spared among more than one region, the structure composed of REGION HEADER and data words is repeated until the detector frame is empty. When all the data have been read out, the CHIP TRAILER is stated [14].
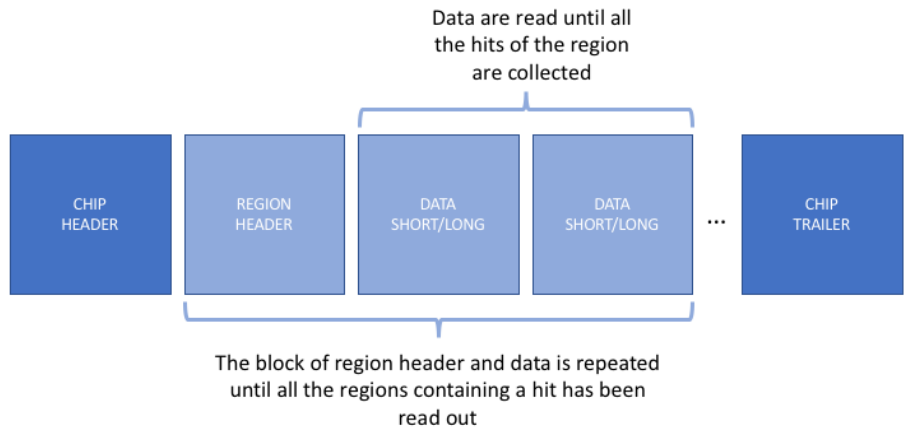
Figure 2.11: Readout logic of ALPIDE.
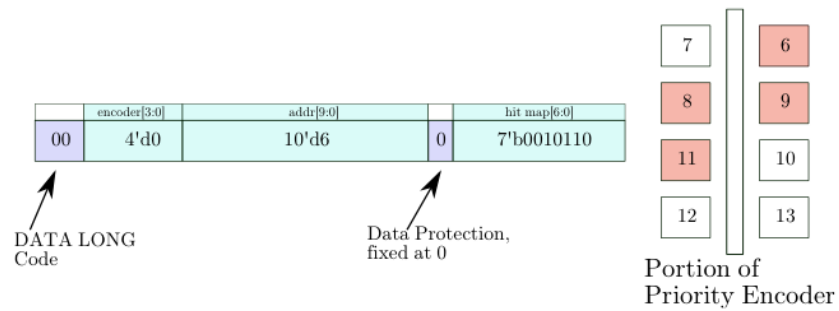
Figure 2.12: ALPIDE DATA LONG structure [14].
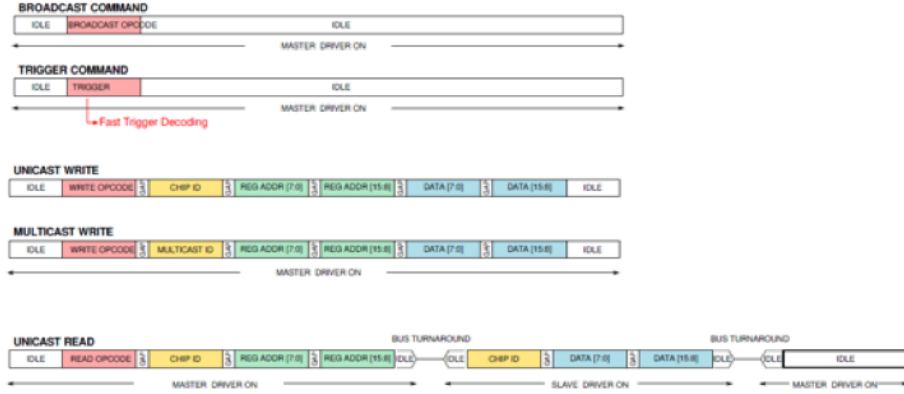
Figure 2.13: Communication protocols of ALPIDE CTRL line [14].

CTRL line communication protocols

The communication protocol along the control line is sketched in figure 2.13. There are different possible communication modes:

- Broadcast mode;
- Unicast and multicast write;
- Unicast read.

The broadcast transmission sends the same command to all the detectors connected to a line. Commands are a set of reserved words used for general configuration and trigger.

The commands for writing registers can be applied to a single target sensor or to all the sensorss connected to a line. In the first case, the address is specified. Instead, a multicast ID is stated. The command is divided in four sections:

- Write operational code;
- Chip ID (or multicast ID);
- Address of target register;
- Data to be written on the register.

The readout of a register can not be multicasted and it is necessary to specify a target detector. The protocol in this case is more complex because it requires a bus turnaround to allow the target detector to answer. The sequence in this case is the following:
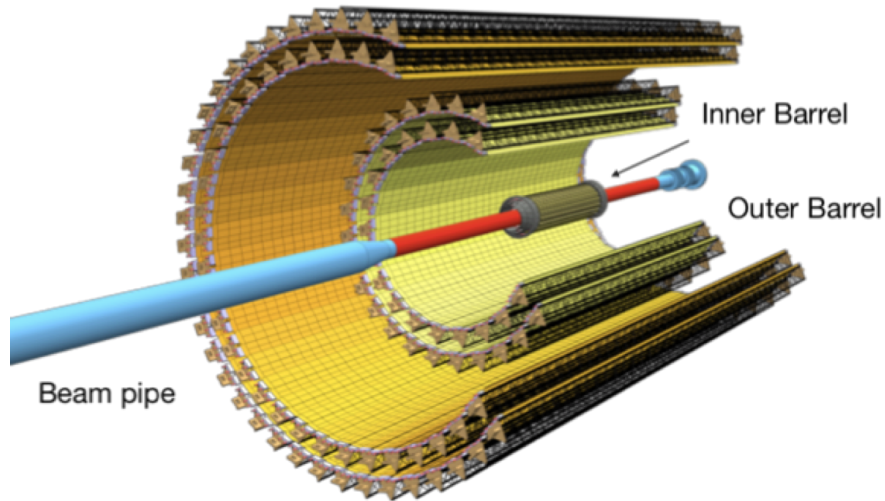
Figure 2.14: Sketch of ALICE ITS [4].

- Read operational code;

- Chip ID;

- Address of the target register;

- Bus turnaround;

- Chip ID;

- Data contained in the register.

The readout of a register requires 65 clock cycles, including the turnaround phase.

2.4.2   ALICE Inner Tracker Upgrade

ALICE (A Large Ion Collider Experiment) is one of the four main experiments of LHC. It is devoted to the study of Quark-Gluon Plasma (QGP) produced in ion-ion collisions [37] .

During long shutdown 2, started at the end of 2018, the collaboration is installing the new Inner Tracker System (ITS), sketched in figure 2.14. The detector is divided into two different sections, the Inner Barrel (IB) and the Outer Barrel (OB). Requirements for the two barrels are reported in table 2.2. The IB is the closer to the beam line and it is composed of three layers of detectors. The OB is divided in two groups of layers, the Middle Layers and the Outer Layers, containing two layers of detector each.

Figure 2.15 shows an exploded view of both IB and OB modules. The IB has a simpler structure to minimise the X_0. Each module is composed of a Flexible
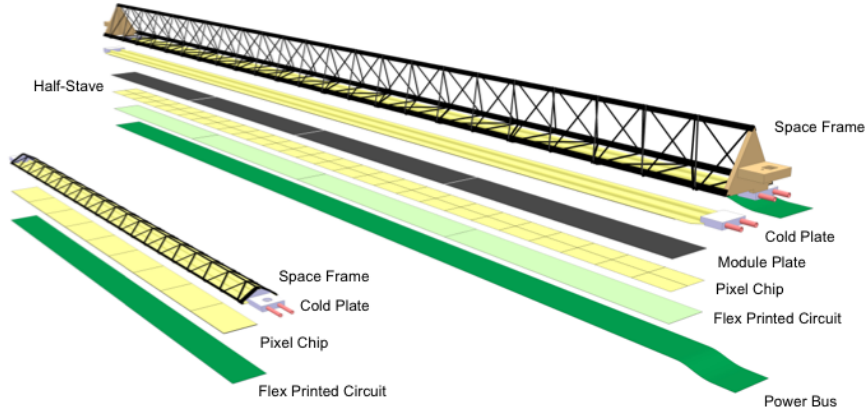
Figure 2.15: ALICE OB and IB modules [4].

Printed Circuit (FPC), a column of nine 50 μm thick sensors and a cold plate in carbon fibre, connected to the space frame that ensure the module to the mechanical structure of the detector. The OB modules have a more complex structure. Because of their length, they are composed of different groups of detectors, called Hybrid Integrated Circuits (HIC), composed of the FPC and the 100 μm thick ALPIDE detectors. Each HIC contains two columns of seven detectors. The power supply is distributed by a dedicated power bus, to avoid tension drops along the module. The mechanical support is granted by the carbon fibre space frames, the cold plate provides cooling. As for the IB, the space frame connects the module to the mechanical structure of the ITS.

Parameter	IB	OB
Chip size $[mm \times mm]$	15×30	15×30
Chip thickness $[\mu m]$	50	100
Spatial resolution $[\mu m]$	5	10
Detection efficiency	> 99%	> 99%
Fake hit rate	$< 10^{-5}$ evt^{-1}pixel^{-1}	$< 10^{-5}$ evt^{-1}pixel^{-1}
Integration time $[\mu s]$	< 30	< 30
Power density $[mW/cm^2]$	< 300	< 100

Table 2.2: Minimum requirements for ALICE ITS Upgrade detector [4].

Detector layout in ALICE IB and OB

The layout and connections of the detectors inside the ALICE staves are reported in figure 2.16.
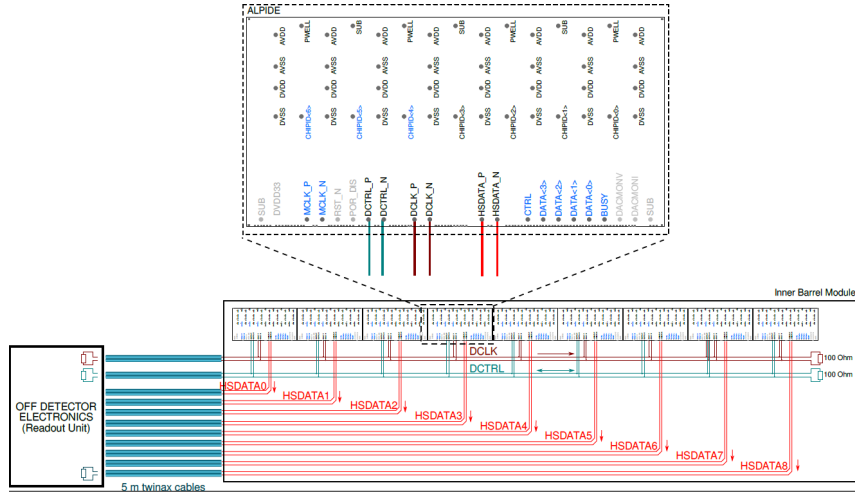
(a) ALICE IB layout.
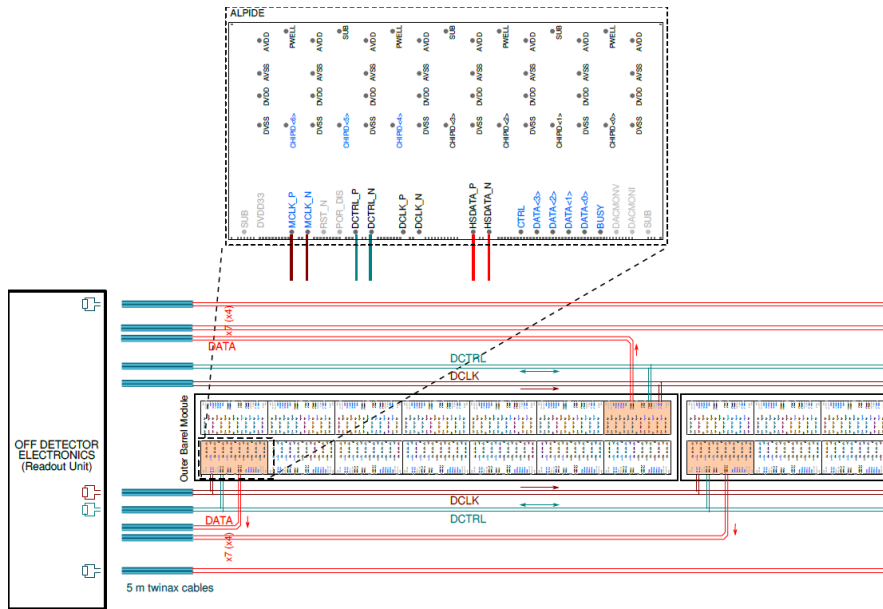
(b) ALICE OB layout.

Figure 2.16: Layout of ALPIDE detectors in ALICE IB and OB [7].
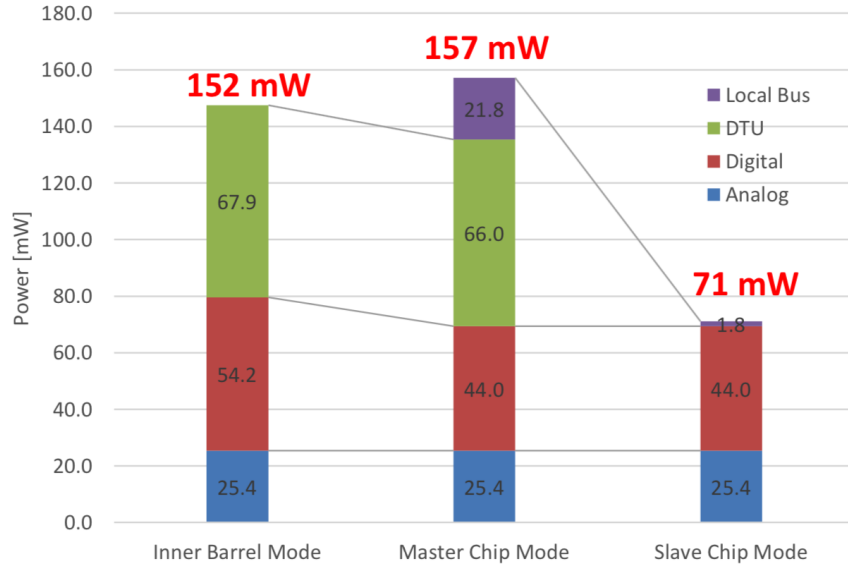
Figure 2.17: Power consumption of ALPIDE detector in different configurations [7].

Detectors of IB (figure 2.16a) are aligned on a single column of nine detectors. They are all connected with the off detector electronics and are read out independently through the High Speed data port. The CTRL and clock lines are distributed in parallel to all the detectors of the line.

OB staves (figure 2.16b) host two columns of seven detectors each. In this case, only one detector for each column is connected as a "master" and communicates with the off detectors electronics. The other six detectors, configured as "slaves" of the columns are connected to the master via the singe line control port.

The master receives the commands from the external readout and transmits the signal to the other detectors. After the trigger command, the master detector collects the data from all the detectors and sends it back to the external readout. The readout of the detector is slower than in IB, but the solution simplifies the connections with the external readout and reduces the power consumption.

2.4.3 Power consumption estimation

In figure 2.17 the main contribution of power consumption in different configurations of ALPIDE are shown (IB, OB master and OB slave).

The IB mode power consumption is divided in the three main contributions expected for a MAPS detector: the analog front-end, the digital circuitry and the DTU. The power consumption for unit of surface for IB can be calculated directly from this value, since all the detectors have the same behaviour. The
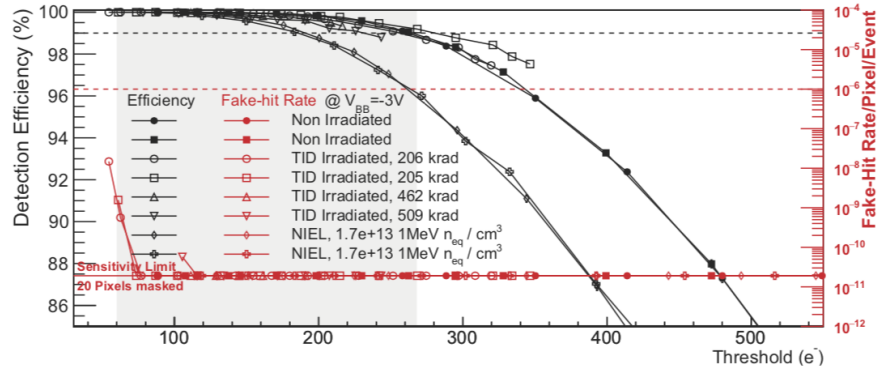
Figure 2.18: Detection efficiency and fake hit rate as a function of the threshold of non irradiated and irradiated ALPIDE detectors with a -3 V back bias applied [60].

value is 34 mW/cm^2.

The OB master detector mode has almost the same analog, digital and DTU consumption, and a contribution due to the handling of the connections with the six slaves. The total power consumption of the single master detector is slightly higher than the IB mode, but this increase is compensated on the full module by the smaller power consumption of the slave detectors. Since they are not directly connected to the DTU, that contribution to the power consumption is 0. The analog and digital power consumption is the same of the previous configurations.

The power consumption for units of surface of OB can be calculated taking into account the different configurations of the sensors, and it is 18.5 mW/cm^2. In both cases, the values are well below the ALICE requirements, reported in table 2.2.

2.4.4 Characterisation of ALPIDE response to high energy particles

ALPIDE has been designed to detect high energy particles emitted by Pb-Pb collisions at LHC. Because of this destination, a vast number of studies with GeV-scale particles have been carried out to characterise the detector response.

The analysis of the sensors has focused on four properties, in particular: efficiency, fake hit rates, spatial resolution and cluster size. The results are shown in [72] for the pALPIDE-2, a full-scale prototypes.

The fake hit and detection efficiency as a function of the threshold current are reported in figure 2.18. The efficiency is well above 99%, as required by ALICE specifications, and the fake hit rate is below 10^{-10} fake-hit/pixel/event for non-irradiated detectors, and rises up to 10^{-7} fake-hit/pixel/event after irradiation. Values are two orders of magnitude lower than the requirements for ALICE upgrade, fixed at 10^{-5} fake-hit rate/pixel/event.
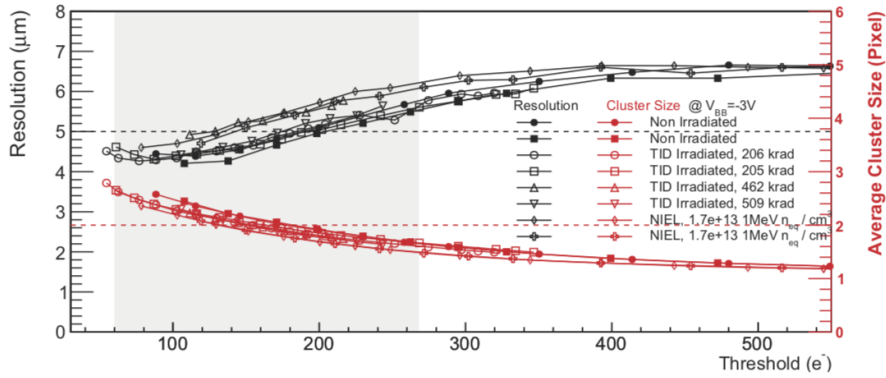
Figure 2.19: Cluster size and spatial resolution as a function of the threshold of non irradiated and irradiated ALPIDE detectors with a -3V back bias applied [60].

Another important property of the detector is the spatial resolution. Because of the digital output, it is strictly related to the cluster size of the event, defined as the number of pixels that share the charge produced by a particle. In figure 2.19 the quantities are reported as a function of the threshold current. The space resolution improves when the cluster size is higher. As already discussed, a cluster size larger than one provides additional information and improves spatial resolution. Higher threshold reduce the cluster dimension and limits the spatial resolution to the pixel pitch/$\sqrt{12}$.

In figure 2.20 the cluster size as a function of the incidence point of the MIP inside the pixel. The measurement has been taken with a laser beam, tuned to mimic the release of MIP inside the silicon. A -3 V back bias is applied to the detector. The plot shows that cluster size spans from about 1.3 to 4 depending on the position of the hit [59].
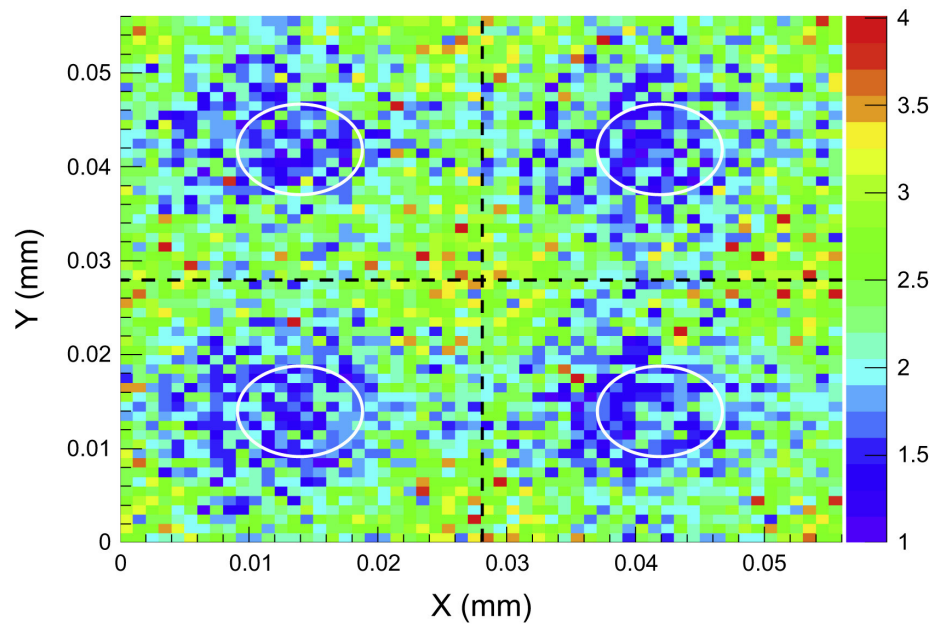
Figure 2.20: Cluster size as a function of hit position in a four pixels domain with a laser beam [59].

Chapter 3

HEPD-02 tracker design and spatialisation

The HEPD-02 project, part of the CSES-02 mission, has been officially approved in February 2019 in Rome. The specifics of the new detector are the same as the HEPD-01, with some modifications aimed to improve the performance and to reduce the energy threshold, in particular for electrons. A scheme of the new detector is shown in figure 3.1.

Among the different subsystems, two undergo some essential changes: the trigger and the tracker. The calorimeters will preserve the general structure of HEPD-01, described in section 1.2.5. It will be composed of a tower of EJ-200 planes and a array of LYSO (Lutetium-yttrium oxyorthosilicate) bars. Five planes of scintillators will be installed on the four sides and on the bottom of the detector.

The tracker description is the main topic of the following sections, so the study focuses on the trigger structure. The main differences on the trigger are: (i) the reduction of the thickness of the bars from 5 mm to 2 or 3 mm, (ii) the increase of plane number from one to two, (iii) one plane of the trigger placed before the tracker, (iv) the bars of the two planes will be placed perpendicular to each other.

The thickness of the bar is still under discussion because they need to ensure the mechanical strength required to resist vibrations during the launch.

The collaboration is oriented towards the 2 mm option to minimise the material budget and reduce multiple scattering. This thickness lowers the energy threshold of the experiment, still guaranteeing sufficient light yield to trigger and efficiently measure dE/dx.

3.1   HEPD-02 tracker

Figure 3.2 shows the proposed design of the tracker. Figure 3.3 schematises the tracker composition. The basic element is the stave, designed on the ALICE
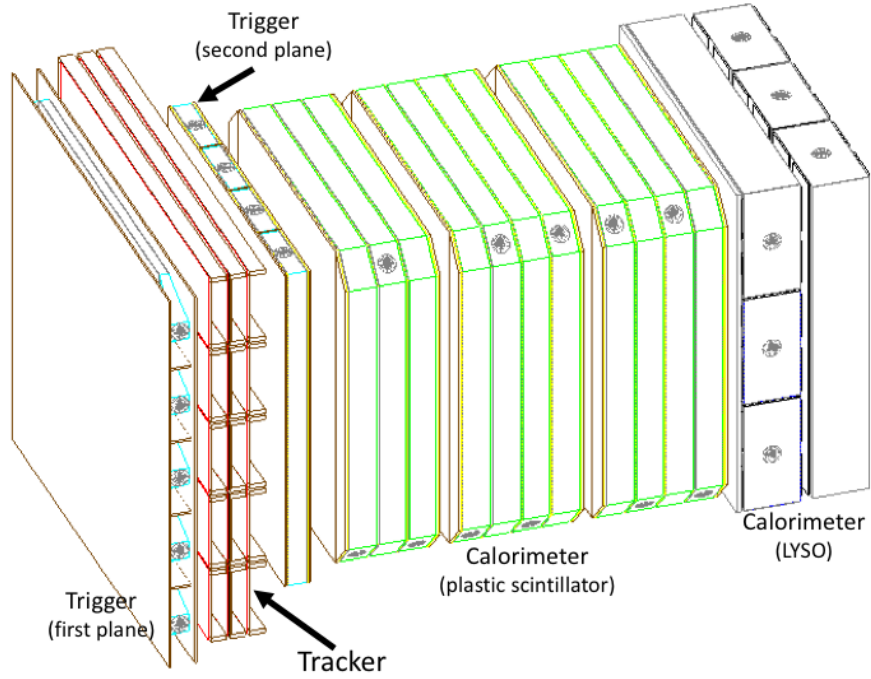
Figure 3.1: HEPD-02 detector structure from GEANT4 simulation. Lateral and bottom scintillator panels are not represented. Courtesy of L. Carfora.
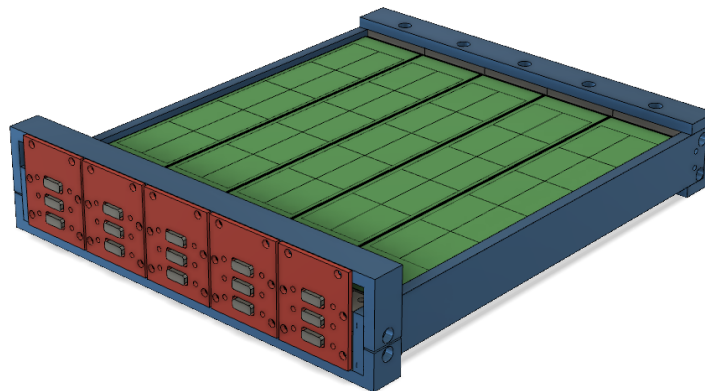
Figure 3.2: Graphic render of HEPD-02 proposed tracker.
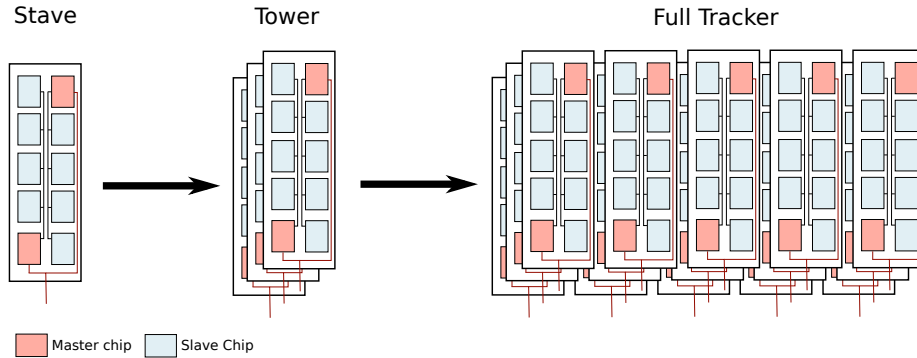
Figure 3.3: Scheme of tracker elements grouping. Courtesy of G. Gebbia.

OB model (see section 2.4.2). Each stave contains ten ALPIDE sensors, placed on two parallel columns of five detectors. The hierarchy of the detectors is the same of ALICE OB: in each column, one detector is configured as master and four as slaves. In this configuration, only the master communicates directly with the readout system, and it collects data from the other four detectors.

Three staves are stacked to form a turret. Between the planes, the distance is 8.6 mm. The turrets are independently operated and are the basic element to compose the tracker, that contains five turrets. The choice of keeping separate turrets has several advantages. The first is that in case of failure of a single section, only 1/5 of the detector is lost. Another is that a smaller system is easier to optimise. In particular, thermal and mechanical requirements are easier to handle in small and compact objects. Once the single turret is ready, five identical objects are placed side by side to form the full detector.

Tracker stave

The stave is composed of three elements: the FPC, the detectors and the carbon fibre cold plate. The sensors are glued and wire-bonded to the FPC, that hosts all the electrical connections to control the detector, read out the signals and to power the sensors. Different designs for the FPC, based on ALICE ITS Upgrade IB and OB designs (see section 2.4.2), have been considered. The choice of the best option for HEPD-02 depends on the results of GEANT4 simulations, as described later in section 3.5.

A second component of the stave whose impact on the performance of the detector must be studied carefully is the carbon fibre cold plate. It is glued on the opposite side of ALPIDE and provides mechanical stability and cooling to the system. ALICE ITS has a comparable element in its design, but its function is only to support and cool the thin structures made of ALPIDE and FPC. In HEPD-02 case, the main function of the plate is to ensure an efficient heat removal from the detectors during operation, then it also has to provide the mechanical robustness to the detector.
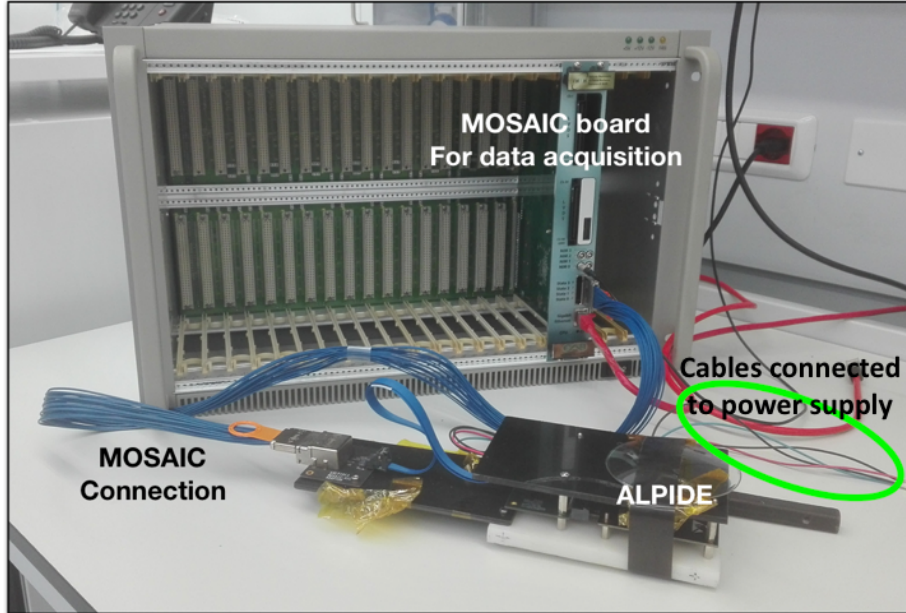
Figure 3.4: Setup for ALPIDE readout installed in Trento Clean Room.

In ALICE ITS, cooling has been delegated to an active system of circulating water, a solution that is not suitable for space applications. For space applications, beeing to cooling provided only by the cold plate, the carbon fibre thickness and orientation must be carefully studied, both with finite element calculation and with direct measurements of thermal conductivity of the prototypes. More information on power dissipation and cooling are in section 3.3.

For nuclei and electrons in the MeV - 100 MeV range, the design of the HEPD-02 stave is the best compromise between (i) mechanical stability and heat-transfer capability and (ii) low material budget.

The acceptance of HEPD-02 is about 300 cm^2sr, to be compared with 400 cm^2sr of HEPD-01 and less than 10 cm^2sr of competitors. The acceptance is mostly driven by the trigger geometry, that in HEPD-02 is smaller than its predecessor.

3.2 Power consumption measurements

—Power consumption characterisation has been carried out in Trento with an ALPIDE bonded to a single-chip carrier board. The setup is shown in figure 3.4. The ALPIDE is connected to the MOSAIC electronic board [39], that provides an interface between the detector and the computer, using a commercial

SAMTEK firefly cable. The MOSAIC is powered up with a VME rack and it is connected to a laptop via Ethernet. The detector bias is provided through a power supplier. Analog and digital channels are separated to estimate the power consumption of the two lines.

The MOSAIC board can provide a 40 MHz clock to the sensor (LHC clock frequency), but for these measurement the clock has been provided using a signal generator, to test different clock frequencies (see section 3.3). The signal generator gives as output a NIM-like signal (squared pulse, the false reference is 0 V, the true is -88 mV) at different frequencies between 40 and 5 MHz. The downclock is possible only if the PLL blocks of the detector are disabled. The signal generator sends the signal to the MOSAIC board, and the board forwards the signal to the ALPIDE. The whole setup is installed inside the clean room of INFN-TIFPA.

3.2.1   Current probes

To measure the current transients, two different current probes have been used: (i) an active current probe, in figure 3.5a (ii) a passive current probe in figure 3.5b. The passive current probe is used to investigate the transients, the active probe measures also the DC contribution. The probes are read out using two different digital oscilloscopes. A 200 MHz $2GS/s$ Tektronix oscilloscope and a 1 GHz 10 GS/s Lecroy oscilloscope. The broader bandwidth of Lecroy oscilloscope allows to characterise the dynamic power consumption of the detector.

The transfer function (TF) of both the probes is shown in figure 3.6. It has been measured using as input signal a sinusoidal wave of amplitude 2 Vpp, produced by the waveform generator and passing through a $R = 1$ $k\Omega$ resistor. The points are calculated according to the formula

$$TF = \frac{V_{res}}{I_{in}}$$

where V_{res} is the voltage measured by the probe and I_{in} is the current flowing on the resitor, calculated as $I_{in} = \frac{V_{in}}{R}$. V_{in} and V_{res} are measured with the oscilloscope. The active probe has a response that is almost constant and equal to 0.1 V/A for frequencies from 1 Hz to 100 kHz, as quoted by the constructor. The passive probe is not sensitive to frequencies below 10 Hz, and it is not fully efficient for frequencies lower than 100 Hz. The gain factor on the plateau is 1 V/A. It ends at about 1 MHz.

Since currents expected are small, less than 200 mA on digital line and less than 20 mA on the analog line, in the measurements the signal is enhanced by making the cable passing five times inside each probe, so there is a factor 5 to take into account in all the results displayed.

3.2.2   Software tested

The first aim of this test is to identify the test sequence, defined by software procedures that consume the most of the power. To test the different detector

(a) Active probe.

(b) Passive probe.

Figure 3.5: Current probes used for the measurements.
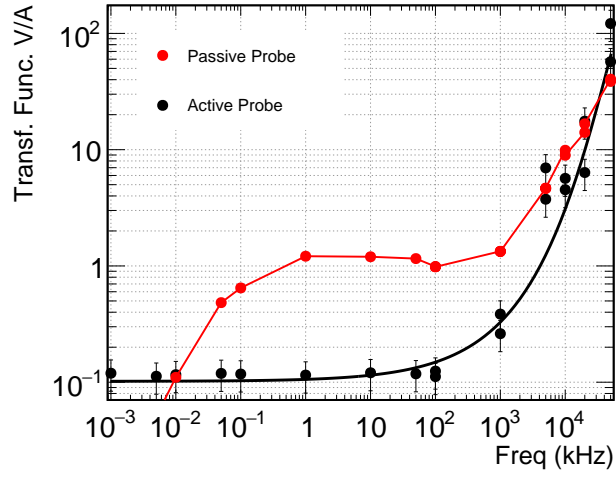
Figure 3.6: Transfer function of the current probes measured as a function of the signal frequency.

Test	CTRL line status	High Speed line status
FIFO test	ON	OFF
Digital scan	ON	ON
Threshold scan	ON	ON

Table 3.1: ALPIDE communication lines status during different tests.

elements (logic blocks and communication lines), three test routines have been selected:

- FIFO test;

- Digital scan;

- Threshold scan.

The use of the different communication lines of ALPIDE during the tests is summarised in table 3.1.

FIFO test

The FIFO (Fan-In Fan-Out) test executes the following operations:

- A pattern is written on DP RAM registers;

- The values are read back;

- The number of errors is reported.

The test repeats the procedure for different patterns. This test checks the RAM health and the correct connection of the detector with the readout. It is considered successful if no errors are reported. The test uses only the control line for both the operations (see section 2.4 for more details on the lines).

Digital scan

The digital scan tests the readout of the detector, that uses the high-speed line. This test can be used to check the power consumption of the high-speed line.

Threshold scan

The threshold scan is designed to calibrate the detector. Each pixel has a charge injector, controlled by two registers that set the quantity of charge injected. A series of pulses of progressively higher charge are injected to evaluate the threshold of each pixel. After each charge injection, the detector is read out and the status of each pixel is checked. The scan is repeated more times for each charge value on each pixel to evaluate the uncertainty on the value obtained. From this scan, it is possible to obtain the minimum number of electrons necessary to take the pixel over threshold. The control of the consumption is particularly critical because of the use of charge injectors and because of the large number of pixel involved (all the pixels of the detector).

The first measurement of the power consumption can be done checking the current flow measured by the power supplier. This first raw measurement can then be refined with the current probes, that are sensitive to the transients.

From all the tests, it appears that analog line consumption is not affected by the operations, as expected. The current flowing in the digital line instead

changes depending on the operation. It reaches the minimum when the clock is not distributed and rises when the CTRL line is used. It rises even more when the high-speed readout is stressed.

3.2.3 Digital line power consumption

Test	Analog current $[mA]$	Digital current $[mA]$	Power consumption $[mW]$
FIFO test	12	53	117
Digital scan	12	134	240
Threshold scan	12	134	240

Table 3.2: Summary of the power consumption measured during different tests with single sensor setup.

During the test, a 1.8 V is applied to both digital and analog lines. Back bias is set to 0 V by grounding the connection. A summary of the results is reported in table 3.2.

FIFO test

Even before the test beginning, the first operation that modifies the power consumption is the clock distribution, as shown in figure 3.7a. The first rising step is a consequence of the clock distribution to the detector.

The use of the passive probe, that has a higher conversion factor allows to identify the two peaks corresponding to the operations of writing and reading with the CTRL line. The noise of the active probe covers the peaks produced by the signal.

By combining the results of both the probes, it is possible to calculate the maximum power consumption of the detector when operated using only the CTRL line. In principle, all the operations can be done along this line, used for the readout during tests of the prototypes.

The current flowing on digital line before the beginning of detector operation, without the clock distribution, is about 16 mA. This value is compatible with the current flow on the analog power line. The value after clock distribution, measured by both the probes, is 45 mA. The amplitude of the overshoot produced by the operations is ≤ 8 mA. The current peak is 70 mA, that corresponds to a power consumption, calculated as the sum of analog and digital currents multiplied for the voltage applied (1.8 V), of 125 $mW/sensor$. The power density is 28 mW/cm^2.

Digital scan

The second test used to study the power consumption is the digital scan. In this case the detector sends out the data through the high speed readout line, which requires the PLL block to be operative. The details of the power consumption during the test are shown in figure 3.8.
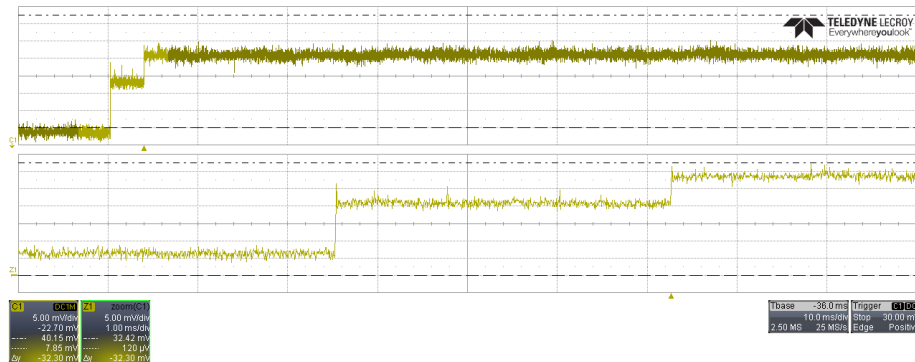
(a) Active probe characterisation: continuous contribution. The voltage (on y axis) is plot as a function of the time.
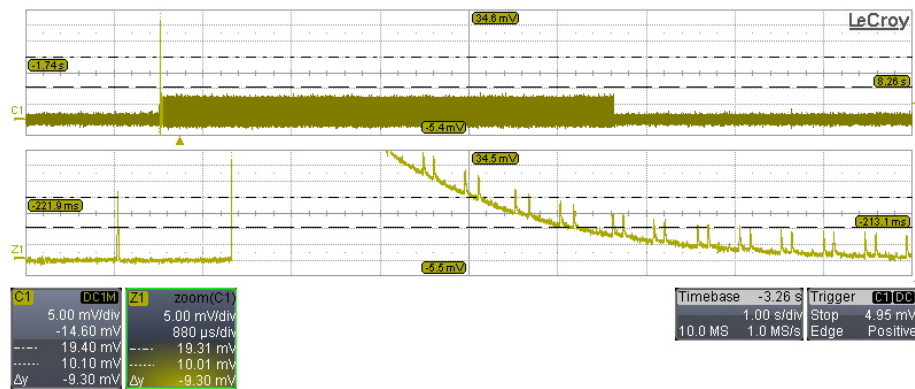
(b) Passive probe characterisation: transients. The voltage (on y axis) is plot as a function of the time.

Figure 3.7: Current flowing in digital power line during FIFO test. The active probe measures the DC contribution, and the passive enhances the details of the transients.
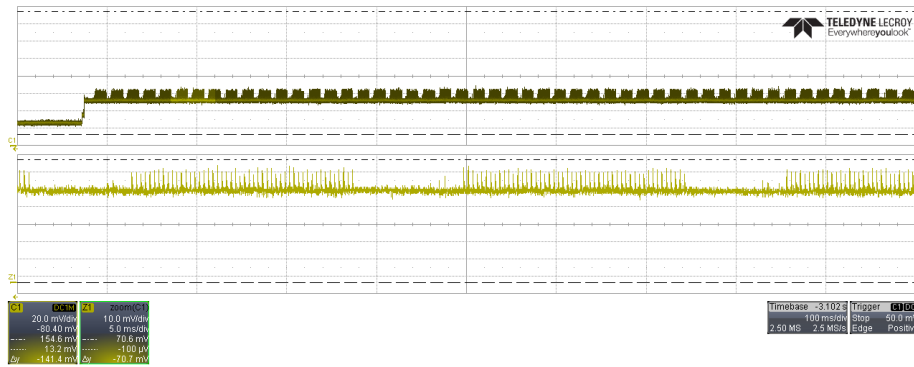
(a) Active probe. The voltage (on y axis) is plot as a function of the time.
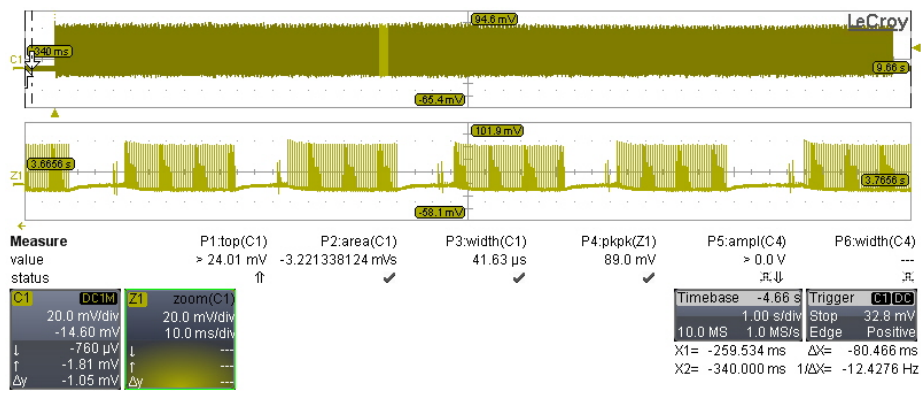
(b) Passive probe. The voltage (on y axis) is plot as a function of the time.

Figure 3.8: Digital scan current flow.
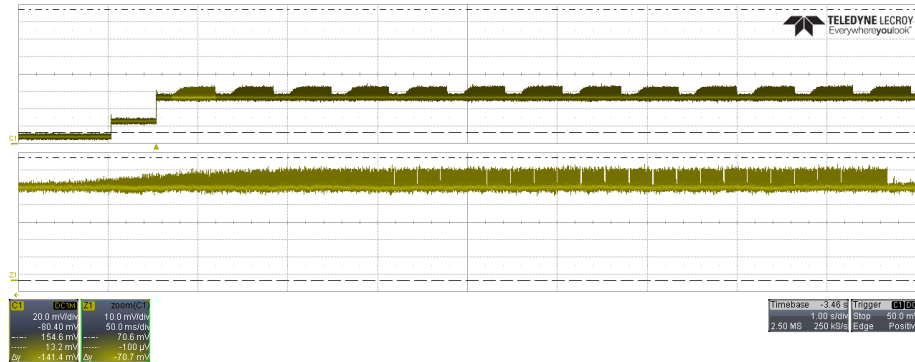
Figure 3.9: Current consumption of threshold scan. Data collected with active probe. The voltage (on y axis) is plot as a function of the time.

The structure is more complex with respect to the FIFO test, and the spikes related to single operations are more pronounced, enough to be observed clearly with both the probes. The double jump due to clock distribution and to the beginning of communications is still visible at the beginning of the test.

In this case, the power consumption can be calculated from the measurements taken with the active probe, that follows up all the signal dynamics. The maximum peak voltage amplitude is 67 mV. By dividing it by five and multiplying by 10, the maximum flowing current value is 134 mA and a 1.8 V potential, that leads to power consumption for the only digital line of 241 mW. The power density, in this case, is 54 mW/cm^2. Values are compatible with those reported by ALICE collaboration and shown in figure 2.17 and reported in section 2.4.3.

Threshold scan

Figure 3.9 shows the threshold scan current absorption. In the figure, it is possible to notice an increasing trend on the amplitude of the spikes connected to the different operations. This increase is coherent with the threshold scan structure, in which for each pixel an increasing amount of charge is injected to evaluate the threshold and the noise.

In figure 3.9, the first part of the threshold scan is shown. The plot on the bottom zooms on a structure, to show the rising trend of the spikes.

The power consumption measured in this case is the same as the digital scan. The charge injection does not require additional power.

3.2.4   Downclocking

A possible way to reduce power consumption is to lower the clock frequency. This operation implies that the fast readout line can not be used. The only test that can be carried out with different clock frequencies is FIFO, that uses only
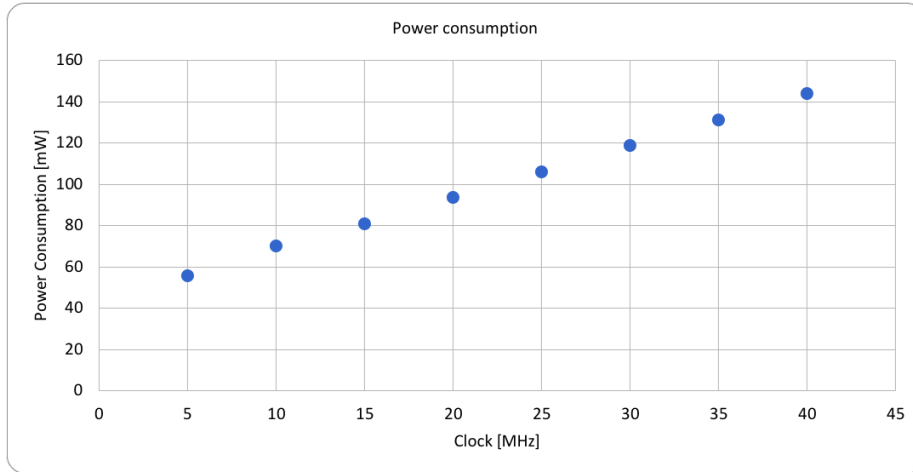
Figure 3.10: Total power consumption of ALPIDE at different clock frequencies.

the CTRL line.

Clock Frequency [MHz]	Digital line current [mA]	Total power consumption [mW]
5	20	56
10	28	70
15	34	81
20	41	94
25	48	106
30	55	119
35	62	131
40	69	144

Table 3.3: Current flowing in the digital line and total power consumption at different clock frequencies for a single ALPIDE configured as master. The power consumption is calculated by taking into account a fixed current flowing in the analog line of 11 mA and the value of the voltage applied by the power supplier (1.8 V).

The power consumption measurements collected with different clock frequencies are shown in table 3.3 and in figure 3.10. The current flowing in the digital line decreases linearly with the clock frequency. It is possible to test the detector for frequencies from 40 MHz to 5 MHz. For lower frequencies, It is not possible to obtain an answer from the detector, probably because of a limitation on the MOSAIC board.

The exercise of downclocking is interesting but has some limits. The first is that the FIFO test is not reading out data from the detector, and it is not possible to verify if there are other consequences on the readout chain. Another

consequence is that the time required by the operation increases linearly with the decreasing of the frequency, that gives the time references for all the digital operations.

3.3 Strategies for power consumption reduction

From the measurements, it is clear that most of power consumption is due to the high-speed data line. The increase depends on the activation of the PLL block, that requires a larger current than the other electronic blocks.

A solution to limit the power consumption should consider readout solutions that exclude this block from the detector readout. It is necessary to find a different way to read out data from the detector. A possible solution is to use the CTRL line.

The data transmission speed on this line is low and depends on the clock frequency. For each operation, it is possible to calculate the clock cycles required and to extrapolate the time as a function of the clock frequency. The procedure consists in reading a couple of registers multiple times until the end of the event is reached. More details on register readout are provided in section 2.4

Power consumption can be further reduced with a smart distribution of the clock signal, that requires coordination between different subsystems. The segmented trigger plane of HEPD-01 helped in reconstructing events from tracker by resolving ambiguity on n plane. For HEPD-02, the idea comes from the fact that the bars of the trigger plane and trigger staves have the same dimensions, and bars of one of the plane have the same orientation. When a particle produces a signal in a bar, the detector readout system distributes the clock only to neighbouring turrets. If the distance between the trigger and tracker plane is small, the probability to find the hit inside the tracker tower above the bar is high. Minimisation of the distance between the two elements reduces the loss of acceptance of the detector for very inclined tracks acceptance of the detector.

This procedure of clock distribution introduces a delay between the signal generation and data collection. The on-pixel analog electronics helps in this procedure by maintaining the signal at the output of the preamplifier for several μs, giving time to the system to produce trigger signal. A measurement of this hold time is reported in section 4.2.

3.4 Cooling

The high power consumption of MAPS detector is a problem that affects all applications, not only the use in space. The power dissipation of the detector produces heat that must be removed to keep the temperature in the optimal functional range.

To guarantee the usability of data for analyses, detector experts define minimum levels of data quality, accounting for operating conditions like temperature, electromagnetic environment, dead-time, and other parameters. The response
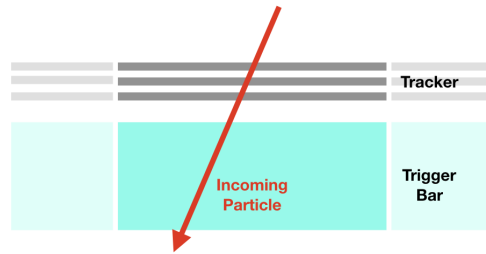
(a) Particle crossing.

(b) Clock distribution.
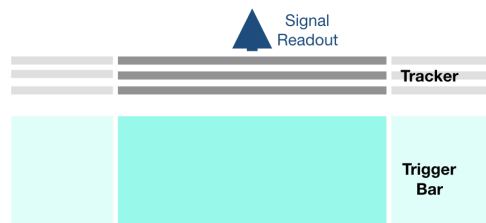
(c) Tracker read out.

Figure 3.11: Clock distribution mechanism.
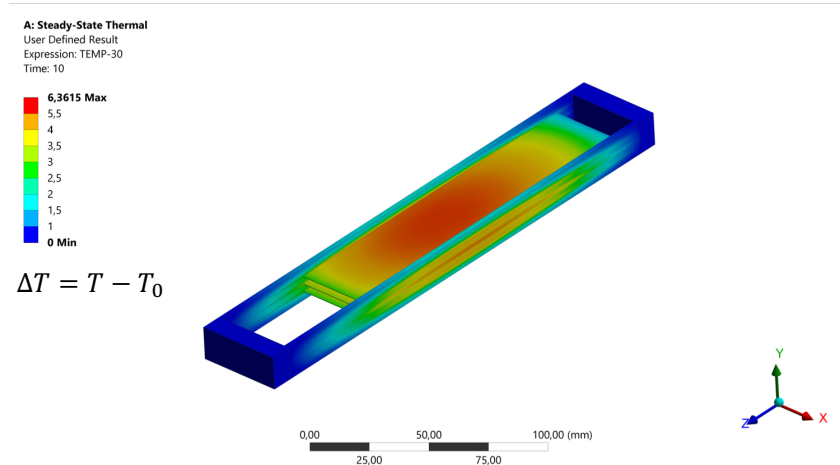
Figure 3.12: Temperature gradient along the turret during detector operations. Courtesy of E. Serra.

of MAPS depends on the operating temperature, as the noise and thresholds vary with temperature. As a consequence, uniform responses are obtained only if temperature gradients among sensors are kept below certain values and constant in time.

Designing the passive cooling system of the apparatus requires to find the best compromise between efficiency in heat removal and structure lightness: thick layers of conductive materials facilitate thermal dissipation, but they worsen the measurement, increasing the threshold and the multiple Coulomb scattering.

ALICE ITS, described in section 2.4.2, will be operated at room temperature (between $20°C$ and $30°C$), and it will be actively cooled using water, circulating inside pipes installed on the mechanical structure of the staves [4], as shown in figure 2.15. This approach increases the material budget in some regions of the stave, reducing the uniformity of the system. At the same time, it provides the reliability and efficiency required for the long-term operation of the detector. Other liquids coolants have been tested, but water provides the best cooling without adding complications connected to the storing and managing of other materials [37].

Before the introduction of the water cooling, a simpler solution was proposed, based on the thermal conductivity of the carbon fibre used for the mechanical support of the detectors and FPC. This system does not provide a temperature gradient sufficiently small along with the ALICE modules, whose length is between about 30 cm for the innermost layers to about 1.5 m for the outermost [4]. For such a long structure, the heat transportation is not efficient,

84

and the temperature is not uniform. This solution is interesting because it provides a uniform dead layer on the detector sensitive region, that can be easily modelled and simulated to evaluate the impact on detection performance.

For HEPD-02 tracker is not possible to provide cooling with water, or with any other system that requires to store materials that could damage the detector in case of losses. In general, the use of passive methods is recommended to improve reliability and lower operational risks. Since the stave of HEPD-02 is only 15 cm long, it is possible to use only the carbon fibre for both mechanical stability and heat remotion. The lower power consumption of the detectors due to the application of strategies discussed (see section 3.3) reduces the heat to be removed and helps to control the gradient.

HEPD-02 will have the same power dissipation system of HEPD-01, based on a radiator plane at about $35°C$, where all the excess heat is conveyed. The HEPD-01 tracker is connected to the radiator via a thermal conductive structure on a single side. For HEPD-02, a structure that connects both the sides of the stave is under development. The tracker has to keep a temperature gradient lower than $5°C$ along the stave.

The efficiency in removing heat depends on: (i) thermal conductivity of the materials, (ii) shape and thickness of the plate.

The material selected for the plate is carbon fibre. The use of different layers of fibres with different orientations helps to optimise the heat control. The total thickness depends on the number of layers that compose the plate. GEANT4 simulation has been used to investigate total thicknesses of carbon fibre plate spanning from 0.3 to 1 mm. The impact of the carbon fibre on physics performance is shown in section 3.5.

A finite element analysis can be used to evaluate the temperature gradient along the stave. The result of this analysis is shown in figure 3.12. To properly set the simulation parameters, measurements of thermal conductivity of the first prototypes have been used. In the analysis, the thermal conductivity of the carbon fibre is set to 200 W/mK along the plane (X and Y directions) and 50 W/mK in Z. Values are kept lower than those measured during tests to be more conservative.

Geometry has a considerable impact on the surface contact between the two materials. The cold plate has a "C" shape to improve the heat exchange because this shape enlarges the contact surface. The height and width of the wings, or ribs, of the fibre can be tuned to maximise the heat removal. At the same time, it is essential for particle tracking to keep the planes as close as possible to avoid to lose acceptance within a single tower. Finite element calculation results show that it is possible to keep the temperature gradient within $5°C$ and $10°C$ by using about 400 μm of a cold plate with ribs of about $1.9 \times 6.6 \ mm^2$. Tests are ongoing on a second version with $1.9 \times 4.6 \ mm^2$ ribs.

The best version of cold plate considered for these studies consists of three layers of K13D2U carbon fibre [62]. Each layer is 80 μm thick. The top and bottom layers fibres are parallel to the shorter dimension of the stave, the central layer is perpendicular to the other fibres, and it is oriented along the stave length. A thin ply surrounds the cold plate to avoid delamination of the fibres. It adds

two layers of 45 μm to the stratigraphy.

With this geometry, there is a gap of 8.6 mm between two planes of the tracker. A power consumption of 120 mW per sensor has been considered, corresponding to 27 mW/cm^2.

The cold plate is also main structural element providing mechanical stability to the turrets.

3.5 GEANT4 simulation of HEPD-02 stratigraphy

A GEANT4 simulation of the HEPD-02 proposed stratigraphy has been used to evaluate the physics performance of the new detector. Various structures have been proposed for the FPC and cold plate, based on the ALICE ITS staves, developed for the IB and OB (see section 2.4.2).

The two configurations have been evaluated in the simulation. The key parameter for the physics is the HEPD-02 tracker material thickness, which determines the proton and electron energy thresholds, impacts on the angular resolution. The results are compared to the performance of the HEPD-01 tracker, composed of two planes of 300 μm thick double-sided silicon microstrip detectors.

To correctly evaluate the performance and to compare it with HEPD-01, the trigger scintillator plane that in HEPD-02 is put before the tracker is not considered (see figure 3.1). The entrance window and thermal blanket located in front of the detector are included in the simulation. Window and thermal blanket of HEPD-01 are used, since significant differences are not expected for the new detector.

The window has a double-layer structure, consisting of a layer of 35 μm thick copper and a layer of 45 μm thick Kapton. The thermal blanket is composed of three planes. Each plane contains:

- 1 layer of double-sided aluminised Mylar, 18-25 μm thick;

- 3 layers of 6 μm thick Mylar;

- 1 layer of 18-25 μm thick single side aluminised Mylar.

Figure 3.13 shows the window and thermal blanket in the simulation. The first structure on the right side is the two layer window, containing Kapton (green) and copper (red). The thinner white lines on the left represent the different layers of the thermal blanket.

The HEPD-01 simulation contains the two planes of 300 μm thick silicon. The distance between the planes is 1 cm. HEPD-01 tracker has two microstrip planes, the HEPD-02 tracker has three pixel detector planes.

The stratigraphy of HEPD-02 tracker plane has multiple layers, shown in figure 3.14. The following layers are present:

- 50 μm thick ALPIDE (yellow);
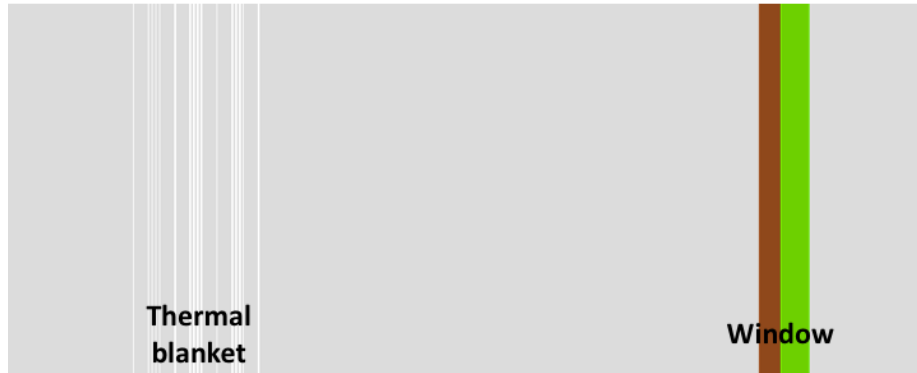
Figure 3.13: GEANT4 simulation of window and thermal blanket of HEPD-01. The same structure has been used also for HEPD-02 simulations.
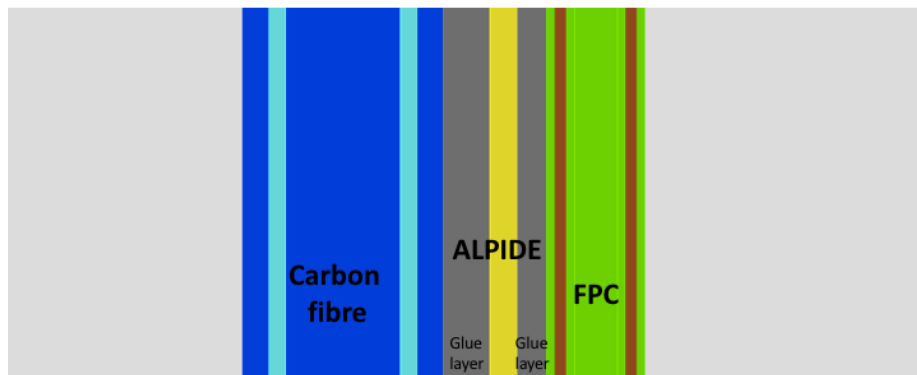
Figure 3.14: Stratigraphy of HEPD-02 stave with FPC designed taking as a model the ALICE Outer Barrel FPC.

Stave Element	Material	Thickness $[\mu m]$	X_0 $[cm]$	X_0 $[\%]$
Glue	Araldite	130	44.37	0.029
ALPIDE	Si	50	9.37	0.053
FPC lines	Cu	36	1.436	0.251
FPC	Kapton	135	28.41	0.048
Cold plate	Carbon fibre	350	26.08	0.134
TOTAL				0.515

Table 3.4: ALICE Outer barrel FPC material budget.

Stave element	Material	Thickness $[\mu m]$	X_0 $[cm]$	$X_0[\%]$
Glue	Araldite	130	44.37	0.029
ALPIDE	Si	50	9.37	0.053
FPC lines	Al	50	8.896	0.056
FPC	Kapton	115	28.41	0.040
Cold Plate	Carbon fibre	350	26.08	0.134
TOTAL				0.312

Table 3.5: ALICE Inner barrel FPC material budget.

- glue (gray);

- carbon fibre (blue and cyan);

- FPC Kapton (green);

- FPC copper (red).

Different FPC and cold plate configurations have been investigated. FPC configurations are described in this section. The FPC represents the most significant contribution to tracker material budget.

3.5.1   ALICE Outer Barrel FPC

The first design proposed for the FPC is the ALICE Outer Barrel design, since structure of the two staves (HEPD-02 and ALICE Outer Barrel) are very similar.

Stave element	Material	Thickness $[\mu m]$	X_0 $[cm]$	$X_0[\%]$
Glue	Araldite	130	44.37	0.029
ALPIDE	Si	50	9.37	0.053
FPC lines	Al	60	8.896	0.067
FPC	Kapton	60	28.41	0.021
Cold Plate	Carbon fibre	350	26.08	0.134
TOTAL				0.304

Table 3.6: LTU Ltd FPC material budget.

Both the configurations have two columns of detectors per stave. The ALPIDE works in master-slave mode, with one master detector for each column. The material budget is summarised in table 3.4.

The total radiation length of the stave is higher than the value of a HEPD-01 tracker plane, which is 0.318% X_0.

The FPC volume contains three layers. The central layer is composed of 75 μm thick Kapton. The other two layers are composed of 48 μm thick Kapton, surrounding a 18 μm thick copper layer, the latter represents the signal and power lines. The material budget is dominated by the thicknesses of the copper lines.

3.5.2 ALICE Inner Barrel FPC

The FPC structure is the similar to the OB FPC. The central Kapton layer is the same, while the external metal layers, that brings the signals and power lines, are composed of 45 μm thick Kapton and 20 μm thick aluminium layers. Because of the lower radiation length of the aluminium compared to copper, the total material budget is significantly lower.

3.5.3 LTU Ltd FPC

A third possible configuration of the FPC is based on the technology developed by LTU Ltd (Ukraine), which employed Single Point Tape Automated Bonding (spTAB) for the four external layers of the ALICE old Inner Tracking System detector (SDD and SSD).

The FPC is composed of polyimide, with aluminium connections. It is similar to the ALICE Inner Barrel FPC, consisting of three layers of 20 μm thick polyimide, and two layers of 30 μm thick aluminium between the polyimide. Table 3.6 reports the total material budget, which is similar to ALICE Inner Barrel FPC.

3.5.4 Effects of different FPCs on physics measurements

The effects of the different FPCs on the performance was studied with GEANT4 Monte Carlo simulations. In HEPD-02 the number of tracking planes has been increased to three to increase the redundancy.

The results for the electron and proton energy threshold are shown in figure 3.15 for electrons and 3.16 for protons. One thousand events, perpendicular to the detector plane, are simulated at each energy. The efficiency is calculated as:

$$Efficiency = \frac{N_{pass}}{N_{TOT}}$$

where N_{pass} is the number of particles crossing the second (third) plane and N_{TOT} is the number of events simulated for each energy.
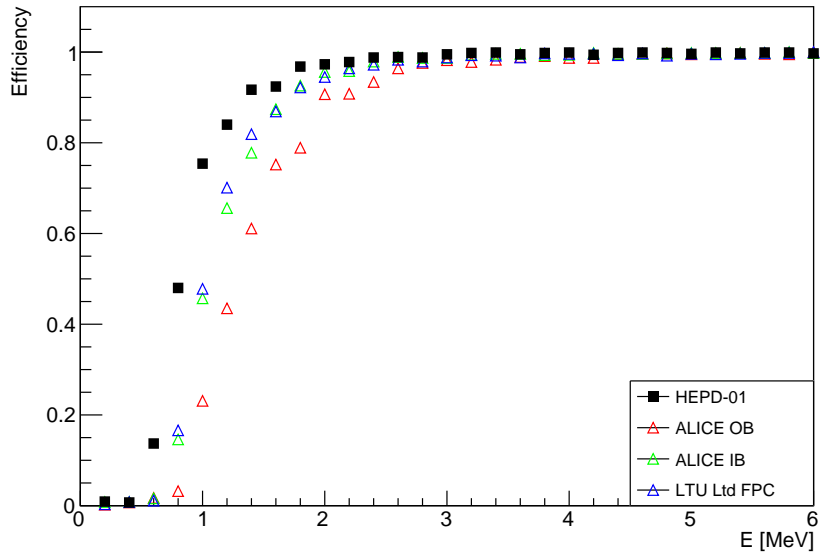
(a) Two plane HEPD-02 tracker.
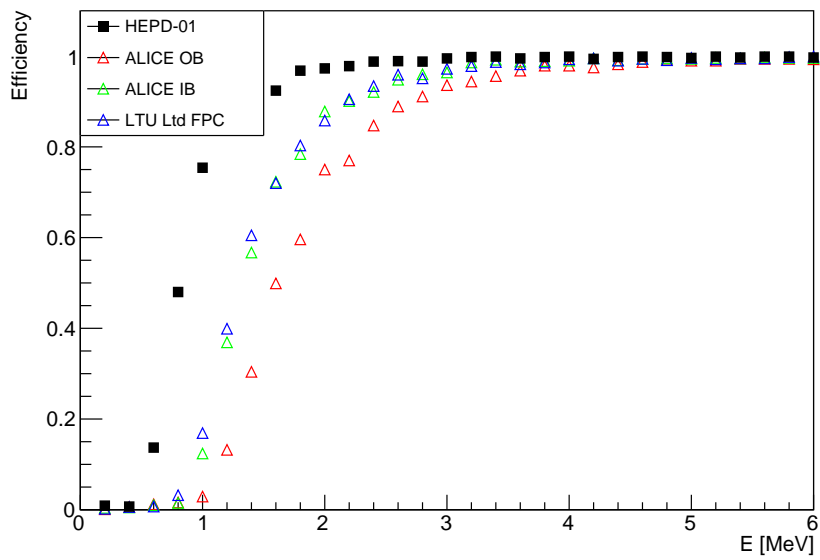
(b) Three plane HEPD-02 tracker.

Figure 3.15: Electron threshold for different FPC configurations.
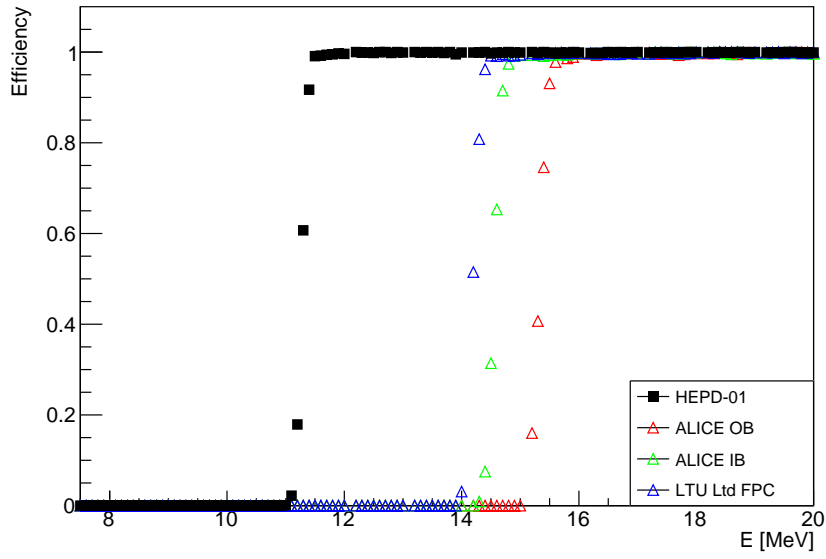
(a) Two plane HEPD-02 tracker.
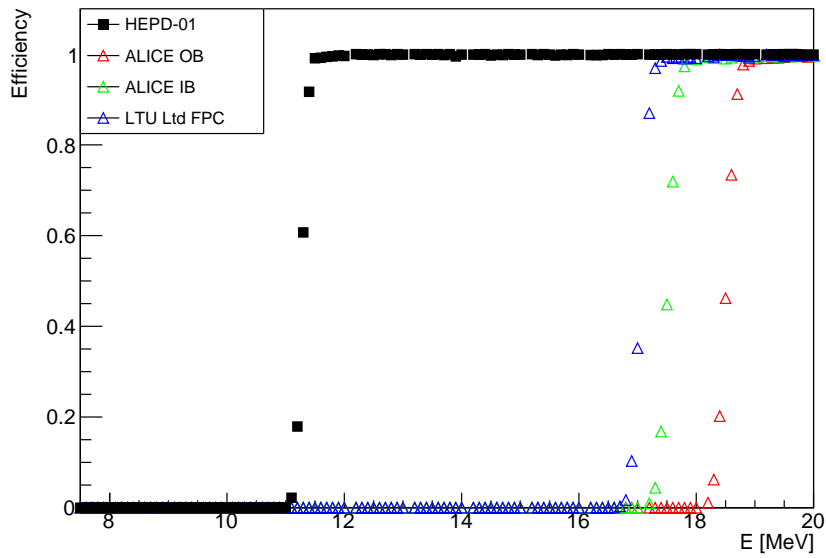
(b) Three plane HEPD-02 tracker.

Figure 3.16: Proton threshold for different FPC configurations.

On the left in figures the efficiency at two tracker staves is reported, on the right the results for three. Results for the two planes provide a direct comparison of the staves with HEPD-01 tracker, which has only two planes.

Comparing the cases of two tracking planes, thresholds pass from 0.8 to 1.3 MeV for electrons and from 11 to 15 MeV for protons, when HEPD-01 and HEPD-02 ALICE OB cases are considered. The case of ALICE IB or LTU Ltd lie in between, but cannot be considered for space application due to lacking qualification of aluminium-grounded PCB for space applications.

The measurement of the incident particle direction is affected by the multiple Coulomb scattering in the tracker. The scattering angle θ_{MS} due to the tracker material is defined here as

$$\theta_{MS} = \arccos\left(\frac{\vec{p}_0 \cdot \vec{p}_{fin}}{\|\vec{p}_0\|\|\vec{p}_{fin}\|} \right)$$

where $\vec{p}_0$ is the initial momentum of the particle, and $\vec{p}_{fin}$ is the momentum of the particle entering the sensitive element (ALPIDE or silicon) of the second plane of the tracker. This definition reports the worst case for tracking: the angle is reconstructed only from the hits of the first two planes[1].

The scattering angle for electrons as a function of the energy of the particle is shown in figure 3.17 for different incidence angles. Results obtained for the IB FPC and LTD FPC are compatible with the results for the HEPD-01 tracker. The OB FPC results in a larger deviation. The angular deviation increases with the incidence angle, as expected since the particle path length in the material increases with angle.

The value calculated with the first two planes gives a good evaluation of the particle incidence direction, since the effects of multiple scattering are minimised. The direction of the particle between the second and third plane is the best estimate of the particle direction when it enters on the calorimeter.

3.5.5 Cold plate stratigraphy

The cold plate is crucial for thermal control of the tracker. The composition and material thickness of the cold plate must be carefully studied to ensure the thermal stability of the tracker and the performance required for the physics measurements.

A good reference for the cold plate is provided by the ALICE design. The structure consists of carbon fibre and graphite layers, organised as follows:

- A layer of 45 μm thick carbon fibre, oriented at 45°;

- A 30 μm thick graphite layer;

- A layer of 80 μm thick carbon fibre, oriented at 45° (opposite to the first layer);

---

[1]More complex algorithms accounting for the third plane can improve the angle determination.
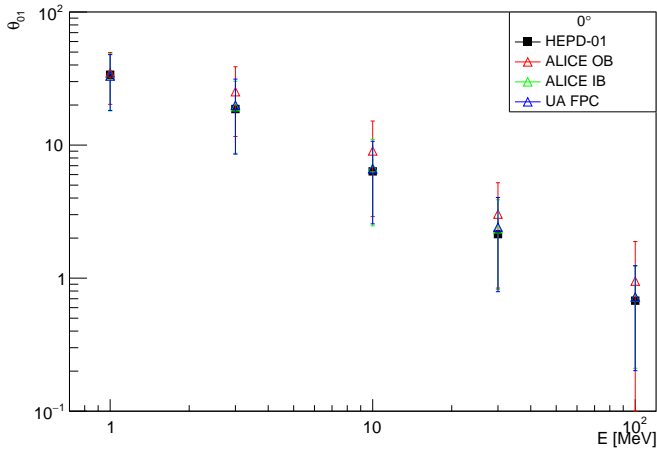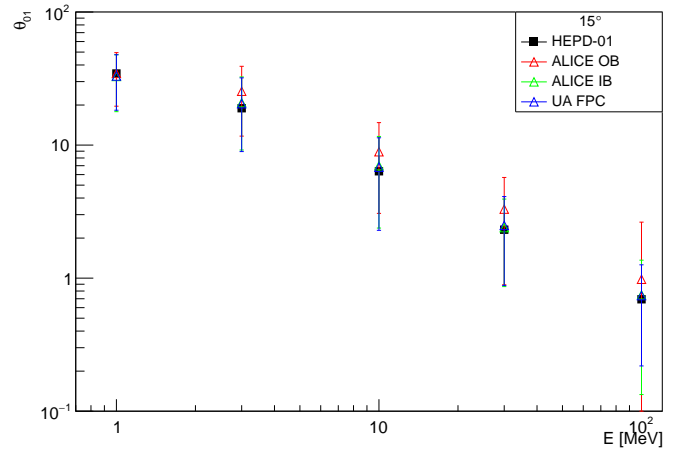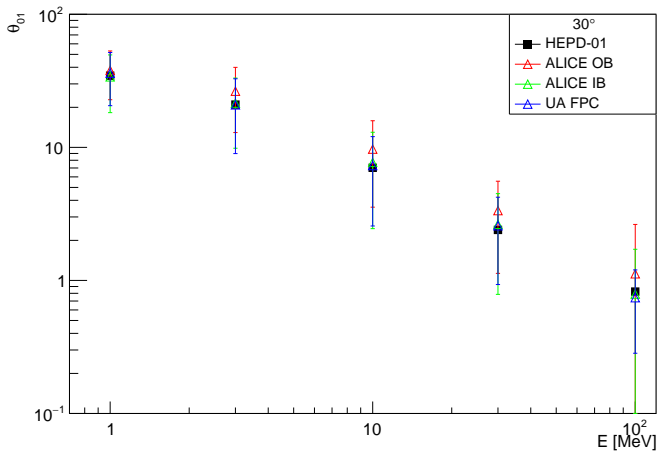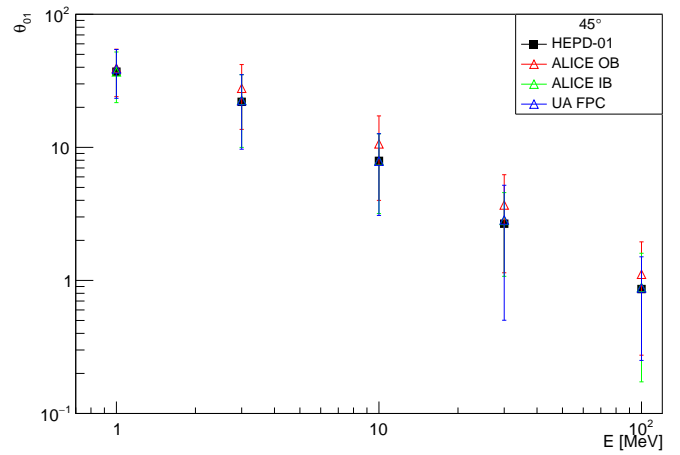
Figure 3.17: Multiple scattering calculated for particle incoming from different angles. For both HEPD-01 and HEPD-02 the angle of the particle entering on the second sensitive element is considered. The results are shown for different energies.

- A 30 μm thick graphite layer

- A layer of 45 μm thick carbon fibre, oriented at 45° (same orientation of the first layer);

The listed materials have nearly the same density, 1.6 g/cm^3. The thickness of ALICE cold plate is not sufficient to provide the necessary thermal stability. The effects on the tracker performances have been studied for an increase of the total thickness from 230 μm to 1 mm, on the three plane HEPD-02 tracker, equipped with ALICE OB FPC. The results are shown in figure 3.18.

One of the requirements for the HEPD-02 is that the energy threshold for electrons must be below 3 MeV. Threshold of a given configuration is when the curve reaches 50% efficiency. All the configurations in figure 3.18a fulfill the requirement.

3.5.6 A plane of the trigger before tracker

The trigger designed for HEPD-02 consists of two segmented planes. Each plane is divided in five bars of EJ-200 plastic scintillator, whose dimensions are designed to superimpose to the tracker turrets (see section 3.3). There are two proposed thicknesses for the bars, 2 or 3 mm. Characterisation of their response to mechanical stress is ongoing. The possible dimension of each bar is then $30 \times 150 \times 2$ mm^3 or $30 \times 150 \times 3$ mm^3.

The collaboration tested a version of the upper detector (tracker and trigger) with a plane of the trigger located before the tracker, directly after the detector window. It is interesting to study if this solution reduces the energy thresholds of the detector. In this case, it is not possible to directly compare the thresholds, again defined as the minimum energy for which a particle crosses all the tracker, with the one obtained for HEPD-01, since the two cases are now significantly different. It is still possible to evaluate the minimum energy for the particles that cross all the trigger and tracker, as shown in figure 3.19.

The study of multiple scattering contributions of this setup gives results to be taken into account. In this case, the comparison with HEPD-01 performance makes more sense, because in this case, the quantities measured are the same in different conditions. Figure 3.20 shows the results for different angles. In the plot, the points represent the mean value of the angle distribution, and the error bars are 1 RMS. Data are extracted from distributions in figure 3.21. As expected, the insertion of material before the tracker worsens the performance of tracking, but in this case, the differences are small.

In particular, looking at the points with energies higher than 10 MeV, the differences on distributions are small. At the same time, the points at 1 MeV are not meaningful for the configurations with the trigger before the tracker, since the number of particles that crosses the second plane of the tracker is small. For energies close to the threshold, at 3 and 10 MeV, the effects of the 2 mm plane are almost negligible.
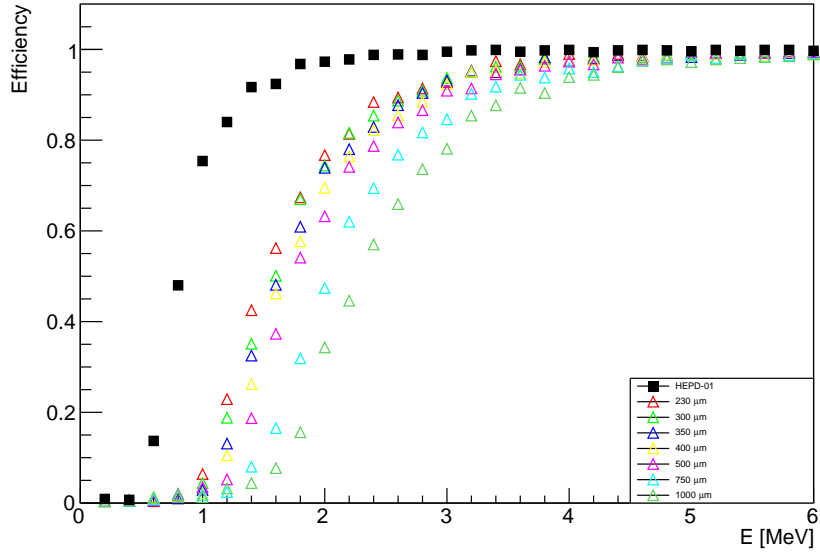
(a) Electrons.
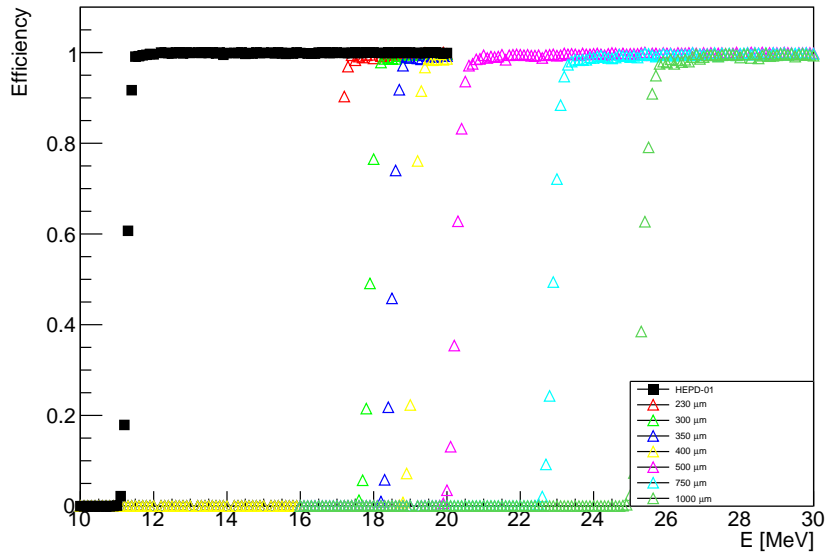
(b) Protons.

Figure 3.18: Threshold for the three plane tracker of HEPD-02 for different thicknesses of the cold plate.
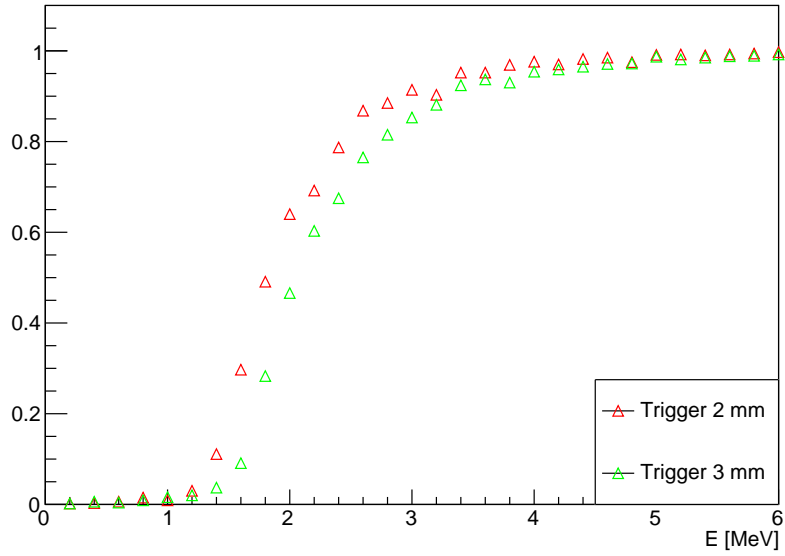
(a) Electrons.
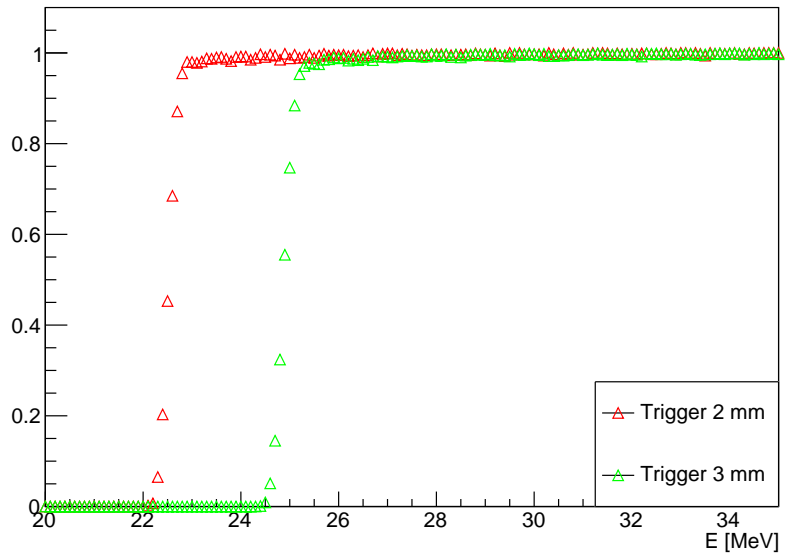
(b) Protons.

Figure 3.19: Minimum energy for which the particle crosses a plane of the trigger and all the tracker. The cold plate thickness is 350 μm, and the FPC is the one based on ALICE OB.
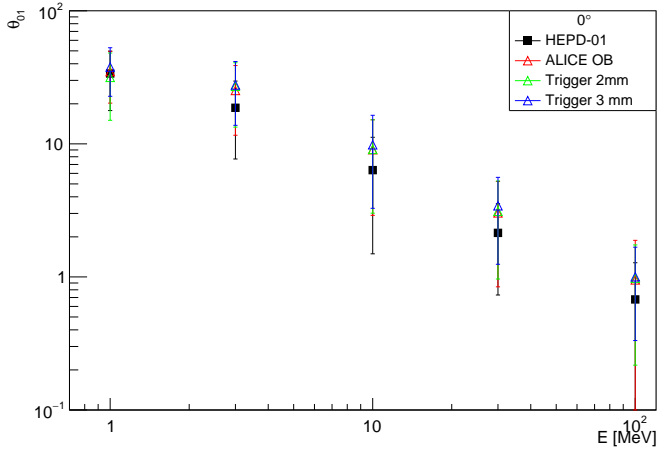
(a) $0°$
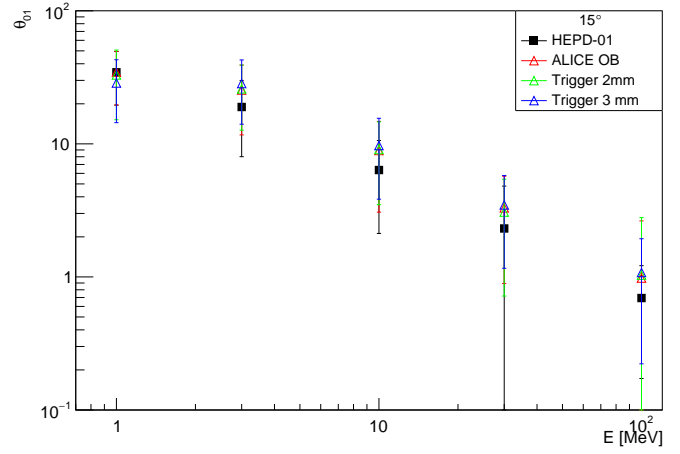
(b) $15°$
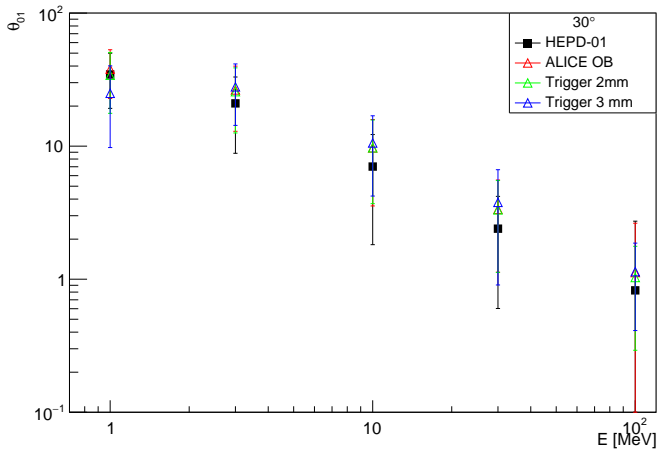
(c) $30°$
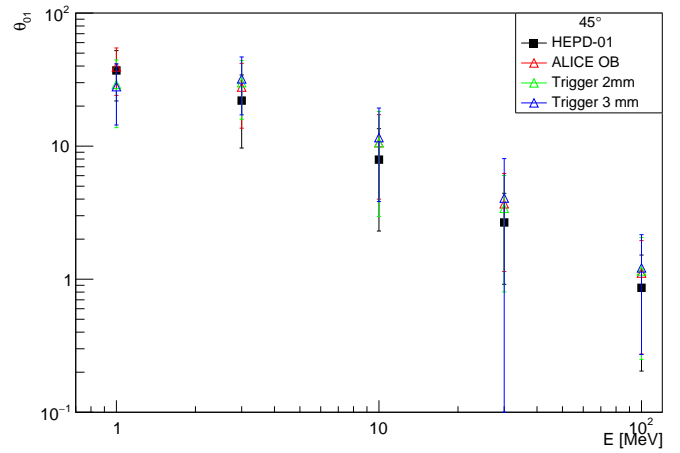
(d) $45°$

Figure 3.20: Multiple scattering between the first two planes of HEPD-02 tracker compared with HEPD-01 tracker for the case in which a plane of the trigger is before the tracker. Investigation of different thicknesses for the trigger plane is ongoing. Results for HEPD-02 tracker without the plane before are reported in red as a further reference.
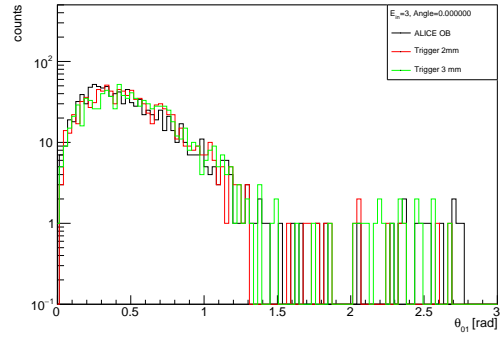
(a) $3\ MeV$
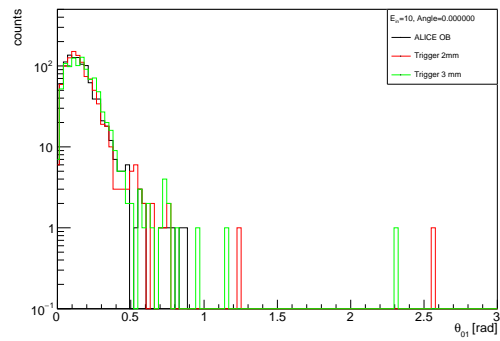
(b) $10\ MeV$
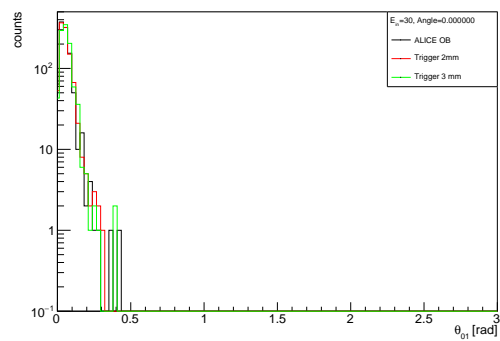
(c) $30\ MeV$

Figure 3.21: Distribution of angles of multiple scattering for different energies. Particle are generated perpendicularly to the detector.
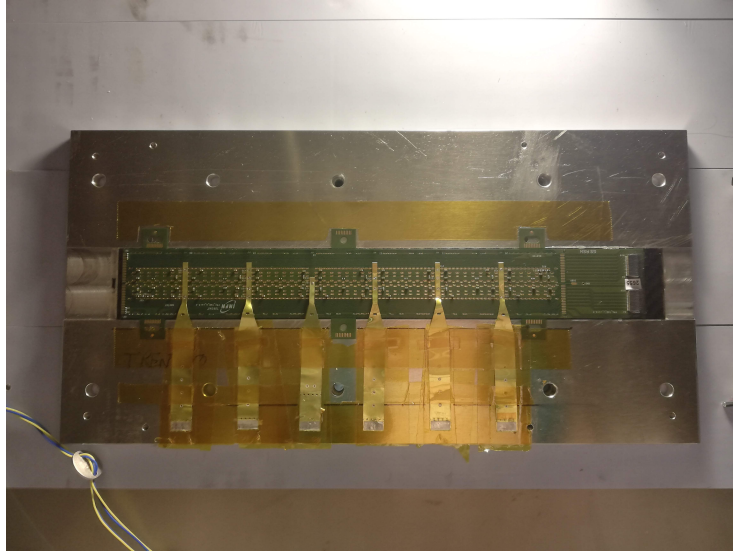
Figure 3.22: DUT after thermal-vacuum test in SERMS.

3.6 Space compliance tests

A first campaign of tests to ensure space compliance has been carried out with an engineering model of the HEPD-02 tracker stave. The device and the test results are described in this section.

3.6.1 Device Under Test (DUT) description

Tests have been carried out on an ALICE Outer barrel HIC (Hybrid integrated circuit, see section 2.4.2), composed by an FPC and two columns of seven ALPIDE detectors. The HIC is glued to a carbon fibre cold plate and hosted on an aluminium jig, designed to transport the HIC. The aluminium jig hosts ten holes, to fix it to the vibration and thermal-vacuum machines. The device is shown in figure 3.22.

The detailed stratigraphy is described in figure 3.23. The different layers of the DUT are glued using Araldite. The thickness of glue layers between the FPC and the ALPIDE is 50 μm, while between ALPIDE and the cold plate is 80 μm. The glue layer between the carbon fibre and the jig is about 70 μm. It has been inserted to ensure mechanical stability during the stress test, in particular during vibration.

The DUT has some differences from the design proposed for the HEPD-02 tracker: (i) it is longer (seven sensors for each column instead of five), (ii) power distribution passes through cross cables, visible in figure 3.22, (iii) Sensors are 100 μm thick, instead of 50 μm.. The differences between the two objects worsen the expected DUT response to stress tests if compared to the HEPD-02

Figure 3.23: Stratigraphy of DUT. Different layers are not in scale.

modules.

The DUT is connected to a FPGA (Field Programmable Gate Array) through a Ethernet port. The FPGA controls the sensors and collects the data, that are stored in a laptop.

3.6.2 Test preparation

Some optimisations are required to reduce the failure risk of pre-qualification tests, in particular: (i) the cross cables, (ii) the connector region not properly glued, (iii) the contact between the carbon fibre and the aluminium. Some pictures taken during the preparation of the DUT are showed in figure 3.24.

Cross cables are challenging in particular for vibration test. If they are left free, they could create unwanted resonances. If not properly fixed, they could introduce stress on the welding to the FPC and break it. In this case, it would not be possible to verify the DUT state after the tests.

For all these reasons, they have been fixed in a position that ensure enough freedom to avoid ruptures and, at the same time, the required stability.

Another critical point of the setup is the region of the Samtec Firefly connector, in which gluing did not connect the FPC to the carbon fibre properly. A layer of Araldite has been added to avoid movements and stress on the structure during the vibration test.

To allow the application of vibration stress along all the three axes of the device, the mechanical workshop of Dipartimento di Fisica realised a dedicated structure. The fixture, shown in figure 3.25, is designed to avoid to insert resonances during the test. The DUT is inserted on the central space and
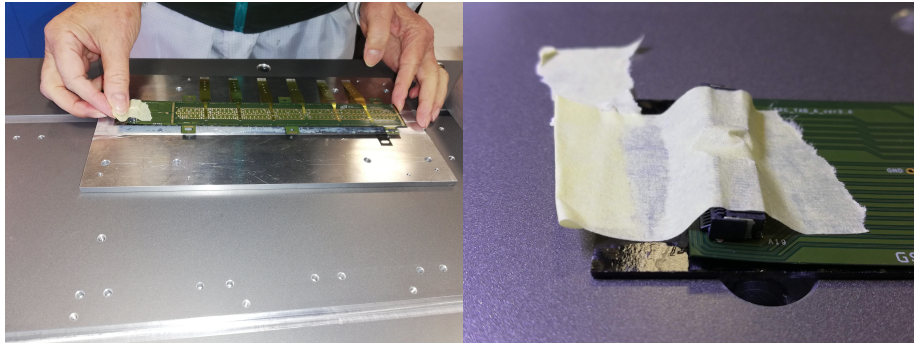
(a) Operations to glue the carbon fibre to the jig.

(b) Connector region gluing.
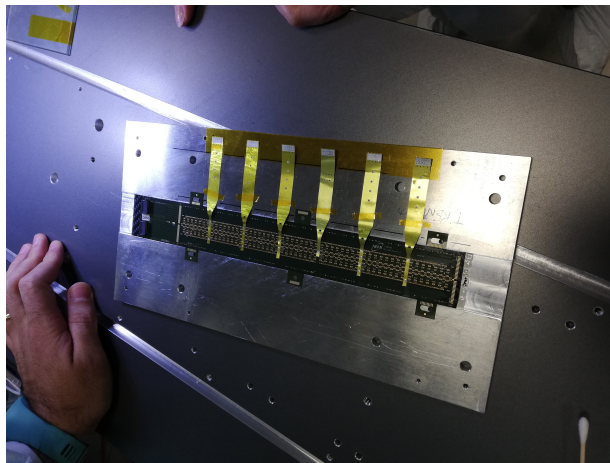
(c) Cross cable setting.

Figure 3.24: Test preparation in Torino clean room.
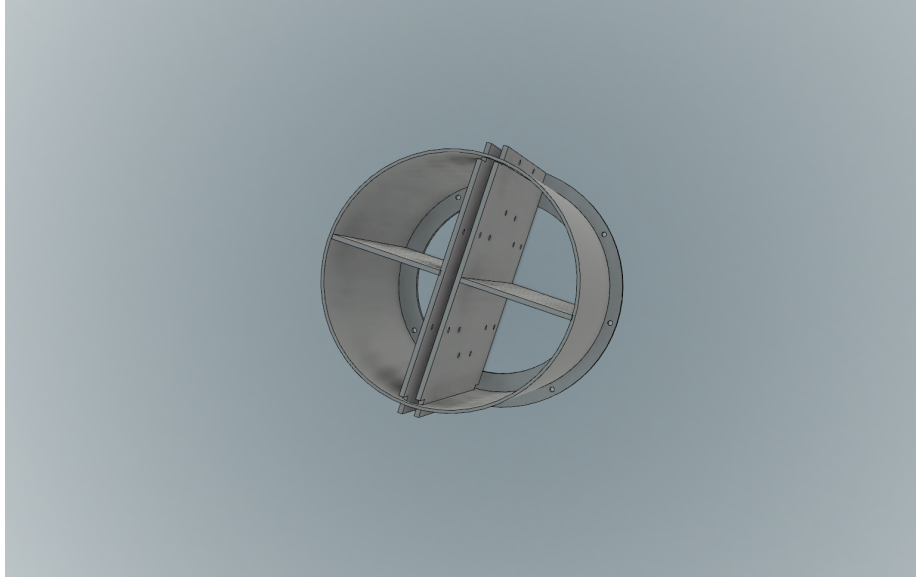
(a) Fixture project.
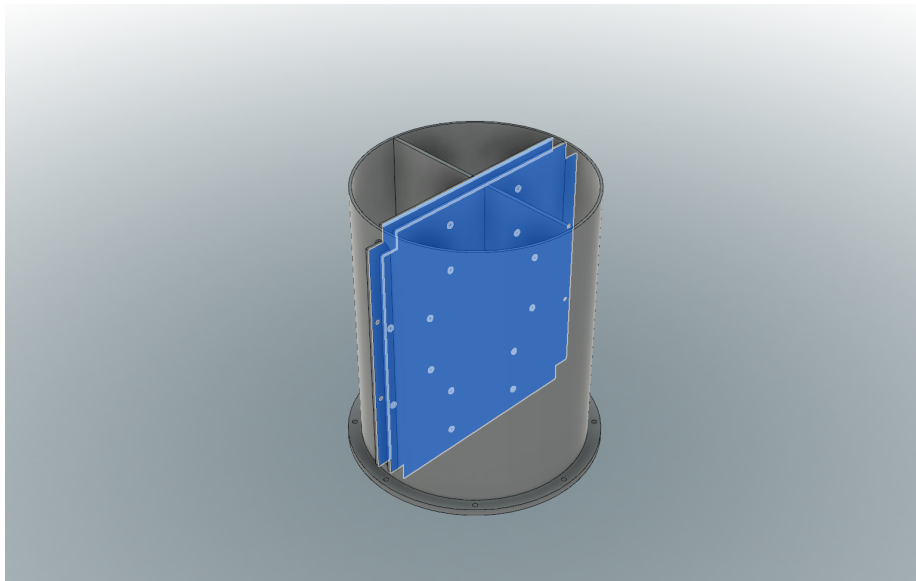
(b) Internal planes details.

Figure 3.25: Fixture for vibration test along x and y axes.
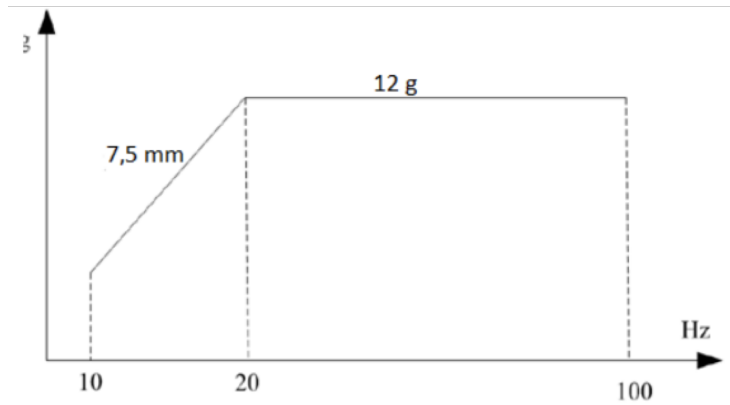
(a) Sinusoidal profile for Qualification test.
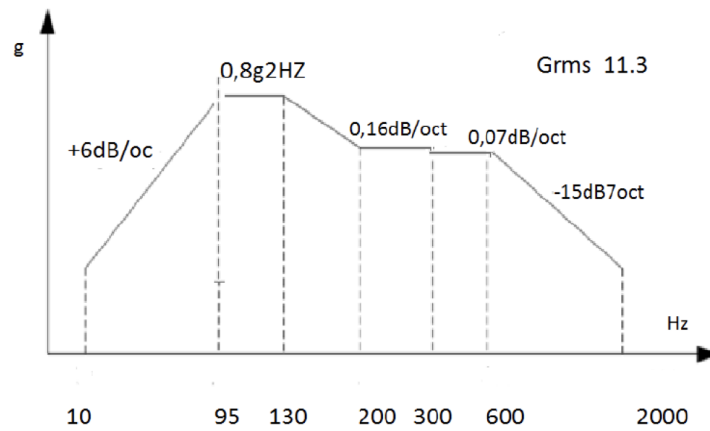
(b) Random profile for Qualification test.

Figure 3.26: Vibration profiles for qualification tests

ensured with the eight M6 bolts. The space between the two planes has been calibrated to ensure the required strength to fix the DUT and to avoid excessive trapping.

Preparation of the DUT for the thermal-vacuum test requires to prepare cables to connect the DUT, located inside the thermal-vacuum chamber, with the equipment located outside. The cables include the power supply and the Ethernet connection to the FPGA.

3.6.3 Vibration test

The Chinese National Space Agency provides the specifications for the vibration test, reported in figure 3.26. Test procedures require to apply the profiles
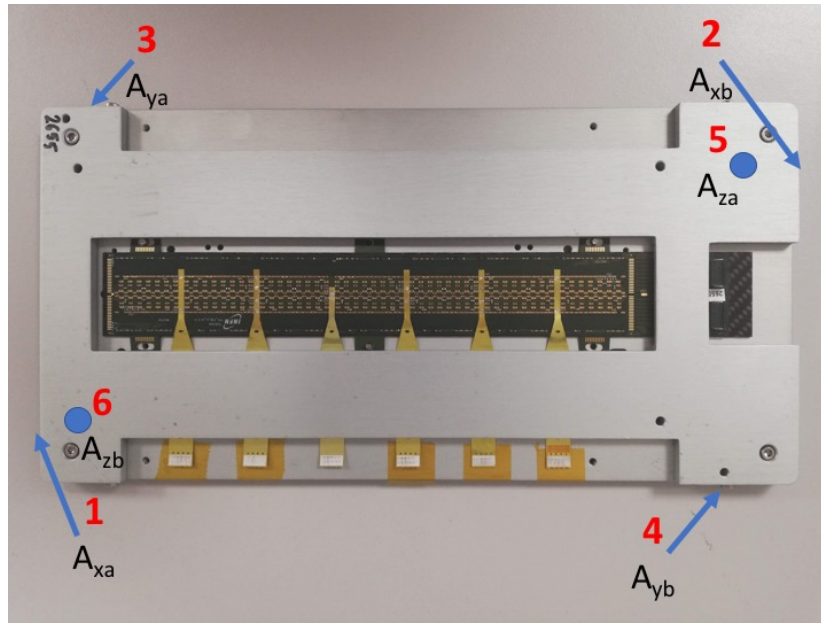
Figure 3.27: Accelerometer proposed position during tests. The capital A indicates the accelerometer, the x,y and z the axis measured and the lowercase a and b indicates the different accelerometers used for each axis.

along all the three axes. For each configuration, at least two accelerometers are installed on DUT, of which at least one is three-axial. Other accelerometers are located on the fixture to evaluate the contribution to the measurement results.

The planned positions of accelerometers on the DUT are shown in figure 3.27. The positions have been followed for x and y axes, for which the fixture structure does not allow to locate more sensors. In case of z axis the cylindrical fixture is not required and it is possible to apply more accelerometers, as shown in figure 3.28.

For each axis, the test procedure is the same:

- Fixture installation;

- Search of resonances;

- DUT installation;

- Search of resonances;

- Sinusoidal test (figure 3.26a);

- Random test (figure 3.26b).

For z-axis, the fixture (an aluminium plane) shows no resonance. The cylindrical fixture for x and y axes has a resonance at about 500 Hz. Its intensity is small enough to allow the test to be carried on.
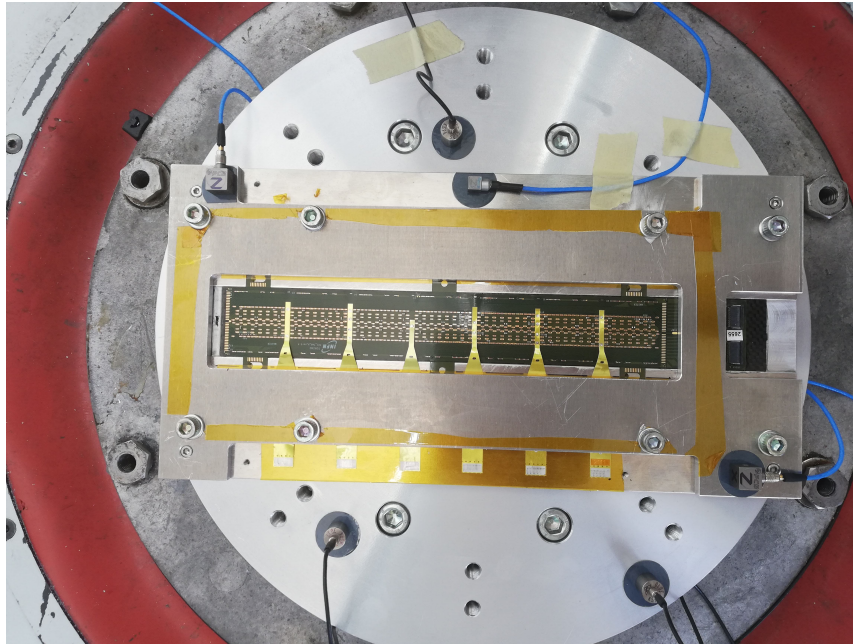
Figure 3.28: Accelerometer positions during vibration test along z axis.

During the test, measurements revealed no resonances but the one already specified for the fixture. After the test of each axis, the DUT is removed from the fixture, and a functionality test is carried on.

After the power-on of the DUT, a FIFO test is run. If no errors are reported, a threshold scan starts. A description of the tests is in section 3.2.2.

All the tests run on the DUT show that its performance are the same before and after the stress tests. In particular, no errors have been reported by FIFO test and the threshold distribution does not show any degradation of the performance.

3.6.4 Thermal-vacuum test

Thermal-vacuum test follows the vibration test to reproduce the sequence of stresses due to the launch: the vibration during the first phase and then the thermal-vacuum.

The test requirements from Chinese space agency are reported in table 3.7. Since the object is small and the thermal coupling very good, the dwell time has been reduced to only two hours. The profile of temperatures applied during the cycles are reported in figure 3.29.

The DUT is installed inside the vacuum chamber and connected to the thermal plate, as shown in figure 3.30. The correct functionality of DUT has been checked before the installation on the vacuum chamber, after the installation
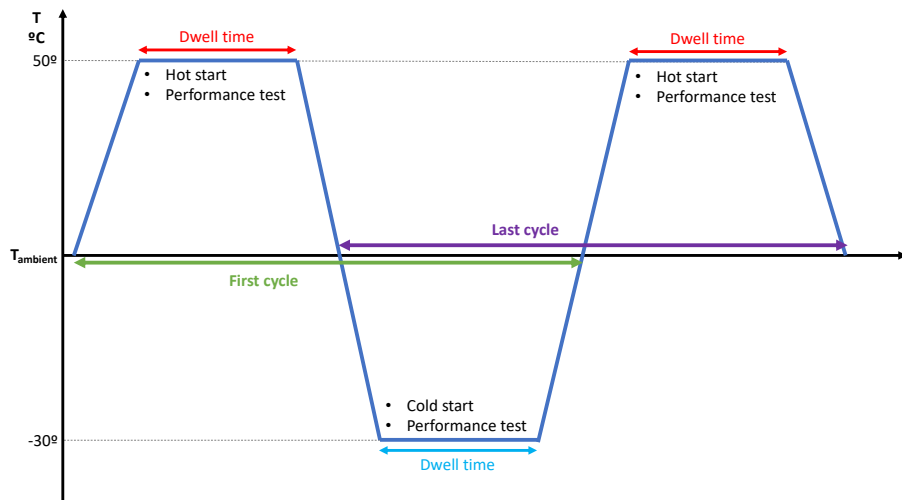
(a) First and last cycle.
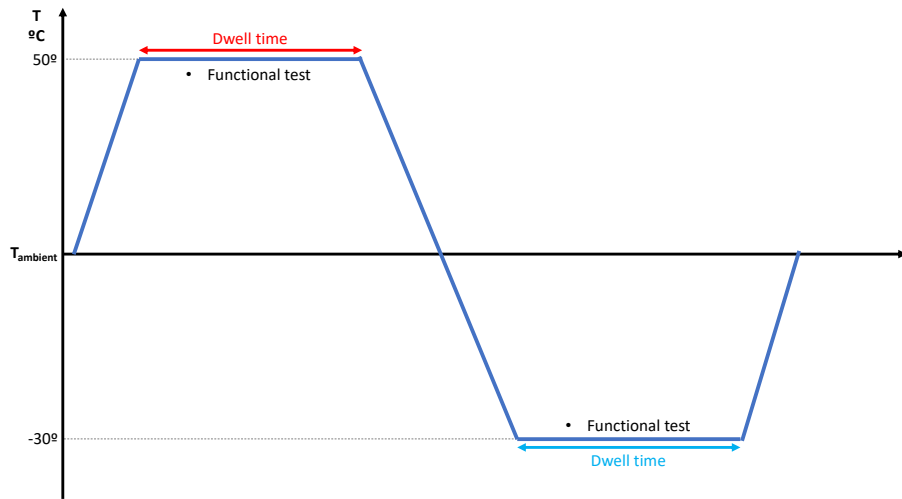
(b) Intermediate cycle.

Figure 3.29: Profile for cycles of thermal-vacuum test.

Parameter	Test Conditions
Pressure	$<6.66\times 10^{-3}$
Hot temperature	$50^{\circ}C$
Cold temperature	$-30^{\circ}C$
Start cycle	Hot (hot start for outgassing)
Number of cycles	6,5
Temperature rate of change	$\leq 1^{\circ}C/min$
Dwell time at T hot and cold	$\leq 4\ hr$

Table 3.7: Thermal-vacuum test conditions.
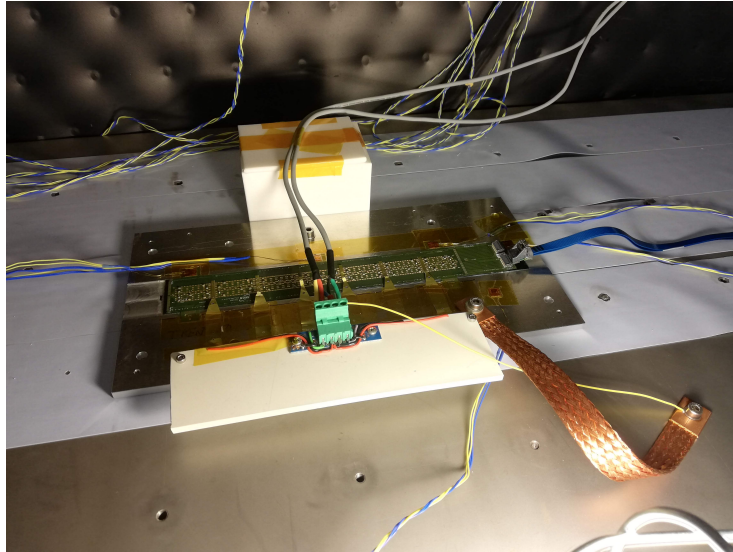
Figure 3.30: DUT installed inside the vacuum chamber.

with the chamber open and after the chamber closure. After the checks, procedures for the realisation of the vacuum begin. Thermal cycles start when the chamber reach a level of about 5×10^{-6} $mbar$.

During the dwell time, two different tests are scheduled. A functional test, in which only basic functionality is checked, and a performance test, that tests the status of the detector more carefully.

The functional test consists in a short routine that lists the addresses of sensors connected to the control line and a FIFO test. The performance test adds to the functional test a threshold scan, and it is in principle required only during the first and last cycle. It has been applied several times during all the cycles, both during dwell phases and during temperature gradients, to increase the level of stress on the DUT.

Threshold maps taken at different temperatures show some differences, as shown in figure 3.31. The z-axis of the plot reports the number of hits recorded by the pixel during the injections. Differences can be due to the different noise level of the detectors, that is temperature related. The structures visible at room temperature are due to the metal pads on silicon (see figure 2.10 for comparison), that change the response of the pixels below. Other features depend on to DUT history (defects of the ALPIDE, dust). They are no more visible at $50°C$ when the noise is higher.

At low temperature (-30°) the small number of pixels over threshold can depend also on the limits of charge injectors, that are not fully efficient. To obtain the plot at -30°C, it was necessary to change the range of charge injection. The range in charge injection and the number of pixels over the threshold for each step are shown in figure 3.32.

The DUT successfully passed all the test and was even able to collect short runs of data with cosmic muons, at -30°C and at 50°C. Time limitations allow only a short data collection at low temperature, with a trigger frequency provided by a signal generator of 1 kHz. The strobe length is set to 900 μs, to minimise the dead time. The DUT recorded a single event compatible with an interaction with a MIP (a cluster of 4 pixels) at -30°C. Because of the short time of acquisition, two events were expected. The number of hits collected during the dwell time at 50°C was compatible with the expected rate. In this case, about 20 events were expected and 27 are recorded. The quality of the sensors installed on the DUT is low, and the dead areas in the rate calculations underestimated. Nevertheless, the detection of patterns compatible with interaction with MIPs, reported in figure 3.33, showed that the detector did not deteriorate during the test and it is still fully efficient.

All the tests are successfully passed.
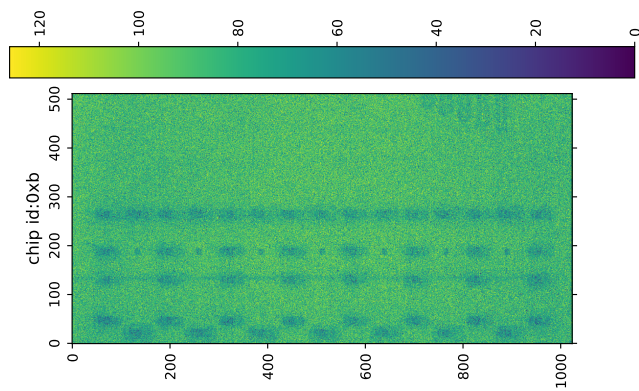
(a) 25°C
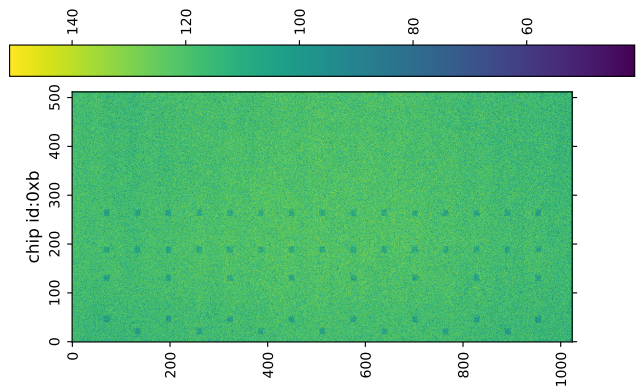
(b) 50°C
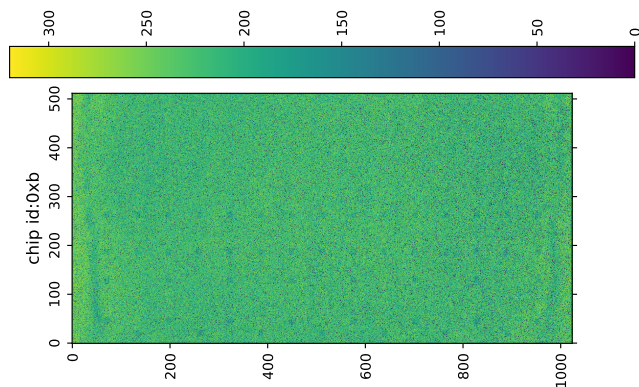
(c) -30°C

Figure 3.31: Maps at different temperatures. The z axis reports the number of times in which each pixel turned on. The number of counts is different for the case of -30°C because the inefficiencies of the injections required a different range of charge injection.
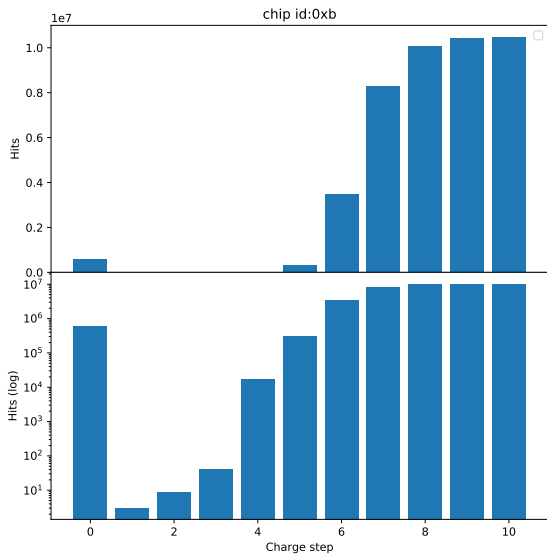
(a) Room temperature (25°C)
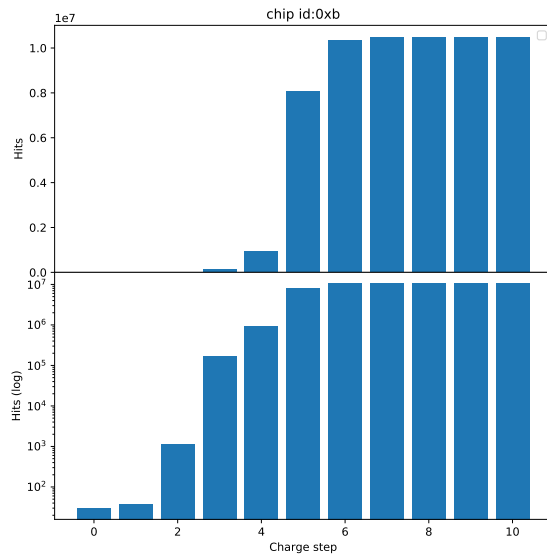
(b) 50°C
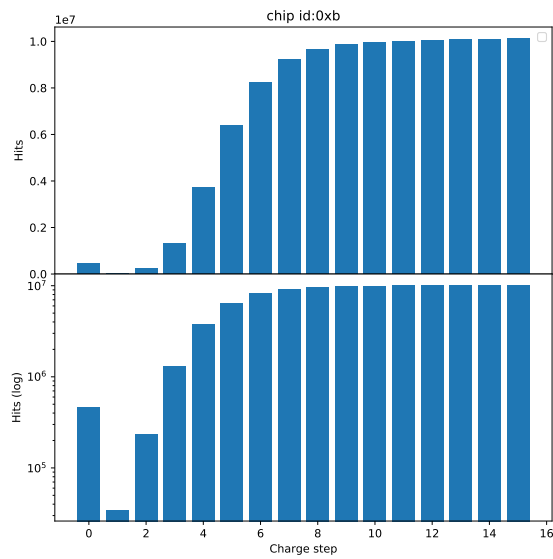
(c) -30°C

Figure 3.32: Number of pixels over threshold on a sensor during each step of charge injection of threshold scan at different temperatures.
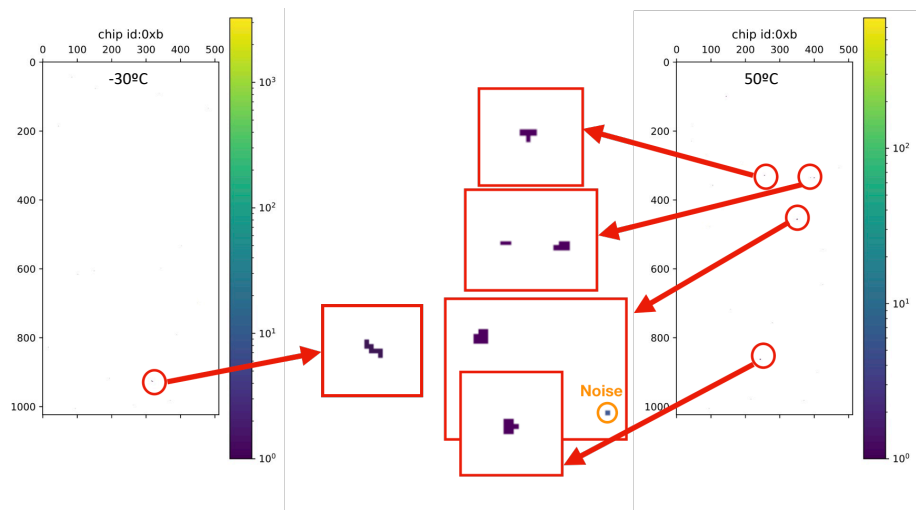
Figure 3.33: Maps of muons collected during thermal-vacuum tests at different temperatures. The figure shows the position of the hit on the detector and the cluster shapes.

Chapter 4

ALPIDE response to low energy nuclei

Being designed for ALICE experiment at LHC, the ALPIDE has been extensively tested with MIPs during the design of the detector. The characterisation with low energy nuclei was not among the ALICE collaboration interests.

It is instead required to use it in HEPD-02, since the experiment aims to investigate electrons between 3 MeV and 100 MeV and protons between 30 MeV and 300 MeV. Some examples of clusters collected with 62 $MeV/a.m.u.$ He during test beam in Catania.

The ALPIDE response to low energy nuclei has been characterised by testing it with different particles at different facilities. It has been irradiated with protons between 20 MeV and 220 MeV at the experimental hall of APSS (Azienda Provinciale Servizi Sanitari) Trento Proton therapy centre and with different nuclei (H, He, C and O) at the "0deg" experimental hall of Laboratori Nazionali del Sud in Catania. The energy of the beams of this facility is 62 $MeV/a.m.u.$ for all the four species.

4.1   Experimental setup

The experimental setup, shown in figure 4.2, is composed by three different detectors: an ALPIDE detector, mounted on single-chip board and read out using a MOSAIC board, developed by ALICE collaboration for APIDE tests [39], and two EJ-200 plastic scintillator bars, $150 \times 30 \times 2$ mm^3 each. The detector positions are schematised in figure 4.3. The scintillators are read out on both sides by PMTs. To correctly collect the light output of thin bars with a Hamamatsu R9880-210 PMT having a diameter of 10 mm, light guides are used. Plexiglass supports are placed behind each thin scintillator bar. The first support, is suitably milled to minimise the interference with the beam, with a resulting geometric factor as large as 100×25 mm^2.
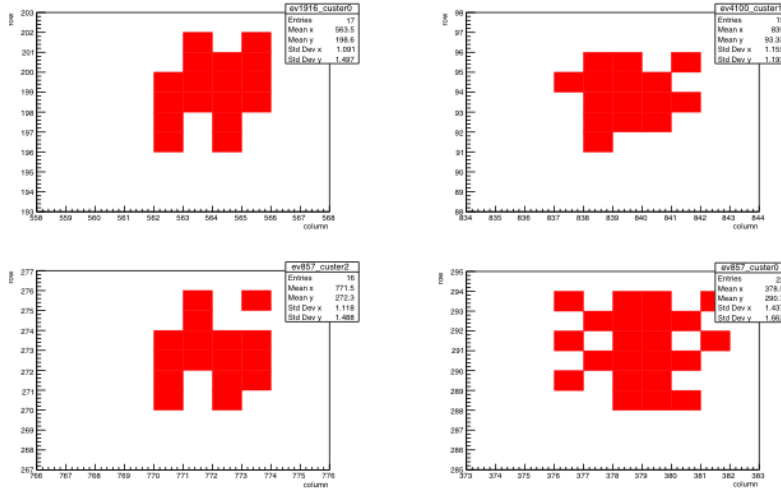
Figure 4.1: Examples of clusters collected during beam test in Catania with a beam of 62 $MeV/a.m.u.$ He.

The two bars have different packaging and optical connections to test different solutions for the future HEPD-02 trigger system. The first bar is wrapped in aluminised mylar and has optical disks between the light-guide and the PMTs, the other is covered with white Teflon tape and has optical grease between the light-guides and the PMTs.

The readout scheme is summarised in figure 4.4. The PMTs output is collected by a CAEN Digitizer DT5730, that acquires data and produces a co-incidence output signal then sent to the MOSAIC board to synchronise the acquisition. Both the MOSAIC board and the Digitizer are controlled with a laptop, that also stores data. MOSAIC is connected through an Ethernet port, the Digitizer through a USB. For each event, waveforms from PMTs and the addresses of pixels over the threshold from ALPIDE are collected.

Detectors are located in a box, designed to facilitate the alignment of the setup and to guarantee a certain number of degrees of freedom for each detector, both translational and rotational. In particular, it is possible to set the distance between the detectors with 5 mm steps and the angle between each detector and the beam. A picture of the box, taken during beam test in Catania, is shown in figure 4.2.

During data taking, the setup is covered with a light-proof cover in aluminium, shown in figure 4.2a, with two windows covered with aluminised Mylar to let the particles hit the detectors with minimum interference. To preserve the dark inside the box, cables for both power supply and readout pass through two exits covered by light traps.
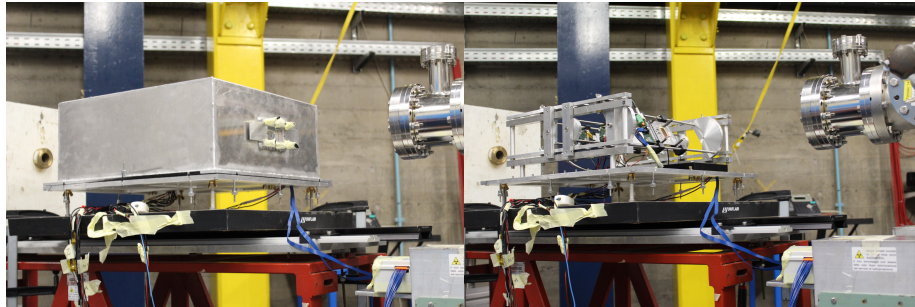
(a)

(b)
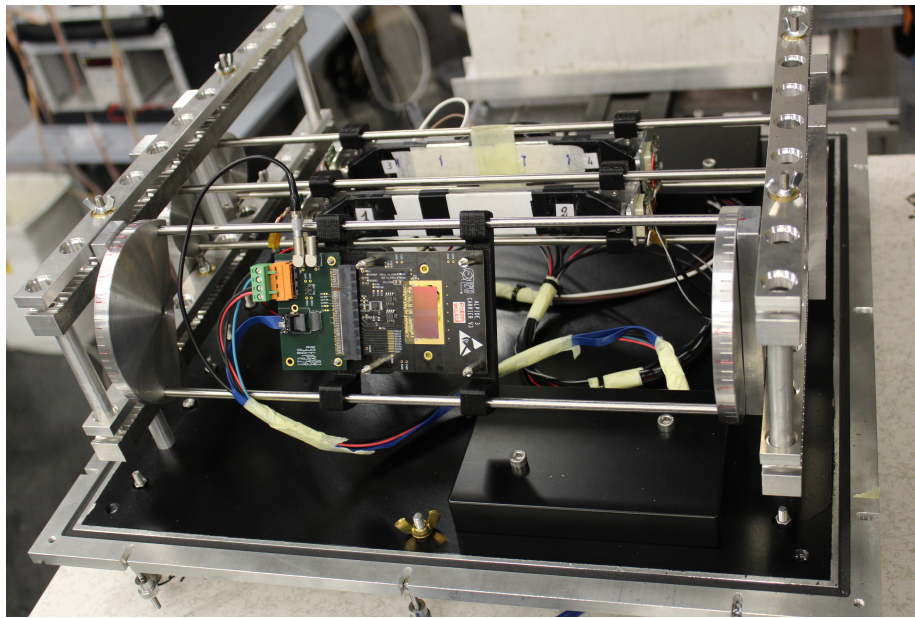
(c)

Figure 4.2: Experimental setup.
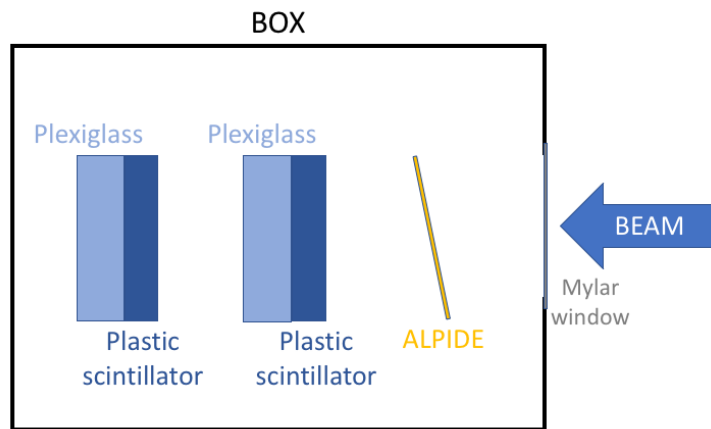
Figure 4.3: Detector order inside the box during beam tests.
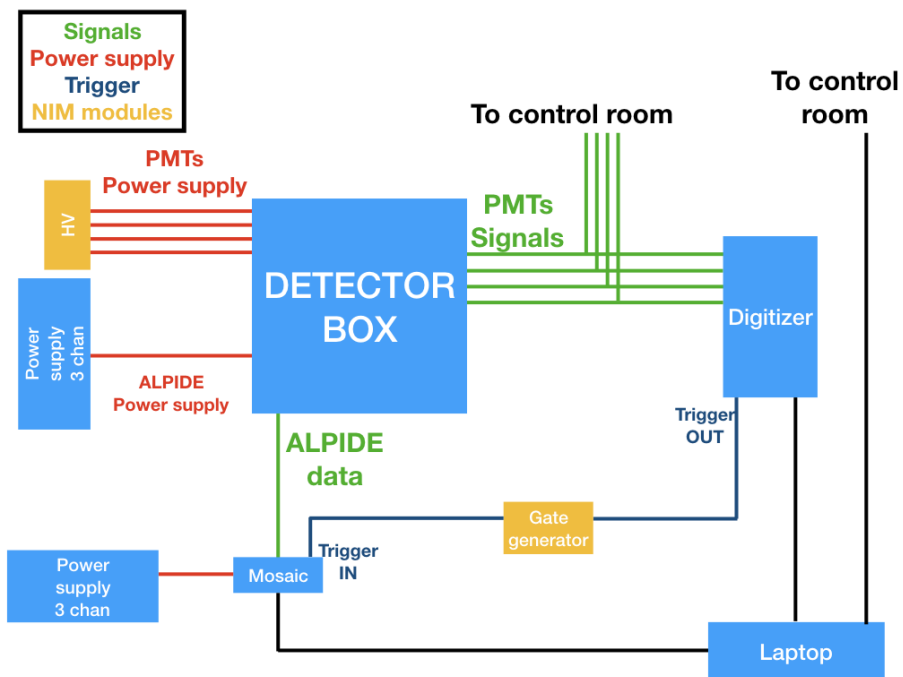
Figure 4.4: Beam test setup and DAQ scheme.

115
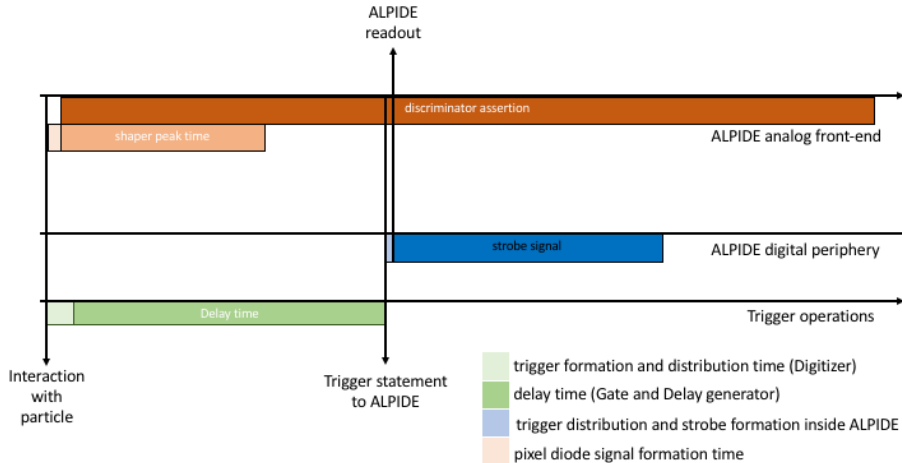
Figure 4.5: Signal statement scheme for ALPIDE and trigger system as a function of the time after interaction.

4.2 Trigger delay study

To reduce the power consumption of HEPD-02 tracker, the clock signal is distributed only to the section of the detector that has the highest probability to be interested by the event. The correct section is selected using the signal from the experiment trigger. This strategy can be applied only if when the trigger is stated, the information on the event is still available on ALPIDE. Since the clock is not active in idle state, it is not possible to store the data on the pixel memory cells. It is then important to know how long is the persistency of the signal at the output of the premplifier.

The ALPIDE documentation reports that the on-pixel preamplifier has a shaping time of about 2 μs [60]. The front-end and the discriminator act as an analogue delay line, with a delay time of about 10 μs. This allows operating the detector in triggered mode when the latency of the incoming trigger is comparable with the peaking time of the front-end [14].

The maximum latency is measured by setting different delays on a "Gate and Delay generator" module, introduced between the Digitizer and the MOSAIC during the test beam in Trento.

A second contribution to the delay is introduced by the Digitizer trigger formation and propagation. It has been measured independently and results to be 180±10 ns if a constant threshold level is applied to generate the coincidences.

Figure 4.5 shows the operations occurring to read out ALPIDE as a function of the time, starting from the particle crossing the detector. After the interaction, the ALPIDE preamplifier shapes the signal and sends it to the discriminator. The output of the discriminator keeps the status for about 6 μs.

116
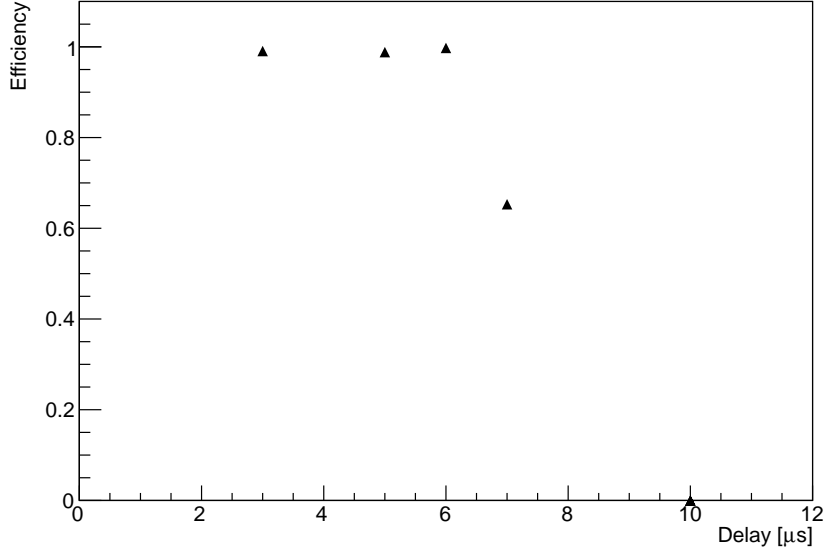
Figure 4.6: Fraction of events with pixels over the threshold as a function of the delay between the trigger generation and propagation to ALPIDE. Errors are smaller than the marker size.

Meanwhile, the Digitizer processes the signal and sends a logic output to the "Gate and Delay generator". After the delay, the signal is sent to ALPIDE, that states a STROBE signal to all the pixels. If the STROBE signal and the output of the discriminator are both positive, the pixel is included on the event readout.

For this study the beam frequency is set to about 50 Hz, to avoid that multiple hits. The proton beam of Trento APSS Proton Therapy centre is set to 220 MeV to maximise the beam collimation, and the ALPIDE detector is perpendicular to the incident beam. The strobe parameter, that sets the length in time of the coincidence window after the trigger propagation, was set to 2 μs. In these controlled conditions, delays between 3 and 10 μs are scanned.

For delays longer than the hold time, the efficiency of ALPIDE is expected to drop, going to zero at about $2 + 6 = 8$ μs, when no events are expected to be shaped and held long enough. The efficiency is calculated as the ratio between the events with at least one hit on ALPIDE and the number of events of the run. The choices of beam energy and ALPIDE position minimise the number of events that does not cross ALPIDE. Nonetheless, (i) the solid angle underlying the ALPIDE sensor is slightly narrower than the one underlying the trigger system; (ii) the beam spot has non-Gaussian tails corresponding to particle tracks as distant as up to 7-10 mm from the beam centre; (ii) multiple scattering effects are never negligible for low-energy nuclei. The three reasons

above mentioned explain why the efficiency at short delays is slightly less than 1. Estimating such an acceptance effect is pointless, as the objective of this study is to check that the loss of efficiency actually occurs at 6 μs, that is the value quoted by the sensor designer for the analog hold of the pixel preamplifier exit [14].

The results are shown in figure 4.6, where the efficiency as a function of the delay set on "Gate and Delay generator" is plotted, since the contribution of the Digitizer is a order of magnitude lower. The efficiency is about 1 for delays shorter than 6 μs and drops rapidly for higher values, as expected.

For all the measurements taken during beam test in Trento, the trigger delay has been set to 1 μs.

4.3 GEANT4 simulations of beam tests

A GEANT4 simulation has been produced for both beam tests, reproducing the distances between the beam exit and the sensors, the distances between the sensors themselves, the effects of materials between the beam exit and detectors (in particular air and the box mylar window).

4.3.1 GEANT4 simulation of Trento beam test

Trento Proton therapy centre provides users with detailed information on beam properties. In particular, they have a set of measurements of the energy and the full width at half maximum for the proton beam at the so-called isocenter, located 125 cm away from the beam exit window. During the test, the setup is aligned to have the ALPIDE at the isocenter of the beam. With this information, the simulation can be used to infer the energy at the exit of the beam and to estimate it at the entrance of the ALPIDE setup, even if not placed at the isocenter. This calibration is dual-purpose:

- it confirms the nominal beam energy values given by the facility;

- it is the base for estimating low energy values obtained with absorbers.

The procedure applied to reconstruct the beam energy is simple: a set of 1000 events is produced, with the nominal energies of the beam acquired during the test. From the events, distribution of the energy of the particles at the isocenter is extracted. The mean value and the σ of the distribution are calculated from a Gaussian fit. Then the mean energy obtained from the fit is plotted as a function of the nominal energy. With a linear fit, shown in figure 4.7, the parameters to reconstruct the correct energy at the exit of the beam are obtained. Table 4.1 shows reconstructed values agree with the nominal energies within 0.5%.

Once the beam energy is known, it is possible to evaluate the effect of different thicknesses of degrader. The use of degrader allows to explore energy less than 70 MeV, the minimum provided by the accelerator.

The degrader is made of a compound called "solid water" [38]. The simulation is the only way to correctly evaluate the energy of the beam in these
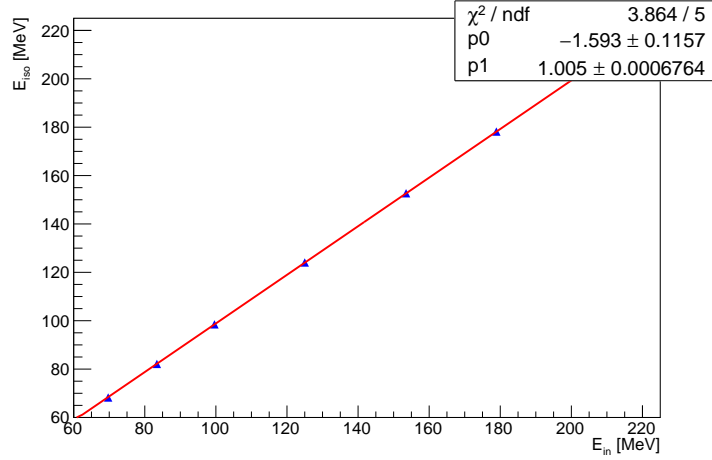
Figure 4.7: Energy at isocenter as a function of the input energy. The results of the fit have been used to reconstruct the input energy that gives the measured value at the isocenter. Error is smaller than the marker size.

Nominal beam energy $[MeV]$	E_{iso} $[MeV]$	Reconstructed beam energy $[MeV]$	E_{dep} $[Me]$
220	218.4	218.9	0.0213
179	178.2	178.9	0.0244
154	152.7	153.5	0.0270
125	124.1	125.1	0.0312
100	98.6	99.7	0.0368
83	82.3	83.5	0.0421
70	68.5	69.7	0.0483

Table 4.1: Energy of the beam: nominal energy, isocenter energy, reconstructed beam energy and energy deposited on ALPIDE active layer extracted from simulation.

conditions, because the facility makes use of a the ionisation chamber for energy estimation, not sensitive to low energies.

The degrader is located in front of the detector box to minimise the beam spread. Table 4.2 reports the values of the energy at isocenter of the beam after it crosses different degrader thicknesses, located 6 cm before the isocenter. The particle energy is set at the value corresponding to the nominal energy of 70 MeV. The degrader material is inserted in the position where it was during the test beam. The value of energy at the isocenter is again extracted from a Gaussian fit on the energy distribution of particles.

Degrader thickness $[mm]$	E_{iso} $[MeV]$	E_{dep} $[MeV]$
15	51.9	0.0597
25	38.0	0.0761
30	29.2	0.0936
35	17.1	0.142

Table 4.2: Energy at isocenter for different degrade thicknesses. The energy of the beam is set to 70 MeV nominal energy. In the last column the energy deposited on ALPIDE active layer is reported.

The values reported as E_{iso}, the energy of the beam at isocenter, in both tables 4.1 and 4.2 are the reference energies for the following analysis. When the energy is obtained directly from the accelerator, the σ calculated from the fit is about 0.13 MeV. When the energy is obtained by inserting a degrader, the σ of the distribution is about 1.3 MeV.

Another important feature added to simulation is the beam spread. The documentation of the beam line gives the value of the Full Width at Half Maximum (FWHM) for the different beam energies. Values are shown in red in figure 4.8.

The spread can be due to the interaction of the particles with the air between the exit window of the beam and the isocenter. From the simulation, the Full Width at Half Maximum (FWHM) of the beam dimension are calculated. The data are reported in figure 4.8 with squares. Values of FWHM are significantly lower than the data quoted in the documentation.

To correctly include the effect, measured values are fit with an exponential function. Fit parameters are implemented on the Event Generator class of the simulation. After the correction, the agreement between measured and simulated data is very good, as shown in figure 4.8.

The energy threshold of the setup has been studied by modifying the values of energy of the beam, although the real measurements on this energy range are obtained with a degrader. In figure 4.9 the fraction of events releasing a signal in both the trigger bars is plot as a function of the energy of the beam. The fraction does not reach 100% because of the beam spread, that is higher for lower energies where the two contributions due to air and to spread correction increase. The rising trend of the plateau confirms this hypothesis. For higher
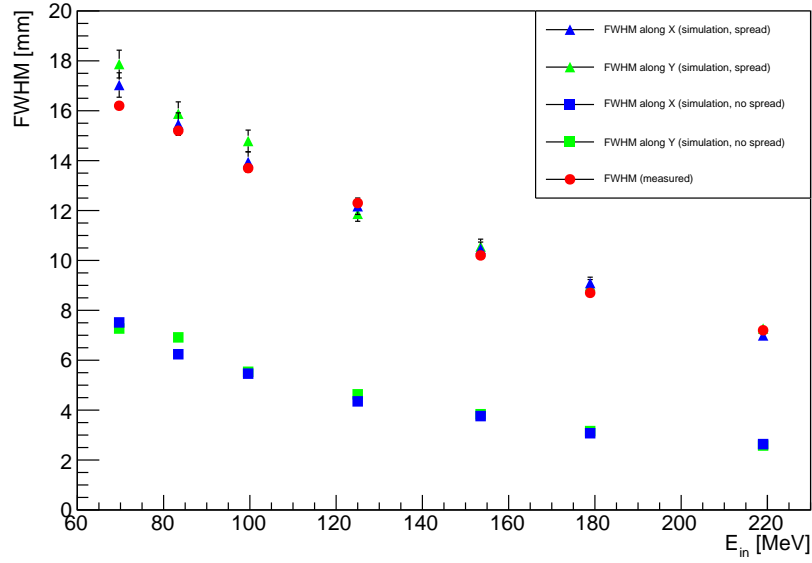
Figure 4.8: FWHM of the beam with only air contribution (squares) and including the beam spread (triangles). The results of simulations are compared with the data provided by the facility documentation.
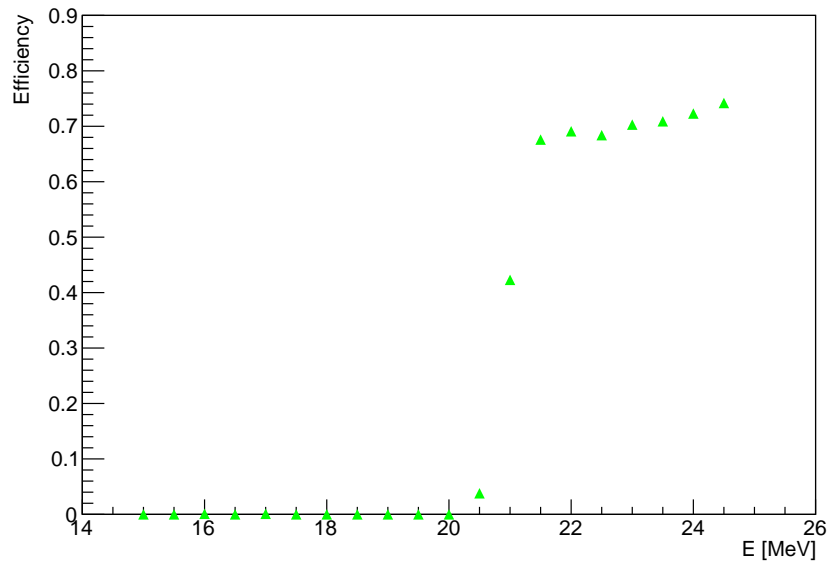
Figure 4.9: Energy threshold for protons.
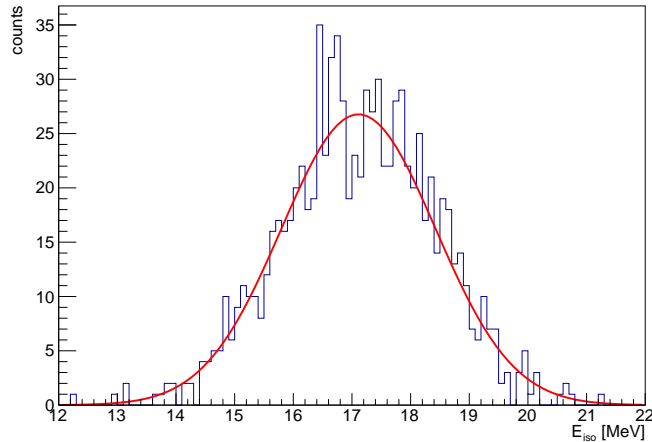
Figure 4.10: Energy at isocenter of the beam after 35 mm of solid water degrader.

energies the FWHM of the beam is lower and all almost all the events cross the detectors.

Figure 4.9 demonstrates that protons with energy less than 20 MeV cannot trigger the experiment. Nonetheless, triggers were observed also when using degraders as thick as 35 mm, corresponding to an average energy of 17.1 MeV (see table 4.2). In fact, figure 4.10 shows that a small fraction of events with energy higher than 20 MeV leaves the degrader, inducing triggers.

After tuning the simulation, it is possible to be confident of the energy deposited by protons inside the ALPIDE epitaxial layer, reported in tables 4.1 and 4.2. This information is the base for further analisys, both of data and simulations.

4.3.2 GEANT4 simulation of Catania beam test

Laboratori Nazionali del Sud gave less information on the beam spill, so the simulation tuning could not be as detailed as for the Trento Proton Therapy Centre. The facility provided four different nuclear species with an energy of 62 $MeV/a.m.u.$, namely H, He, C and O.

The simulation was performed with the same approach adopted for the Trento proton beam line, accounting for different distances and particle species. The intrinsic beam spread is not included in the simulation.

4.4 Cluster definition: from stacked analysis to cluster finding algorithm

Since the ALPIDE has a binary output, all the physics information must be retrieved from the distribution of pixels over the threshold. A group of pixels related to the same impinging particle constitutes a structure called "cluster".

It is interesting to study the clusters created by a particle passing through the ALPIDE detector without applying identification algorithms. The main aim of this analysis is to define the general features of clusters and use them to set the best parameters for a cluster selection. The correct identification of a cluster is a crucial point of the analysis. A correct reconstruction of the effects of a crossing particle in a controlled environment, such as a beam test, is the key for any further analysis to be performed with flight data.

During the test, the ALPIDE was operated with 0 V back bias for most of the runs. The value of back bias is specified when data sets with different polarisation are shown. The threshold of the setup was $166 \pm 10 \ e^-$, and it was regularly checked monitored during the test.

The analysis can be divided in the following steps:

- rejection of multi-cluster events;

- alignment and stack of the events;

- Analysis.

The strategy applied to select the events with only one cluster starts with the calculation of the RMS along both x and y directions for all the events. To identify the events with a single cluster, the RMS distributions is studied, shown in figure 4.11.

4.4.1 Event selection

Cluster finding and analysis tools were tuned on two data sets, taken at the APSS PTC in January 2019. They represent the lowest and highest energy protons obtainable and exploitable for the experimental setup under consideration. Table 4.3 reports the energy and the number of events of each data set.

Sizeable differences are expected between 218.4 MeV protons and 17.1 MeV protons (the energy of the 17 MeV energy distribution triggering the experiment, see section 4.3.1). The average energy loss in silicon of 218.4 MeV protons is about 3.3 MeV/g cm^2, whereas for 17.1 MeV protons $dE/dx \simeq$ 20 MeV/g cm^2. In the latter case, six times more charge diffuse in silicon, fires pixels and shape the cluster.

The distributions for 17 MeV protons (figures 4.11a and 4.11b) show a peak at ~ 1 pixel and few counts for values higher than 2 pixels. The behaviour of the 218.4 MeV protons is similar. To give a reference for the RMS values, need only consider that for the minimum size cluster of size 2, $RMS_{x/y} = 0.71$. For a bigger 4×4 cluster (size 16), $RMS_x = RMS_y = 1.12$. Events with only a

Energy at beam exit [MeV]	Degrader [mm]	Energy at the detector [MeV]	Number of events
218.9	–	218.4	35000
178.9	–	178.2	112000
153.5	–	152.7	110000
125.1	–	124.1	109000
99.7	–	98.6	103000
83.5	–	82.3	100000
69.7	–	68.5	103000
69.7	15	51.9	107000
69.7	25	38.8	102000
69.7	30	29.2	102000
69.7	35	17.1	420000

Table 4.3: Proton data sets used for tuning tools of cluster finding and analysis. Data taken at the APSS PTC.
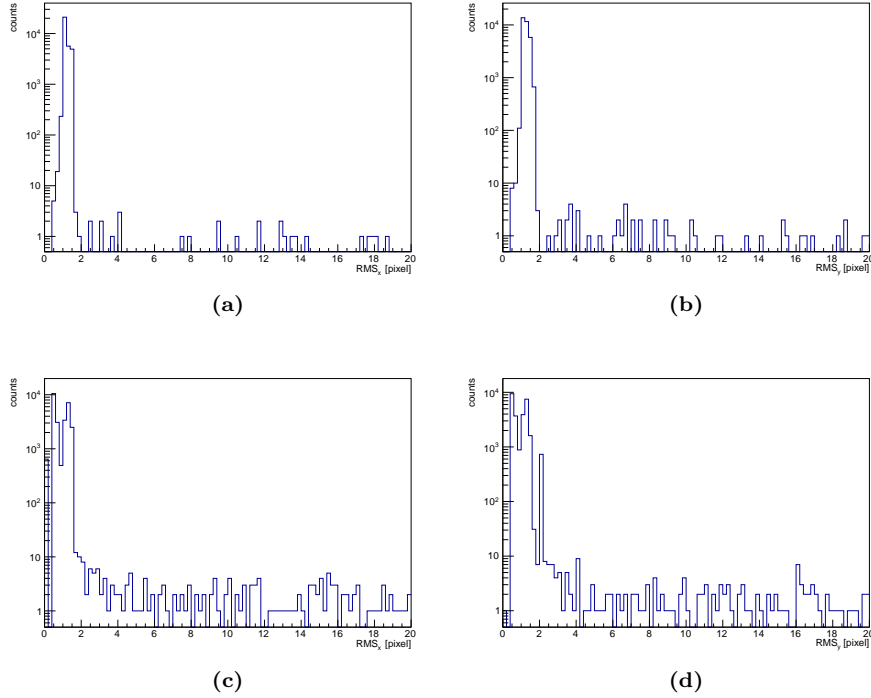
Figure 4.11: Distribution of RMS of pixels over threshold along x and y direction for each event of two different runs, one acquired with 17.1 MeV protons (figures 4.11a and 4.11b), the other with 218.4 MeV protons (figures 4.11c and 4.11d). The main peak contains all the events with a single cluster, the other counts are related to events with more clusters.

(a) 17 MeV **(b)** 218.4 MeV
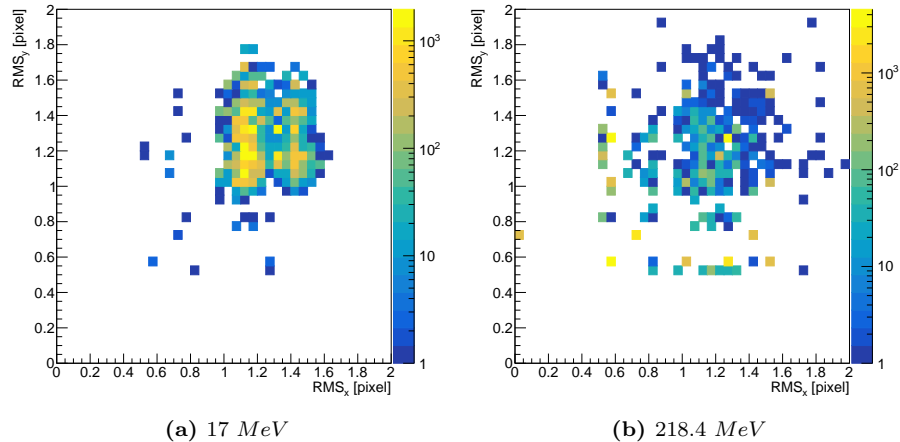
Figure 4.12: Distribution of RMS_x versus RMS_y for 218.4 MeV and 17 MeV protons. The double structure is more evident on figure 4.12b, corresponding to 218.4 MeV protons, but there are hints of a similar effect on figure 4.12a, corresponding to 17 MeV protons.

pixel over threshold are rejected. The correlation between RMS_x and RMS_y by plotting the RMS_x versus RMS_y, as shown in figure 4.12 for datasets.

Both for 17 MeV and 218.4 MeV protons the effect of the finite size of pixels is visible. At 218.4 MeV (figure 4.12b), four combinations are favoured, where RMS_x or RMS_y are equal to 0.55 or 1.25 respectively. These values correspond to well-defined cluster shapes. Favoured combinations are visible also for 17 MeV protons, where RMS_x and RMS_y show excesses around 1.15 and 1.35.

These structures are barely visible in figures 4.11, where the coarse binning aims at showing the separation of single-cluster events ($RMS_{x/y} < 2$) and multi-cluster events ($RMS_{x/y}$ up to 17.1 and higher).

Another difference in the two data sample is the "event length" (EL), defined as the total number of pixels over threshold. For a higher energy release, the cluster is expected to be larger than for a low energy deposit. The EL is small for 218.4 MeV, about 4 pixels for each event. The number is close to the value quoted by ALICE collaboration for MIPs [60], although the 218.4 MeV protons energy release is about twice the MIP release(3.3 MeV/gcm^2 vs 1.68 MeV/gcm^2). The event size for 17 MeV protons is about 12 pixel. Figure 4.14 shows the EL distribution for 17 MeV and 218.4 MeV proton events selected with $RMS_x < 2$ and $RMS_y < 2$. Different populations are visible in both cases, with EL=12 acting as separator for the 17 MeV plot. As it will be clear later, EL=12 correspond to a particular cluster shape, quite frequent for 20 keV energy deposits. It is possible to check if there is a dependence on the event size by plotting the RMS_x and RMS_y as a function of this quantity. The plots

shown in figure 4.13 have been obtianed applying the following selection:

- $\text{RMS}_y < 2.$ for EL versus RMS_x;

- $\text{RMS}_x < 2.$ for EL versus RMS_y.

Plots in figure 4.13 allow some considerations:

- the RMS is correlated with the event length;

- x and y directions are slightly different because of the non perfectly squared shape of ALPIDE pixel;

- the event length is larger for larger energy deposit in silicon, as expected;

- quasi-MIP particles (at 218.4 MeV dE/dx is twice the MIP's one) clearly show higher than average energy releases, compatible with Landau-Vavilov tails.

- low event lengths are compatible with a limited number of cluster shapes and RMS values, as expected.

Only the events for which the $\text{RMS}_x < 2$ and $\text{RMS}_y < 2$ are included in all the following analysis. This strict selection is strict enough to select only events with a single cluster are accepted. The selection is effective for primary protons traversing the ALPIDE sensor. The fraction of events triggered by an isolated secondary electron has been found to be negligible.

4.4.2 Event stacking

The event selection discussed in the previous section is the base for the next step of the analysis, i.e. event stacking. The purpose here is to represent on a map the probability that a given pixel is fired by a proton of a certain energy. By construction, the integral of this map will be the average cluster size. The procedure followed to compute the maps is:

- re-calculation of mean value along x and y;

- Subtraction of the mean value to all the x and y coordinates of the pixels;

- Fill of 2D histogram with the resulting new coordinates of the pixels.

After all events have been processed, the histogram is normalised by dividing for the number of entries. Figure 4.15 shows the result of these operations for all energies available (see table 4.3). All distributions are centred to 0 for x and y coordinates because of the construction. They also show circular symmetry, as expected.

In figure 4.16 the cluster size is plot as a function of the energy of the beam at isocenter, where the ALPIDE detector was aligned during the beam test. For the energies obtained from the beam (from 70 MeV to 218.4 MeV), the isocenter energy values are provided from a direct measure available for the

(a)

(b)

(c)

(d)
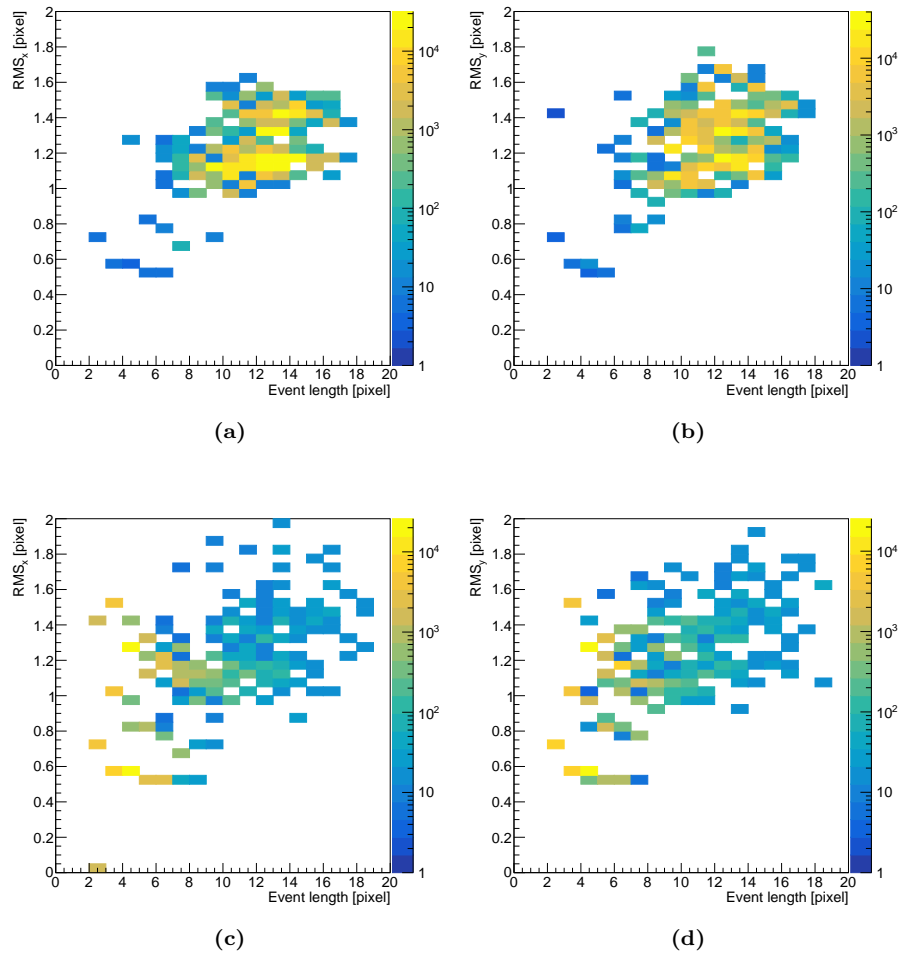
Figure 4.13: In the figures, the values of RMS_x and RMS_y are shown as a function of the event length.

(a) 17 *MeV* protons　　　　　　**(b)** 218.4 *MeV* protons
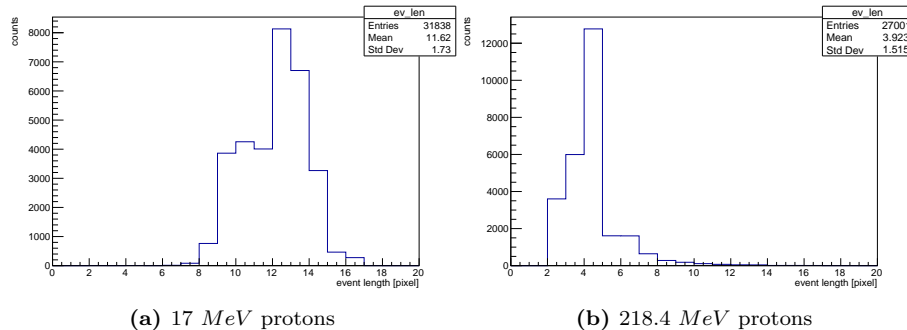
Figure 4.14: Size of events with $RMS_x < 2$ and $RMS_y < 2$ for 17 *MeV* protons and for 218.4 *MeV*.

facility users. The distribution is regular and grows quickly at low energies, where the energy deposition increases.

The RMS and the mean of the distribution, both on x and on y, are checked. The mean is expected to be 0 along both the axes, and the RMS to be comparable. The two quantities are represented as a function of the energy of the beam at the isocenter in figures 4.17 and 4.18.

The values of the mean are compatible with 0, as expected. The RMS distributions show a small discrepancy between x and y coordinates. The effect is primarily due to the difference of the pixel size along directions x and y: $s_x/s_y = 1.088$. An asymmetry as large as $\approx 9\%$ is expected when distances long 10 pixels or more are considered. For distances as low as 5 pixels or less, like the diameters of clusters under consideration, the discreteness of pixelisation diminishes the impact of the asymmetry.

All values of cluster size, mean x, mean y, RMS x and RMS y are reported in table 4.4.

4.4.3　Clustering algorithm test

The analysis of the stacked clusters gives the cluster size. The next step is the selection of the best algorithm for the analysis and its tuning. Many cluster finding algorithms are available on the market, defined in libraries as sklearn [1], that provides several choices. The main problem is most of them require as input parameter the number of clusters per frame, that is not known in advance.

Among the possible candidates, DBSCAN (Density-Based Spatial Clustering of Applications with Noise), from Python sklearn library [1] has been selected. The algorithm takes as input two parameters: the minimum number of elements (pixels) that form a cluster and the maximum distance of an element from the others to include it in the cluster.

From the previous analysis, it is possible extrapolate the best values of these parameters: the minimum pixels of a cluster is set to two, and the maximum

(a) 17.1 *MeV*　　**(b)** 29.2 *MeV*　　**(c)** 38.0 *MeV*

(d) 51.9 *MeV*　　**(e)** 68.5 *MeV*　　**(f)** 82.3 *MeV*

(g) 98.6 *MeV*　　**(h)** 124.1 *MeV*　　**(i)** 152.7 *MeV*

(j) 178.2 *MeV*　　**(k)** 218.4 *MeV*
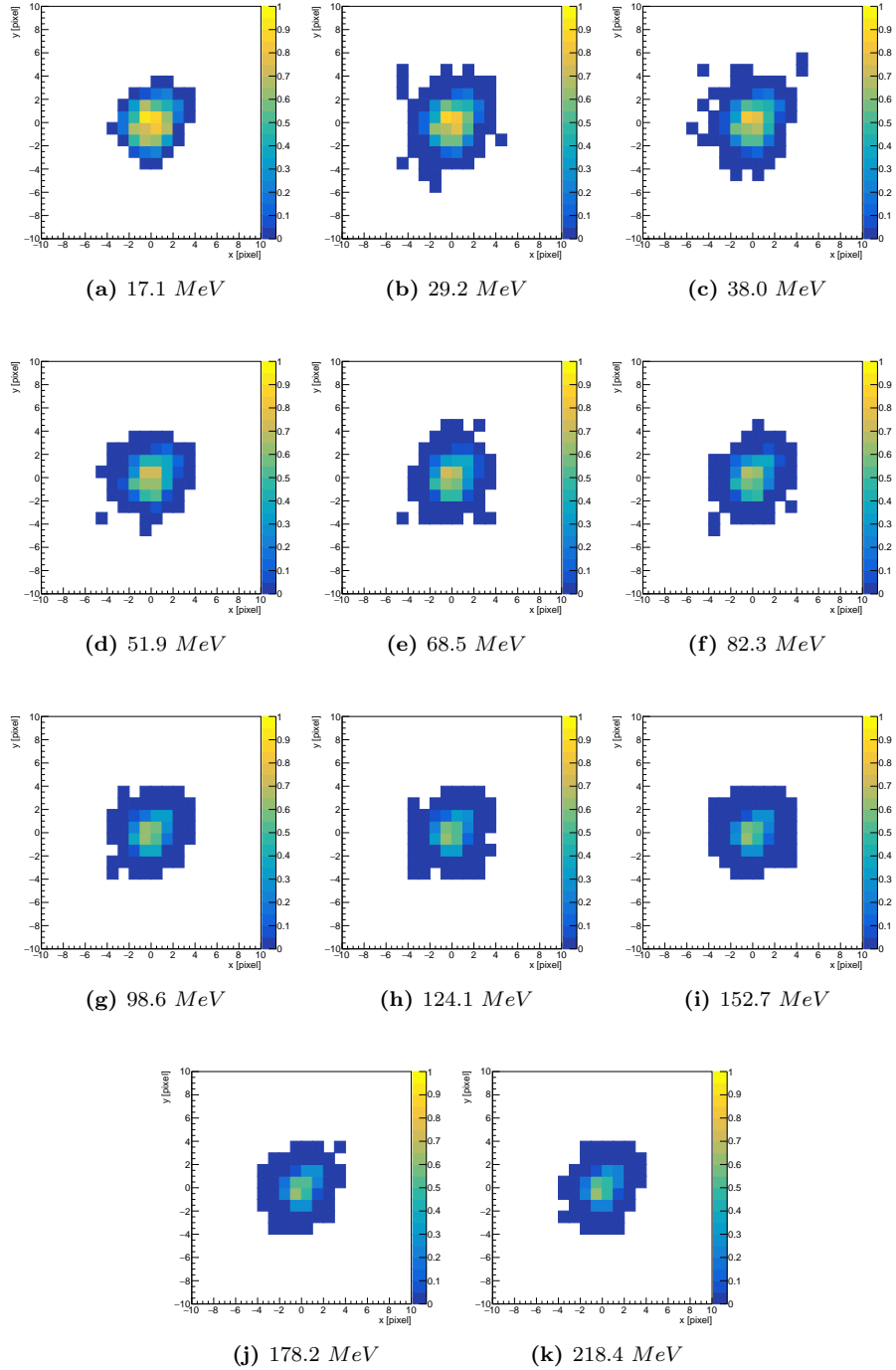
Figure 4.15: The plot shows the stacking of the clusters for 17 *MeV* and 218.4 *MeV* protons.

129
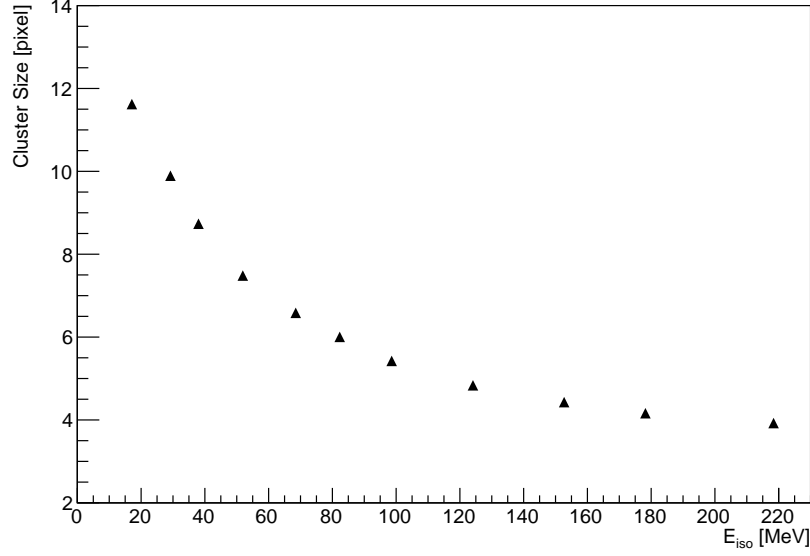
Figure 4.16: Cluster size distribution obtained from the integral of the stacked clusters normalised distributions. The statistic error extracted is reported, but it is smaller than the size of the points on the plot.

E_{iso} [MeV]	Cluster size [pixel]	Mean$_x$ [pixel]	Mean$_y$ [pixel]	RMS_x [pixel]	RMS_y [pixel]
218.9	3.9	-5.5×10^{-9}	1.6×10^{-8}	0.87	0.89
178.2	4.2	-1.5×10^{-7}	-6.5×10^{-8}	0.88	0.91
152.7	4.4	9.7×10^{-8}	-4.2×10^{-8}	0.90	0.93
124.1	4.8	-1.4×10^{-7}	5.9×10^{-8}	0.92	0.96
98.6	5.4	-1.1×10^{-7}	4.0×10^{-8}	0.94	0.99
82.3	6.0	3.5×10^{-8}	-8.9×10^{-9}	0.96	1.02
68.5	6.6	4.8×10^{-8}	-2.6×10^{-8}	0.99	1.04
51.9	7.5	-9.3×10^{-8}	-1.3×10^{-8}	1.02	1.07
38.0	8.7	-6.5×10^{-9}	-3.5×10^{-8}	1.06	1.12
29.2	9.9	-3.4×10^{-8}	3.0×10^{-8}	1.11	1.16
17.1	11.6	-8.3×10^{-8}	-2.9×10^{-8}	1.17	1.22

Table 4.4: Cluster size, mean and RMS calculated from the stacked analysis.
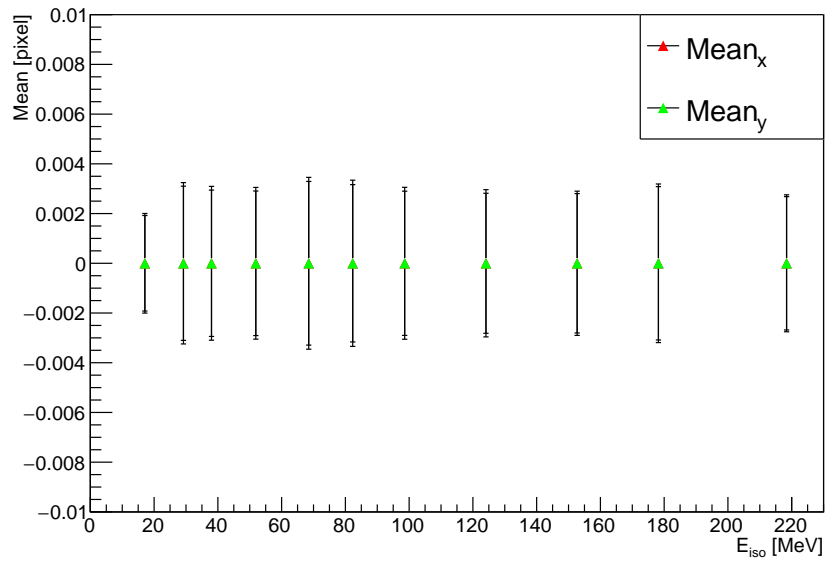
Figure 4.17: Distribution of the mean values of stacked clusters histograms along x and y as a function of the energy of the beam at the isocenter. The values for x axis are not visible because the y values perfectly overlap them. The compatibility with 0 is extremely good.
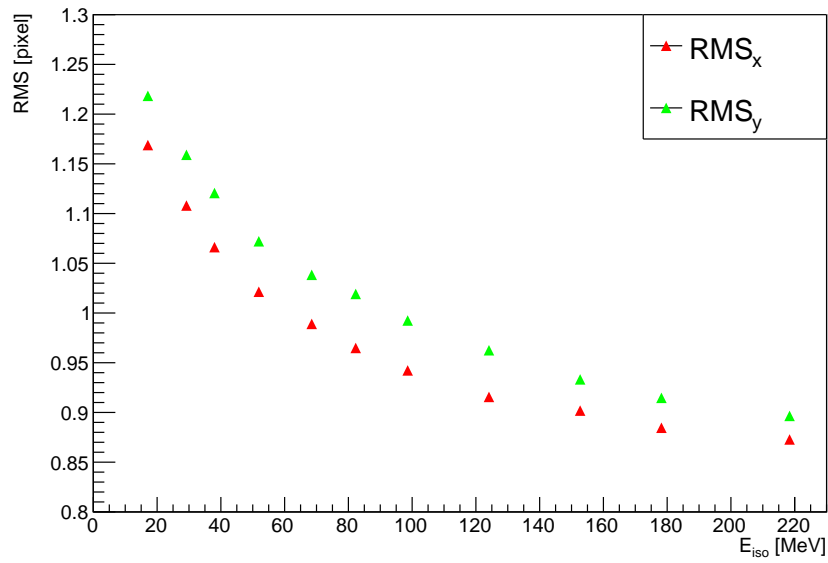
Figure 4.18: Distribution of the RMS of stacked clusters histograms along x and y as a function of the energy of the beam at the isocenter. Uncertainties are not visible because of the order of 0.001 pixels. The values for y results to be systematically higher than values for x.

(a) 17.1 *MeV* **(b)** 29.2 *MeV* **(c)** 38.0 *MeV*

(d) 51.9 *MeV* **(e)** 68.5 *MeV* **(f)** 82.3 *MeV*

(g) 98.6 *MeV* **(h)** 124.1 *MeV* **(i)** 152.7 *MeV*

(j) 178.2 *MeV* **(k)** 218.4 *MeV*
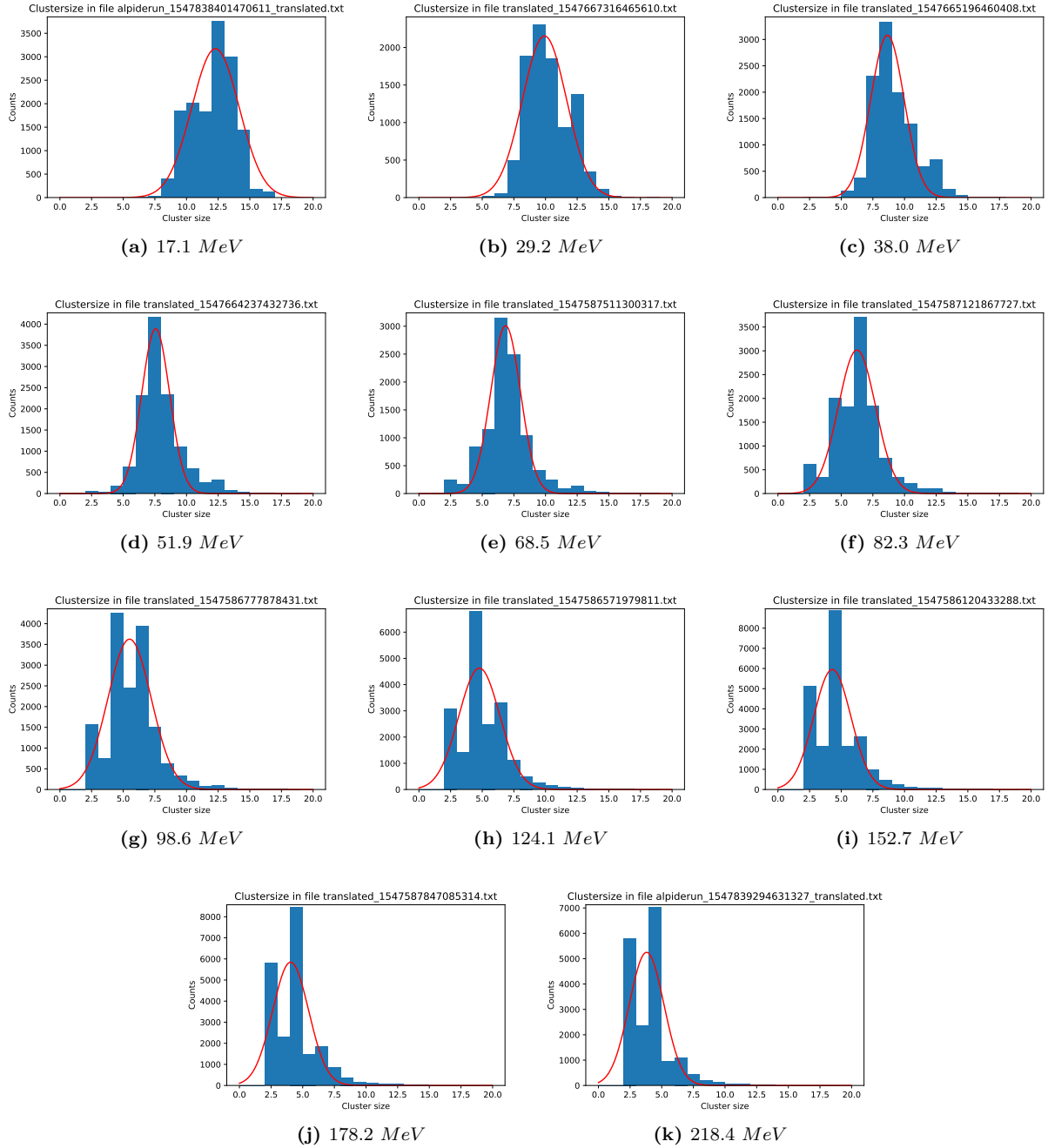
Figure 4.19: Cluster size distributions obtained applying DBSCAN algorithm to the data samples in table 4.3. Data are fitted with a Gaussian function to get mean and σ.

133
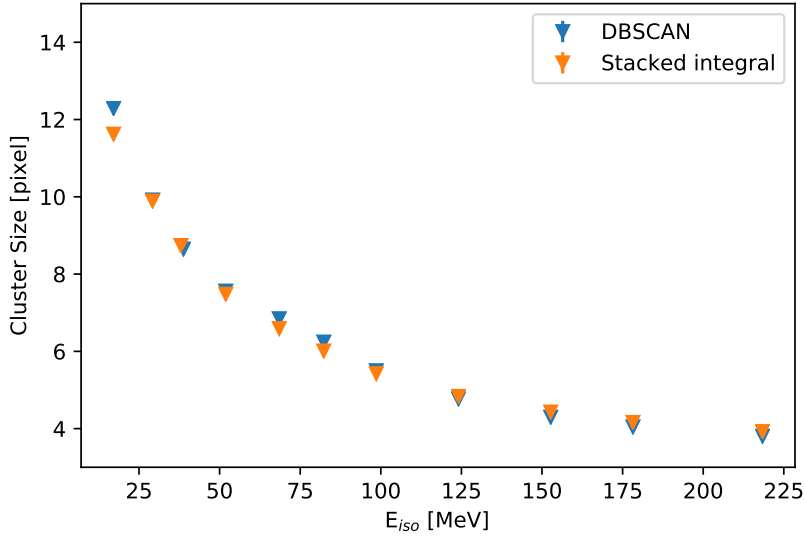
Figure 4.20: Cluster size evaluated with different techniques on the same data sets, collected with protons of different energies. The results are given as a function of the primary particle energy.

distance of a pixel from the others of the cluster is set to two.

The cluster size distributions obtained from the data sets collected at different energies (see table 4.3) are reported in figure 4.19. The Gaussian fit provides a good esteem of the mean value and σ of the distribution, but it is not able to describe other features of the distributions, such as double peaks structures, visible mainly for energy of the primary larger than 98.6 MeV. When the energy deposited is low there is a preference for even cluster sizes (2, 4 or 6 pixels). This effect is less relevant for low energy protons, where the charge produced by the interaction gives rise to a larger number of less regular clusters.

The comparison between cluster size obtained from mean of the fits shown in figure 4.19 and stacked analysis results is shown in figure 4.20. The results are compatible for the full range explored. The only energy value that show a slightly difference is 17.1 MeV.

The results provided by DBSCAN proves that the algorithm is reliable and can be applied to identify clusters for all the future analyses.

4.4.4 Cluster size dependence on impinging particle charge

The cluster analysis described in previous sections has been applied to data collected in Catania with different nuclei. In this case, the results are plot as a function of the Z of the impinging particle. Results are shown in figure 4.21 and reported in table 4.5. As said before, the energy of the particle is 62 $MeV/a.m.u.$ for all the three species.
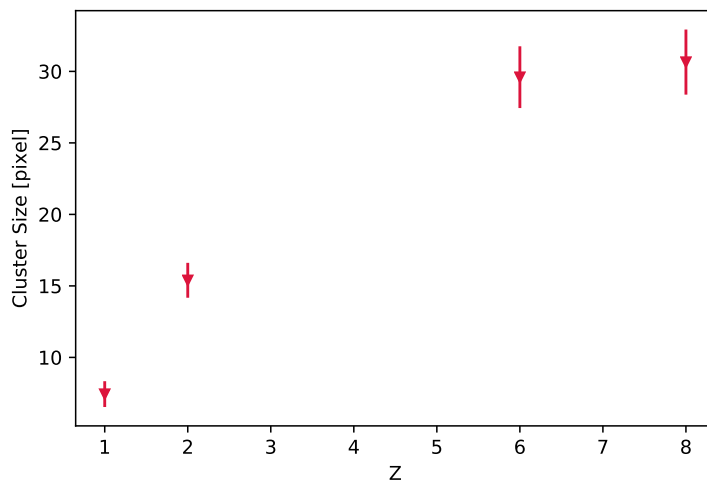
Figure 4.21: Cluster size as a function of the Z of the particle. The beam energy is 62 $MeV/a.m.u.$ for all the four species.

Particle	Cluster Size [pixel]
H	7.4
He	15.4
C	29.6
O	30.7

Table 4.5: Cluster size for different nuclei. The energy is 62 $MeV/a.m.u.$ for all the four species.

From figure 4.21 and table 4.5, it is clear that there is a separation on cluster size between the different species.

Particle	Input Energy [MeV]	Energy deposited [MeV]	Cluster size [pixel]
p	218.9	0.0213	3.9
p	178.2	0.0244	4.2
p	152.7	0.0270	4.4
p	124.1	0.0312	4.8
p	98.6	0.0368	5.4
p	82.3	0.0421	6.0
p	68.5	0.0483	6.6
p*	62	0.0523	7.4
p	51.9	0.0597	7.5
p	38.0	0.0761	8.7
p	29.2	0.0936	9.9
p	17.1	0.142	11.6
He*	248	0.204	15.4
C*	744	0.352	29.6
O*	992	3.319	30.7

Table 4.6: Cluster size for different values of energy deposited in silicon active layer. Starred particles are collected at LNS in Catania. The input energy is the energy at the isocenter for data collected in Trento and the energy at the beam exit for data collected in Cataia.

All results described in previous sections show a clear dependence of the cluster size on the energy deposited by the primary particle. Table 4.6 and figure 4.22 quantify such a dependence for the ALPIDE case (epitaxial layer 27 um thick, see section 4.5 for details).

4.5   ALPIDE response to inclined tracks

Facility	Particle	Energy [MeV]	Angle [°]	Back bias [V]
Trento APSS	proton	218.9	0, 30, 45, 60, 75, 80	0, -3, -6
Trento APSS	proton	17.1	0, 30, 45, 60, 75, 80	0, -3, -6
Catania LNS	H	62	0, 30, 45, 60, 75, 80	0
Catania LNS	He	248	0, 30, 45, 60, 75, 80	0
Catania LNS	C	744	0, 30, 45, 60, 75, 80	0
Catania LNS	O	992	0, 30, 45, 60, 75, 80	0

Table 4.7: Summary of the data set of measurements collected with particle hitting ALPIDE with different incidence angles.

During the beam tests performed with ALPIDE, a set of measurements devoted to the study of the response of the detector to inclined tracks was
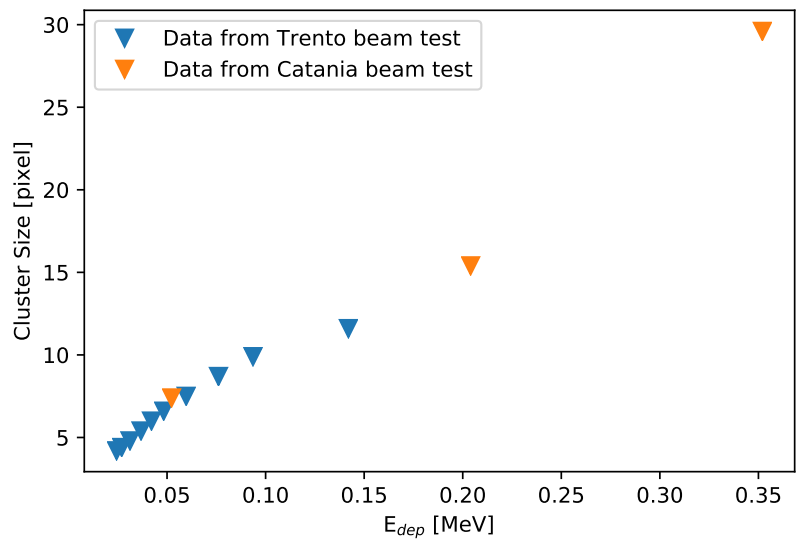
Figure 4.22: Cluster size as a function of the energy deposited in silicon for all the available data set. The value for oxygen is not included but it is reported in table 4.6.
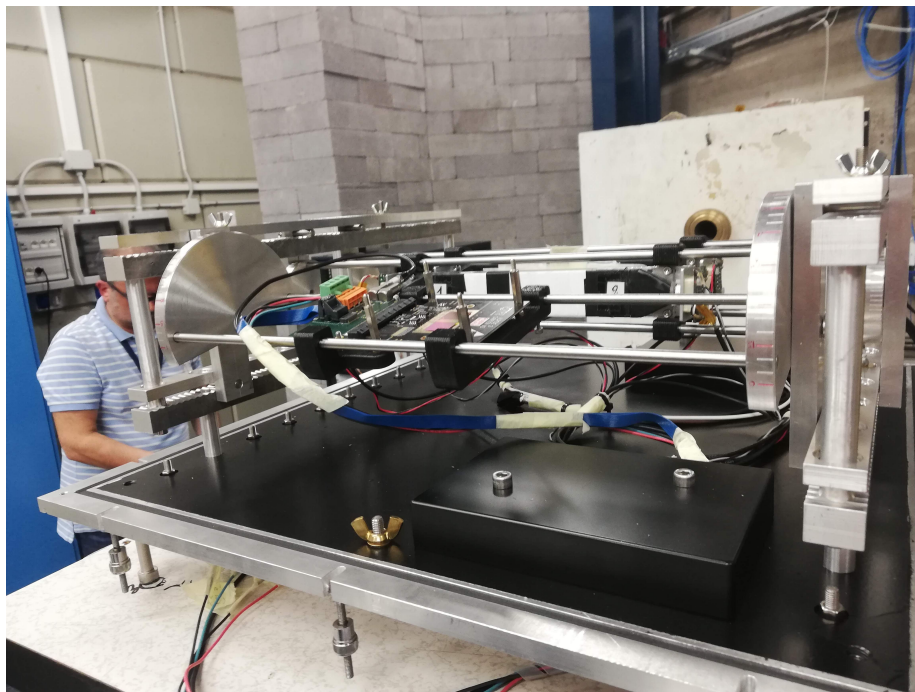
Figure 4.23: Setup with inclined ALPIDE during tests in Catania.

acquired. Thanks to the good control of mechanical alignment of the setup, it is possible to explore angles from $0°$ (beam perpendicular to the detector) to $80°$, as shown in figure 4.23.

During the beam test in Catania, the dependence on the angle for different nuclei (H, He, C, O) is explored, spanning from $Z=1$ to $Z=8$. The scans are performed with $0\ V$ back bias. In Trento, the different configurations have been tested with $218.4\ MeV$ and $17.1\ MeV$ protons at different back bias values, namely $0\ V$, $-3\ V$, $-6\ V$. In table 4.7 all angles and energies are reported.

It is possible apply the stacked analysis on the data from Trento beam test to check the shape evolution of the clusters at different angles. The cluster shape is expected to change from a circular shape to an elongated shape as the angle between the impinging particle and the detector increases.

To reject multi-cluster events, the RMS cut described in section 4.4.1 is relaxed to $RMS_x < 4$ and $RMS_y < 2$. Clusters are expected to elongate along x axis and the RMS_x to increase. The particle crosses a broader region of the detector along this axis because of setup orientation, as shown in figure 4.23 (see sketch in figure 4.3).

The evolution of cluster shape at different angles is shown in figure 4.24 for $17\ MeV$ protons and in figure 4.25 for $218.4\ MeV$ protons. For low energy protons, there is no significant change in the cluster shape up to an angle of $75°$. For the last two figures, corresponding to $75°$ and $80°$ the effects of the detector orientation is clearly visible.

Looking at the $218.4\ MeV$ protons, the change of shape is visible already for $60°$. In this case, the pixel dispersion is large, but taking into account the centre of the distribution (yellow region), where most counts are located, the elongated shape is well defined. The effect is more evident than for low-energy protons because of the lower intrinsic cluster size. At large angles, the major axis a_M of the cluster is determined by the inclination, while the minor one a_m is always determined by the intrinsic cluster size. Consequently, the ratio a_M/a_m is larger for lower energy deposits, i.e. for higher primary energy.

The first aim of these measurements is to study how the cluster size changes when the particle hits the detector with a certain angle. However, with these data it is also possible to probe more deeply the structure of the sensor.

4.5.1 Modelling clusters from inclined tracks

To describe the model built for the ALPIDE response, the first step is the simple case in which the particle hits the detector perpendicularly to the surface. In this case the particle crosses only one pixel. The average cluster size for MIPs is about 3 [60], as reported in ALICE documentation.

The "intrinsic cluster size" IC is defined as the size of the typical cluster associated with average energy deposits of particles with a certain energy impinging on the detector perpendicularly. These typical clusters are always assumed to be circular, with an associated "effective radius", as large as $r_{eff} = \sqrt{IC/\pi}$. A graphic representation of this case is shown in figure 4.26a. The diffusion-driven

(a) $0°$

(b) $30°$

(c) $45°$

(d) $60°$

(e) $75°$

(f) $80°$
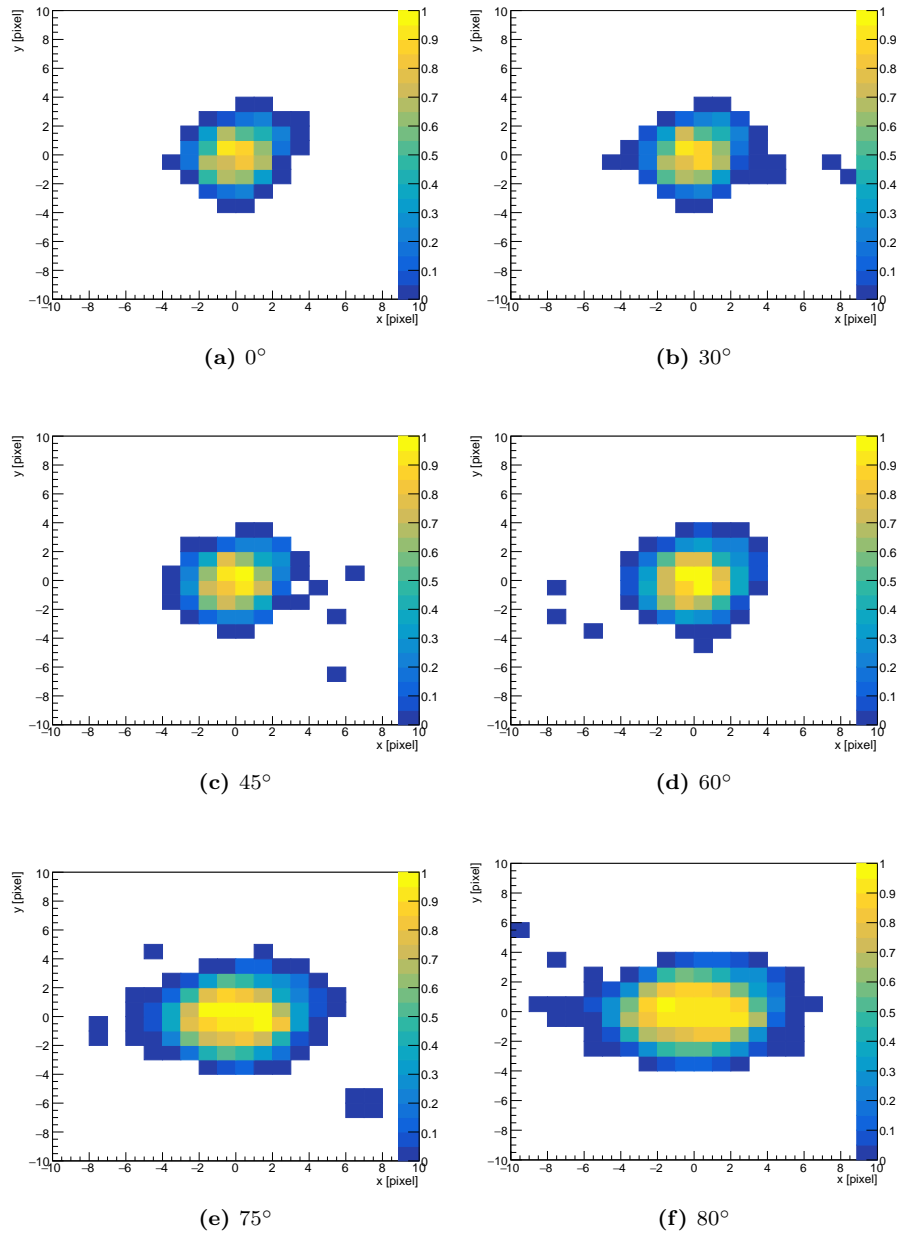
Figure 4.24: Stacked analysis of 17.1 MeV protons at different angles.

139

(a) 0°

(b) 30°

(c) 45°

(d) 60°

(e) 75°

(f) 80°
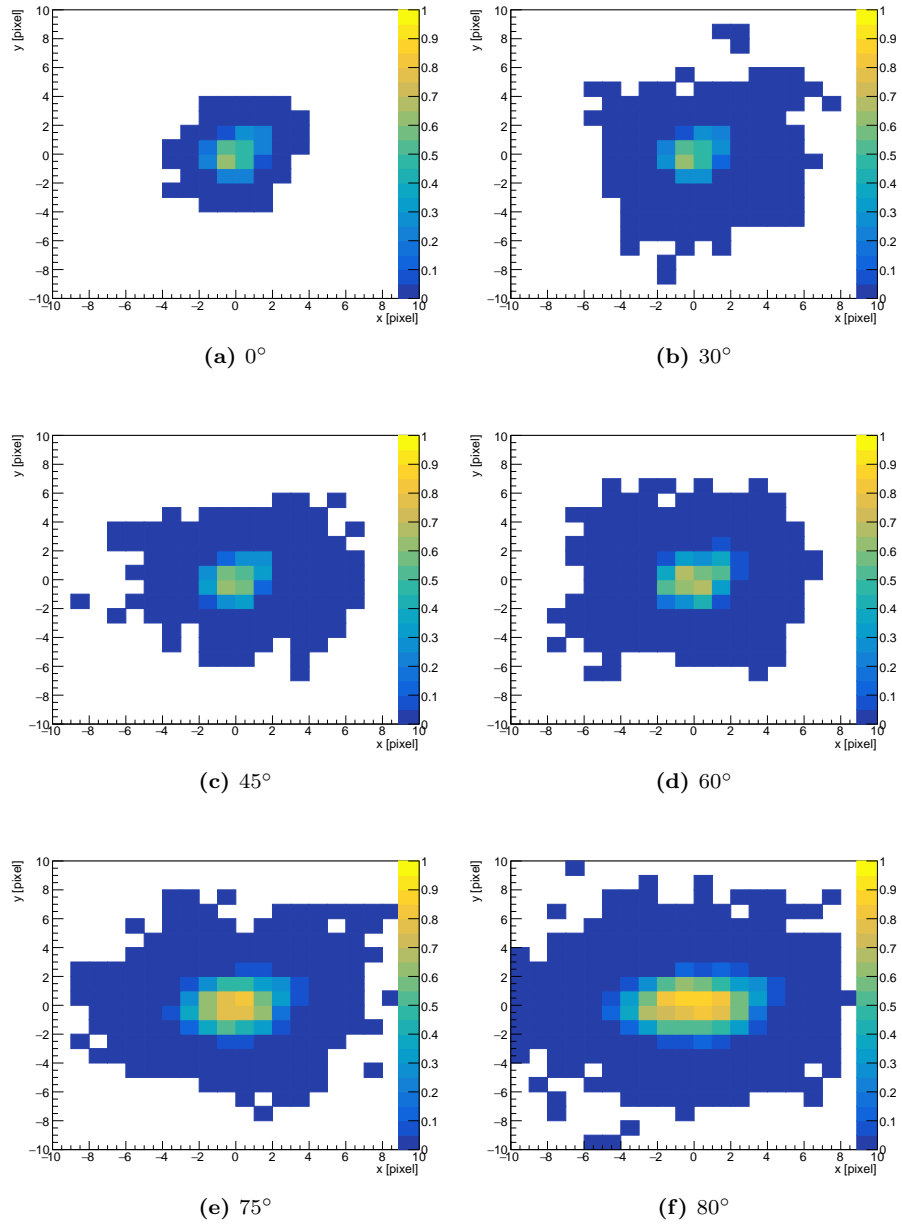
Figure 4.25: Stacked analysis of 218.4 MeV protons at different angles.
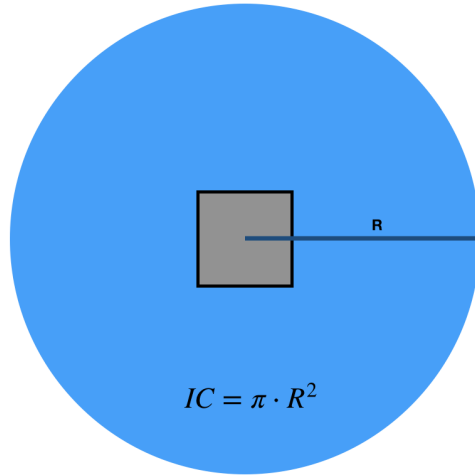
(a)
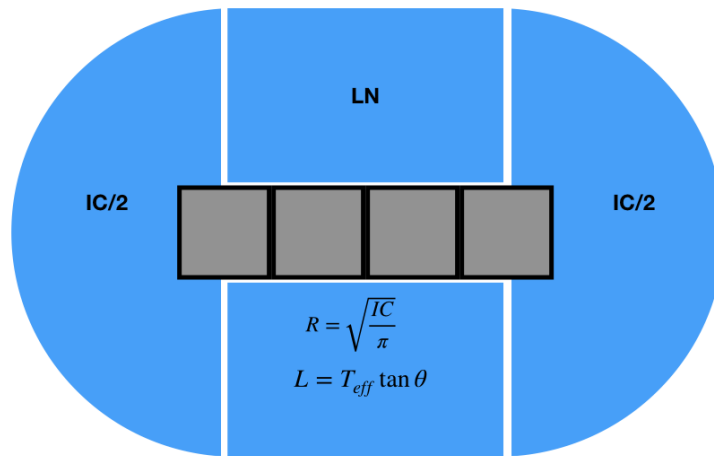
(b)

Figure 4.26: Effect of the passage of a particle perpendicular to the detector (4.26a) and inclined of an angle θ with respect to the normal direction. Symbols are explained in detail on the text.

charge collection is the reason why this parameter is sensitive to the amount of charge deposited (see table 4.6).

For the sake of simplicity and also because it matches with the available experimental data, the work is based on the assumption that the angle between the particle arrival direction and the line perpendicular to the sensor always lies in the xz plane. When the particle that hits the detector comes from a direction different from the normal of the sensor plane, the number of pixels where the particle releases energy is given by the formula:

$$N = 1 + T_{eff} \tan \theta$$

where θ is the angle between the particle direction and the normal to the sensor plane and T_{eff} is the effective thickness of the active volume in units of pixel side. As a first approximation, T_{eff} can be taken as thick as the epitaxial layer of the detector.

From figure 4.26b it is possible to see how to estimate the number of pixel hit:

- the area of the inner rectangle with base $N - 1$ and height $2R = 2\sqrt{\pi}IC$

- the boundary semicircular regions, with area IC

All the contribution summed are summarised in the expression

$$CS = IC \left(1 + 2\sqrt{\frac{\pi}{IC}} \cdot T_{eff} \tan \theta \right)$$

that gives the value of the cluster size as a function of the angle.

The model built for the interaction of inclined particles is simple and, as shown in the next section, very effective. Nevertheless, it has some important limits to be discussed.

- Clusters are assumed to be circular;

- IC is a function of the energy deposited, that is not constant along the track;

- If and pixel pitch$/T_{eff}$ widely differs from 1, the model is not true anymore.

The assumption that the distribution of pixels over threshold around a track is approximately circular is not necessarily true. Since the pixels are squared and have a pitch of 28 μm[1], this assumption is not correct, and the differences are particularly significant for the events with small cluster size, where the squared shape of the cluster is hardly compensated by a statistical fluctuation of the pixels on a single event.

---

[1]ALPIDE pixels are not perfectly squared, the pixel pitch is 29.24×26.88 μm^2. Because of the slightly difference, the pixels are assumed to be squared with 28 μm pitch.

Cluster Size [pixel]	Shape	$2R_{real}$ [pixel]	$2R_{calc}$ [pixel]
1	□	1	1.13
4		2	2.26
5		2.83	2.52
9		3	3.39
12		4	3.91
16		4	4.51

Table 4.8: The table report, as a function of the cluster size, the most regular distribution that can be obtained, the real diameter of the distribution($2R_{real}$) and the diameter calculated in circular approximation ($2R_{calc}$).

Table 4.8 shows, for some value of cluster size, the most regular shape of the cluster and its minimum possible radius, calculated as

$$R_{calc} = \sqrt{\frac{IC}{\pi}}$$

It is clear that the approximation fails, in particular when the cluster is a square or when the cluster size is small.

A second critical point is that the IC is a function of the energy deposited, but the model considers this energy deposit constant for all the pixels hit by the particle.

The energy deposited by the particle along the track is not constant. It can be approximated as only for MIPS and not for highly ionizing particles like the nuclei considered in this work.

Another implicit approximation regards the IC to be used to calculate r_{eff}. It is assumed to be related to the IC for 0° tracks via the relation $r_{eff} = \sqrt{IC/\pi}$. Nonetheless, IC is a function of the energy deposited in the pixel, which is in turn related to the track inclination. The larger the angle, the longer the particle path in the pixel, the larger the energy deposited. Until the particle passes to the next pixel, that is determined by the pixel pitch.

Assuming no dependence of IC on the arrival angle induces a systematic bias on the model, particularly important for layouts where the pixel pitch is much smaller than the epitaxial depth or layouts in the opposite situation. In the first case very inclined tracks will traverse many pixels releasing less energy than for a 0° track. In the second case, very inclined tracks will release on each pixel much more energy than 0° ones.

In ALPIDE, the pixel pitch (28 μm) is close to the thickness of the epitaxial layer of the sensor, that is quoted to be between 20 and 40 μm [88]. The
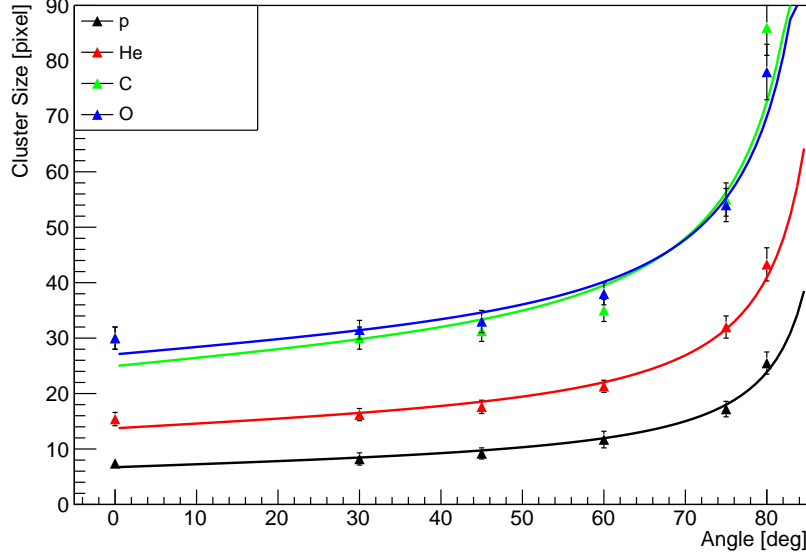
Figure 4.27: Cluster size as a function of the angle for different nuclei.

ratio between the pitch and the epitaxial thickness is then close to 1. As a consequence, the bias from the assumption of IC being constant is negligible.

Inclined tracks for nuclei

Data from the beam test in Catania are discussed in this first section. During the test, data with different nuclei (H, He, C, O) with an energy of 62 $MeV/a.m.u$ are collected.

The clusters have been identified using the DBSCAN library. Only the events with a single cluster are included, and the distribution of the cluster size is fit with a Gaussian function. The mean and the error on the mean are plotted on the graphic shown in figure 4.27. The model is applied with two free parameters, IC and T. Figure 4.27 reports the data and the fit obtained from measurements.

From figure 4.27 it is possible to notice that the model describes very well the behaviour of protons and helium, whereas the agreement is not good for carbon and oxygen.

From each fit two parameters are obtained, IC and T, that are reported in figure 4.28 as a function of Z. Both the parameters are reported in units of pixels. This is the natural dimension for the cluster size, and it is used also for the sensitive volume thickness because of the definition given for T. It can be easily reported in μm by multiplying it for 28 μm, the pixel pitch.

The points for oxygen and carbon (Z=6 and Z=8) are less reliable than the
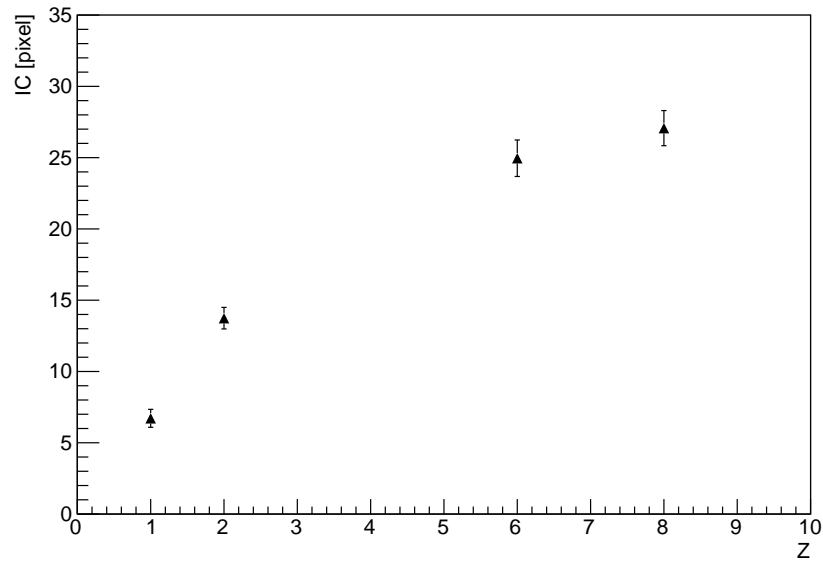
(a)
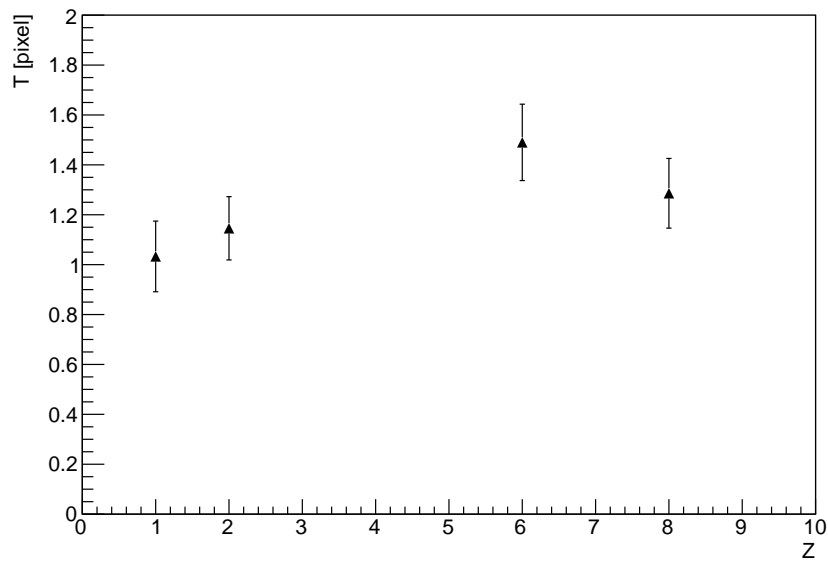
(b)

Figure 4.28: Parameters from the fit in figure 4.27. Both IC and T are in pixel and plot as a function of the Z of the impinging particle.

points for proton ($Z = 1$) and helium ($Z = 2$) because of the worst quality of the fit. The estimated IC is lower than the value of cluster size for events collected at $0°$, and the results for T are not accurate.

By considering only the results for protons and helium nuclei, the IC is the value of cluster size at $0°$, and the two values obtained for T are well compatible with each other. From the two data, the value obtained is

$$T_{eff} = 1.10 \pm 0.02 \text{ pixels}$$

That can be easily translated in μm, obtaining an active thickness of 30.8 ± 0.6 μm. The value is perfectly compatible with the interval quoted by the designers and producers, between 18 and 40 μm [88].

Inclined tracks for protons

As said at the beginning of the chapter, the measurement at different angles were repeated with protons. In this case two different energies were tested, the lowest for which the setup can produce trigger signal (about $17.1 MeV$) and for the higher available from the Trento accelerator, 218.4 MeV.

For both energies, data at different angles were collected. Moreover, different back bias values have been applied. Figure 4.29 shows the cluster size as a function of the angle. Whereas the cluster size at $0°$ changes as a function of the back bias for the low energy protons, for 218.4 MeV protons is almost the same for the three different back bias considered.

Although the 218.4 MeV proton is not a MIP, the ionisation six times smaller than for a $17.1 MeV$ proton (see table 4.6), and the charge generated is collected by a smaller number of pixels. The increase of the depletion region of the p-n junction caused by the applied back bias does not influence the collection as in the case in which the amount of generated charge is higher and spared on more electrodes.

Energy [MeV]	Back bias [V]	IC [pixel]	T_{eff} [pixel]
218.9	0	2.92	1.24
218.9	-3	2.69	0.96
218.9	-6	2.40	0.99
17.1	0	11.13	0.99
17.1	-3	6.44	0.81
17.1	-6	4.99	0.81

Table 4.9: Values of IC and T_{eff} obtained from fit on different data sets.

In this case, all the data set are well described by the fit applied, from which the parameters shown in figure 4.30 and reported in table 4.9 are extracted. The plot of IC (figure 4.30a) shows that the intrinsic cluster size decreases as the absolute value of the back bias increases, whereas the values are almost constant for 218.4 MeV protons. This fact can be easily explained since the amount of charge generated for high energy protons is lower, and the electrodes
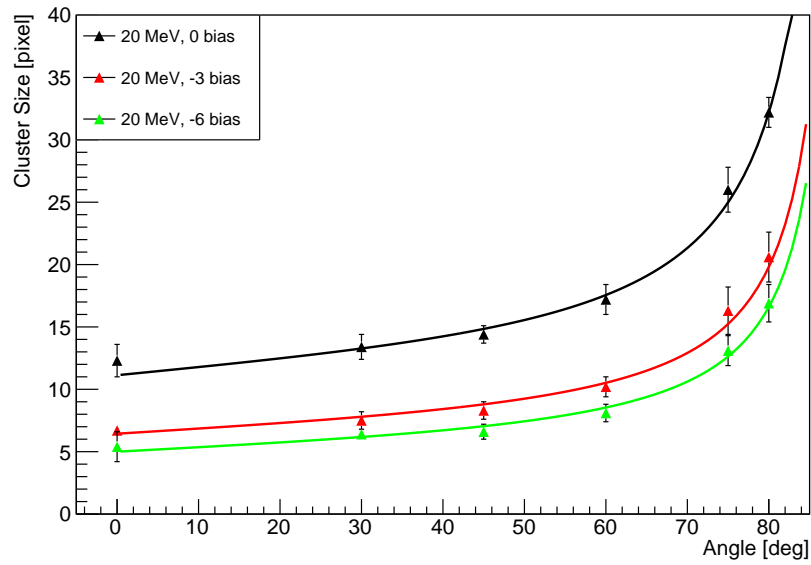
(a) 17.1 MeV
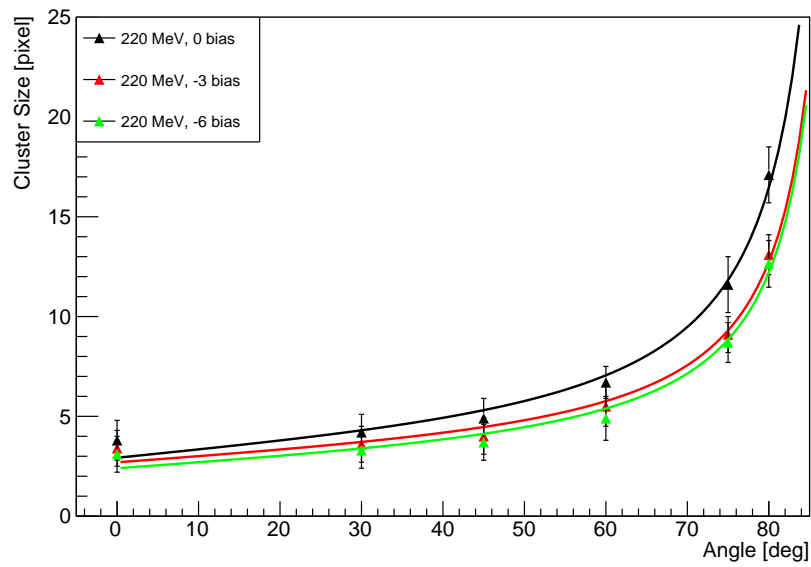
(b) 218.4 MeV

Figure 4.29: Cluster size as a function of the angle for 17.1 MeV protons and 218.4 MeV protons for different back bias values.
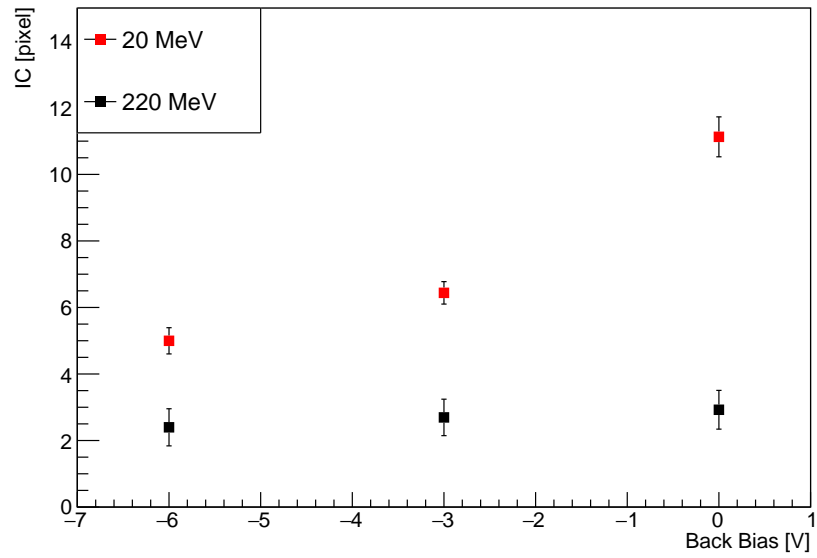
(a)
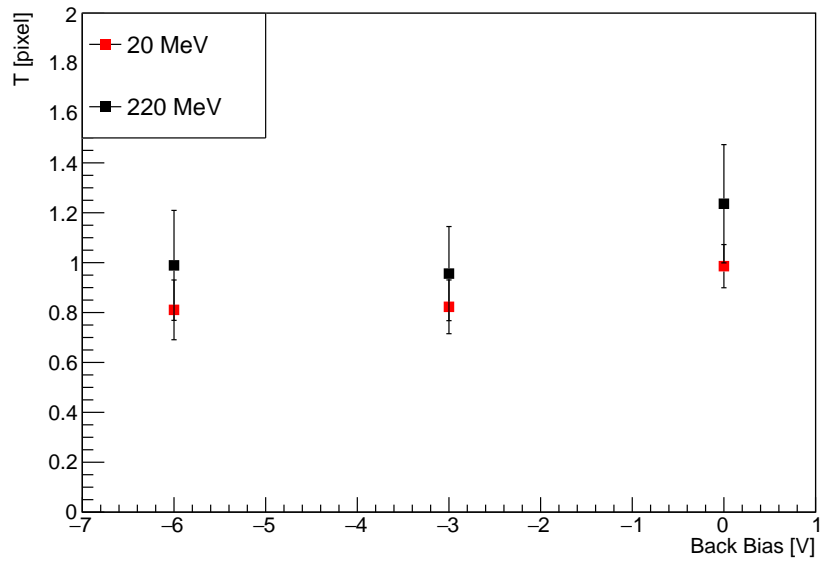
(b)

Figure 4.30: Parameters from the fit in figure 4.29. IC and T are plot as a function of the back bias.

collect it before it can spread. It is a leverage to regulate the cluster dimensions. In HEPD-02 operations, it will be useful to regulate the event dimensions and reduce it in case of high fluxes of nuclei.

The plot of T_{eff} is particularly interesting in this case, since the quality of the fit is better than in the case of nuclei in previous section. All values obtained are compatible within the error bars. However, the value calculated for 218.4 MeV protons is systematically higher than the value calculated for 17.1 MeV protons. For lower energy this model describes the situation as if the particle saw a thicker active volume. The origin of this effect is still under investigation. Effects of spatial charge and effective field (charge screening) are the work hypothesis.

Figure 4.30b shows that the increase on the back bias absolute value causes a small decrease of the T_{eff} values for both the 218.4 and 17.1 MeV protons. Again, in this model, drying the electron dynamics inside the silicon with the electric field, translates into a reduction of the effective thickness available for charge production.

The obtained value for T_{eff} is

$$T_{eff} = 0.96 \pm 0.03 \text{ pixels}$$

corresponding to 27.1 μm. Because of the good quality of the fit, this value is the reference thickness of the detector.

4.6 TCAD simulation

Technology Computer-Aided Design (TCAD) [2] is a tool devoted to simulate fabrication processes and operations of semiconductor devices. It applies finite element method to solve differential equations that describe the structural and electric properties of the devices. It is a powerful tool to investigate features that are not directly accessible by measurements, such as electric fields.

The simulation results are studied to characterise the response of the ALPIDE detector to low energy nuclei. In particular, the first goal is to reproduce the value of cluster size obtained from measurements. The fine tuning of the simulation allows to export the results in more complex tools, that will be the reference for data analysis during characterisation of the detector and flight operations. The study reported here deals with nominal conditions of operation for the HEPD-02 case, namely 0 V back-bias. It focuses only on perpendicular tracks, as the inclined case can be derived from geometrical considerations.

To compare the simulation results with the data, the number of electrons collected by each electrode must be evaluated. Then this value is compared with the threshold of the pixels to find if it is over threshold and calculate the cluster size.

The simulation proceeds through three different steps:

- Sentaurus Device Editor (SDE);

- Sentaurus Device (SDEVICE) steady state simulation;

- SDEVICE transient simulation.

The first step is the Sentaurus Device Editor or SDE, where the geometry of the device is defined, the doping profiles and the mesh. In this simulation, the process simulations are not inserted, since the device description is accurate enough with the only SDE construction.

The second step is a Sentaurus Device (SDEVICE) simulation, in which the collecting n-wells are polarised to 1.4 V, the nominal value of ALPIDE electrodes [14]. The back bias is set to 0 V. The Physics case under study is that of a fast transient charge deposit in a stationary environment, either for the silicon crystal and for the electric field distribution. As a consequence, a steady state model was used to describe the polarisation, acting on each electrode with small steps, to avoid dynamic effects and to ensure convergence.

The third step is again a SDEVICE simulation, including now the transient. Interaction is simulated with the "Heavy Ion" model, that reproduces the impact of a particle on the device. The TCAD configuration settings are summarised in table 4.10.

Simulation	Electrodes number	Electrodes position (figure)	Thicknesses $[\mu m]$	LET $[pC/\mu m]$
Hit on electrode	16	4.33a	30, 25, 20	1.28×10^{-5}
				4.8×10^{-5}
				1.8×10^{-4}
Hit between four electrodes	9	4.38	30, 25, 20	1.28×10^{-5}
				4.8×10^{-5}
				1.8×10^{-4}
Hit between 2 electrodes	12	4.43	30, 25, 20	1.28×10^{-5}
				4.8×10^{-5}
				1.8×10^{-4}

Table 4.10: List of simulation configurations.

The model requires as input parameter the amount of charge generated per length unit, the Linear Energy Transfer (LET). The charge deposition is constant along all the particle track. The approximation has some sense in case of MIPs, but it is less effective for particles whose LET changes along the path, e.g. stopping nuclei. Nevertheless, the thickness of the active region of the device is small enough to consider the changes in charge deposition a second order effect. The good agreement between simulations and data shows that the approximation does not affect significantly the simulation quality. Future work will include non-constant LETs in the simulation.

The LET is calculated from the GEANT4 simulation of the test beam setup, from which the energy deposited in the active volume of the detector is obtained (see section 2.4).

4.6.1 TCAD domain construction

From section 4, the cluster size spans from about three pixels for MIPS to about 12 for low energy protons and even to tens of pixels for low energy heavy nuclei. A domain as large as 6×6 or 7×7 is needed to properly account and correct for boundary effects. Concerning time, the pixel analog front-end has an integration time of about 2 μs (see section 2.4), that is the minimum time interval after the transient to study to compare the results of simulations with the measurements.

The construction of such a large simulation, with a mesh properly defined to provide acceptable uncertainties on the solution, required computing power not available in Trento. The follow up of the domain for a considerable time demands large storage capacity, that is less critical than the computational power to obtain, but still to be adequately handled.

Domain symmetry

To reduce the simulated domain dimensions it is possible to exploit its symmetries. If the hit position is suitably chosen and the energy is release perpendicularly across the silicon, it is possible to perform calculations only on a quarter of the intended domain. The hypothesis is verified by comparing the results for pixels at the same distance from the hit positions in the simulations run.

The total dimensions of the simulation domain are $84 \times 84 \times 50$ μm^3 for all the three cases. By taking into account the symmetry, it is possible to interpolate the results for a $168 \times 168 \times 50$ μm domain.

For all the simulations, three different epitaxial thicknesses are studied, regularly spread along with the possible values (between 40 μm and 19 μm [88]). The selected values are 30 μm, 25 μm and 20 μm. It is important to check the response for different thicknesses because the detectors that will be installed in HEPD-02 will come from multiple batches and could have different epitaxial thicknesses. For this reason, all the detectors will be characterised before the experiment integration.

Mesh description

Mesh$_x$ [μm]	Mesh$_y$ [μm]	Mesh$_z$ [μm]	X$_{max}$ [μm]	Y$_{max}$ [μm]	Z$_{max}$ [μm]
0.1	0.1	1	3	3	T_{epi}
0.5	0.5	1	10	10	T_{epi}
1	1	2	28	28	T_{epi}
2	2	4	84	84	T_{epi}

Table 4.11: Mesh refinement in different regions. Distances are calculated from the hit position.

A second strategy to reduce computational power requirements is to apply a "smart" mesh grid that gradually enlarges while moving away from the hit position. In the region closest to the hit, for a volume that is $3 \times 3 \times T_{epi}$ μm^3,

where T_{epi} is the depth of the epitaxial layer, the mesh is $0.1 \times 0.1 \times 1$ μm^3. Then it becomes to $0.5 \times 0.5 \times 1$ μm^3 for a volume of $10 \times 10 \times T_{epi}$ μm^3. In the rest of the volume $28 \times 28 \times T_{epi}$ μm^3, corresponding to one pixel volume centered around the hit, the mesh is $1 \times 1 \times 2$ μm^3. The rest of the epitaxial is divided by a grid with a pitch $2 \times 2 \times 4$ μm^3. The mesh is also refined around the collection N wells, to improve the design resolution. The grid is $0.2 \times 0.2 \times 1$ μm^3 in a region of $6 \times 6 \times 3$ μm^3 around the electrode. On the substrate the mesh is enlarged to $10 \times 10 \times 10$ μm^3. The mesh description is summarised in table 4.11.

Computing time goes as $e^{N_{mesh}}$, where N_{mesh} is the number of points of the mesh. Moreover, the computing power available limited the maximum number of nodes to 2×10^5. Under these constraints, the best solution is to maximise the refinement around the hit region, since the error made in this first stage propagates to the whole simulation. The lower precision on the rest of the mesh degrades the shape of the current signal, an acceptable drawback for this analysis, focusing on the integral of the signal and not on the signal itself.

LET $[pC/\mu m]$	E_{dep} in 20 μm $[MeV]$	E_{dep} in 25 μm $[MeV]$	E_{dep} in 30 μm $[MeV]$
1.28×10^{-5}	5.8×10^{-3}	7.2×10^{-3}	8.6×10^{-3}
4.8×10^{-5}	0.021	0.027	0.032
1.8×10^{-4}	0.081	0.10	0.12

Table 4.12: Energy deposition corresponding to different LET values.

For each thicknesses the simulations runs with three different values of LET: 1.8×10^{-4} $pC/\mu m$, 4.8×10^{-5} $pC/\mu m$ and 1.28×10^{-5} $pC/\mu m$. The conversion to energy deposition for the different thicknesses is reported in table 4.12. The three values span from MIP energy release (the lower value) to the energy release of ~ 30 MeV protons and allow to compare simulation results with data.

The doping profiles are another important factor of the simulation. They determinate the dimensions of the depletion region and the resistivity of the material, modifying the cluster size significantly.

For ALPIDE, the values are reported in [88]:

- Collection N well: $N_D \sim 1 \times 10^{17}$ cm^{-3}

- P well: $N_A \sim 1 \times 10^{16}$ cm^{-3}

- Epitaxial layer: $N_A \sim 1 \times 10^{12}$ cm^{-3}

- Substrate: $N_A \sim 1 \times 10^{19}$ cm^{-3}

From the doping values it is possible calculate the built-in potential of the junction V_{bi} at thermal equilibrium, given by

$$V_{bi} = \frac{k_B T}{q} \ln \left(\frac{N_D N_A}{n_i^2} \right)$$
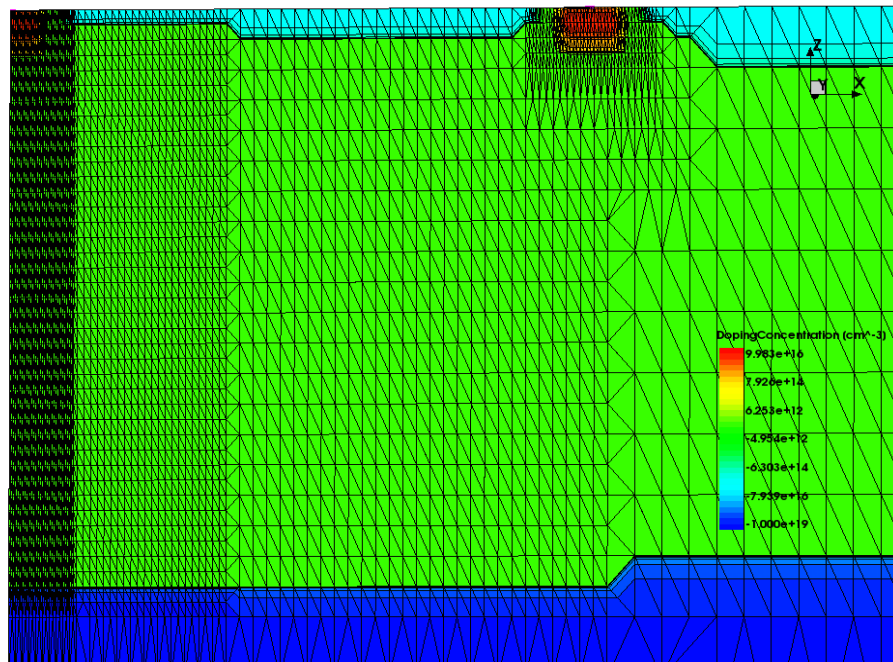
Figure 4.31: Doping profile of the simulation. The epitaxial layer is in green, the p-well in cyan and the substrate in blue. The electrodes are in red. Different thicknesses of the p-wells depend on the mesh refinement.
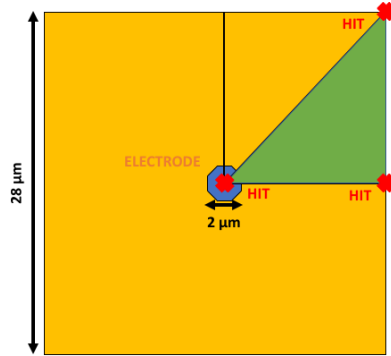
Figure 4.32: Graphic representation of a ALPIDE pixel, centred on collection electrode. To describe the detector response from the results of TCAD simulation, the hit positions (indicated by the red crosses) must be transformed to be inside the area highlighted in green.

Where k_B is the Boltzmann constant, T is the temperature, q the unit charge and n_i the intrinsic carrier concentration. To calculate the depth of depletion region, the external potential $V_{ext} = 1.4\ V$ applied to the well must be considered. The depletion region d can then be expressed as

$$d = d_n + d_p = \sqrt{\frac{2\epsilon}{q}\left(\frac{1}{N_A} + \frac{1}{N_D}\right)(V_{bi} - V_{ext})}$$

In this case, ϵ is the dielectric constant in silicon. Due to the huge difference in the doping concentration, the term $1/N_D$ can be neglected. Because of doping concentration imbalance, the depletion region extends on the low-doped epitaxial layer.

The doping concentration difference between the epitaxial and the P well and substrate confines the charges produced inside the epitaxial layer by the incoming particle. The substrate reflects the charges that diffuse downward, and the P well insulates the electronics on the surface of the pixels and facilitates the collection on n-wells by removing the competition with the field around the p-on-n transistors, implanted to realise the on-pixel readout.

The different domains are built to evaluate the effects of energy deposition in three different positions inside a pixel:

1. Hit on a collecting electrode;

2. Hit in the middle between four electrodes;

3. Hit between two electrodes.

The first case minimises the distance between the electrode and the hit, the second maximise it and the third case is expected to give an intermediate behaviour. Hit positions inside a pixel are shown in figure 4.32. The study of

154
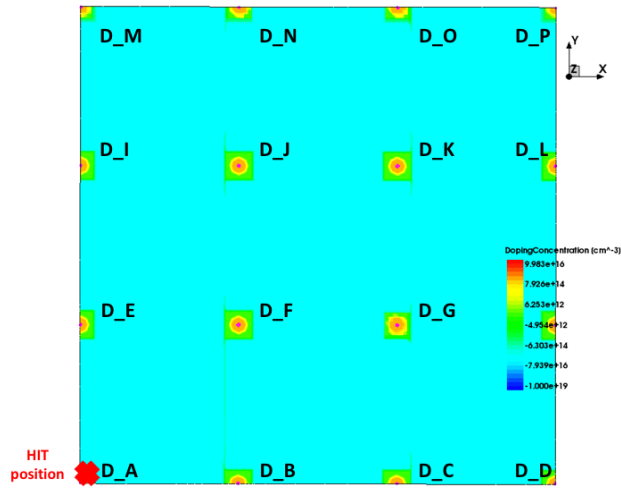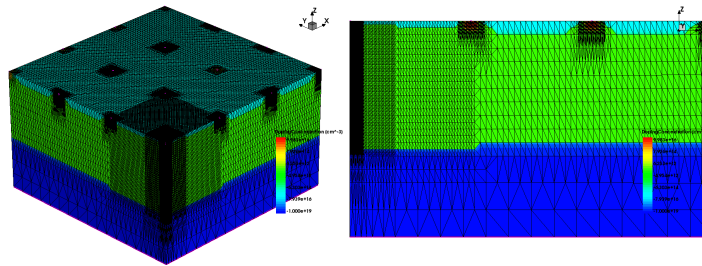
Figure 4.33: Simulation domain. The grid represents the mesh and the colour the doping concentration on the different regions.

these limit cases gives an overview of the detector response in different conditions, with the results that shown in the following sections.

4.6.2 First simulation: particle impinging on a collection electrode

In the first simulation, shown in figure 4.33 the grid is composed of 4×4 electrodes, labelled as reported in figure 4.33a. The particle hits the detector on the D_A electrode. The hit position is indicated with a red cross.

In this case, the quarter of domain simulated has a further internal symmetry: diodes symmetrically above and below the diagonal collect the same charge. In table 4.13 the distance of electrodes from the hit position and the shape factor are reported. The shape factor is applied to correct for the reduced area of electrodes on the simulation boundaries.

Electrode	X [μm]	Y [μm]	Distance [μm]	Shape factor
D_A	0	0	0	4
D_B	28	0	28	2
D_C	56	0	56	2
D_D	84	0	84	4
D_E	0	28	28	2
D_F	28	28	39.6	1
D_G	56	28	62.6	1
D_H	84	28	88.5	2
D_I	0	56	56	2
D_J	28	56	62.6	1
D_K	56	56	79.2	1
D_L	84	56	101.0	2
D_M	0	84	84	4
D_N	28	84	88.5	2
D_O	56	84	101.0	2
D_P	84	84	118.8	4

Table 4.13: Position of the electrodes with respect to the the hit position. From the distance it is possible to notice that some electrodes are equidistant from the hit and then they are expected to collect the same amount of charge. The last column reports a "shape factor", that is applied to collected data to correct the fact that electrodes on the borders of the domain cover only a half or a quarter of the surface they should have.

The simulation follows up the charge diffusion for 2 μs. It records different parameters, and among them the current collected by the electrodes at different time intervals. Data are sampled more finely in the first tens of nanoseconds (about ten samples/ns), to be more accurate in the description of the first part of the signal generation where transients demand more accuracy.

Time evolution of charge diffusion

To test the quality of the simulation, a follow-up of the evolution of the electron diffusion during the 10 ns after the energy deposition on the detector is analysed. The analysis is run on all the epitaxial thicknesses but only for the intermediate value of energy deposition.

With a step of 1 ns, the electron density profile in the middle of the epitaxial layer is considered, and fit it with a Gaussian function. The σ is expected to evolve according to the law

$$\sigma = \sqrt{D_e t}$$

where D_e is the electron diffusion coefficient and t is the drift time. Since the charge generation follows a Gaussian profile with a finite σ_0, this must be taken into account in order to correctly evaluate the diffusion coefficient. The correct formula to fit the data is then

$$\sigma = \sqrt{D_e t + \sigma_0^2}$$

Both D_e and σ_0^2 are free parameters of the fit. In figure 4.34 the time evolution of σ over time is shown, the different series corresponding to the three different epitaxial thicknesses simulated. Whereas for 30 μm and 25 μm the fit describes well the data behaviour, for 20 μm domain it is possible notice that after 5 ns the data trend changes. The feature is still under investigation.

The diffusion coefficients obtained from the fit is 30.3±0.4 cm^2/s for 20 μm epitaxial thickness, 27.3±0.06 cm^2/s for 25 μm, and 26.22±0.02 cm^2/s. The value of σ_0^2 is about 0.25 μm^2, and it is coherent with the simulation parameter.

The result is consistent with the limit value reported in the literature for pure diffusion, equal to 36 cm^2/s [31]. In the ALPIDE sensor the diffusion parallel to the sensor plane is slower than in pure silicon, because of the weak field favouring the charge collection and the collection itself.

Cluster size calculation

In figures 4.35, 4.36 and 4.37 the charge collected by the electrodes for the different thicknesses and LETs tested are shown. The simulation directly calculates the current as a function of the time, and the charge is obtained from its integral. The number of electrons is calculated by dividing the charge for the electron charge e. The curves are corrected for the shape factor reported in table 4.13. The red line corresponds to 150 electrons, approximately the threshold

Figure 4.34: Evolution of σ of the electron density distribution over time during the first 10 ns after charge generation.

set during test beams for ALPIDE. A single register sets the thresholds on the whole sensor, and there are fluctuations of the order of 10 electrons.

When counting electrodes above threshold, the internal symmetry of the quarter must be accounted for. Moreover, the simulation domain is a quarter of the full domain considered.

Thresholds are set for the whole ALPIDE. The thresholds of the pixels are not exactly the same, and are distributed around the value imposed by the register 0x060E[2] with a Gaussian distribution, whose σ depends on the detector quality. When the cluster size from simulations is evaluated, it is necessary to take into account the fluctuations. Pixels that collect a number of electrons very close to the threshold could be included in the cluster or not. For this reason, when there is this kind of uncertainty two results are given. In the first result, pixels that collect a number of electrons significantly ($> 10\ e^-$) larger of the average threshold are counted, in the second case, if necessary, the pixels that collect a number of electrons of the order of the threshold are included.

For 30 μm epitaxial layer, the calculated cluster sizes are reported in tables 4.35, 4.36 and 4.37.
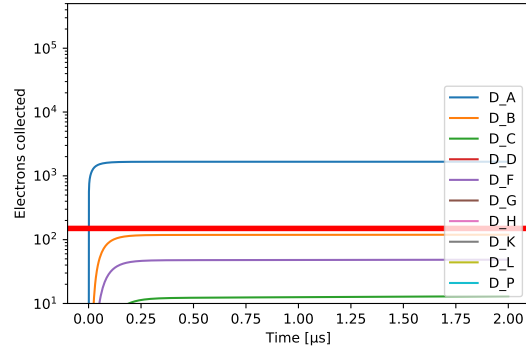
(a) 1.28×10^{-5} $pC/\mu m$.
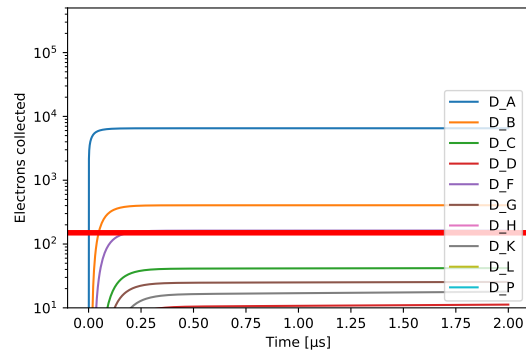
(b) 4.8×10^{-5} $pC/\mu m$.
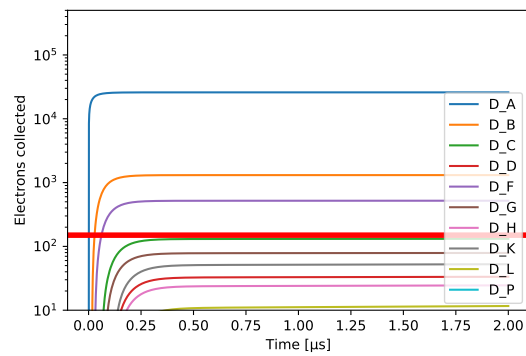
(c) 1.8×10^{-4} $pC/\mu m$.

Figure 4.35: Charge collected by different electrodes for the different LET in 30 μm thick epitaxial layer for particle hitting on D_A electrode.
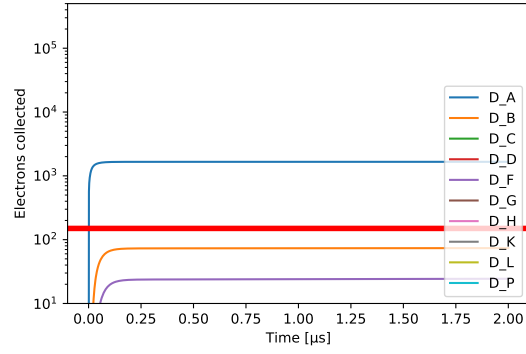
(a) 1.28×10^{-5} $pC/\mu m$.

(b) 4.8×10^{-5} $pC/\mu m$.

(c) 1.8×10^{-4} $pC/\mu m$.

Figure 4.36: Charge collected by different electrodes for the different LET in 25 μm thick epitaxial layer for particle hitting on D_A electrode.
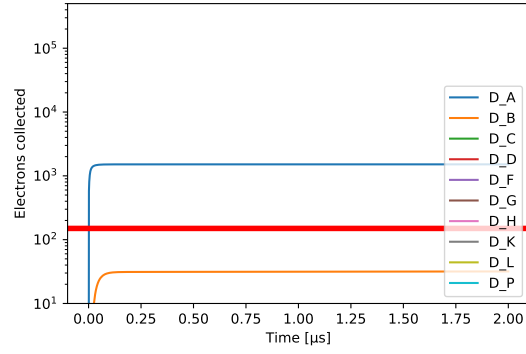
(a) 1.28×10^{-5} $pC/\mu m$.

(b) 4.8×10^{-5} $pC/\mu m$.

(c) 1.8×10^{-4} $pC/\mu m$.

Figure 4.37: Charge collected by different electrodes for the different LET in 20 μm thick epitaxial layer for particle hitting on D_A electrode.

| LET | Minimal CS | Maximal CS |
$[pC/\mu m]$	[pixel]	[pixel]
$1.28{\times}10^{-5}$	1	5
$4.8{\times}10^{-5}$	5	9
$1.8{\times}10^{-4}$	9	13

(a) 30 μm epitaxial

| LET | Minimal CS | Maximal CS |
$[pC/\mu m]$	[pixel]	[pixel]
$1.28{\times}10^{-5}$	1	1
$4.8{\times}10^{-5}$	5	5
$1.8{\times}10^{-4}$	9	9

(b) 25 μm epitaxial

| LET | Minimal CS | Maximal CS |
$[pC/\mu m]$	[pixel]	[pixel]
$1.28{\times}10^{-5}$	1	1
$4.8{\times}10^{-5}$	5	5
$1.8{\times}10^{-4}$	9	9

(c) 20 μm epitaxial

Table 4.14: Cluster size for particle hitting on a electrode with different LET.
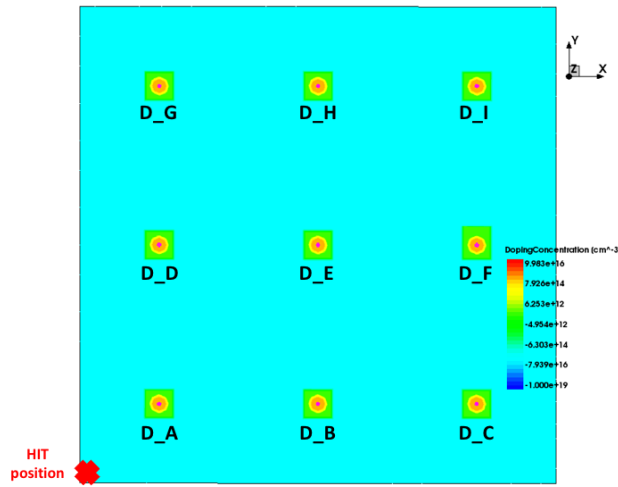
Figure 4.38: Simulation domain for the hit between 4 electrodes.

4.6.3   Second simulation: hit between 4 electrodes

Figure 4.38 reports the electrode position for the second simulation, in which the particle hits the detector in the middle between four electrodes. The general structure of the domain is the same of the previous case.

Electrode	X [μm]	Y [μm]	Distance [μm]	Shape factor
D_A	14	14	19.8	1
D_B	42	14	44.3	1
D_C	70	14	71.4	1
D_D	14	42	44.3	1
D_E	42	42	59.4	1
D_F	70	42	81.6	1
D_G	14	70	71.4	1
D_H	42	70	81.6	1
D_I	70	70	99.0	1

Table 4.15: Electrode position with respect to the hit and shape factor.

Table 4.15 reports the electrode position and distance from the hit point. In this case, the shape factor is always one exploiting the internal symmetry of the quarter. As in the previous case, it is possible to collect data only from subset of electrodes, since in some cases the distance from the hit position is the same.

Time evolution of charge diffusion

In figure 4.39 is reported the evolution of the σ of the electron density distribution during the first 10 ns after generation and the fit with the formula reported in the previous section.

The coefficient diffusion extracted from the fit is 35.96 ± 0.04 cm^2/s for 30 μm epitaxial thickness, 38.57 ± 0.05 cm^2/s for 25 μm and 39.28 ± 0.04 cm^2/s for 20 μm thick epitaxial. These values are compatible with the previous case, yet a but higher. The transverse diffusion is actually helped by the internal field between the electrodes, as illustrated in figure 4.49. The value of σ_0^2 is about 0.30 μm^2 for all the three cases. This last value is compatible with the previous result and with the input parameters of the simulation.

In this case the values of the coefficient diffusion is higher than the expected value. It is possible that the electrode distribution on the surface favours a small drift towards the centre of the detector.

Cluster size calculation

The values of charge collected as a function of the time are reported in figures 4.40, 4.41 and 4.42 for all the three epitaxial thicknesses studied.

---

[2]Threshold level is also affected by the configuration of other registers setting the current reference. The value on this register sets the current reference of the discriminator [14]
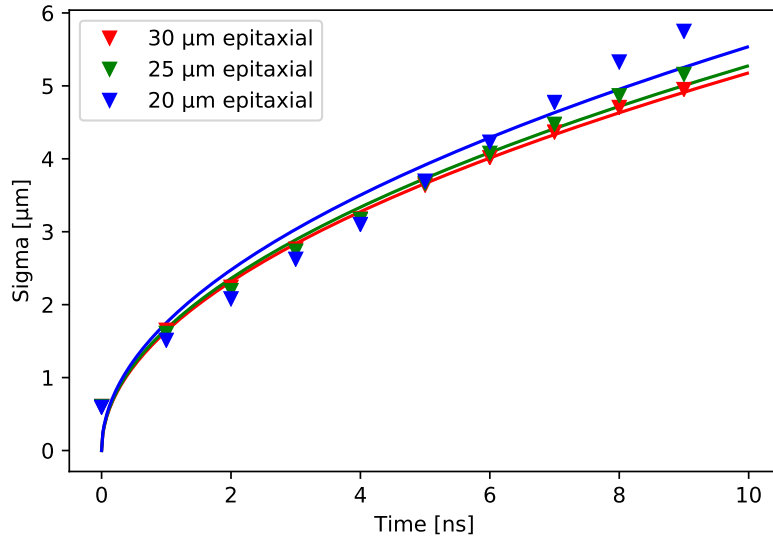
Figure 4.39: Evolution of σ of the electron density distribution over time during the first 10 ns after charge generation.

The cluster size is calculated for all the configurations. By taking into account the symmetries of the simulation, for the different thicknesses of epitaxial layer the results are shown in tables 4.16a, 4.16b and 4.16c.

4.6.4 Third simulation: particle impinging between two electrodes

The third simulation takes into account the case in which the detector is hit in the middle between two collection electrodes. On the top of the domain a 3×4 grid of collection electrodes is placed, as shown in figure 4.43. The mesh refinement is the same as the previous cases.

In this case, the symmetry inside the simulated domain is lower, and all the electrodes must be considered singularly, as shown in table 4.17.

Time evolution of charge diffusion

In figure 4.44 the evolution of σ of the electron density distribution along the first 10 ns after the charge generation. The fit limits have been already discussed and other features of the plot in the previous sections.

The values obtained for the diffusion coefficient D_e are 32.060±0.014 cm^2/s for 30 μm epitaxial thickness, 34.077±0.015 cm^2/s for 25 μm and 34.438±0.019 cm^2/s for 20 μm. The values of σ_0^2 are about 0.3 μm^2.
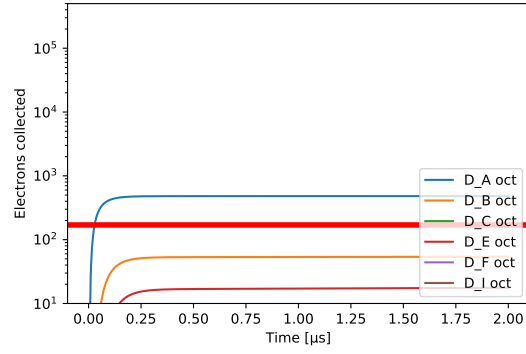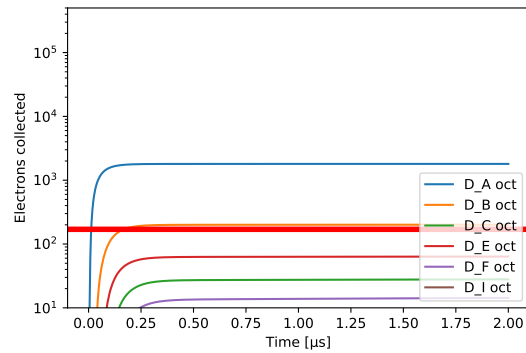
(a) 1.28×10^{-5} $pC/\mu m$.

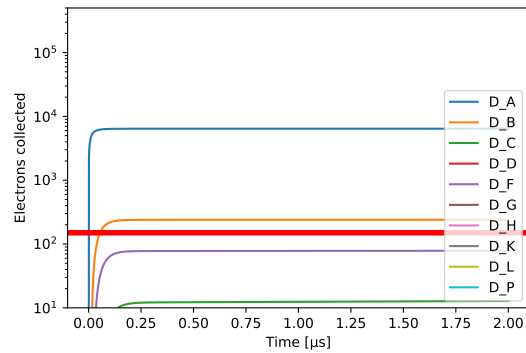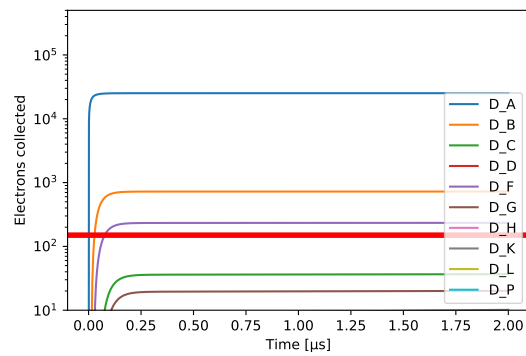**(b)** 4.8×10^{-5} $pC/\mu m$.
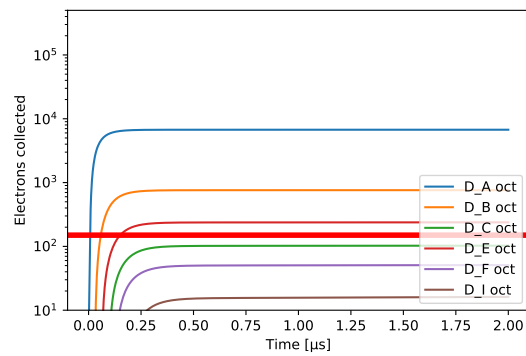
(c) 1.8×10^{-4} $pC/\mu m$.

Figure 4.40: Charge collected by different electrodes for the different LET in 30 μm thick epitaxial layer for particle hitting between four electrodes.
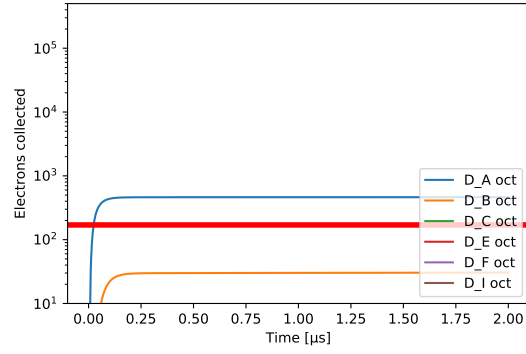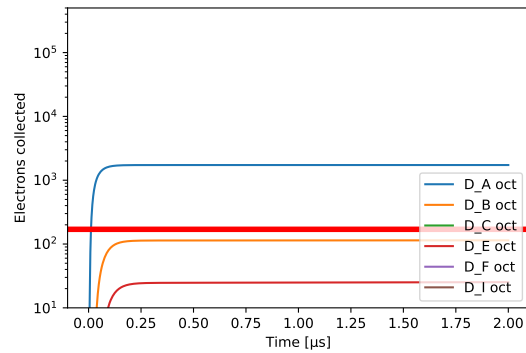
(a) 1.28×10^{-5} $pC/\mu m$.
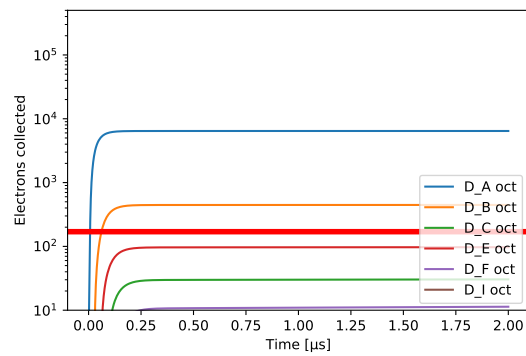
(b) 4.8×10^{-5} $pC/\mu m$.

(c) 1.8×10^{-4} $pC/\mu m$.

Figure 4.41: Charge collected by different electrodes for the different LET in 25 μm thick epitaxial layer for particle hitting between four electrodes.
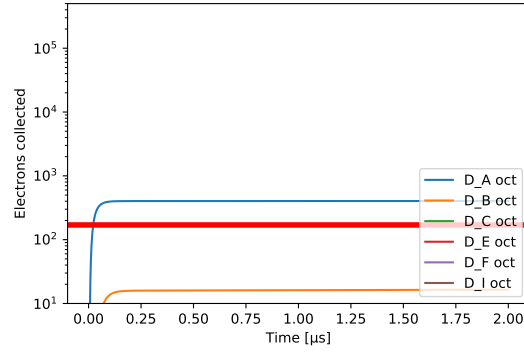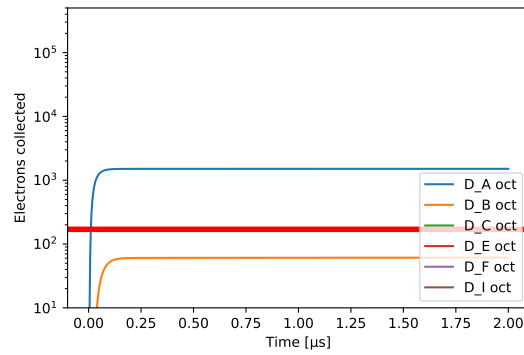
(a) 1.28×10^{-5} $pC/\mu m$.

(b) 4.8×10^{-5} $pC/\mu m$.
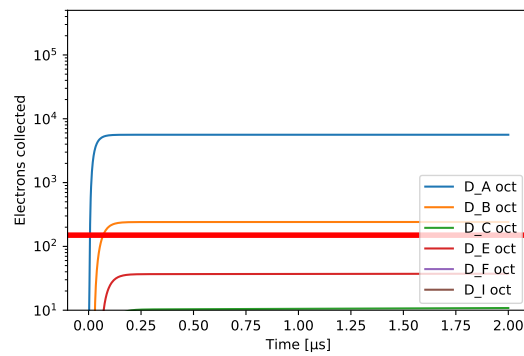
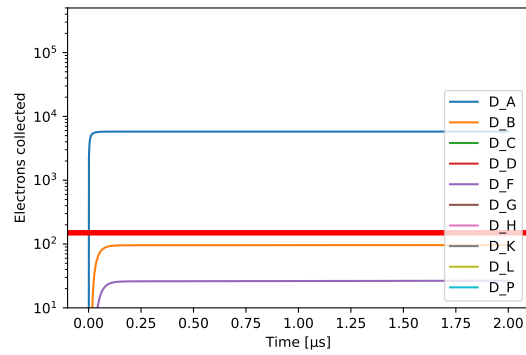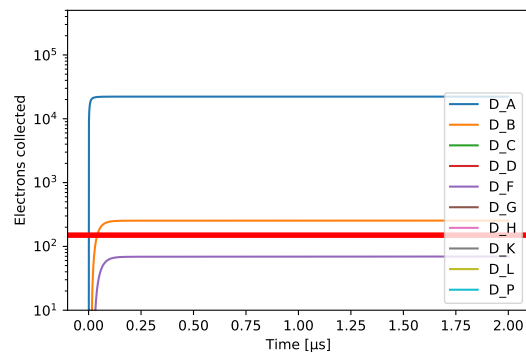**(c)** 1.8×10^{-4} $pC/\mu m$.

Figure 4.42: Charge collected by different electrodes for the different LET in 20 μm thick epitaxial layer for particle hitting between four electrodes.

LET	Minimal CS	Maximal CS
$[pC/\mu m]$	[pixel]	[pixel]
1.28×10^{-5}	4	4
4.8×10^{-5}	4	12
1.8×10^{-4}	16	16

(a) 30 μm epitaxial

LET	Minimal CS	Maximal CS
$[pC/\mu m]$	[pixel]	[pixel]
1.28×10^{-5}	4	4
4.8×10^{-5}	4	4
1.8×10^{-4}	12	12

(b) 25 μm epitaxial

LET	Minimal CS	Maximal CS
$[pC/\mu m]$	[pixel]	[pixel]
1.28×10^{-5}	4	4
4.8×10^{-5}	4	4
1.8×10^{-4}	12	12

(c) 20 μm epitaxial

Table 4.16: Cluster size for particle hitting between 4 electrodes with different LET.
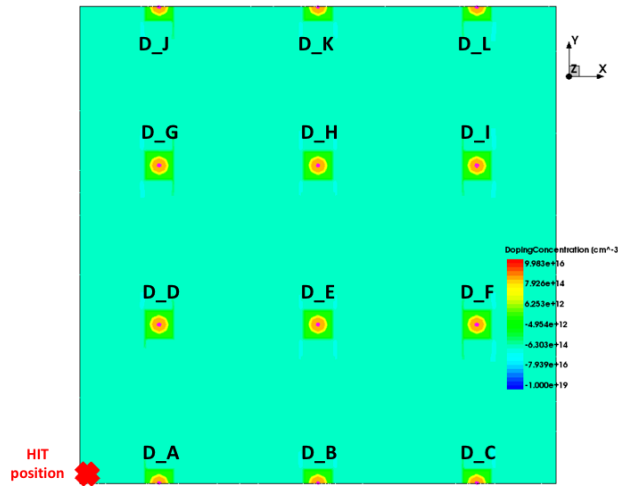
Figure 4.43: Simulation domain.

Electrode	X [μm]	Y [μm]	Distance [μm]	Shape factor
D_A	14	0	14	2
D_B	42	0	42	2
D_C	70	0	70	2
D_D	14	28	31.3	1
D_E	42	28	50.5	1
D_F	70	28	75.4	1
D_G	14	56	57.7	1
D_H	42	56	70	1
D_I	70	56	89.6	1
D_J	14	84	85.2	2
D_K	42	84	93.9	2
D_L	70	84	109.3	2

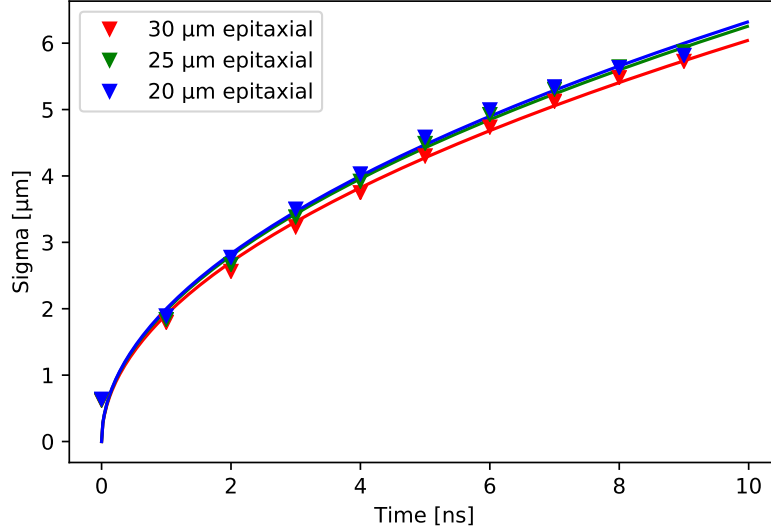**Table 4.17:** Electrode position with respect to the hit and shape factor.
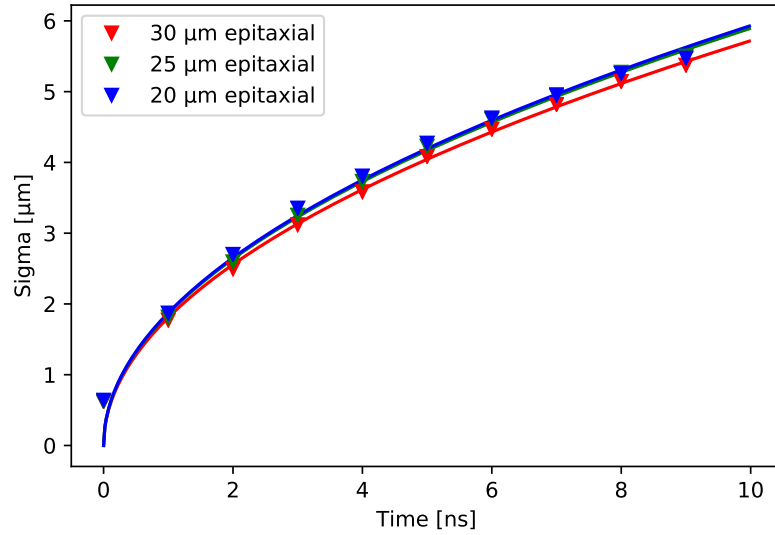
Figure 4.44: Evolution of σ of the electron density distribution over time during the first 10 ns after charge generation.

The values are lower than the limit of 36 cm^2/s.

Cluster size calculation

Charge collection curves for all the electrodes are shown in figures 4.45, 4.46 and 4.47.

LET $[pC/\mu m]$	Minimal CS [pixel]	Maximal CS [pixel]
1.28×10^{-5}	2	6
4.8×10^{-5}	12	12
1.8×10^{-4}	16	16

(a) 30 μm epitaxial

LET $[pC/\mu m]$	Minimal CS [pixel]	Maximal CS [pixel]
1.28×10^{-5}	2	2
4.8×10^{-5}	6	6
1.8×10^{-4}	12	12

(b) 25 μm epitaxial

LET $[pC/\mu m]$	Minimal CS [pixel]	Maximal CS [pixel]
1.28×10^{-5}	2	2
4.8×10^{-5}	6	6
1.8×10^{-4}	6	12

(c) 20 μm epitaxial

Table 4.18: Cluster sizefor particle hitting between two electrodes with different LET.

The results are reported in tables 4.14a, 4.18b and 4.18c.

4.6.5 Simulation results comparison

Table 4.19 reports the cluster sizes computed for the configurations described in the previous sections. In figure 4.48 the logarithm of the charge collected by electrodes as a function of the distance from the hit position is plotted for the three simulations. The analysis is carried on for the LET=1.8×10^{-4} $pC/\mu m$ case.

It is clear that the points related to the simulations in which the particle does not cross the electrode are comparable. In contrast, the amount of charge collected at the same distance when the particle hits the electrode is significantly smaller than in the other cases.

Data from the same simulation follow an identifiable trend, but some points. The corresponding electrodes are located on the boundary of the domain sim-
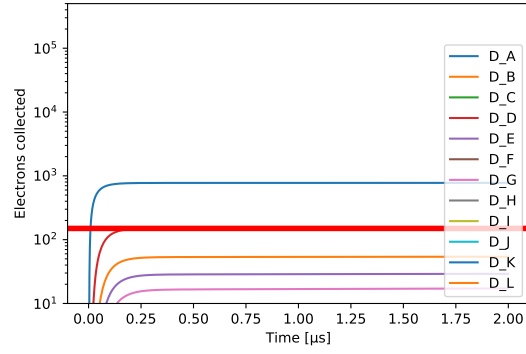
(a) 1.28×10^{-5} $pC/\mu m$.
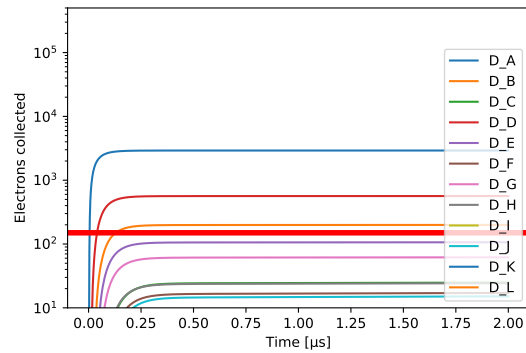
(b) 4.8×10^{-5} $pC/\mu m$.
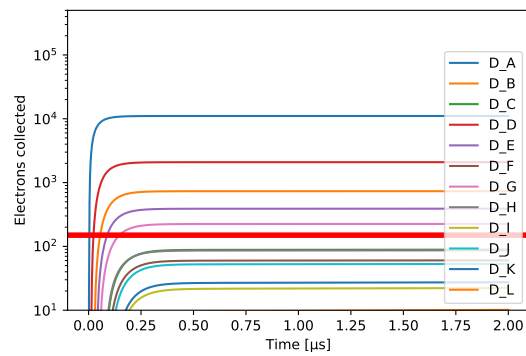
(c) 1.8×10^{-4} $pC/\mu m$.

Figure 4.45: Charge collected by different electrodes for the different LET in 30 μm thick epitaxial layer for particle hitting between two electrodes.
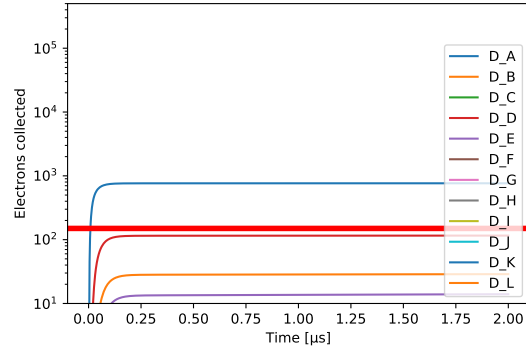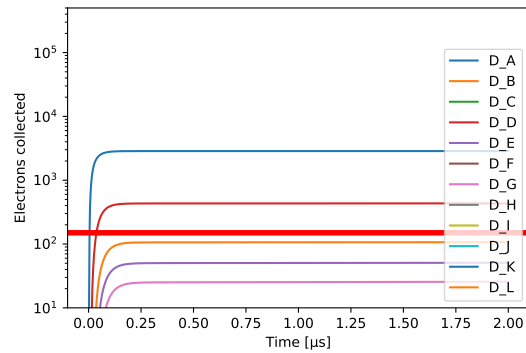
(a) $1.28 \times 10^{-5} \ pC/\mu m$.
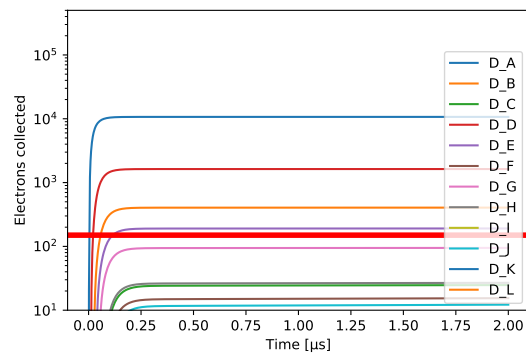
(b) $4.8 \times 10^{-5} \ pC/\mu m$.

(c) $1.8 \times 10^{-4} \ pC/\mu m$.

Figure 4.46: Charge collected by different electrodes for the different LET in 25 μm thick epitaxial layer for particle hitting between two electrodes.
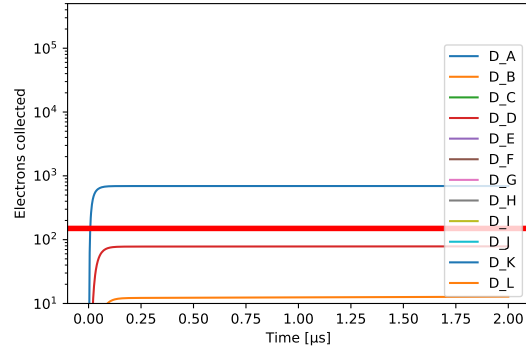
(a) 1.28×10^{-5} $pC/\mu m$.
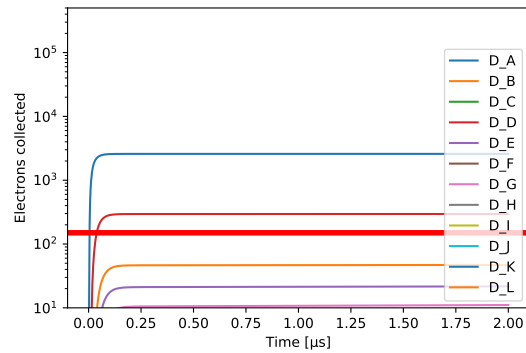
(b) 4.8×10^{-5} $pC/\mu m$.
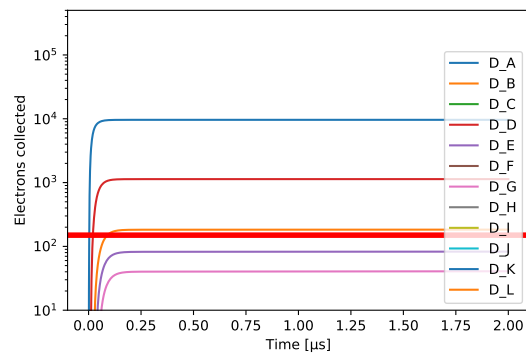
(c) 1.8×10^{-4} $pC/\mu m$.

Figure 4.47: Charge collected by different electrodes for the different LET in 20 μm thick epitaxial layer for particle hitting between two electrodes.

| Configuration	LET [$pC/\mu m$]	Thickness [μm]	Minimal CS	Maximal CS
Hit on electrode	$1.8{\times}10^{-4}$	30	9	13
Hit on electrode	$1.8{\times}10^{-4}$	25	9	9
Hit on electrode	$1.8{\times}10^{-4}$	20	9	9
Hit on electrode	$4.8{\times}10^{-5}$	30	5	9
Hit on electrode	$4.8{\times}10^{-5}$	25	5	5
Hit on electrode	$4.8{\times}10^{-5}$	20	5	5
Hit on electrode	$1.28{\times}10^{-5}$	30	1	5
Hit on electrode	$1.28{\times}10^{-5}$	25	1	1
Hit on electrode	$1.28{\times}10^{-5}$	20	1	1
Hit between 4 electrodes	$1.8{\times}10^{-4}$	30	16	16
Hit between 4 electrodes	$1.8{\times}10^{-4}$	25	12	12
Hit between 4 electrodes	$1.8{\times}10^{-4}$	20	12	12
Hit between 4 electrodes	$4.8{\times}10^{-5}$	30	4	12
Hit between 4 electrodes	$4.8{\times}10^{-5}$	25	4	4
Hit between 4 electrodes	$4.8{\times}10^{-5}$	20	4	4
Hit between 4 electrodes	$1.28{\times}10^{-5}$	30	4	4
Hit between 4 electrodes	$1.28{\times}10^{-5}$	25	4	4
Hit between 4 electrodes	$1.28{\times}10^{-5}$	20	4	4
Hit between 2 electrodes	$1.8{\times}10^{-4}$	30	16	16
Hit between 2 electrodes	$1.8{\times}10^{-4}$	25	12	12
Hit between 2 electrodes	$1.8{\times}10^{-4}$	20	6	12
Hit between 2 electrodes	$4.8{\times}10^{-5}$	30	12	12
Hit between 2 electrodes	$4.8{\times}10^{-5}$	25	6	6
Hit between 2 electrodes	$4.8{\times}10^{-5}$	20	6	6
Hit between 2 electrodes	$1.28{\times}10^{-5}$	30	2	6
Hit between 2 electrodes	$1.28{\times}10^{-5}$	25	2	2
Hit between 2 electrodes	$1.28{\times}10^{-5}$	20	2	2

Table 4.19: Summary of cluster size obtained with all the configurations of TCAD simulation.
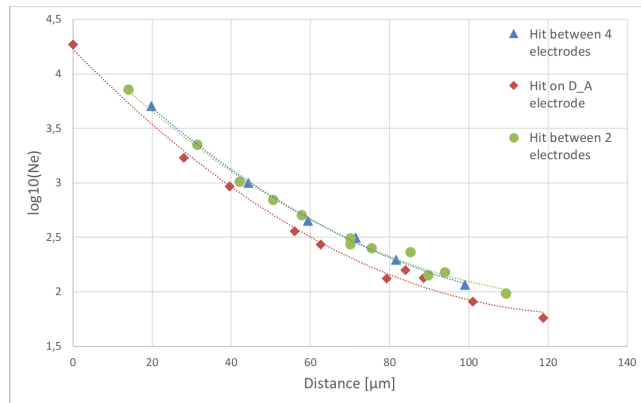
(a) 30 μm
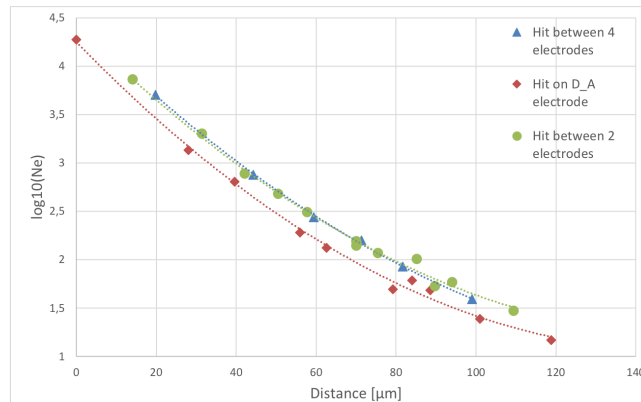
(b) 25 μm
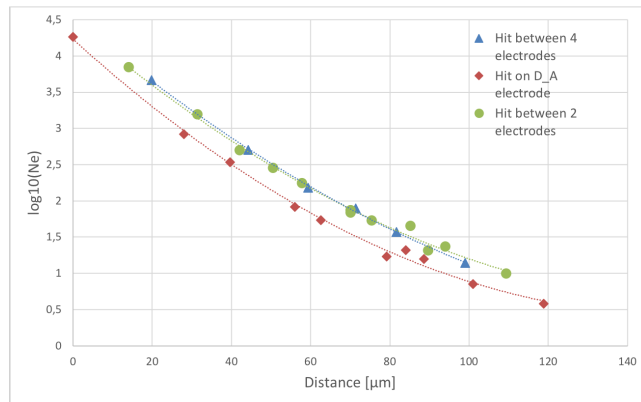
(c) 20 μm

Figure 4.48: Charge collected by electrodes for the different configurations and different epitaxial thicknesses with 1.8×10^{-4} $pC/\mu m$.

ulation, affected by discontinuity effects. This hypothesis is supported by the fact there are not misbehaving electrodes in the simulation without electrodes on the boundary.

To understand the different behaviour of the simulations, it is possible to compare the fraction of charge collected by the first neighbour electrodes for the three cases. When the particle hits the electrode directly, the first neighbour is D_A itself (figure 4.33a). When the hit is in the middle between four electrodes, the first neighbours are four replicas of D_A (figure 4.38). In the third case, the first neighbours are two replicas of D_A (figure 4.43).

The value must be normalised to the charge collected by the whole domain taken into account. There are two possibilities: (i) sum up the contributions from all the electrodes, properly scaled for the shape factors and the number of repetition on the domain, (ii) to calculate it from LET.

Thickness [μm]	Electrons calculated	Hit on electrode	Hit between 4	Hit between 2
30	34000	34700	35300	35400
25	28000	29300	30000	30100
20	22500	23600	24700	24700

Table 4.20: Expected number of electrons calculated from LET and thickness is compared with the total number of electrons collected in the different simulation configurations.

Values calculated with the two methods are slightly different. The sum of charges collected by electrodes is about 1% higher than expected, as reported in table 4.20. The effect could depend on the error induced by the mesh. A second possible explanation is the contributions from charges generated on the substrate that may cross the potential barrier in the region of the hit.

In table 4.21, the fraction of charge collected by one of the first neighbour electrodes is reported. The case reported on the first row shows that when particle impinges on the electrode, D_A collects the most of the charge.

Simulation	Fraction of charge 30 μm	Fraction of charge 25 μm	Fraction of charge 20 μm
Hit on D_A	54%	64%	76%
Hit between 4	15%	17%	19%
Hit between 2	21%	25%	29%

Table 4.21: Charge collected by the set of first neighbour electrode with respect to the charge produced by interaction.

To explain the observations, it is interesting to look at the electric field calculated from the simulation and reported in figure 4.49, where the colour scale represents the z component of the field and the arrows the direction of the total field. It is possible to separate two regions. The first one starts on the detector surface and extends for about 15 μm. The field is different in the region immediately below the n-well and on the other regions of pixel. When a particle
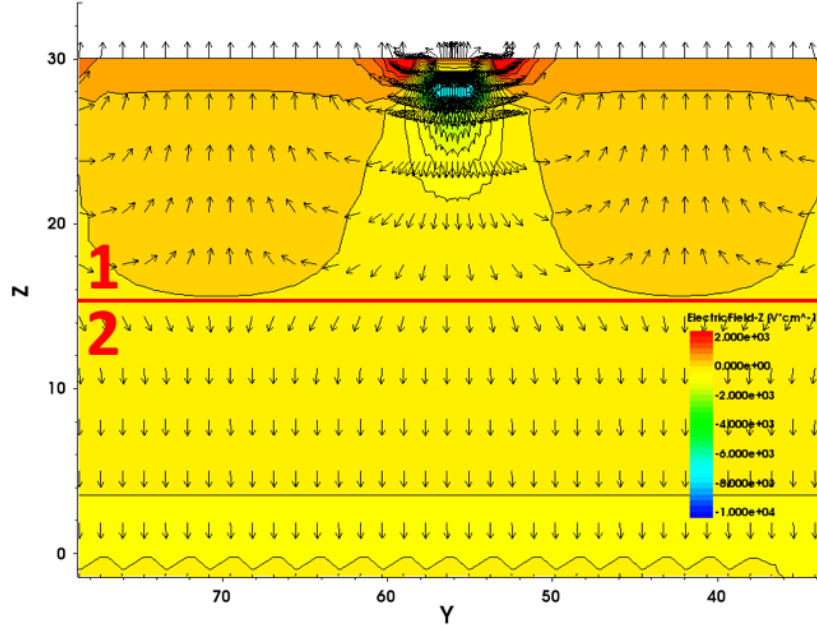
Figure 4.49: Electric field on detector epitaxial layer. Colour scale represents the electric field component along z-axis; the arrows report the direction of the total electric field. The density of arrows depends on the field intensity on the different regions.

hits the collection electrode, the electrode collects most of the charge produced by the interaction, because the charge is trapped. If the charge is generated far from the electrode, it can diffuse and is shared by several electrodes.

A second region runs from about 15 μm from the detector surface to the end of the epitaxial. In this region the charge diffuses almost freely independently of the hit position.

In figure 4.49 the field is shown for 30 μm thick epitaxial layer. However, since the geometry of the detector surface, the applied voltages and the doping are the same for all the thicknesses, the only thing that changes is the thickness of the region of free diffusion, labelled as region two in the figure.

This assumption is supported by the fact that the fraction of charge collected by the first electrode with respect to the total amount of deposited charge is inversely proportional to the epitaxial thickness, as shown in table 4.21. The ratio between thicknesses of region one and two increases when the total thickness decreases.
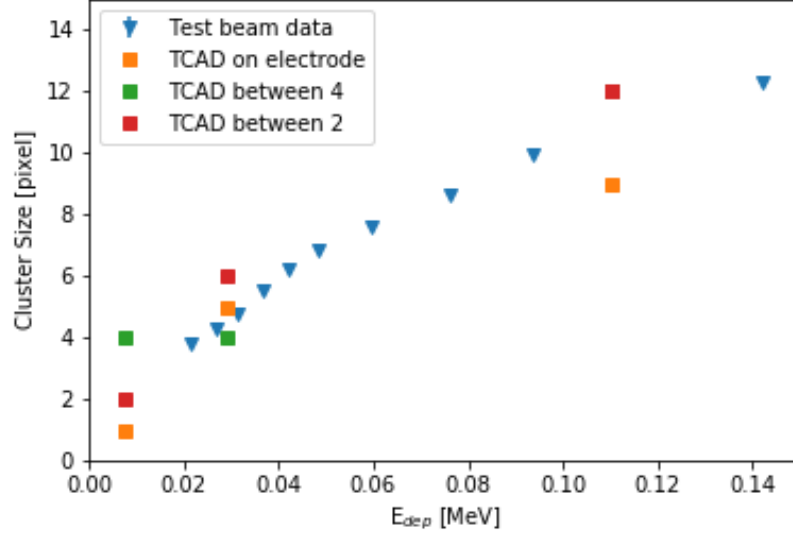
Figure 4.50: Cluster size measured with protons and calculated from TCAD simulation with 25 μm thick epitaxial layer. The results are reported as a function of the energy deposited in silicon.

4.6.6 Comparison between TCAD results and experimental data

A good check to test the quality of the TCAD simulation is to compare the values of cluster size obtained with the data collected during the test beam with protons (see table 4.6). From the inclined tracks, the thickness of the epitaxial layer is evaluated to be about 27.1 μm. The closest simulation is the 25 μm epitaxial layer, whose results will be used in the comparison.

To compare the results, the cluster size is reported as a function of the energy deposited on ALPIDE, calculated from GEANT4 simulation. The conversion of LET into energy deposited is calculated as:

$$E_{dep} = \frac{LET \times T \times 3.6eV}{e}$$

where T is the epitaxial thickness and e is the electron charge. 3.6 eV is the average energy required to produce an electron-hole pair in silicon [36]. Data are shown in figure 4.50.

Results reported in figure 4.36 are very good, as TCAD predictions bracket the experimental data, as expected. In fact, the impact point is uniformly distributed in data and the average cluster size for a given deposited energy must lay between the minimum and the maximum, which are determined by

the impact position. The result is even more remarkable when the following three aspects are considered:

- a unique TCAD threshold is used to compare with data, where thresholds are distributed around a certain value (see section 4.6.2 and following);

- the TCAD calculation is taken as it is, i.e. no smearing is introduced to account for fluctuations in charge diffusion, collection and pre-amplification;

- the order of cluster sizes for the different positions of the hit change as expected. For instance, the on-electrode CS for MIPs is lower than the infra-electrode CS: this is due to the geometry of clusters, i.e. the first and fourth row of table 4.3. For Edep=30 keV, instead, on-electrode CS is higher than the infra-electrode CS, repsectively 3rd and 2nd row of table 4.3.

Chapter 5

Future developments of MAPS detector

This chapter gives a short overview of some of the most promising detectors that are currently under development.

5.1 MIMOSIS

A direct evolution of ALPIDE is MIMOSIS detector, under development for the Micro Vertex Detector (MVD) of Compressed Baryonic Matter (CMB) experiment at GSI [46]. The application has radiation hardness and timing requirements different with respect to ALPIDE. Optimisation of the technology is ongoing to realise a depleted detector and to move the readout logic from a triggered system to a continuous framing.

The detector is realised using the same 180 nm Towejazz technology, the same of ALPIDE. The in-pixel amplifier-shaper-discriminator system and the double column structure is the same of ALPIDE. The trigger logic is removed and substituted with sample-and-hold system ruled by a tunable global shutter signal, with a default value of 5 μs [40].

In the prototype, both AC and DC coupled pixels are realised. In the AC coupled version the amplifier is protected from the depletion voltage using a capacitor. In this way it is possible to apply higher voltages to the buffer to deplete the detector. This approach is compatible with the "modified" 180 nm TowerJazz process, designed to allow depletion of the detectors.

The readout structure is based on the readout of the columns via a priority encoder that collects data from two columns at a frequency of 20 MHz. The maximum number of pixel that can be recorded in a double-column is limited by the number of clock cycles between two frames. Double columns are grouped on regions of eight and connected to the same memory buffer 100 words deep. The buffer adds a region header to reduce the bit number used to code the information. Four regions are collected in a "super regions" with a buffer depth
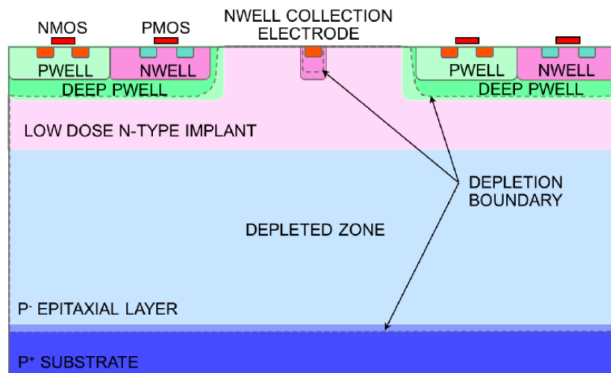
Figure 5.1: TJ MALTA pixel cross section [49].

of 256 words. The transmission is driven by a 32-bit priority encoder working at 40 MHz. The data are then stored in a central elastic buffer suited to process a maximum of 3200 words in 5 μs and a depth of 16384 words. The buffer can store up to five events that are then sent out using eight 320 $Mbps$ buffers to reach the downlink speed required. In the case of lower data flux, it is possible to reduce the number of channels to save power.

The first prototype, MIMOSIS-0, has been realised in 2018 and tested. The amplification chain has been tested using in-pixel pulse injector signals. The noise level is found with a procedure close to the ALPIDE threshold scan test fixing a threshold level. It is compatible with the values obtained for ALPIDE, between 10 and 20 electrons for different pixel configurations.

A first full-scale prototype has been submitted in 2019. If the full-scale prototype will have the same performance of the prototype, it will be a solid alternative to ALPIDE, improving the radiation hardness (from the 10^{13} n_{eq} to 10^{15} n_{eq} from the test) and the readout speed.

5.2   TJ MALTA

ATLAS experiment is investigating Depleted MAPS for the outermost pixel layers of Phase-II upgrade of the Inner Tracker detector (ITk). Requirements of radiation hardness and timing are more challenging than for ALICE and lead to some interesting design modification. The detector radiation tolerance is at least 10^{15} n_{eq}/cm^2 for non-ionising energy dose and 80 $MRad$ of the total dose. The timing resolution required is 25 ns for a hit rate up to 10 MHz/cm^2.

Two different large-scale prototypes have been realised, TJ Monopix and TJ MALTA. Among the two, MALTA has the most innovative readout system. It is realised in TowerJazz 180 nm imaging CMOS technology and processed to allow depletion of the sensitive region.

The matrix has 512×512 pixels with a pitch of 36.4 μm, each equipped with

a small collection diode ($\sim 2~\mu m$ electrodes, with a capacitance $<5~pF$) and a full readout modelled on the ALPIDE in-pixel circuitry. A low-doped n-type layer is inserted under the deep p-well that hosts the circuitry to allow the full depletion of the detector, as shown in figure 5.1. The epitaxial layer is about 25 μm thick and highly resistive ($>1~k\Omega cm$).

The readout is organised in double columns organised in 2×8 pixels groups sharing the same address, transmitting the hit position to the periphery via a parallel data bus. Signals have an adjustable duration from 0.5 to 2 ns and a maximal latency of 8 ns for propagation. The end of the column merges the information on a common data bus controlled by an arbitration circuit. The final 40-bit world containing hit position, column address, timestamp and hit merger delay is transmitted off-detector on a parallel port using LVDS drivers, proved to work up to 5 Gb/s [49]. The power consumption of the sensor is about 80 mW/cm^2.

The prototypes have been tested for noise and threshold using charge pulse injection. Due to some limits of the control circuitry, the masking function was not enabled. A high threshold is set to reduce the impact of noisy pixels. The price of this setting is a reduced detection efficiency, 96% on average before the irradiation and 74% after the irradiation. Inefficiencies were located at the corner of the pixels. The noise levels also result higher than expected from the simulation.

Two approaches have been proposed to correct the inefficiencies, due also to the large pixel dimensions with respect to the collection diode. They will be tested in future prototypes: an additional p-type implant at the pixel corner or a gap on n layer. From TCAD simulations, the effects are comparable.

If the development of TJ MALTA will solve the problems described, general-purpose experiments at LHC, and in particular ATLAS and CMS, will be able to use MAPS for the first time.

5.3   MuPix

The MuPix detectors are under development to fulfil the requirements of Mu3e experiment at PSI, aimed to search for lepton flavour violation [28].

The experiment requires an ultra-thin tracker capable of working in high rate conditions. HV-CMOS is an elective choice because it combines drift charge collection and integrated readout, that provide a fast readout with an excellent fill factor.

After a series of small prototypes, the first large-scale device realised is MuPix8. It consists of a 128×200 pixel matrix realised in AMS aH18 technology. The prototype is $10.8 \times 19.5~mm^2$, half of the full-scale desired detector, that will be about $20 \times 20~mm^2$. The pixel pitch is $81 \times 80~\mu m^2$ [22].

The readout structure is divided into three blocks. The first block is inside the pixel and consists of the test pulse injector, the amplification and a line driver. Each pixel is connected point-to-point to its periphery, in which the signal is discriminated and the hit flag stored with a 10-bit timestamp and a

second 6-bit word to measure the impulse length and reduce time jitter. A state machine then reads the information with a priority encoder scheme and transmitted to LVDS output ports.

In this prototype, the columns reach the dimension of the final design. From the previous version, problems related to cross-talk between pixels were reported, because of the large number of point-to-point connections. In this case, the number of lines increases, as well as the cross talk. A new current-based transmission scheme is implemented and tested in two of the three regions of the matrix to reduce the effects.

Correction of the timestamp of the events using the pulse height measure reduces the problem of time jitter. Three different methods are explored: time-over-threshold with a constant threshold, time-over-threshold with a voltage ramp as a threshold and a second method that implements two threshold levels. The first is set close to the signal baseline to sample the startup, and a second higher threshold to discriminate signal from noise [22].

The prototype is still under characterisation. From the study of the results obtained from the different tests, the best configuration for the full-scale future device will be selected and realised.

The project is in its early stages, but if the performance will fulfil the expectations, it will be a valid alternative to TJ MALTA.

5.4 JadePix

In the framework of the R&D of the Circular Electron Positron Collider (CEPC), the development of a JadePix family started, and the first prototype, JadePix-1, has been delivered and charcterised before and after irradiation.

The conceptual design is close to the ALPIDE approach, with the readout implanted on a deep p-well on the surface of the wafer. As ALPIDE, the detector is realised on 180 nm CMOS process and it is operated without depletion [35].

The prototype is 7.9×3.9 mm^2 and contains two matrices, one with 33×33 μm^2 pixels, the other with 16×16 μm^2 pixels. Matrices are further divided in 20 sections to explore different geometries of electrodes. Each sector can be read autonomously in rolling shutter mode. The integration time depends on the clock frequency and set to 24 μs.

The data collected with ^{55}Fe source provides a measurement of the gain of the detector. The analysis focuses on the single pixel clusters, that collect almost all the charge of the event. From the peaks produced by K_α and K_β, whose energies are known, it is possible to calculate the conversion from energy to ADC counts.

The spatial resolution has been evaluated from measurements acquired at DESY with 4.4 GeV electron beam. The device is inserted on a EUDET telescope, that allows to reconstruct the tracks of incoming particles. From the analysis, the resolution is 5 μm for 33×33 μm^2 pixels and 3.5 μm for 16×16 μm^2 pixels.
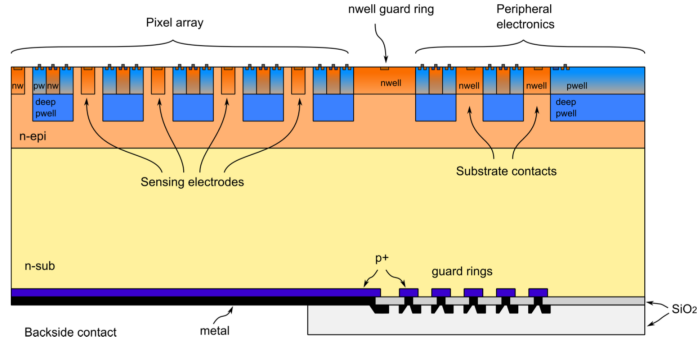
Figure 5.2: SEED main characteristics [64].

The characterisations of the prototypes are the references for the future developments of future devices.

5.5 ARCADIA

Requirements	
Pixel pitch $[\mu m]$	20 - 25
Thickness $[\mu m]$	50 - 100
Scalability $[cm]$	Up to $\sim 4 \times 4$
Hit rate $[MHz/cm^2]$	10 to 100
Timing resolution $[ns]$	10
Power consumption $[mW/cm^2]$	<20
Radiation hardness $[Mrad]$	1

Table 5.1: ARCADIA requirements.

ARCADIA (Advanced Readout CMOS Architecture with Depleted Integrated sensor Arrays) is an R&D project aimed to realise a full-scale prototype of a MAPS detector.

The development of the detector is experiment independent, and the collaboration has three main lines that drive the development. Together with the requirements of space applications, the other two driving interests are medical application, for which a fast timing and low voltages are mandatory, and future colliders, that require a high radiation hardness and an improved spatial resolution. The goal requirements set by the collaboration are in table 5.1.

For both space applications and future colliders, the scalability is another crucial aspect, to allow a simplified readout of large surfaces detectors. The two share the same interest also in power consumption reduction since the surface of detectors for collider experiments is usually huge.

The sensor of ARCADIA is based on the development carried out by SEED project, aimed to develop a innovative technology and realise a small scale prototype.

The prototype is realised on an n-doped substrate. A negative voltage applied to a p+ backside electrode provides full depletion, as shown in figure 5.2. A deep p-well is implanted on the top of the detector to avoid pMOS transistors competition with collection n-type electrodes, as seen for ALPIDE.

A thin p-type epitaxial layer with a resistivity lower than the substrate is inserted on the top of the n-substrate to gain better control of the electric potential. The accurate tuning of the doping profiles and the different characteristics of the substrate allows to polarise the collection electrode with a small voltage, about 1 V. This allows the implementation of a readout electronic readout based on 1.2 V MOS transistors [64].

The requirement of a fully depleted detector implies the application of a back bias widely higher than the values eventually applied to ALPIDE. The actual value required depends on the thickness of the detector. However, it is in general higher than 200 V. With these values implied, and it is important to avoid early breakdown, that depends on the quality of backside processing, in particular on the interface between the silicon surface and the deposited passivation layer.

In the first production, among the test structures produced, a set of samples was devoted to the investigation on the number of guard rings required to control the breakdown. It resulted that a small number of floating rings is enough to ensure a full depletion of all the investigated thicknesses.

The prototypes realised have an area of 2×2 mm^2 and have a pixel pitch of 50 μm. The matrix, containing 24×24 pixels, is the staring point to design and test performance of the new technological concept. The prototype has been named MATISSE (Monolithic AcTIve pixel SenSor Electronics) [63] and has been tested with both laser and radioactive sources to evaluate if the real performance is compatible with the expectations given by simulations.

The agreement resulted very good for the most interesting features, such as the power consumption, the linearity of the charge injection with respect to the voltage and the gain, studied using a source of ^{55}Fe [63].

The readout of ARCADIA is not defined yet. It will be fabricated at LFoundry in 110 nm technology. The strong requirements for power consumption reduction drive to the research of innovative solutions to reach the goals of the collaboration.

The ARCADIA is the only detector under development that has a work package devoted to the spatialisation of the detector. I am a member of the team dedicated to this task.

Conclusions

This thesis reports the activities carried out in Trento to prepare the first use ever of MAPS detectors for a space experiments. In space, silicon detectors with pixel geometry have never been used before, and monolithic readout has never been tested, even for microstrip geometry. In this sense, the activity is doubly innovative.

If successful, the project will enter the operation phase at the same time when thousands ALPIDE will be hit by particles from interactions produced at the LHC. Such a time coincidence is remarkable, because ground-established technologies usually need 10-20 years to be ready for space usage.

Critical points of microstrip affecting the use for future applications in space are the following:

1. Microstrip (double and single side) are fabricated on dedicated infrastructures, that are not easy to find because of the high costs/profits ratio charged on the industries because of the small market.

2. Microstrip technology is reaching the limits of its development. Decreasing the strip pitch below 50 μm causes problems of capacitive coupling between the strips and on metallisation.

3. The on-line management of microstrip detector data (zero-suppression, common noise reduction, cluster selection) on flight requires on-board intelligence that costs in terms of men power, power consumption and readout speed.

On the other hand, the microstrip detector technology is mature, fully optimised for space and with low power consumption.

Main advantages of current MAPS technology are the following:

1. They are realised with standard CMOS processes in big industrial facilities. Sharing the infrastructures with large-scale industrial projects ensures continuous updates of technology and reduces the production costs. For example, detector released in 2010 (MIMOSA-26 and MIMOSA-28) were realised in 350 nm technology, wheras detectors currently under development (ARCADIA) are realised in 110 nm. In ten years the improvement is a factor 3.

2. The development is driven by an active community, currently proposing a large number of different designs for MAPS has been designed and developed: the total depletion of the silicon and fast electronic implementation are just two of aspects of the development, together with the reduction of pixel pitch.

3. The integrated electronics and binary output allow to immediately use the data from the tracker, with no need of dedicated front-end electronics, complex and power consuming algorithms.

4. The detector thickness is a factor 6 lower than standard silicon detector. The small thickness reduces the material budget and increases the tracking performance.

In 2017, the author, together with the AstroParticle Physics (APP) group of Università di Trento, formulated the first proposal for the use of the MAPS ALPIDE for the tracker of HEPD-02 payload, hosted by the CSES-02 mission. After the first proposal, an intense program of tests, design, development and space qualification that involved also other groups (Torino and Firenze) started. This program allowed to choose the MAPS technology for the realisation of HEPD-02 tracker, that is expected to be launched in 2022. The active area of the tracker will be about 700 cm^2.

This work reports the results of tests and space qualification carried out between 2017 and 2019. The response of the ALPIDE to low energy nuclei and electrons has been characterised ex-novo. Being designed for ALICE ITS, the response to MIPs was fully characterised, but the study of interaction with particle in the MeV energy range was not explored. The characterisation has been performed out using a single sensor setup, tested with particle beams at different facilities in Italy. In parallel with the experimental work, a semi-analytical model to foresee the cluster dimension has been developed. The model will be the basis of the future event reconstruction software. For the aspects connected to space qualification and system sizing, an ALICE OB stave, opportunely modified, has been used as engineering model of HEPD-02 tracker stave. The module passed vibration and thermal-vacuum tests and allowed to estimate the power consumption of the tracker. The same module is currently the bench test for the development of the firmware devoted to control and management of the apparatus.

The work reported in this thesis stimulated important developments on MAPS use for space applications. As detailed in chapter 5, the ARCADIA project aims to realise a multi-purpose HV-CMOS MAPS prototype. Particle detection in space is included among the specific applications taken into account during the development, with a particular attention on power consumption reduction. The ARCADIA team[1], as well as the astroparticle physics community,

---

[1]The author is a member of the "space applications" workpackage of the ARCADIA project.

look forward the completion of the HEPD-02 project that must be regarded as milestone on the passage from silicon microstrip detectors to pixel for tracking particles in space.

Bibliography

[1] sklearn.base API Reference. https://scikit-learn.org/stable/modules/classes.html. Accessed: 2019-11-29.

[2] TCAD. https://www.synopsys.com/silicon/tcad.html. Accessed: 2019-08-2.

[3] AA Abdo, BT Allen, T Aune, D Berley, S Casanova, C Chen, BL Dingus, RW Ellsworth, L Fleysher, Roman Fleysher, et al. The large-scale cosmic-ray anisotropy as observed with Milagro. *The Astrophysical Journal*, 698(2):2121, 2009. doi:https://doi.org/10.1088/0004-637X/698/2/2121.

[4] Betty Abelev, J Adam, D Adamova, MM Aggarwal, G Aglieri Rinella, M Agnello, A Agostinelli, N Agrawal, Z Ahammed, N Ahmad, et al. Technical design report for the upgrade of the ALICE inner tracking system. *Journal of Physics G: Nuclear and Particle Physics*, 41(8):087002, 2014. doi:https://doi.org/10.1088/0954-3899/41/8/087002.

[5] O Adriani, L Bonechi, M Bongi, G Castellini, R D'Alessandro, A Gabbanini, M Grandi, P Papini, SB Ricciarini, P Spillantini, et al. The magnetic spectrometer of the PAMELA satellite experiment. *Nuclear Instruments and Methods in Physics Research Section A: Accelerators, Spectrometers, Detectors and Associated Equipment*, 511(1-2):72–75, 2003. doi:https://doi.org/10.1016/S0168-9002(03)01754-6.

[6] Oscar Adriani, GC Barbarino, GA Bazilevskaya, R Bellotti, Mirko Boezio, EA Bogomolov, L Bonechi, M Bongi, Valter Bonvicini, S Bottai, et al. An anomalous positron abundance in cosmic rays with energies 1.5–100 GeV. *Nature*, 458(7238):607, 2009. doi:https://doi.org/10.1038/nature07942.

[7] Gianluca Aglieri Rinella. Overview of the ALPIDE pixel sensor chip with focus on readout features. https://indico.cern.ch/event/666016/contributions/2722251/attachments/1523408/2380925/20170914-ALPIDE-FoCal-Study-Aglieri.pdf.

[8] M Aguilar, J Alcaraz, J Allaby, B Alpat, G Ambrosi, H Anderhub, L Ao, A Arefiev, P Azzarello, E Babucci, et al. The Alpha Magnetic Spectrometer (AMS) on the International Space Station: Part I–results from the test flight on the space shuttle. *Physics Reports*, 366(6):331–405, 2002. doi: https://doi.org/10.1016/S0370-1573(02)00013-3.

[9] M Aguilar, J Alcaraz, J Allaby, B Alpat, G Ambrosi, H Anderhub, L Ao, A Arefiev, P Azzarello, Luca Baldini, et al. Cosmic-ray positron fraction measurement from 1 to 30 GeV with AMS-01. *Physics Letters B*, 646(4):145–154, 2007. doi:https://doi.org/10.1016/j.physletb.2007.01.024.

[10] M Aguilar, L Ali Cavasonza, B Alpat, G Ambrosi, L Arruda, N Attig, S Aupetit, P Azzarello, A Bachlechner, F Barao, et al. Antiproton flux, antiproton-to-proton flux ratio, and properties of elementary particle fluxes in primary cosmic rays measured with the Alpha Magnetic Spectrometer on the International Space Station. *Physical Review Letters*, 117(9):091103, 2016. doi:https://doi.org/10.1103/PhysRevLett.117.091103.

[11] M Aguilar, L Ali Cavasonza, B Alpat, G Ambrosi, L Arruda, N Attig, P Azzarello, A Bachlechner, F Barao, A Barrau, et al. Towards understanding the origin of cosmic-ray electrons. *Physical review letters*, 122(10):101101, 2019. doi:https://doi.org/10.1103/PhysRevLett.122.101101.

[12] M Aguilar, L Ali Cavasonza, G Ambrosi, L Arruda, N Attig, P Azzarello, A Bachlechner, F Barao, A Barrau, L Barrin, et al. Towards understanding the origin of cosmic-ray positrons. *Physical review letters*, 122(4):041102, 2019. doi:https://doi.org/10.1103/PhysRevLett.122.041102.

[13] J Alcaraz, B Alpat, G Ambrosi, Ph Azzarello, R Battiston, B Bertucci, J Bolmont, M Bourquin, WJ Burger, M Capell, et al. The Alpha Magnetic Spectrometer silicon tracker: Performance results with protons and helium nuclei. *Nuclear Instruments and Methods in Physics Research Section A: Accelerators, Spectrometers, Detectors and Associated Equipment*, 593(3):376–398, 2008. doi:https://doi.org/10.1016/j.nima.2008.05.015.

[14] ITS ALICE. ALPIDE-3 operations manual. 2016.

[15] Giovanni Ambrosi, Simona Bartocci, Laurent Basara, Roberto Battiston, William J Burger, Luca Carfora, Guido Castellini, Piero Cipollone, Livio Conti, Andrea Contin, et al. The HEPD particle detector of the CSES satellite mission for investigating seismo-associated perturbations of the Van Allen belts. *Science China Technological Sciences*, 61(5):643–652, 2018. doi:https://doi.org/10.1007/s11431-018-9234-9.

[16] M Amenomori, S Ayabe, XJ Bi, D Chen, SW Cui, LK Ding, XH Ding, CF Feng, Zhaoyang Feng, ZY Feng, et al. Anisotropy and corotation of

galactic cosmic rays. *Science*, 314(5798):439–443, 2006. `doi:https://doi.org/10.1126/science.1131702`.

[17] M Amenomori, XJ Bi, D Chen, SW Cui, LK Ding, XH Ding, C Fan, CF Feng, Zhaoyang Feng, ZY Feng, et al. On temporal variations of the multi-TeV cosmic ray anisotropy using the Tibet III Air Shower Array. *The Astrophysical Journal*, 711(1):119, 2010. `doi:https://doi.org/10.1088/0004-637X/711/1/119`.

[18] Yasuo Arai, T Miyoshi, Y Unno, T Tsuboyama, S Terada, Y Ikegami, R Ichimiya, T Kohriki, K Tauchi, Y Ikemoto, et al. Development of SOI pixel process technology. *Nuclear Instruments and Methods in Physics Research Section A: Accelerators, Spectrometers, Detectors and Associated Equipment*, 636(1):S31–S36, 2011. `doi:https://doi.org/10.1016/j.nima.2010.04.081`.

[19] WB Atwood, Aous A Abdo, Markus Ackermann, W Althouse, B Anderson, M Axelsson, Luca Baldini, J Ballet, DL Band, Guido Barbiellini, et al. The Large Area Telescope on the Fermi gamma-ray space telescope mission. *The Astrophysical Journal*, 697(2):1071, 2009. `doi:https://doi.org/10.1088/0004-637X/697/2/1071`.

[20] WB Atwood, R Bagagli, Luca Baldini, R Bellazzini, G Barbiellini, F Belli, T Borden, A Brez, M Brigida, GA Caliandro, et al. Design and initial tests of the tracker-converter of the Gamma-ray Large Area Space Telescope. *Astroparticle Physics*, 28(4-5):422–434, 2007. `doi:https://doi.org/10.1016/j.astropartphys.2007.08.010`.

[21] WB Atwood, GLAST Collaboration, et al. Gamma large area silicon telescope (GLAST) applying silicon strip detector technology to the detection of gamma rays in space. *Nuclear Instruments and Methods in Physics Research Section A: Accelerators, Spectrometers, Detectors and Associated Equipment*, 342(1):302–307, 1994. `doi:https://doi.org/10.1016/0168-9002(94)91444-3`.

[22] H Augustin, N Bergerb, S Dittmeiera, F Ehrlerc, J Hammericha, A Herkerta, L Hutha, D Immiga, J Kroegera, I Perićc, et al. MuPix8-A large-area HV-MAPS chip. In *26th International Workshop on Vertex Detectors*, 2017. `doi:https://doi.org/10.22323/1.309.0057`.

[23] Philipp Azzarello, Giovanni Ambrosi, R Asfandiyarov, P Bernardini, B Bertucci, Alessio Bolognini, F Cadoux, M Caprai, I De Mitri, M Domenjoz, et al. The DAMPE silicon–tungsten tracker. *Nuclear Instruments and Methods in Physics Research Section A: Accelerators, Spectrometers, Detectors and Associated Equipment*, 831:378–384, 2016. `doi:https://doi.org/10.1016/j.nima.2016.02.077`.

[24] Amir A Bahadori, Edward J Semones, Ramona Gaza, Martin Kroupa, Ryan R Rios, Nicholas N Stoffle, Thomas Campbell-Ricketts,

Lawrence S Pinsky, and Daniel Turecek. Battery-operated independent radiation detector data report from exploration flight test 1. 2015. doi:https://krex.k-state.edu/dspace/bitstream/handle/2097/34592/TP-2015-218575.pdf?sequence=1&isAllowed=y.

[25] B Bartoli, P Bernardini, XJ Bi, I Bolognino, P Branchini, A Budano, AK Calabrese Melcarne, P Camarri, Z Cao, R Cardarelli, et al. Medium scale anisotropy in the TeV cosmic ray flux observed by ARGO-YBJ. *Physical Review D*, 88(8):082001, 2013. doi:https://doi.org/10.1103/PhysRevD.88.082001.

[26] J Baudot, G Bertolone, A Brogna, G Claus, C Colledani, Y Degerli, R De Masi, A Dorokhov, G Doziere, W Dulinski, et al. First test results of MIMOSA-26, a fast CMOS sensor with integrated zero suppression and digitized output. In *2009 IEEE Nuclear Science Symposium Conference Record (NSS/MIC)*, pages 1169–1173. IEEE, 2009. doi:https://doi.org/10.1109/NSSMIC.2009.5402399.

[27] Hans Bichsel. Straggling in thin silicon detectors. *Reviews of Modern Physics*, 60(3):663, 1988. doi:https://doi.org/10.1103/RevModPhys.60.663.

[28] A. Blondel, A. Bravar, M. Pohl, S. Bachmann, N. Berger, M. Kiehn, A. Schöning, D. Wiedner, B. Windelband, P. Eckert, H. C. Schultz-Coulon, W. Shen, P. Fischer, I. Perić, M. Hildebrandt, P. R. Kettle, A. Papa, S. Ritt, A. Stoykov, G. Dissertori, C. Grab, R. Wallny, R. Gredig, P. Robmann, and U. Straumann. Research proposal for an experiment to search for the decay $\mu \longrightarrow$ eee, 2013. arXiv:arXiv:1301.6113, doi:https://arxiv.org/abs/1301.6113.

[29] V Bonvicini, G Barbiellini, M Boezio, E Mocchiutti, Paolo Schiavon, G Scian, A Vacchi, G Zampa, N Zampa, D Bergström, et al. The PAMELA experiment in space. *Nuclear Instruments and Methods in Physics Research Section A: Accelerators, Spectrometers, Detectors and Associated Equipment*, 461(1-3):262–268, 2001. doi:https://doi.org/10.1016/S0168-9002(00)01221-3.

[30] Maurizio Boscardin, Luciano Bosisio, G-F Dalla Betta, Paolo Gregori, Irina Rachevskaia, and Nicola Zorzi. Development of ALICE microstrip detectors at IRST. *Nuclear Instruments and Methods in Physics Research Section A: Accelerators, Spectrometers, Detectors and Associated Equipment*, 461(1-3):188–191, 2001. doi:https://doi.org/10.1016/S0168-9002(00)01203-1.

[31] R Brunetti, C Jacoboni, F Nava, L Reggiani, G Bosman, and RJJ Zijlstra. Diffusion coefficient of electrons in silicon. *Journal of Applied Physics*, 52(11):6713–6722, 1981. doi:https://doi.org/10.1063/1.328622.

[32] Jorge Casaus. The AMS-02 experiment on the ISS. In *Journal of Physics: Conference Series*, volume 171, page 012045. IOP Publishing, 2009. `doi: https://doi.org/10.1088/1742-6596/171/1/012045`.

[33] M Casolino, P Picozza, F Altamura, A Basili, N De Simone, V Di Felice, MP De Pascale, L Marcelli, M Minori, M Nagni, et al. Launch of the space experiment PAMELA. *Advances in Space Research*, 42(3):455–466, 2008. `doi:https://doi.org/10.1016/j.asr.2007.07.023`.

[34] Paolo W Cattaneo, HERD collaboration, et al. The space station based detector HERD: precise high energy cosmic rays physics and multimessenger astronomy. *Nuclear and Particle Physics Proceedings*, 306:85–91, 2019. `doi:https://doi.org/10.1016/j.nuclphysbps.2019.07.013`.

[35] Liejian Chen, Y Zhang, Hongbo Zhu, X Ai, M Fu, R Kiuchi, Y Liu, Z Liu, X Lou, Y Lu, et al. Characterization of the prototype CMOS pixel sensor JadePix-1 for the CEPC vertex detector. *Journal of Instrumentation*, 14(05):C05023, 2019. `doi:https://doi.org/10.1088/1748-0221/14/05/C05023`.

[36] AG Chynoweth and KG McKay. Threshold energy for electron-hole pair-production by electrons in silicon. *Physical Review*, 108(1):29, 1957. `doi: https://doi.org/10.1103/PhysRev.108.29`.

[37] ALICE collaboration et al. Letter of intent for the upgrade of the ALICE experiment. Technical report, CERN-LHCC-2012-012, LHCC-I-022, 2012.

[38] Chris Constantinou, FH Attix, and Bhudatt R Paliwal. A solid water phantom material for radiotherapy x-ray and γ-ray beam calibrations. *Medical physics*, 9(3):436–441, 1982. `doi:https://doi.org/10.1118/1.595063`.

[39] G De Robertis, G Fanizzi, F Loddo, V Manzari, and M Rizzi. A MOdular System for Acquisition, Interface and Control (MOSAIC) of detectors and their related electronics for high energy physics experiment. In *EPJ Web of Conferences*, volume 174, page 07002. EDP Sciences, 2018. `doi:https://doi.org/10.1051/epjconf/201817407002`.

[40] M Deveaux, B Arnoldi-Meadows, G Bertolone, G Claus, A Dorokhov, M Goffe, A Himmi, K Jaaskelainen, P Klaus, M Koziel, et al. Observations on MIMOSIS-0, the first dedicated CPS prototype for the CBM MVD. *arXiv preprint arXiv:1909.05614*, 2019. `doi:https://doi.org/10.1016/j.nima.2019.162653`.

[41] Yongwei Dong, Mario Nicola Mazziottai, Tianwei Bao, Giovanni Ambrosi, Roland Walter, Ming Xu, Junjing Wang, Xiaojun Bi, Oscar Adriani, Ivan De Mitri, et al. A novel 3-D calorimeter for the High Energy cosmic-Radiation Detection (HERD) facility onboard China's Future Space Station. *PoS*, page 253, 2017. `doi:https://doi.org/10.22323/1.301.0253`.

[42] A Dorokhov, G Bertolone, J Baudot, C Colledani, G Claus, Y Degerli, R De Masi, M Deveaux, G Dozière, W Dulinski, et al. High resistivity CMOS pixel sensors and their application to the STAR PXL detector. *Nuclear Instruments and Methods in Physics Research Section A: Accelerators, Spectrometers, Detectors and Associated Equipment*, 650(1):174–177, 2011. doi:https://doi.org/10.1016/j.nima.2010.12.112.

[43] Jordi Duarte-Campderros, Esteban Curras, Marcos Fernandez, Gervasio Gomez, Andrea Garcia, Javier Gonzalez, Esther Silva, Ivan Vila, Richard Jaramillo, Marco Meschini, et al. Results on proton-irradiated 3D pixel sensors interconnected to RD53A readout ASIC. *arXiv preprint arXiv:1903.12531*, 2019. doi:https://doi.org/10.1016/j.nima.2019.162625.

[44] CE Fichtel, DL Bertsch, J Chiang, BL Dingus, JA Esposito, JM Fierro, RC Hartman, SD Hunter, G Kanbach, DA Kniffen, et al. The first energetic gamma-ray experiment telescope (EGRET) source catalog. *The Astrophysical Journal Supplement Series*, 94:551–581, 1994. doi:https://doi.org/10.1086/192082.

[45] Eric R Fossum. CMOS image sensors: Electronic camera-on-a-chip. *IEEE transactions on electron devices*, 44(10):1689–1698, 1997. doi:https://doi.org/10.1109/16.628824.

[46] V Friese. The CBM experiment at GSI/FAIR. *Nuclear Physics A*, 774:377–386, 2006. doi:https://doi.org/10.1016/j.nuclphysa.2006.06.018.

[47] AM Galper, P Picozza, O Adriani, M Ambriola, GC Barbarino, A Basili, GA Bazilevskaja, R Bellotti, M Boezio, EA Bogomolov, et al. International russian-italian mission "RIM-PAMELA". In *Particle Physics On The Eve Of LHC*, pages 199–206. World Scientific, 2009.

[48] P Giubilato, M Battaglia, D Bisello, M Caselle, P Chalmet, L Demaria, Y Ikemoto, K Kloukinas, SC Mansuy, S Mattiazzo, et al. Monolithic pixels on moderate resistivity substrate and sparsifying readout architecture. *Nuclear Instruments and Methods in Physics Research Section A: Accelerators, Spectrometers, Detectors and Associated Equipment*, 731:146–153, 2013. doi:https://doi.org/10.1016/j.nima.2013.04.042.

[49] Bojan Hiti, Tomasz Hemperek, Ivan Berdalović, Nuria Egidos Plaja, Valerio Dao, Tienyang Wang, Wermes Norbert, Magdalena Münker, Igor Mandić, Abhishek Sharma, et al. Development of the monolithic "MALTA" CMOS sensor for the ATLAS itk outer pixel layer. *PoS*, page 155, 2019. doi:https://doi.org/10.22323/1.343.0155.

[50] Alan Hoffman, Markus Loose, and Vyshnavi Suntharalingam. Cmos detector technology. *Experimental Astronomy*, 19(1-3):111–134, 2005. doi:https://doi.org/10.1007/s10686-005-9013-2.

[51] J Kemmer. Improvement of detector fabrication by the planar process. *Nuclear Instruments and Methods in Physics Research Section A: Accelerators, Spectrometers, Detectors and Associated Equipment*, 226(1):89–93, 1984. doi:https://doi.org/10.1016/0168-9002(84)90173-6.

[52] Thomas Kirn, AMS-02 TRD Collaboration, et al. The AMS-02 TRD on the International Space Station. *Nuclear Instruments and Methods in Physics Research Section A: Accelerators, Spectrometers, Detectors and Associated Equipment*, 706:43–47, 2013. doi:https://doi.org/10.1016/j.nima.2012.05.010.

[53] Yuji Kishimoto, Shinichi Sasaki, Kiwamu Saito, Kazutoshi Takahashi, Tadayoshi Doke, Kentaro Miuchi, Tetsuhito Fuse, Aiko Nagamatsu, Yukio Uchihori, Hisashi Kitamura, et al. Basic performance of a position-sensitive tissue-equivalent proportional chamber (PS-TEPC). *Nuclear Instruments and Methods in Physics Research Section A: Accelerators, Spectrometers, Detectors and Associated Equipment*, 732:591–594, 2013. doi:https://doi.org/10.1016/j.nima.2013.05.149.

[54] U Kötz, KU Pösnecker, E Gatti, E Belau, D Buchholz, R Hofmann, R Klanner, G Lutz, E Neugebauer, HJ Seebrunner, et al. Silicon strip detectors with capacitive charge division. *Nuclear Instruments and Methods in Physics Research Section A: Accelerators, Spectrometers, Detectors and Associated Equipment*, 235(3):481–487, 1985. doi:https://doi.org/10.1016/0168-9002(85)90097-X.

[55] Martin Kroupa, Amir Bahadori, Thomas Campbell-Ricketts, Anton Empl, Son Minh Hoang, John Idarraga-Munoz, Ryan Rios, Edward Semones, Nicholas Stoffle, Lukas Tlustos, et al. A semiconductor radiation imaging pixel detector for space radiation dosimetry. *Life sciences in space research*, 6:69–78, 2015. doi:https://doi.org/10.1016/j.lssr.2015.06.006.

[56] G La Vacca et al. Search for cosmic ray anisotropy with the Alpha Magnetic Spectrometer on the International Space Station. *arXiv preprint arXiv:1612.08957*, 2016. doi:arXiv:1612.08957.

[57] Xavier Llopart, Rafael Ballabriga, Michael Campbell, Lukas Tlustos, and Winnie Wong. Timepix, a 65k programmable pixel readout chip for arrival time, energy and/or photon counting measurements. *Nuclear Instruments and Methods in Physics Research Section A: Accelerators, Spectrometers, Detectors and Associated Equipment*, 581(1-2):485–494, 2007. doi:https://doi.org/10.1016/j.nima.2007.08.079.

[58] K Lübelsmeyer, A Schultz von Dratzig, M Wlochal, G Ambrosi, P Azzarello, R Battiston, R Becker, U Becker, B Bertucci, K Bollweg, et al. Upgrade of the Alpha Magnetic Spectrometer (AMS-02) for long term operation on the International Space Station (ISS). *Nuclear Instruments and Methods in Physics Research Section A: Accelerators, Spectrometers,*

Detectors and Associated Equipment, 654(1):639–648, 2011. `doi:https://doi.org/10.1016/j.nima.2011.06.051`.

[59] M Mager, ALICE Collaboration, et al. ALPIDE, the Monolithic Active Pixel Sensor for the ALICE ITS upgrade. *Nuclear Instruments and Methods in Physics Research Section A: Accelerators, Spectrometers, Detectors and Associated Equipment*, 824:434–438, 2016. `doi:https://doi.org/10.1016/j.nima.2015.09.057`.

[60] P Martinengo, Alice Collaboration, et al. The new Inner Tracking System of the ALICE experiment. *Nuclear Physics A*, 967:900–903, 2017. `doi:https://doi.org/10.1016/j.nuclphysa.2017.05.069`.

[61] G Mazza, G Aglieri Rinella, F Benotto, Y Corrales Morales, T Kugathasan, A Lattuca, M Lupi, and I Ravasenga. A 1.2 Gb/s Data Transmission Unit in CMOS 0.18 μm technology for the ALICE Inner Tracking System front-end ASIC. *Journal of Instrumentation*, 12(02):C02009, 2017. `doi:https://doi.org/10.1088/1748-0221/12/02/c02009`.

[62] Kimiyoshi Naito, Yoshihisa Tanaka, Jenn-Ming Yang, and Yutaka Kagawa. Tensile properties of ultrahigh strength pan-based, ultrahigh modulus pitch-based and high ductility pitch-based carbon fibers. *Carbon*, 46(2):189–195, 2008. `doi:https://doi.org/10.1016/j.carbon.2007.11.001`.

[63] Serena Panati, J Olave, A Rivetti, L Pancheri, F Cossio, P Giubilato, D Pantano, S Mattiazzo, MD Da Rocha Rolo, and N Demaria. MATISSE: A versatile readout electronics for Monolithic Active Pixel Sensors characterization. In *2017 IEEE Nuclear Science Symposium and Medical Imaging Conference (NSS/MIC)*, pages 1–4. IEEE, 2017. `doi:https://doi.org/10.1109/NSSMIC.2017.8532806`.

[64] L Pancheri, J Olave, S Panati, A Rivetti, F Cossio, M Rolo, N Demaria, P Giubilato, D Pantano, and S Mattiazzo. A 110 nm CMOS process for fully-depleted pixel sensors. *Journal of Instrumentation*, 14(06):C06016, 2019. `doi:https://doi.org/10.1088/1748-0221/14/06/C06016`.

[65] Sherwood I Parker, Christopher J Kenney, and Julie Segal. 3D—A proposed new architecture for solid-state radiation detectors. *Nuclear Instruments and Methods in Physics Research Section A: Accelerators, Spectrometers, Detectors and Associated Equipment*, 395(3):328–343, 1997. `doi:https://doi.org/10.1016/S0168-9002(97)00694-3`.

[66] Mark Pearce. The status of the PAMELA experiment. *Nuclear Physics B-Proceedings Supplements*, 113(1-3):314–321, 2002. `doi:https://doi.org/10.1016/S0920-5632(02)01858-3`.

[67] Anna Peisert. Silicon microstrip detectors. In *Instrumentation in High Energy Physics*, pages 1–79. World Scientific, 1992. `doi:https://doi.org/10.1142/9789814360333_0001`.

[68] I Perić, Christian Kreidl, and Peter Fischer. Particle pixel detectors in high-voltage CMOS technology—new achievements. *Nuclear Instruments and Methods in Physics Research Section A: Accelerators, Spectrometers, Detectors and Associated Equipment*, 650(1):158–162, 2011. doi:https://doi.org/10.1016/j.nima.2010.11.090.

[69] P Picozza, AM Galper, G Castellini, O Adriani, F Altamura, M Ambriola, GC Barbarino, A Basili, GA Bazilevskaja, R Bencardino, et al. PAMELA–a Payload for Antimatter Matter Exploration and Light-nuclei Astrophysics. *Astroparticle physics*, 27(4):296–315, 2007. doi:https://doi.org/10.1016/j.astropartphys.2006.12.002.

[70] L Pinskya, T Campbell-Rickettsa, A Empla, S Georgea, L Tlustosa, D Tureceka, D Fryb, M Kroupab, R Riosb, E Semonesb, et al. An update on Medipix in space and future plans (Medipix2, 3 & 4). In *6th International Workshop on Analogue and Mixed-Signal Integrated Circuits for Space Applications*, 2016.

[71] Hao Qiu, STAR Collaboration, et al. STAR heavy flavor tracker. *Nuclear Physics A*, 931:1141–1146, 2014. doi:https://doi.org/10.1016/j.nuclphysa.2014.08.056.

[72] Gianluca Aglieri Rinella, ALICE Collaboration, et al. The ALPIDE pixel sensor chip for the upgrade of the ALICE Inner Tracking System. *Nuclear Instruments and Methods in Physics Research Section A: Accelerators, Spectrometers, Detectors and Associated Equipment*, 845:583–587, 2017. doi:https://doi.org/10.1016/j.nima.2016.05.016.

[73] D Robinson, P Allport, L Andricek, J Bohm, C Buttar, JR Carter, A Chilingarov, AG Clark, D Ferrère, J Fuster, et al. Silicon microstrip detectors for the ATLAS SCT. *Nuclear Instruments and Methods in Physics Research Section A: Accelerators, Spectrometers, Detectors and Associated Equipment*, 485(1-2):84–88, 2002. doi:https://doi.org/10.1016/S0168-9002(02)00536-3.

[74] Philipp Roloff. The EUDET high resolution pixel telescope. *Nuclear Instruments and Methods in Physics Research Section A: Accelerators, Spectrometers, Detectors and Associated Equipment*, 604(1-2):265–268, 2009. doi:https://doi.org/10.1016/j.nima.2009.01.069.

[75] XuHui Shen, XueMin Zhang, ShiGeng Yuan, LanWei Wang, JinBin Cao, JianPing Huang, XingHong Zhu, Picozzo Piergiorgio, and JianPing Dai. The state-of-the-art of the China Seismo-Electromagnetic Satellite mission. *Science China Technological Sciences*, 61(5):634–642, 2018. doi:https://doi.org/10.1007/s11431-018-9242-0.

[76] MWE Smith, Derek Brindley Fox, DF Cowen, P Mészáros, G Tešić, J Fixelle, I Bartos, P Sommers, Abhay Ashtekar, G Jogesh Babu, et al.

197

The astrophysical multimessenger observatory network (AMON). *Astroparticle Physics*, 45:56–70, 2013. doi:https://doi.org/10.1016/j.astropartphys.2013.03.003.

[77] W Snoeys. Monolithic pixel detectors for high energy physics. *Nuclear Instruments and Methods in Physics Research Section A: Accelerators, Spectrometers, Detectors and Associated Equipment*, 731:125–130, 2013. doi:https://doi.org/10.1016/j.nima.2013.05.073.

[78] Walter Snoeys, James D Plummer, Sherwood Parker, and Christopher Kenney. PIN detector arrays and integrated readout circuitry on high-resistivity float-zone silicon. *IEEE Transactions on Electron Devices*, 41(6):903–912, 1994. doi:https://doi.org/10.1109/16.293300.

[79] Francesca Spada. AMS-02 on the international space station. *EPJ Web of Conferences*, 70, 03 2014. doi:10.1051/epjconf/20147000026.

[80] M Tavani, G Barbiellini, A Argan, F Boffelli, A Bulgarelli, P Caraveo, PW Cattaneo, AW Chen, V Cocco, E Costa, et al. The AGILE mission. *Astronomy & Astrophysics*, 502(3):995–1013, 2009. doi:https://doi.org/10.1051/0004-6361/200810527.

[81] Anita Topkar, Bharti Aggarwal, Pourus Mehta, Arvind Singh, PK Mukhopadhyay, GP Srivastava, RK Choudhury, Rao Prabhakar, et al. Silicon microstrip sensors and pad detectors for physics experiments. In *Proceedings of DAE-BRNS national symposium on nuclear instrumentation-2010*, 2010.

[82] R Turchetta. Spatial resolution of silicon microstrip detectors. *Nuclear Instruments and Methods in Physics Research Section A: Accelerators, Spectrometers, Detectors and Associated Equipment*, 335(1-2):44–58, 1993. doi:https://doi.org/10.1016/0168-9002(93)90255-G.

[83] R Turchetta. CMOS monolithic active pixel sensors (MAPS) for scientific applications: Some notes about radiation hardness. *Nuclear Instruments and Methods in Physics Research Section A: Accelerators, Spectrometers, Detectors and Associated Equipment*, 583(1):131–133, 2007. doi:https://doi.org/10.1016/j.nima.2007.08.226.

[84] R Turchetta, JD Berst, B Casadei, G Claus, C Colledani, W Dulinski, Y Hu, D Husson, JP Le Normand, JL Riester, et al. A monolithic active pixel sensor for charged particle tracking and imaging using standard VLSI CMOS technology. *Nuclear Instruments and Methods in Physics Research Section A: Accelerators, Spectrometers, Detectors and Associated Equipment*, 458(3):677–689, 2001. doi:https://doi.org/10.1016/S0168-9002(00)00893-7.

[85] A Tykhonov, G Ambrosi, R Asfandiyarov, P Azzarello, P Bernardini, B Bertucci, A Bolognini, F Cadoux, A D'Amone, A De Benedittis, et al.

198

Internal alignment and position resolution of the silicon tracker of DAMPE determined with orbit data. *Nuclear Instruments and Methods in Physics Research Section A: Accelerators, Spectrometers, Detectors and Associated Equipment*, 893:43–56, 2018. `doi:https://doi.org/10.1016/j.nima.2018.02.105`.

[86] I Valin, C Hu-Guo, J Baudot, G Bertolone, A Besson, C Colledani, G Claus, A Dorokhov, G Dozière, W Dulinski, et al. A reticle size CMOS pixel sensor dedicated to the STAR HFT. *Journal of Instrumentation*, 7(01):C01102, 2012. `doi:https://doi.org/10.1088/1748-0221/7/01/C01102`.

[87] James A Van Allen. The geomagnetically trapped corpuscular radiation. *Journal of Geophysical Research*, 64(11):1683–1689, 1959. `doi:https://doi.org/10.1029/jz064i011p01683`.

[88] Jacobus Willem van Hoorn. Study and development of a novel silicon pixel detector for the upgrade of the ALICE Inner Tracking system. Technical report, 2015. `doi:http://inspirehep.net/record/1429449/`.

[89] Martin Walt. *Introduction to geomagnetically trapped radiation*. Cambridge University Press, 2005.

[90] M Walter and AW Wolfendale. Early history of cosmic particle physics. *The European Physical Journal H*, 37(3):323–358, 2012. `doi:https://doi.org/10.1140/epjh/e2012-30020-1`.

[91] Fuyue Wang, Benjamin Nachman, and Maurice Garcia-Sciveres. Ultimate position resolution of pixel clusters with binary readout for particle tracking. *Nuclear Instruments and Methods in Physics Research Section A: Accelerators, Spectrometers, Detectors and Associated Equipment*, 899:10–15, 2018. `doi:https://doi.org/10.1016/j.nima.2018.04.053`.

[92] P Zuccon et al. The AMS silicon tracker: Construction and performance. *Nuclear Instruments and Methods in Physics Research Section A: Accelerators, Spectrometers, Detectors and Associated Equipment*, 596(1):74–78, 2008. `doi:https://doi.org/10.1016/j.nima.2008.07.116`.